UNIVERSITY OF SOUTHAMPTON

FACULTY OF ENGINEERING, SCIENCE
AND MATHEMATICS
SCHOOL OF OCEAN AND EARTH SCIENCE

CONTROLS ON SEDIMENTATION IN SUBMARINE CANYONS: NAZARE, SETUBAL AND CASCAIS CANYONS, WEST IBERIAN MARGIN

Raquel Georgina Arzola

Thesis for the degree of Doctor of Philosophy

December 2008

ABSTRACT

This thesis presents one of the most comprehensive studies on submarine canyons yet. It integrates data on the geology, geochemistry, sedimentology and oceanography of the Nazaré, Setúbal and Cascais canyons, west Iberian margin, in order to constrain the processes and controls of past and present sedimentation in this area. The results indicate that, during the glacial stages, turbidity currents are the dominant process of sediment transport, erosion and deposition in these canyons. Turbidity currents are mostly in the form of small-volume, high-frequency events that are generated by fluvial and hydrodynamic processes, and the flows remain mainly within the upper canyon. A smaller proportion of turbidity currents are large-volume, low-frequency, seismic-triggered events that flush through the entire canyons. Catastrophic mass wasting is most prominent in Setúbal Canyon due to its closer proximity to the region's active fault zone along the southern Iberian margin.

During the Holocene, sedimentary activity in Setúbal and Cascais canyons continued in the form of frequent, canyon-flushing turbidity currents that ceased abruptly ca 6.4 ka. This interval corresponds to both a regional aridification event that affected the Mediterranean and northern African regions, and to a decline in rising sea level. A combination of the two events is interpreted as being the direct cause of the cessation in sedimentary activity on the continental margin. In Nazaré Canyon, sedimentary activity during the last ~1000 years has been dominated by a mid-canyon resuspension depocentre that is controlled by small-volume, low-energy, hydrodynamic-generated turbidity currents. This depocentre provides a unique high-resolution record of recent sedimentation in a deep-sea setting, preserving a potential forest fire debris signal that is linked to a change in climate during the Little Ice Age.

The conclusions from this work are that sedimentation in the west Iberian canyons is controlled by the complex interplay between several variables, the most important ones being the source and supply of sediment, the hydrodynamic conditions on the shelf and slope, and the canyon morphology. The sedimentary activity in the river-fed Setúbal and Cascais canyons is found to be affected more by regional climatic changes than by eustatic sea-level changes, and in Nazaré Canyon by the supply of sediment along the shelf.

To Janet
In loving memory

CONTENTS

Appendices (on CD-ROM)

LIST OF FIGURES

LIST OF TABLES

DECLARATION OF AUTHORSHIP

I, Raquel Georgina Arzola, declare that this thesis, ‘Controls on sedimentation in submarine canyons: Nazaré, Setúbal and Cascais canyons, west Iberian margin’, and the work presented in it are my own and have been generated by me as the result of my own original research.

I confirm that:

1. This work was done wholly while in candidature for a research degree at this University;
2. Where any part of this thesis has previously been submitted for a degree or any other qualification at this University or any other institution, this has been clearly stated;
3. Where I have consulted the published work of others, this is always clearly attributed;
4. Where I have quoted from the work of others, the source is always given. With the exception of such quotations, this thesis is entirely my own work;
5. I have acknowledged all main sources of help;
6. Where the thesis is based on work done by myself jointly with others, I have made clear exactly what was done by others and what I have contributed myself;
7. Parts of this work have been published as:

Arzola, R.G., Wynn, R.B., Lastras, G., Masson, D.G., Weaver, P.P.E. (2008). Sedimentary features and processes in the Nazaré and Setúbal submarine canyons, west Iberian margin. *Marine Geology* **250**, 64-88.

Lastras, G., **Arzola, R.G.,** Masson, D.G., Wynn, R.B., Huvenne, V., Huhnerbach, V., Canals, M. (2009). Geomorphology and evolution of the

Central Portuguese Submarine Canyons, Western Iberian Margin. *Geomorphology* **103**, 310-329.

Arzola, R.G., Weaver, P.P.E., Masson, D.G., Wynn, R.B. (submitted). Regional and eustatic climate control on turbidite sedimentation on the west Iberian margin. *Journal of Sedimentary Research*.

Arzola, R.G., Masson, D.G., Roberts, A.P., Weaver, P.P.E. (submitted) A forest fire record from the last 1000 years preserved in a deep-sea setting: Nazaré Canyon, west Iberian margin. *Quaternary Science Reviews.*

Signed: Raquel G. Arzola

Date: 18/12/2008

ACKNOWLEDGEMENTS

Many people have been involved, directly or indirectly, in the successful completion of this thesis. First and foremost, I'd like to thank my trio of supervisors, who played an important role in this Ph.D.: Russ for his detailed training in core identification and the time he dedicated to me in discussions and general career advice, Doug for his honest suggestions and invaluable discussions, and Phil for initially taking me on as a research assistant back in 2004 and for giving me the opportunity to study for an MRes that subsequently led to this Ph.D. I wouldn't be here if it weren't for them and I couldn't have asked for a better team.

Many colleagues helped with or were responsible for obtaining data for this thesis, both in and out of NOCS. They are, in no particular order, Veerle Huvenne, Guy Rothwell, Fran Rowlands, Pawel Gaça, Andrew Roberts, Liao Chang, Carlos César Jesus, Darryl Green, Doug Connelly, John Marshall, Shir Akbari, Richard Pearce, Jeremy Sothcott and Belinda Alker. Extra special thanks go to Ross Williams and Xiang Sungchao for all the time and patience that they dedicated to me. Finally, thanks to Alexis Vizcaíno, Eulàlia Gracia, Henko de Stigter and Kostas Kiriakoulakis for invaluable discussions throughout the Ph.D., and to Tjeerd van Weering and Justin Dix for helpful corrections to the original thesis manuscript.

I would also like to thank the Masters and crew of cruises D297, CD157 and JC10 for making them such successful and enjoyable experiences, with special thanks to Jez Evans for his masterful piston coring.

Finally, thanks to my friends and colleagues at NOCS – Sarah, Abi, Pierre, Mark, Mike and members of the basketball team. Last but not least to the Arzolas, Smiths and especially John for the continued cheerleading!

CHAPTER 1

Introduction

1.1 Submarine canyons – a review

1.1.1 What are submarine canyons?

Submarine canyons are incisions in the continental shelf and/or slope that occur along both active and passive margins throughout the world. Examples of well-studied canyon systems are those along the US Atlantic coast (Prior and Doyle, 1985; Stanley et al., 1986; Gardner, 1989; Segall et al., 1989; Sanford et al., 1990), those off the coast of California (Paull et al., 2003; Mullenbach et al., 2004; Puig et al., 2004a; Paull et al., 2005; Drexler et al., 2006), the Var Canyon (e.g. Piper and Savoye, 1993; Mulder et al., 1998; Klaucke et al., 2000; Mulder et al., 2001) and the Zaire/Congo Canyon (Babonneau et al., 2002; Khripounoff et al., 2003). Such studies have found that submarine canyons are typically incised into the bedrock by several hundreds of metres, which results in a steeply-sided, V-shaped geomorphology that widens out to become more U-shaped away from the continental slope, and that they are dominated by erosional sedimentary processes.

Submarine canyons differ from submarine channels because the latter are incised into unconsolidated sediment, typically in a relatively low-gradient deep-sea fan that extends basinward from a canyon mouth, and are dominated by depositional elements such as levees and lobes. They are thus commonly referred to as channel-levee systems or complexes, or even fan valleys, and examples include the Var Fan system (Piper and Savoye, 1993), Monterey Fan system (Masson et al., 1995 and Normark, 1999), and Hueneme and Amazon fan systems (Piper and Normark, 2001). However, there is no clear definition to separate a canyon from a channel because they are morphologically variable and usually merge from one to the other (Mayall et al., 2006; Wynn et al., 2007). The west Iberian margin canyons do not have well-developed distal channel-levee or fan systems, therefore the entire feature, from the proximal incised head to the distal mouth, is termed a canyon in this thesis.

Our knowledge of the morphological features and sedimentary processes in deep-sea canyon and channel systems made its greatest advances during the 1950s and 1960s. Pioneering studies on the causes and processes of sediment flow in canyon and channel systems (e.g. Heezen and Ewing, 1952; Menard, 1964; Morgenstern, 1967; Shepard and

Buffington, 1968; Shepard et al., 1969) drew on the newly published experimental concepts of density gradients, autosuspension, bankful flow and flow expansion (Kuenen, 1950, 1955; Menard, 1955; Bagnold, 1962). Along with the mid-1960s' technological advances in continuous seismic reflection profiling, 3.5 kHz high-resolution profiling, sidescan sonar imaging and sediment sampling methods (Normark and Piper, 1991), the result was a significant amount of data being generated and published on upper canyon and shelf sedimentary processes. However, much less was (and still is) known about the active sedimentary processes taking place in the deeper fan and channel systems and in the steep and rugged middle to lower canyon sections, due mainly to difficulties in sampling and direct monitoring of gravity flows (e.g. Khripounoff et al., 2003; Paull et al., 2003; Xu et al., 2004). Studying the sedimentary processes in these hard to reach areas still requires drawing on the results of experimental, outcrop and model analogues of canyon and channel systems (e.g. Bagnold, 1962; Komar, 1971, 1975; Parker et al., 1987; Clark and Gardiner, 2000; Cronin et al., 2000; Elliott, 2000; Peakall et al., 2000; Kneller, 2003).

1.1.2 Oceanographic processes

Submarine canyons are deep incisions in the continental slope. They therefore have a big impact on the movement of water masses both vertically and laterally along continental margins, despite only covering a relatively narrow area, and affect the movement of sediment from onshore to offshore, the surface productivity and ecosystem functioning in slope environments.

Areas of continental slope with high critical gradients, i.e. which match the angle at which internal waves travel (typically 3º, Zhang et al., 2008), have been shown to strengthen the internal waves (e.g. Holloway, 1996; Zhang et al., 2008), and these waves become reflected and focused within incised canyon heads (Cacchione and Southard, 1974; Cacchione and Drake, 1986). Very high current velocities have therefore been documented within several canyon systems, typically one order of magnitude higher than on the adjacent open slope, e.g. Baltimore Canyon (Gardner, 1989), Monterey Canyon (Petruncio et al., 1998; Kunze et al., 2002), Guadiaro Canyon (Puig et al., 2004b) and Nazaré Canyon (Vitorino et al., 2002a, b). High down-canyon current velocities have also been associated with dense shelf water cascading (Canals et al., 2006), whereby cold and dry winds, blowing from inland, cool the coastal waters, causing them to become denser and sink, overflow the shelf edge and cascade down-slope for several hundreds of metres. Although the oceanographic conditions on the west Iberian margin are unsuitable for this process to occur, it is the dominant oceanographic process in some other continental margins around the world, some of which have canyons (Shapiro et al., 2003; Ivanov et al., 2004; Durrieu de Madron et al., 2005).

Wind also has an impact on the movement of waters in canyons. Coriolis-driven Ekman transport of surface waters can lead to seasonal upwelling and downwelling regimes on continental margins, depending on wind direction. Where canyons are present on the margin, they funnel these vertical movements of water through them (Kampf, 2007), leading to an enhancement of the effects, such as biological productivity due to upwelling (e.g. Alt-Epping et al., 2007), in the vicinity of the canyons. Other oceanography-controlled processes are bottom currents (e.g. Faugères and Stow, 1993; Wynn and Stow, 2002), but these are more important in distal channel-levee systems than in submarine canyons.

1.1.3 Sedimentary processes

Background marine sedimentation is composed mainly of pelagic material, i.e. calcareous tests of planktonic organisms falling from the surface of the ocean to the sea floor. Where it becomes mixed with fine-grained terrigenous sediment grains, as it sinks through the water column, it is termed hemipelagic sediment. The sedimentation rate of hemipelagite is typically only a few cm per ka in the open ocean.

Other sedimentary processes involve the active movement of sediment into, through and out of canyons. Some processes are controlled by oceanography. Longshore drift acts both as a source of sediment input into a canyon system and a method of dispersing it (Oliveira et al., 2002b; Vitorino et al., 2002b). This is especially important in places where there is no river in direct contact with the canyon head, in which case the currents have the important role of bringing sediment to the canyon from rivers elsewhere. However, in some cases a very strong longshore drift may limit the cross-slope transfer of sediments from the coast to the head of a canyon, e.g. in Nazaré Canyon off Portugal (van Weering et al., 2002). Semidiurnal internal tides that are focused on steep continental margins produce high bottom shear velocities, and these inhibit deposition of fine sediment on steep slopes, giving rise to resuspension cells and nepheloid layers in canyons (e.g. Gardner, 1989; Cacchione et al., 2002; McCave and Hall, 2002; Puig et al., 2004b; de Stigter et al., 2007). Downwelling causes enhanced transport of suspended sediment down canyons (e.g. Oliveira et al., 2007), and dense shelf water cascading processes have been found to transport suspended sediment and organic carbon particles from the shelf to the deep-sea via canyons (e.g. Hill et al., 1998; Canals et al., 2006; Palanques et al., 2008), and erode the sea floor into large-scale furrows up to 10 m deep (e.g. Cap de Creus Canyon, Canals et al., 2006).

Sedimentary processes active in canyons but unrelated to oceanography include those caused by sediment instability. Preconditioning factors (Canals et al., 2004; Masson et al., 2006) that reduce sediment strength and stability include underconsolidation and high permeability, causing geological weakness (Pinheiro et al., 1996; Terrinha et al., 2003; Puig et al., 2004a). This may be created by accumulation of sediment in a wedge or prism at the canyon head, shelf break or canyon flanks until it eventually fails (e.g. the 1979 Nice event on the Var Fan, Cochonat et al., 1993; Mulder, 1993; Mulder et al., 1994; Klaucke and Cochonat, 1999). Steep slopes have also been interpreted as another preconditioning factor leading to sediment failure in the upper canyon (Mullenbach et al., 2004; Puig et al., 2004a), although other authors argue that there is no evidence for steep slopes per se causing failures and that increases in slope through time (e.g. due to sedimentation or tectonics) are more important in generating instability (Hühnerbach et al., 2004; Masson et al., 2006). Initial failure may be triggered by an earthquake (e.g. the abyssal plain turbidite produced by the 1755 AD Lisbon earthquake, Thomson and Weaver, 1994, and the 1929 Grand Banks event on the Laurentian Fan, Hughes Clarke et al., 1990; Piper et al., 1999a) or a storm surge (e.g. La Jolla Canyon, Inman et al., 1976; Shepard et al., 1977). All of these triggers require a certain amount of sediment availability, instability and softness in order for deformation and failure to occur (Jones and Omoto, 2000), and the resultant submarine landslides (slumps and slides) and rock falls may vary in size from a small number of displaced blocks to thousands of km^3 of failed sediment (Masson et al., 2006).

Gravity flows (also known as density flows or currents) are the means by which sediment particles are transported most efficiently down a continental slope (at least in terms of distance and velocity). They are the dominant form of sediment transport in many submarine canyons. There are two main types of gravity flow: turbidity currents and debris flows.

1.1.3.1 Turbidity currents

These are the turbulent and dilute end-member of gravity flows, characterised by Newtonian rheology (Dott, 1963; Lowe, 1979). Their main particle-support mechanism is the upward component of fluid turbulence (Middleton and Hampton, 1976; Mulder and Alexander, 2001) and their driving force is the density difference between the cloud of suspended sediment particles and the ambient water (Lowe and Guy, 2000). They are therefore composed mainly of non-cohesive sand or silt grains transported by bedload traction in the basal layer, with the muddy fraction carried in a suspension cloud above.

There are two main ways in which turbidity currents can be formed in a submarine canyon: either as a continuation of a turbulent suspended sediment plume of water at a river mouth or as a transformation from cohesive landslides/debris flows (Normark and Piper, 1991; Mulder and Syvitski, 1995). In both cases, certain triggers and preconditioning factors are required for a turbidity current to be initiated and sustained. The former situation requires a fluvial plume of suspended sediment to be transported directly into a canyon head, and the density of the plume to be greater than that of the ambient fluid (Shepard et al., 1977; Hay et al., 1982, Hay et al., 1987a, b; Mulder et al., 2001). Turbidity currents formed in this way are thus termed hyperpycnal (literally ‘low-flowing, high-density’) because their especially high density, more so when flowing into seawater, results in a dense underflow that ‘hugs’ the sea floor (e.g. in the Var Canyon, Mulder et al., 2001). Cable breaks off several rivers (e.g. Magdalena and Congo/Zaire rivers, Heezen and Hollister, 1971; Khripounoff et al., 2003) correlate with times of peak discharge, suggesting the occurrence of hyperpycnal turbidity currents as a result of fluvial plumes entering the ocean. Generation of a turbidity current via transformation of a landslide or debris flow (see following section), requires a critical proportion of non-cohesive sediment, i.e. sand or silt, that can be transported by turbulence (Middleton and Hampton, 1976; Mulder and Alexander, 2001). This can either be present in the failed sediment or be eroded from the sea floor during early passage of the flow.

The frequency of turbidity currents is commonly related to the rate of sediment supply from the coast. This means that periods of increased fluvial supply, e.g. during winter storms, will lead to higher volumes of sediment entering and/or accumulating at the head of the canyon, making failures more likely to occur, especially with the strong wave agitation associated with winter storms (e.g. Traykovski et al., 2000; Puig et al., 2004a).

The deposits produced by turbidity currents are known as turbidites. The currents' turbulent nature means that they are typically very erosive, particularly in upper canyon depths, resulting in the turbidite deposits frequently being of greater volume than the estimated initial flow volume (Piper, 1970; Mulder and Cochonat, 1996; Khripounoff et al., 2003; Talling et al., 2007). Volumetrically, turbidites are the most significant clastic accumulations in the deep sea (Kneller and Buckee, 2000) and make up much of the world's largest sedimentary bodies (e.g. the Bengal Fan, Bouma et al., 1985) and most important deep-water hydrocarbon reservoirs. On slopes, turbidite deposits tend to taper in thickness and grain size with distance from the source (e.g. Talling et al., 2004; Amy et al., 2005, Fig. 1.1A). This tapering is due to flow non-uniformity (change in velocity over space at a given point in time, i.e. within the flow, Kneller and Branney, 1995), resulting in a quasi-steady depletive flow (i.e. a non-uniform current with a negative downflow velocity gradient).

The internal structure of a 'typical' surge-type turbidity current deposit is controlled by the sediment grain sizes and flow volume (Fig. 1.1A). Deceleration of individual grains occurs continuously as long as there is sufficient turbulent energy to allow the current to pass (Bagnold, 1962; Kneller and Branney, 1995). This results in larger (sand to silt) grains moving towards the base where they are transported along a rapidly-moving basal traction layer that grades upwards and develops parallel to wavy laminae towards the top. These are intervals T*a* to T*d* (after Bouma, 1962), and reflect the upper to lower flow regime of the turbidity current. The finer clay fraction deposits out of a suspension cloud behind the coarser, rapidly-moving part of the flow, and makes up the broad interval T*e* (used in this thesis, after Bouma, 1962), which can also be subdivided into three gradual intervals T*e*1-3 (after Piper, 1978). This is overlain by a pelagic to hemipelagic interval. Hyperpycnal turbidity currents undergo the same sedimentary processes during flow and deposition, but their deposits have a coarsening-upward basal unit beneath a 'classic' fining-upward unit (Fig. 1.1B), which correspond to the periods of increasing and decreasing discharge at the river mouth, respectively (Mulder et al., 2001).

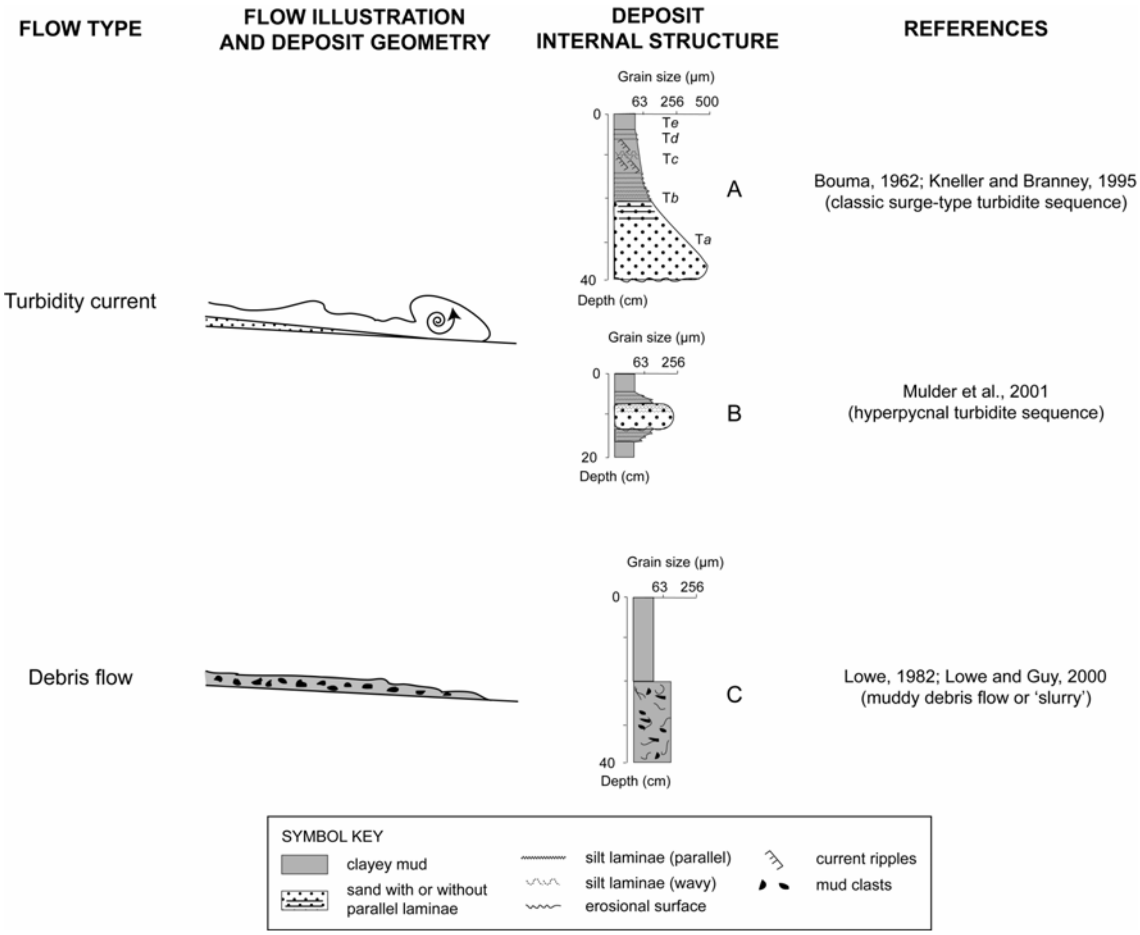

Fig. 1.1. Diagrams showing the internal structure and bed geometry of the most common types of gravity flow deposit in deep-water settings.

1.1.3.2 Debris flows

Another common gravity flow in submarine canyons is the debris flow. Debris flows are laminar and non-Newtonian or plastic (Dott, 1963; Johnson, 1970) and have a yield strength, which may be caused by cohesive strength due to muddy sediment (e.g. Hampton, 1975) or by frictional strength due to interlocking of grains (e.g. Talling et al., 2007). They flow when their driving force (the weight of the flow driven by gravity) can overcome the yield strength (Hampton, 1975; Hampton et al., 1996). Flow is interrupted when their driving force cannot be overcome by their yield strength. This usually occurs when the slope decreases or when the flows' effective 'weight' decreases, e.g. due to thinning. Therefore, debris flows do not thin indefinitely with distance like turbidity currents, and instead their entire sediment body 'freezes' en-masse, resulting in a wedge-shaped, ungraded deposit (e.g. Talling et al., 2004; Amy et al., 2005; Fig. 1.1C). The typical deposit (termed debrite) is a mass of displaced blocks of sediment and/or rock, anything from mm to tens of cm in size, embedded in a disrupted finer-grained matrix, and are typically muddy in order to maintain their high cohesive strength (e.g. Hampton, 1975; Lowe, 1982).

1.1.4 Canyon morphology

1.1.4.1 Effects of gravity flows

Submarine canyons are thought to evolve from small rills on the upper slope through which sediment can become trapped and accumulate. As the sediment accumulations become oversteepened, they fail and develop into gravity flows that are funnelled down the rills (Pratson et al., 1994; Pratson and Coakley, 1996). These localised slope failures enlarge the rills until they evolve into a headward-eroding canyon that advances upslope by sediment flow-driven retrogressive failure (Twichell and Roberts, 1982; Farre et al., 1983; Pratson and Coakley, 1996). The canyon is extended downslope by gravity flow erosion and undercutting of the continental slope bedrock (Daly, 1936; Baztan et al., 2005), leading to the typical V-shaped, incised canyon morphology with stepped terraces on the canyon walls (e.g. Lastras et al., 2009).

1.1.4.2 Effects of morphology

A striking feature of most submarine canyons and channels is their sinuosity (e.g. Kenyon et al., 1995; Babonneau et al., 2002; Lastras et al., 2009). The main causes of sinuosity in channels have been identified as constructional processes, including lateral stacking (Clark and Pickering, 1996; Gardner et al., 2003) and lateral accretion (Peakall et al., 2000; Abreu et al., 2003; Mayall et al., 2006), as well as sea-floor topography and tectonics (Cronin, 1995; Mayall and Stewart, 2000; Mayall et al., 2006). Canyons are dominantly erosive and therefore the controls on sinuosity are different to those in submarine channels. Faulting has been shown to have an important effect (Lastras et al., 2009). However, the controls of sinuosity in submarine canyons remain poorly understood.

The sinuous and confined character of submarine channels has been shown to control the evolution and flow processes of gravity flows. Turbidity currents will experience changes in the lateral velocity of the flow that, combined with centrifugal forces, cause superelevation of the flow at outer bends (Keevil et al., 2006) and potential flow stripping (Piper and Normark, 1983; Fildani et al., 2006). This results in depositional heterogeneity, with thick sandy channel fill facies and spilling over of less dense sediment to form interbedded ribbon sand and mud deposits on levees (Peakall et al., 2000; Keevil et al., 2006). These processes may occur in the lower canyon section, but in the deeply incised upper canyon section, the greater vertical thickness of gravity flows (≥100 m) is the main factor causing depositional heterogeneity (e.g. Cronin and Kidd, 1998; Salles et al., 2007). Turbidites in canyons thus do not produce long tapering deposits, but thin-bedded deposits on terraces and thick sands in the thalweg. Only very large, mixed sand- and mud-rich flows will be efficient enough to flush through the canyon and form distal fan sheet geometries (Mutti, 1979; Mutti and Normark, 1987).

1.1.5 Sea level and canyons

Higher sedimentation rates are observed on continental margins during glacial stages (e.g. Shanmugam and Moiola, 1982; Weaver et al., 2000). This is because lower sea levels expose the continental shelves, leading to better connectivity between fluvial systems and canyon heads. Sedimentation on continental margins is especially enhanced at the start and end of glacial stages due to falling sea levels and high sediment availability, respectively (Weaver and Kuijpers, 1983). Sea level fluctuations can also influence the type of flow-initiation process and gravity flow generated at the head of a canyon (Normark and Piper, 1991). Falling sea level (regression) will lead to fluvial incision and the generation of hyperpycnal turbidity currents, slumps and landslides. During rising sea level (transgression), flooding of the shelf will cut off fluvial sedimentation into the canyon, leading to dominant pelagic sedimentation and episodic flows from local canyon wall sources triggered by events such as storms or earthquakes. Oscillations in sea level can also change the locus of sediment supply into the canyon if it has a number of tributaries at different depths, e.g. Monterey Canyon (Normark and Piper, 1991).

1.2 Rationale

Previous work on submarine canyons has established that they are major pathways for the transport of sediment, associated pollutants and organic carbon from land to the deep ocean (e.g. Berner, 1982; van Weering et al., 2002; Canals et al., 2006; Richter et al., in press). However, the frequency, timing and dynamics of gravity flows in most modern canyons are poorly constrained, as is their overall role in the offshore export of sediment. This is due mainly to the difficulties involved in direct monitoring of flows in canyons (Khripounoff et al., 2003; Paull et al., 2003; Xu et al., 2004), and also to the technological problems that arise when sampling in such rugged canyon topography.

The submarine canyons of the west Iberian margin have been an attractive study area for the past 30 years. Their large variation in size, which includes the largest canyon in the entire European continent (Nazaré Canyon), and the different sediment sources enable comparisons to be made between the canyons despite their close proximity to one another. Additionally, they can be easily accessed from major ports of European countries with scientific sea-going fleets. Recently, the canyons of the west Iberian margin were studied within the EC-EUROSTRATAFORM project, which attempted to relate modern sedimentation to preserved strata on continental margins, and included the investigation of the role of these canyons in offshore sediment flux. With current oil and gas exploration moving to deeper locations, the hydrocarbon industry is increasingly investing in research to understand how sediment is transported down canyons and what controls the formation of high net:gross deposits associated with them. Large and accessible canyon systems such as those on the west Iberian margin are potential modern analogues for buried hydrocarbon-bearing systems.

Research on these canyons continues as part of the Hotspot Ecosystem Research on the Margins of European Seas (HERMES) project (Weaver et al., 2004) - an international, multidisciplinary research programme investigating the effects of physical processes on Europe’s deep marine ecosystems and seafloor environments. Following the discovery of a diverse but fragile deep water ecosystem, which includes corals and stalked crinoids (de Stigter et al., 2007; Pattenden, submitted), in the commercially trawled and fished west Iberian canyon system, it is now more vital than ever to fully understand how submarine canyon systems work.

1.3 Aim and objectives

The main aim of this thesis is to carry out a full investigation of the sedimentary processes of the west Iberian canyons, and to add a valuable contribution to the wider knowledge and understanding of these and other submarine canyon systems worldwide. It has the following specific objectives:

1. To document the features and processes of sediment transport and deposition within the Nazaré and Setúbal canyons, differentiating in particular between processes in the upper and lower canyon sections;

2. To investigate the controls on turbidite deposition in the Nazaré, Setúbal and Cascais canyons and the Tagus Abyssal Plain, distinguishing between eustatic sea level changes, regional climate and seismicity;

3. To apply this research to that of canyon systems worldwide.

1.4 Thesis structure

Chapters 1-3 provide the introduction and setting to the main work in this thesis. The major findings are presented in the three subsequent chapters. Chapter 4 provides an integrated investigation of the sedimentary features observed throughout Nazaré and Setúbal canyons and of the processes responsible for their generation. Chapter 5 investigates a distinctive high magnetic susceptibility signal recorded in sediments in a high sedimentation rate area in Nazaré Canyon. These high sedimentation rates are first presented in Chapter 4, but the sediments are described in more detail in Chapter 5 with a more accurate age-depth model and the use of different analyses in order to identify the cause of the high-magnetic susceptibility sediments. Chapter 6 presents a stratigraphic correlation based on radiocarbon dates that go back to the last glacial and spans across Setúbal and Cascais canyons and the Tagus Abyssal Plain. Finally, Chapter 7 summarises the key findings presented in Chapters 4-6 and discusses their wider implications.

Each of Chapters 4-6 has been prepared as an individual paper, therefore they contain some overlapping introductory information. Chapter 4 was published in the April 2008 issue of Marine Geology (volume 250, pages 64-88). At time of submission of this thesis, Chapter 5 had been submitted to Quaternary Science Reviews and Chapter 6 was in review with Journal of Sedimentary Research. All of these papers were written primarily by me, with guidance and contributions from my supervisors Phil Weaver, Doug Masson and Russell Wynn. Additionally, the section on canyon geomorphology in Chapter 4 and Figs. 4.1-4.3 were contributed by Galderic Lastras, and Andrew Roberts contributed to the section on remanent magnetisation in Chapter 5. For the sake of clarity and conciseness, the references for each of these chapters have been omitted and are included instead in the main reference list at the end of the thesis.

CHAPTER 2

Regional setting

2.1 Location

The west Iberian margin lies between 37º and 43.5º N and encompasses the continental shelf, slope and rise off Portugal and the southwest and northwest corners of Spain. It is incised by several submarine canyons, with the highest density being in the Central Portuguese margin (37.5º - 40.5º N). Nazaré, Setúbal-Lisbon and Cascais are the canyons that incise this part of the margin and that make up the subject of this thesis.

2.2 Onshore geology and tectonic setting

Iberia has a very diverse geology due to its unique tectonic history (Gibbons and Moreno, 2002 and references therein), and has one of the most complete Palaeozoic sedimentary sequences in Europe. Iberia was originally connected to west France along its northern margin, but rifting associated with the opening of the Atlantic Ocean 120 Ma caused the opening of the Bay of Biscay and the separation of both land masses as Iberia rotated anti-clockwise away from France over some 30 Ma. Western Iberia therefore shares the same Variscan basement geology as the northwest of France. Eastern Iberia remained a submerged ocean basin until compressional tectonics during the Alpine Orogeny (from mid-Cretaceous times until mid-late Miocene) caused its uplift and exposure, and the activation of the left lateral Azores-Gibraltar zone along the southern Iberian margin, which has remained active up to the present (Fig. 2.1). Sedimentary and historical records of palaeoearthquakes on the western Iberian margin indicate that large earthquakes (Mw ≥6) have experienced a return period of between 475 and ~2000 years during the Holocene (Peláez and López Casado, 2002; Gràcia et al., 2003; Vizcaino et al., 2006).

Tertiary and Quaternary crustal extension produced extensive normal faulting in the Iberian ranges that developed into several large-scale basins (Gutiérrez-Elorza et al., 2002). The Douro (or Duero) basin covers approximately 50,000 km^2 and has a mean altitude of 850 m. It has mountainous margins and is drained almost entiely by a single river of the same name that debouches at the city of Porto on the central west Iberian margin. Characteristic Douro basin deposits are mainly fluvial, but also aeolian, sands. The Tejo (also known as Tagus or Tajo) basin originally stretched all the way from central eastern Iberia to the SW margin, but early Miocene uplift of central eastern Iberia divided it into an upper Tejo-Madrid basin and a lower Tejo basin (Gutiérrez-Elorza et al., 2002; Fig. 2.1). The latter lies on the SW Iberian margin and is drained by the Tagus River, which leads into the Tagus Estuary at the city of Lisbon. The Quaternary sedimentary cover is mainly composed of fluvial quartzite and gravel sediments and sandy aeolian dune sediments.

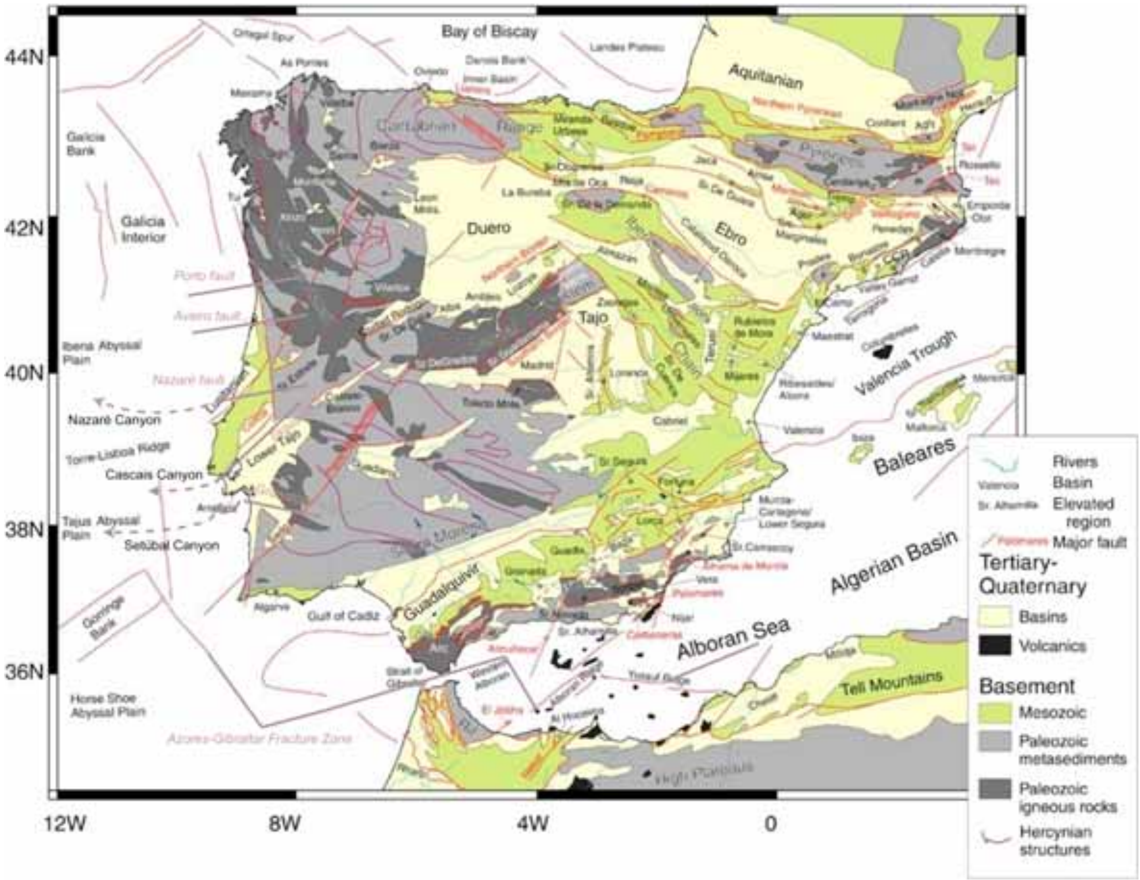

Fig. 2.1. Geological map of Iberia with locations of major and canyon-axial faults and river basins (modified with permission from Andeweg, 2002).

2.3 Marine geology and geomorphology

The west Iberian margin evolved as a non-volcanic rifted continental margin that is mainly composed of metamorphic rocks of Mesozoic age with a >1000 m thick Cenozoic sediment cover on the shelf (Coppier and Mougenot, 1982; Jouanneau et al., 1998; Alves et al., 2003). Compressional tectonics during the Alpine Orogeny led to the reactivation of ENE-WSW-trending, late-Variscan strike-slip faults, both onshore and offshore (Pinheiro et al., 1996). The submarine canyons of the west Iberian margin formed along these strike-slip faults and share the same orientation (Alves et al., 2003; Lastras et al., 2009; Fig. 2.1). These faults are therefore thought to be the slope weaknesses through which sediment was initially funnelled and which developed into the present canyon systems, primarily by downslope-eroding flows and later widened by upslope-eroding retrogressive slope failure (Pratson et al., 1994; Pratson and Coakley, 1996). The exposed late Oligocene-early Miocene rocks give a lower age limit for initial canyon incision along the margin (Alves et al., 2003) , although a more precise age cannot be constrained.

The main canyons on the Central Portuguese margin all trend ENE-WSW and all indent the narrow shelf apart from Cascais Canyon (Fig. 2.2). At ~210 km, Nazaré Canyon is the longest canyon of the entire west Iberian margin, and the most deeply incised with a maximum incision of 3500 m (Lastras et al., 2009). It has a small tributary in its upper section (Vitória Canyon) and leads from the shelf into the Iberian Abyssal Plain at approximately 5000 m water depth (WD). It has a sinuosity index (total length divided by straight length) of 1.26. Setúbal Canyon is the next largest canyon at ~175 km length and with a ≤2200 m incision, and leads from the shelf adjacent to the Sado Estuary into the Tagus Abyssal Plain (approx. 4800 m WD). It has a relatively large tributary called Lisbon Canyon (~37.5 km length, 1000 m incision), which leads from the Tagus Estuary, and their combined mean sinuosity index is 1.20. Cascais Canyon (~88 km length, ≤1800 m incision) lies just north of Setúbal Canyon and has the highest sinuosity index of all at 1.44 (Lastras et al., 2009). Axial slope angles in the canyons range from 10-15º for the upper sections, 5º for the middle sections, <5 º for the lower sections and 1º in the abyssal plains (Lastras et al., 2009). These contrast with the average slope angles for the adjacent open slopes of 6-7º (Weaver and Canals, 2003; Lastras et al., 2009; Fig. 2.2).

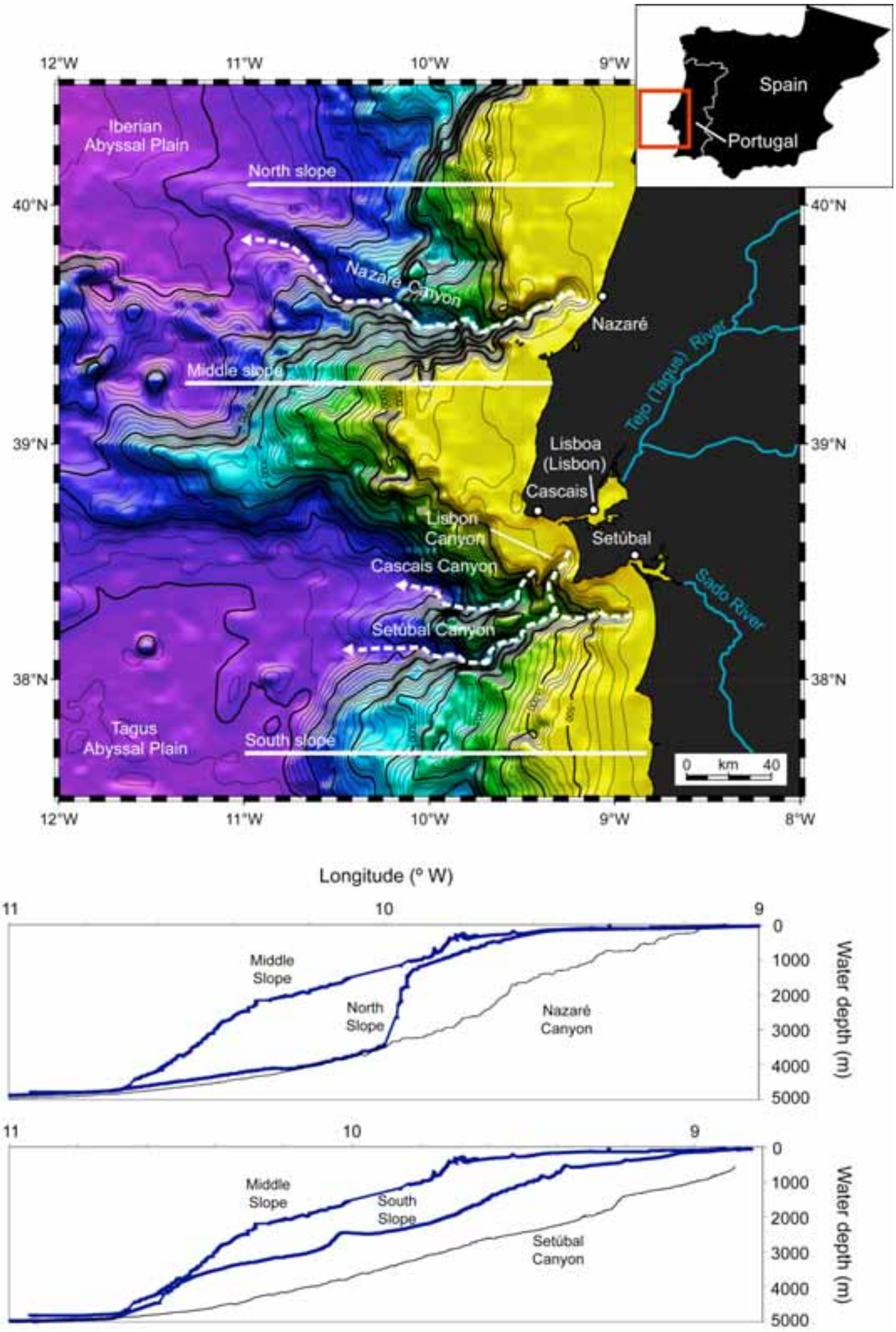

Fig. 2.2. Bathymetric image of the submarine canyons on the west Iberian margin. Contours are every 100 m and outlined in bold every 500 m. Downslope profiles of Nazaré and Setúbal canyons and of three open slope areas are indicated on the map and shown below. Both canyons (in black) are clearly incised into the continental slope (in blue) and have a steeper upper section but gentler middle and lower sections than the adjacent slopes. Open slope gradient data courtesy of H. de Stigter.

In order to simplify the description of the canyons in this thesis, we have chosen the upper-middle-lower sections classification by Vanney and Mougenot (1990); Schmidt et al. (2001); van Weering et al. (2002); and de Stigter et al. (2007). For Nazaré, Setúbal and Cascais canyons, the upper section lies at ~0-2700 m WD, the middle section at ~2700-4000 m WD and the lower section is beyond ~4000 m WD. In Chapter 4, however, the upper and middle sections of Nazaré and Setúbal canyons have been grouped together and are collectively referred to as the upper section because they show no significant differences in the sedimentary features and processes between them. In addition, the thalweg is considered to be the deepest incised part of the canyon floor, and within the broad flat-floored lower canyon, thalweg refers to secondary channels cut into the canyon floor.

2.4 Oceanography

The main shelf dynamics that take place along the west Iberian margin are related to the seasonal evolution of two major atmospheric systems, the Azores High and the Iceland Low (e.g. Fiúza et al., 1982), which are driven mainly by wind. During the summer months (July to September) the Azores High is located over the central North Atlantic and the Iceland Low is weak. These conditions cause the weather systems crossing the Northern Atlantic to remain at higher latitudes than the west Iberian margin, therefore resulting in low energy wave conditions off Iberia during the summer (Pires, 1985). This zonal gradient of atmospheric pressure during the summer is enhanced by the development of a thermal low over central Iberia (Ferreira, 1984), and drives a regime of sustained northerly winds along the margin that lead to offshore Ekman transport of surface waters and consequential upwelling (Fraga, 1981; Fiúza, 1983). Internal waves that develop at the shelf edge move along the outer shelf and, during highly energetic upwelling events, may reach the middle area of the shelf and result in episodic remobilisation of the fine sediment accumulations (Douro Mud Patch) immediately offshore of the Douro River mouth (Vitorino et al., 2002a).

In winter, the Azores High is displaced to its most southern position and the Iceland Low is reinforced (e.g. Fiúza et al., 1982). Eastward-moving low pressure systems and associated fronts passing over the North Atlantic now move towards the west Iberian margin, leading to highly energetic wave conditions (Pires, 1985). Wind directions are reversed and become more westerly and southerly (Fiúza et al., 1982), resulting in a poleward flow of about 20–30 cm s^{-1} in the water column (Vitorino et al., 2002a) and in the development of a downwelling regime along the shelf. Mixing processes cause the shelf waters to become more homogeneous during the winter and the thermocline occurs at depths of 80–100 m, intersecting the outer shelf/upper slope topography as a bottom front (Vitorino et al., 2002a).

After wind, a second factor that affects the mid-shelf currents is tides. Tidal currents in the west Iberian margin are dominated by the semidiurnal (M2) tide and have magnitudes of a few cm s^{-1} (Alonso et al., 1993; Vitorino and Coelho, 1998; McCave and Hall, 2002; Vitorino et al., 2002a). The most recent studies show that the tidal orientation or polarisation is cross-shore, i.e. parallel to the canyon axes along the margin, with bottom intensification. This suggests that the canyons play a major role in channeling tidal currents, especially towards the northern part of the margin (Oliveira et al., 2002; Vitorino et al., 2002a).

The movement of sediments on the west Iberian shelf and their export to the deep sea is largely controlled by the regional oceanographic conditions. The main sources of sediment into Setúbal, Lisbon and Cascais canyons are the Tagus and Sado Rivers, which debouch near these canyons’ heads (e.g. Jouanneau et al., 1998; Fig. 2.2). Despite the absence of a river leading into Nazaré Canyon and the high amount of sediment that remains trapped on the northern shelf (Jouanneau et al., 1998, 2002), the upper part of this canyon cuts across most of the width of the shelf, enabling it to intercept sediment from longshore currents (van Weering et al., 2002; de Stigter et al., 2007). Suspended sediment transport along the shelf is mainly southerly (e.g. Drago et al., 1998; van Weering et al., 2002); however, several studies present contrasting models of sediment supply into Nazaré Canyon from both the south and north, and even from the coast adjacent to the canyon head (e.g. Drago et al., 1998; Oliveira et al., 2002, 2007). The sediment in all the canyons of the west Iberian margin is mainly terrigenous in origin and composed of organic-rich mud and medium- to coarse-grained sands (Dias et al., 2002; Jouanneau et al., 2002; Oliveira et al., 2002; van Weering et al., 2002) with carbonate-rich hemipelagic clays of marine origin (Alt-Epping et al., 2007).

2.5 How this thesis fits in with previous studies

This thesis draws on the extensive work done on the geology and sedimentology of the west Iberian margin and submarine canyons over the past 30 years to characterise the sedimentary processes that take place throughout the Nazaré and Setúbal canyons (Chapter 4). Geochemical and lithological data are combined with studies on the region’s Holocene climate and forest fire history to uncover a unique forest fire signal in Nazaré Canyon with a regional climatic origin (Chapter 5). Finally, studies on the region’s climate change since the last glacial have been applied to the first detailed canyon-to-abyssal plain bed correlation in the area to identify what controls canyon sedimentation in the Setúbal-Lisbon and Cascais canyons (Chapter 6).

CHAPTER 3

Methods and database

3.1 Cruise work

A large proportion of the data used in this Ph.D. research were collected during a number of cruises to the west Iberian margin. Some piston cores were collected during cruises D155 (1985) and D187 (1989), but the majority of multi-beam bathymetry data, sidescan sonar data and sediment core acquisitions were carried out during EC-EUROSTRATAFORM cruises 64PE219 (2003) and CD157 (2004), and HERMES cruises D297 (2005) and CD179 (2006). The Remotely Operated Vehicle (ROV) *Isis* was deployed and additional sediment cores collected during HERMES cruise JC10 (2007). I was involved in all three HERMES cruises, including having the role of Principal Geologist during one 2-week leg of cruise CD179.

3.1.1 Multi-beam bathymetry

Multi-beam bathymetry surveys were carried out using a hull-mounted Kongsberg Simrad EM12 system. This multibeam echo sounding system operates at a frequency of 13 kHz. 81 beams make up a total beam width of between 1.8 and 3.5°. The swath width is up to 3.5 times the water depth, which can be accurately surveyed from 50 to 11,000 m. Under ideal conditions, this accuracy can be up to 0.25 % of the total depth. The surveys were calibrated using sound velocity profiles (SVP) and expendable bathythermograph (XBT) data. The swath bathymetry was logged continuously during all cruises using Mermaid software and displayed in real-time using Merlin software.

3.1.2 Sidescan sonar

Medium-resolution deep-towed sidescan sonar mapping was carried out using the TOBI system (Towed Ocean Bottom Instrument), developed at the National Oceanography Centre, Southampton (NOCS). This system operates at a frequency of 30 kHz and has a swath width of ca 6 km. It was towed at ca 400 m above the seafloor at a speed of 1-2 knots, and allows accurate surveying of seafloor features.

3.1.3 Seismic profiles

Shallow seismic profiles were collected continuously along all ship tracks using a 3.5 kHz echo-sounder system; this sub-bottom profiling system has a penetration depth of around 10-50 m, depending on lithology.

3.1.4 ROV footage

High-resolution video and photographic footage from the NERC (Natural Environment Research Council) ROV *Isis* was used for ground-truthing the sidescan sonar data on seafloor sediment cover and geological features in and around the canyons.

3.1.5 Sediment core collection

The above datasets were integrated in order to choose specific target sites along the canyon systems for sediment coring. Piston and trigger cores were recovered from these targeted sites and served to ground-truth the geophysical data (see Appendix A1). Cores have an estimated accuracy on the sea floor of between 50 and 200 m, based on the amount of drift experienced by the corer and vessel, and on the position of the sidescan sonar data relative to the bathymetry.

3.2 Sediment core analysis

A total of 33 piston cores, and accompanying trigger cores, were used in this Ph.D. research, with lengths varying between 50-75 cm for trigger cores and 1-13 m for piston cores. The different laboratory analyses that were carried out on them are described below.

3.2.1 Multi-sensor core logging

Aside from visual inspection and logging, the cores were also logged in order to obtain accurate physical property profiles and to determine changes in lithology and so distinguish between turbidites, debrites and hemipelagic sediment. The combination of multi-sensor core logging and visual analysis was deemed sufficient for distinguishing between the clayey turbidite T*e* interval of Bouma (1962) and the hemipelagic interval, without the use of detailed grain size plots for each of the 33 studied cores, and successful radiocarbon dating in Chapter 6 supports these lithological interpretations. For the purpose of simplicity, the Bouma T*e* classification (Bouma, 1962) was used in place of the Piper T*e*1-3 classification (Piper, 1978).

The Geotek^{TM} multi-sensor core logger (housed by BOSCORF at NOCS) is an automated, non-destructive and high resolution system that measures bulk density (gamma ray attenuation), P-wave velocity and low-field magnetic susceptibility (using a Bartington MS2E point sensor) at 1 cm intervals down split cores. Higher resolution magnetic susceptibility measurements were taken for U-channel samples (4 cm^2 cross-section) with a Bartington MS2C loop sensor at 0.5 cm intervals, applying a volume correction factor of 2.02 (Sagnotti et al., 2003).

3.2.2 Grain size analysis

Bulk grain size measurements were carried out using the Malvern Laser Mastersizer 2000 particle sizer at NOCS. The laser diffraction method works under the Mie theory of particle diffraction, whereby particles of a given size diffract light through a given angle, which increases with decreasing particle size, assuming that particles are spherical and in a dilute suspension (McCave and Syvitski, 2007). The wet sample was added to reverse osmosis water and calgon, which disperses the particles and prevents them from agglutinating.

3.2.3 ^{210}Pb dating

Alpha spectrometric determination of ^{210}Po activity in sediment is used as a proxy for ^{210}Pb activity, and the change in ^{210}Pb activity with sediment depth provides an accurate age-depth model for the last 100 years of sediment deposition (after Appleby and Oldfield, 1978). The decaying ^{210}Po activity with sediment depth is measured and converted to ^{210}Pb activity. Excess ^{210}Pb is then calculated by subtracting the value of constant ^{210}Po at depth. The excess ^{210}Pb is plotted against depth and a best fit straight line (or lines) calculated. The sediment accumulation rate is then calculated from the equation l/m, where l is the natural log divided by the ^{210}Pb half-life and is equal to 0.031, and m is the gradient of the natural log of excess ^{210}Pb plotted against depth. See Appendix A2 for experimental method.

3.2.4 Accelerator mass spectrometry (AMS)

The purpose of this method is to obtain an accurate age-depth model by dating carbonate-bearing organisms (i.e. foraminifera) within the sediment. Only hemipelagite with sufficient foraminifera was sampled, avoiding debrites and turbidite mud units because they typically contain insufficient organisms, and collected, where possible, directly below any redeposited unit of interest, as this minimises the risk of sampling reworked sediment (Thomson and Weaver, 1994). Approximately 1-4 cm^3 of sediment was sampled per horizon, washed through a 63 μm sieve and dried under a hot lamp. 10-20 mg of planktonic foraminifera (approximately 1000 individuals) were picked under a binocular microscope in order to yield the minimum 1-2 mg of carbon required. The main planktonic species found in these cores were *Globigerina bulloides, Globorotalia scitula, Neo-globoquadrina pachyderma, Globorotalia truncatulinoides, Globigerinoides ruber, Globorotalia inflata, Globoritalia hirsuta, Orbulina universa*.

The picked samples were dated by the AMS method at the NERC Radiocarbon Laboratory in Scotland and at Beta Analytic in Florida. The results were returned as conventional radiocarbon ages and converted to calibrated (Cal) radiocarbon ages. This conversion was done using the latest MARINE04 database and IntCal04 calibration curve (after Stuiver and Reimer, 1993; Stuiver et al., 1998; Hughen et al., 2004; Reimer et al., 2004). This calibration uses a 400-year reservoir age for a deep-sea setting, which is valid up to 21,786 Cal a BP. For older ages, the Fairbanks0107 calibration curve of Fairbanks et al. (2005) was used instead with a 255-year reservoir age. Age ranges are reported as 2 sigma (i.e. 95 % confidence limit).

3.2.5 Environmental magnetic analyses

These analyses were carried out with the specific aim of determining the cause of a high magnetic susceptibility signal in mid-Nazaré Canyon cores (see Chapter 5 for more detail). In order to measure the remanent magnetisation of the sediment, U-channel samples (4 cm^2 cross-section) were collected directly from the middle of each core section. These were run through the 2-G Enterprises cryogenic magnetometer at NOCS to measure natural (NRM), anhysteretic (ARM) and isothermal (IRM) remanent magnetisation at 1 cm intervals (Weeks et al., 1993; Roberts, 2006). The measurement sequence was as follows.

- The NRM was measured and progressively stepwise alternating field (AF) demagnetised at 5, 10, 15, 20, 25, 30, 40, 50, 60 and 80 mT. The NRM was measured after each demagnetisation treatment.
- An ARM was imparted using a 90 mT AF and an axial 0.05 mT DC bias field. The ARM was then measured and progressively AF demagnetised at 10, 20, 30, 40, 50, 60, 80 and 90 mT.
- An $IRM_{900\ mT}$ (or SIRM) was imparted to the U-channel samples by applying a 900 mT DC field using a 2-G Enterprises pulse magnetiser, and was then measured and progressively demagnetised at 10, 20, 30, 40, 50, 60, 80, 90 and 100 mT. An $IRM_{-300\ mT}$ was then imparted by applying a 300 mT DC field to the sample in the opposite direction to the SIRM. This allows calculation of the S-ratio ($-IRM_{-300\ mT}$/SIRM) and of the HIRM or ‘hard IRM’ ((SIRM - $IRM_{-300\ mT}$) / 2, e.g. King and Channell, 1991).

Magnetic hysteresis properties (i.e. the magnetic mineral’s ‘memory’ of the applied field after its removal) were measured along with first-order reversal curves (FORCs; Roberts et al., 2000) on 0.5 g samples using a Princeton Measurements Corporation vibrating sample magnetometer. In each case, 100 FORCs were measured with an averaging time of 200 ms. The FORC data were processed using the FORCinel software package (Harrison and Feinberg, 2008) and a smoothing factor of 5 (c.f. Roberts et al., 2000).

3.2.6 X-ray diffraction (XRD)

XRD was carried out by C. C. Jesus at the University of Aveiro for the mineralogical identification of bulk sediment. This involved removal of the carbonate content from sediment samples by dissolution with acetic acid (10 %). The resultant ~2 g of sample were run through an X-ray diffractometer where the incidence angle of the diffracted X-ray through the crystalline sample is converted to crystal structure and thus mineralogy of the sample. This method has an accuracy of ≥1 %.

3.2.7 Scanning electron microscope (SEM)

Sediment samples were impregnated with resin and polished, and visually analysed using a Zeiss Leo 1450VP SEM. Chemical and reflective backscatter analysis of the sediment grains was carried out using a Princeton Gamma Tech (IMIX-PTS) X-ray energy dispersive spectrometer (EDS). Real time data were processed using the SmartSEM software.

3.2.8 Micro X-ray fluorescence (XRF)

XRF analysis was carried out to obtain non-penetrative and non-destructive surface elemental concentration data and high-resolution radiographs of split cores. A Cox^{TM} ITRAX machine (housed by BOSCORF at NOCS) was used, which measures X-rays at 45º to the incident X-ray beam using a Si drift X-ray detector (energy resolution of 140 eV at 5.9 keV). The Si drift detector then measures the energy produced by the X-ray beams as they are reflected from the core surface (energy resolution of 140 eV at 5.9 keV). Tube voltage and current values of 30 kV and 30 mA respectively were used in combination with an exposure time of 20 s and measurement step-size of 500 μm. The data were then processed using the Q-Spec software (after Croudace et al., 2006).

3.2.9 Total and inorganic carbon measurements

Total carbon content was analysed by heating the sample and measuring the amount of carbon dioxide liberated by heat-decomposition of the total carbon content. To determine the inorganic carbon content, the sample was treated with a phosphoric acid solution to acid-decompose the inorganic carbon content only, as the acid does not affect the organic carbon content. The calculation of the % dry weight of carbon is a function of ‘counts’ of CO_2 (a measurement of electrical activity in the cell directly related to the amount of CO_2 produced) corrected by subtracting the counts of CO_2 from a blank sample, per unit mass. The organic carbon is inferred as the difference between the two determinands. The instruments used in both analyses were manufactured by UIC Inc.

3.3.10 Vitrinite reflectance measurement

In order to determine the presence of vitrinite (charcoal) in a sediment sample, the carbonate and silicate content of the sediment samples was removed by digestion in hydrochloric and hydrofluoric acids, leaving only the organic matter. The organic matter was mounted on slides, polished (after Hillier and Marshall, 1988), analysed (using a Zeiss UMSP 50 reflectance microscope calibrated with a diamond standard reflectivity of 5.227) and measured (using a x40 antiflex objective under cedar oil at a refractive index of 1.515). In order to make the reflectance analysis as unbiased as possible, the grain closest to the centre of the field of view was measured each time, regardless of what the grain was, and only one measurement was made per field of view. Approximately 300 random measurements were made for each homogenised slide.

CHAPTER 4

Sedimentary features and processes in the Nazaré and Setúbal submarine canyons, west Iberian margin[1]

---

[1] Published as Arzola, R.G., Wynn, R.B., Lastras, G., Masson, D.G., Weaver, P.P.E. (2008). Sedimentary features and processes in the Nazaré and Setúbal submarine canyons, west Iberian margin. *Marine Geology* **250**, 64-88.

4.1 Abstract

Here we present part of the first complete sidescan sonar dataset of the Nazaré and Setúbal canyons, west Iberian margin, which, in combination with multibeam bathymetry, shallow seismic profiles and precise piston coring of intra-canyon targets, are used to characterise the sedimentary dynamics of these deep-sea settings. The results show that Nazaré and Setúbal canyons are highly complex environments. They display a range of sedimentary features and processes that reflect changes in downslope canyon geometry and a transition from erosive proximal to more depositional distal sections. The proximal (upper) sections of both canyons are characterised by a deeply incised, narrow, V-shaped thalweg, flanked by small gullies and terraces. Numerous small and localised intra-canyon landslides and rock avalanches occur in this section, triggered by instability processes that are preconditioned by the steep topography. Sequences of stacked thin-bedded, fine-grained turbidites occur locally on intra-canyon terraces, and are interpreted to be the result of small-volume, possibly river flood-generated turbidity currents that do not appear to reach the lower canyon. In Nazaré Canyon these turbidites are associated with abundant coalified organic fragments. Part of the upper section in Nazaré Canyon has acted as an apparent depocentre through the Holocene, with very high sedimentation rates related to enhanced nepheloid layer activity. Much larger slope failures are sourced from the shelf-break and canyon head and are the result of occasional releases of large volumes of sediment, likely related to earthquake activity. These failures rapidly evolve into large-volume, high-energy, sand-rich turbidity currents that flush the entire canyon and dominantly deposit in the lower canyon and distal abyssal plains. This episodic turbidity current activity results in highly heterogeneous sediment distribution across the distal (lower) U-shaped floor of both canyons, with abundant erosional scours and depositional bedforms such as sediment waves. Our results highlight the complex interplay of sedimentary processes operating within major canyon systems, and have potential implications for efficient characterisation of hydrocarbon reservoirs, accurate spatial and temporal prediction of geohazards, and the distribution of benthic ecosystems in canyon environments.

4.2 Introduction and aims

Previous work on submarine canyons has established that they are major pathways for the transport of sediment (and associated pollutants and organic carbon) from land to the deep ocean (e.g. Berner, 1982; van Weering et al., 2002; Canals et al., 2006). Sediment enters the canyon heads from fluvial and/or along-shelf transport sources, and accumulate in a sediment pile in the upper section over time, producing a temporary sediment reservoir (Mastbergen and van den Berg, 2003). Failure of this prograding sediment can occur due to higher supply rates and/or faster progradation and intense resuspension caused by energetic bottom currents at the canyon head during storms and floods (e.g. Mulder et al., 2001; Liu et al., 2002; Puig et al., 2004a). Failure in the upper canyon can also be preconditioned by instability processes leading to sediment oversteepening on the steep slopes (Mullenbach et al., 2004; Puig et al., 2004a) or initiated by earthquake-triggered deformation and liquefaction of sediment (e.g. Jones and Omoto, 2000). The transport of this failed sediment therefore generally involves low frequency, high-energy, sediment gravity flows (e.g. Normark and Piper, 1991; Puig et al., 2004a; Canals et al., 2006), rather than continuous sedimentation. However, the frequency, timing and processes of gravity flows in most modern canyons are poorly constrained, as is their overall role in the offshore export of sediment. This is due to the difficulties involved in direct monitoring of flows in canyons (Khripounoff et al., 2003; Paull et al., 2003; Xu et al., 2004), and also the technological problems that arise when sampling in such rugged canyon topography.

Submarine canyons along European continental margins have recently been extensively studied as part of the EC-EUROSTRATAFORM project, which attempted to relate modern sedimentation to preserved strata on continental margins, and included investigating the role of canyons in offshore sediment flux. This research has continued as part of the Hotspot Ecosystem Research on the Margins of European Seas (HERMES) project (Weaver et al., 2004), an international, multidisciplinary research programme investigating the effects of physical processes on Europe's deep marine ecosystems and seafloor environments. In particular, the two projects have generated a significant amount of new data from Nazaré and Setúbal canyons, offshore west Iberia (Fig. 4.1). Here, we present some of these new data, including part of the first complete deep-towed sidescan sonar map of both canyons (Fig. 4.2), in combination with multibeam bathymetry and shallow seismic profiles. This detailed geophysical coverage has facilitated precise piston coring of intra-canyon targets such as terraces and bedforms.

The principal aims of this study are to (1) highlight key geophysical and sedimentary features observed in Nazaré and Setúbal canyons, using high-resolution geophysical data in combination with a suite of accurately targeted piston cores; and to (2) interpret the processes responsible for generating the observed features. It should be noted that, due to the lack of piston cores in the upper canyon sections, the interpretation at these depths can only be geomorphological, and this is described in detail in the accompanying paper by Lastras et al. (2009) rather than here. Additionally, the stratigraphic evolution of these canyons is beyond the scope of this paper, and will be addressed in future publications.

Our results will have potential implications for three main areas of applied research: 1) the hydrocarbon industry – predicting variations in vertical connectivity and lateral extent of sandy deposits in deep-water channel systems will lead to a better understanding of heterogeneity within these types of reservoir, 2) geohazards – predicting the catastrophic effects and flow processes of large gravity flows and slope instabilities will help to reduce potential damage to continental margin infrastructures and communities, and 3) benthic ecosystems – the Portuguese canyons are known to host fragile benthic ecosystems such as cold-water corals (unpublished HERMES data), so understanding the sedimentological effects on their abundance and distribution will be vital for our understanding of how these ecosystems survive in this environment.

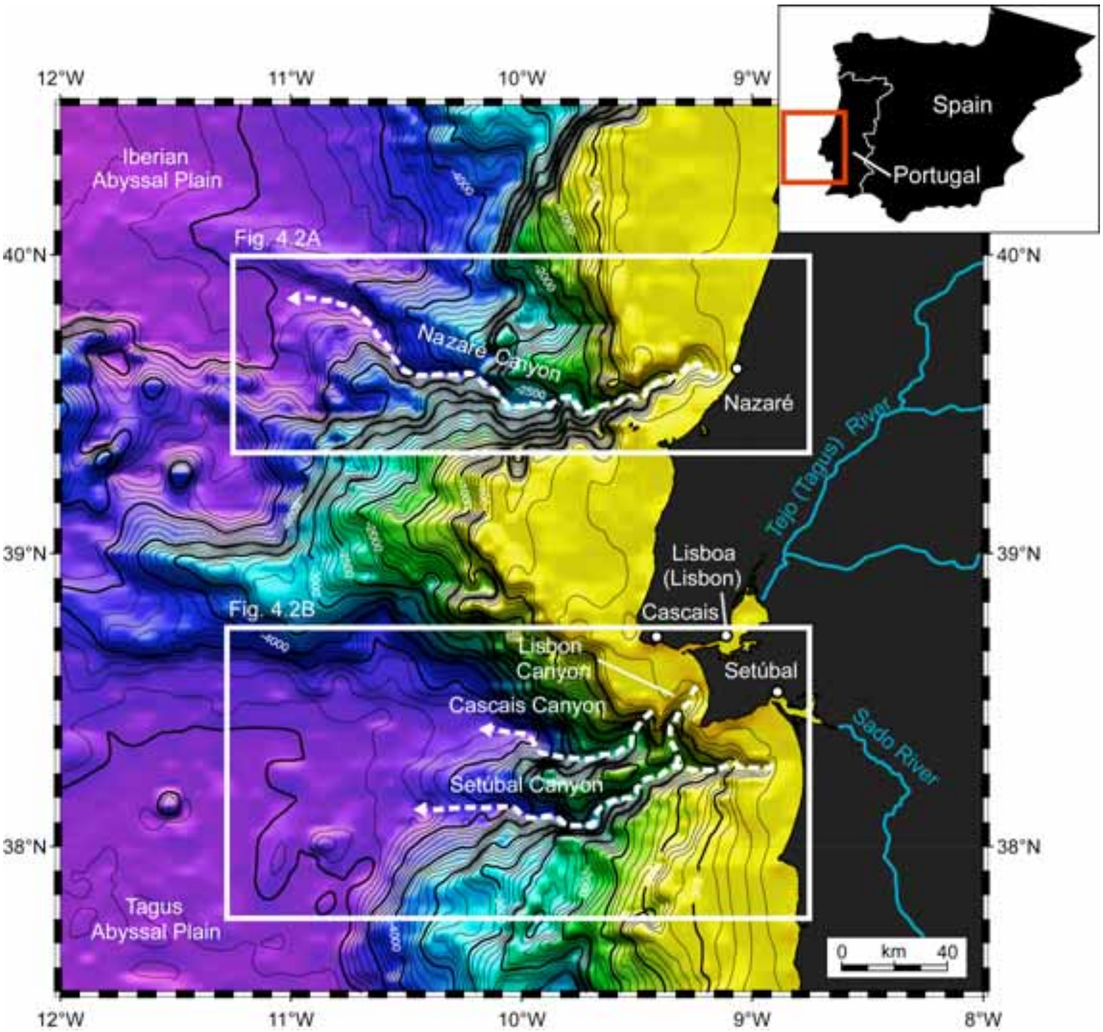

Fig. 4.1. Bathymetry map of the west Iberian margin showing the locations of the Portuguese canyons. Contours are every 100 m and outlined in bold every 500 m.

4.3 Methods and database

This study is based on geophysical and sedimentological data collected during cruise D155 (1985), EC-EUROSTRATAFORM cruises 64PE219 (2003) and CD157 (2004), and HERMES cruises D297 (2005) and CD179 (2006), all to the west Iberian margin. High-resolution multibeam bathymetry surveys were carried out using a 13 kHz Kongsberg Simrad EM12 echo-sounder system. Medium-resolution deep-towed sidescan sonar mapping was carried out using the TOBI system (Towed Ocean Bottom Instrument), developed at the National Oceanography Centre, Southampton, which allowed accurate surveying of seafloor features along the entire length of both canyons.

In addition, shallow seismic profiles were collected continuously along all ship tracks using a 3.5 kHz echo-sounder system; this system also operates as a sub-bottom profiler as it has a penetration depth of around 10-50 m, depending on lithology.

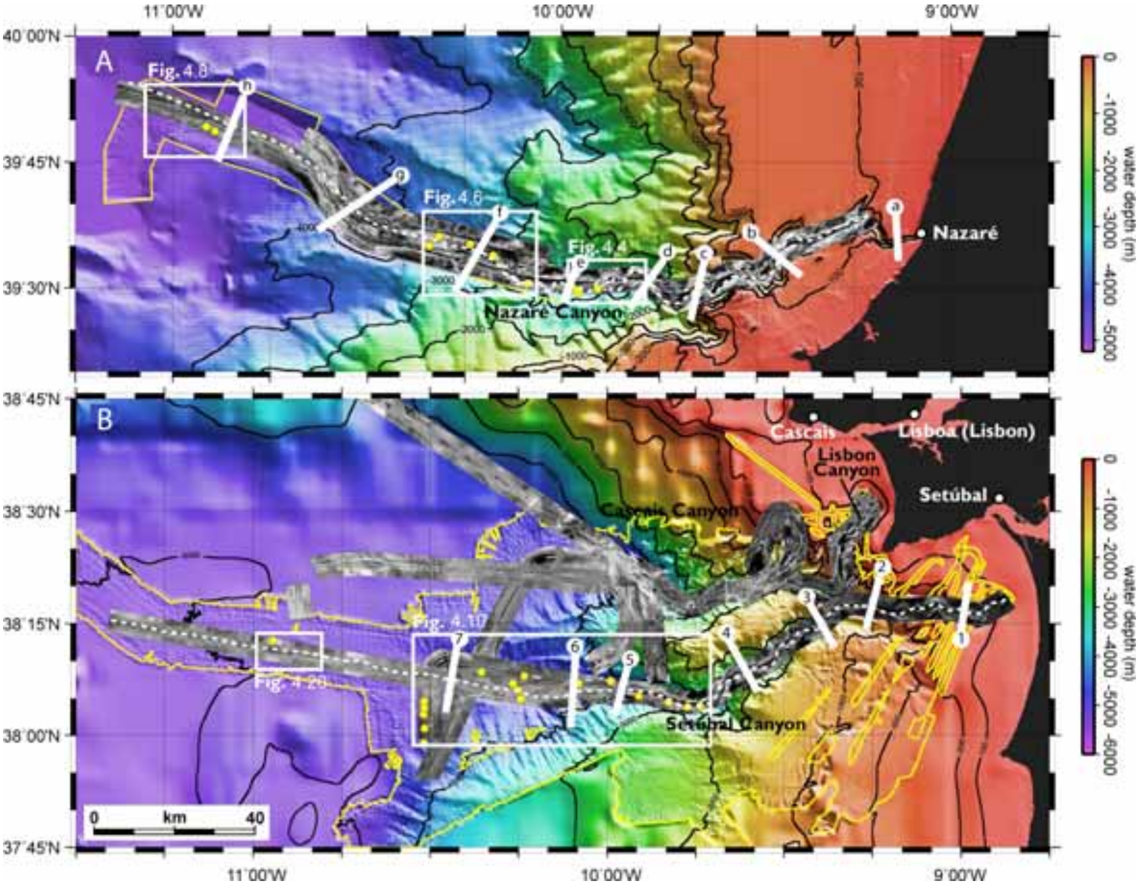

Fig. 4.2. Extent of sidescan sonar coverage of (**A**) Nazaré and (**B**) Setúbal, Lisbon and Cascais canyons. Yellow dots represent piston core locations. Bold white lines labelled 0-7 and a-h represent strike profiles and dashed white lines represent dip profiles, both shown in Fig. 4.3. Area marked by the yellow line represents high-resolution multibeam swath bathymetry coverage. Contours are 100 m, 200 m, 500 m, 1000 m, then every 1000 m.

Piston cores were recovered from accurately targeted sites along the two canyon systems in order to ground-truth the geophysical data. Targets selected were typically no less than 1 km across in order to ensure the highest accuracy. Piston cores were visually inspected (including estimates of grain size), photographed and run through a Geotek™ multi-sensor core logger, which measures p-wave velocity, gamma density and magnetic susceptibility down-core in order to interpret changes in lithology and sedimentary structures with depth (these profiles are not included in this paper). ^{210}Pb analysis was carried out for specific piston cores to estimate sediment accumulation rate (Appleby and Oldfield, 1978). Only cores with a well-developed oxidation front at the top were used, as this represents the top of the core and is proof that little, if any, surficial sediment was lost during coring, which would otherwise give spurious sedimentation rates.

4.4 Regional setting and canyon morphology

The west Iberian continental margin (Fig. 4.1) consists of a gently sloping, narrow shelf (averaging 20-30 km wide with a ~1° gradient dipping westwards), which is connected to the relatively steep (up to 6°) continental slope (Weaver and Canals, 2003). This slope is incised by several submarine canyons of ~200 km length, which narrow the shelf to <15 km at their heads. Highest canyon density occurs in the central part of the margin, known as the Lisbon margin (38°-40° N). The Tagus River dominates sediment supply to the shelf in this area, which is composed of thick (>1000 m) Cenozoic sediments draping a Mesozoic substrate (Jouanneau et al., 1998; Alves et al., 2003).

The Nazaré and Setúbal canyons (Figs. 4.1 and 4.2) are the two largest canyons of the west Iberian margin. They are both located on the central (Lisbon) part of the margin and oriented roughly perpendicular to the coast in an east-west direction. Nazaré Canyon, situated ~100 km north of Lisbon, cuts across the shelf almost to the beach, but is not connected to a major river system. Distally the canyon leads into the Iberian Abyssal Plain, some 210 km from the coast at a water depth (WD) of 5000 m. About 30 km south of Lisbon, the Lisbon and Setúbal canyons extend seawards across the shelf from the mouths of the Tagus and Sado Rivers, respectively. Lisbon Canyon connects to Setúbal Canyon as a tributary at ~2000 m WD, and Setúbal Canyon then continues downslope until it reaches the Tagus Abyssal Plain at ~4840 m WD, some 175 km from the canyon head.

In order to simplify the description of the canyons, we have chosen the upper-middle-lower sections classification by Vanney and Mougenot (1990); Schmidt et al. (2001); van Weering et al. (2002); and de Stigter et al. (2007). However, because the upper and middle sections show no significant differences in morphology or sedimentary features, they have been grouped together and are collectively referred to here as the upper section. Thus, the upper section reaches down to the base of the continental slope (4000 m WD), and the lower section is the area beyond this depth. The thalweg is considered to be the deepest incised part of the canyon floor. In the broad flat-floored lower canyon, thalweg refers to secondary channels cut into the canyon floor.

4.4.1 Morphology of Nazaré Canyon

The upper Nazaré Canyon (<4000 m WD) is narrow and V-shaped (Fig. 4.3); it is deeply incised into the continental shelf and slope, with a maximum incision depth of 2-2.5 km and a narrow <100 m-wide thalweg. Sinuosity values mostly fall between 1.2 and 1.9, with the highest sinuosity at 1500-1700 m WD. The average axial slope angle down to 4000 m WD is approximately 2º.

Beyond 4000 m WD, the narrow canyon floor gradually widens to 8-10 km and the axial slope decreases to 0.6º. The cross-sectional profile of the lower canyon is U-shaped with more gently sloping walls and a reduced sinuosity of ~1.1. The broad canyon floor is itself incised by a 0.5-1 km-wide thalweg in its upper part, which is 5-10 times wider than in the upper section.

4.4.2 Morphology of Setúbal Canyon

The gross morphology of Setúbal Canyon is similar to that of Nazaré Canyon (Fig. 4.3). The upper section (<4000 m WD) is narrow and V-shaped with a maximum incision depth of 1.5-2 km, a ~100 m-wide thalweg, an average axial slope of 2º and a sinuosity index of 1.2-1.4, decreasing to 1.1 or less below 3000 m WD. Gullies are incised into the sidewalls (Figs. 4.1-4.3), while a large tributary called Lisbon Canyon converges with Setúbal Canyon at ~2000 m WD. Lisbon Canyon is also V-shaped with steep, gullied walls (Lastras et al., 2009), but it will not be described further in this paper.

The lower section of Setúbal Canyon (>4000 m WD) is wider (>10 km-wide canyon floor) and U-shaped, with a reduced sinuosity of ≤1.1 and a lower axial slope angle of

0.6°. There are no indications, either from the bathymetry or sidescan sonar data, for a thalweg channel incised in the lower Setúbal Canyon floor.

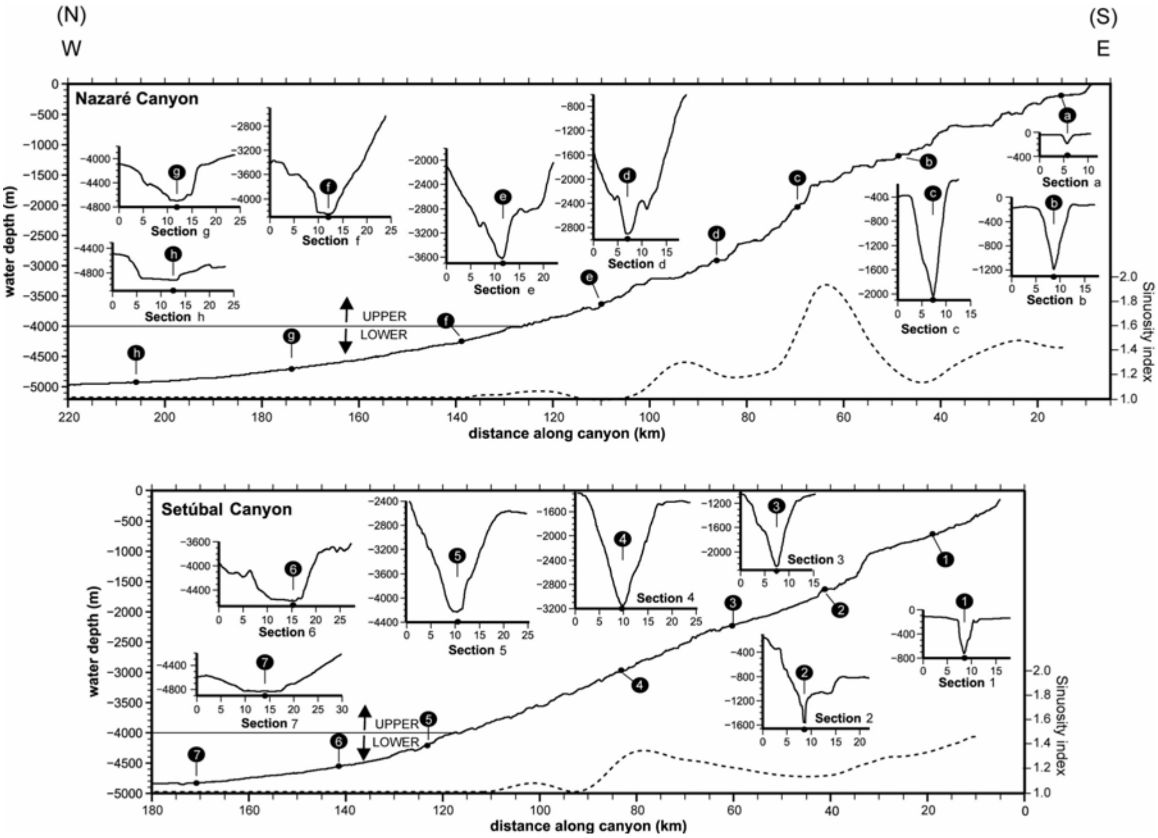

Fig. 4.3. Strike bathymetric profiles of Nazaré and Setúbal canyons (white lines in Fig. 4.2; profiles are taken facing upslope, i.e. north is on left). A clear distinction can be made between the steep, deeply incised upper section, and the much flatter lower section in both canyons, with the boundary at ~4000 m water depth (WD) in both. Terraces and gullies are also visible. Vertical exaggeration is 12.5x. The sinuosity index is highest in the upper sections and decreases considerably towards the lower sections.

4.5 Geophysical and sedimentary observations of sediment features

4.5.1 Nazaré Canyon

4.5.1.1 Terraces, turbidites and high sedimentation rates in the upper Nazaré Canyon

The upper Nazaré Canyon (<4000 m WD) is characterised by rugged topography and steep slopes, with abundant gullies incising into semi-circular-shaped erosional scarps (Fig. 4.4). Intra-canyon terraces are observed only in the steepest locations, where the narrow V-shaped canyon has undergone multiple phases of incision into surrounding bedrock and semi-lithified sediments. TOBI sidescan sonar observations of terraces reveal them to be long and narrow, oriented roughly parallel to the canyon axis. The occurrence of wider terraces on the ‘inner bank’ of sinuous bends (Fig. 4.4) may indicate lateral canyon migration through enhanced outer bank erosion (e.g. Mayall et al., 2006).

Cores D15738 and D15739 were recovered from 40-60 m-high terraces at ~3500 m WD (Fig. 4.5). They are both composed of thick sequences of dark greenish-brown, greatly bioturbated silt-mud turbidites, some of which have thin, medium sand-sized, bases. These deposits are mostly <1-2 cm thick, but occasionally up to 10 cm, and are rich in black carbonaceous fragments and mica. They are also found dominating nearby core D15756 (Figs. 4.6-4.7). A very different turbidite is also present in cores D15739 and D15756. It is markedly thicker and composed of cleaner siliciclastic sand than the carbonaceous turbidites. This type of turbidite contains abundant mica but is less organic-rich (photographed in Fig. 4.5). These clean sand units have a sharply erosive top and base, with faint lamination but no obvious grading, implying a Bouma T*a* sequence (after Bouma, 1962). Investigation of bulk sedimentation rates in cores D15738 and D15739, using ^{210}Pb analysis (see methods section), reveals high average rates in the order of 0.46-0.87 cm yr^{-1} in the upper ~1.5 m (Fig. 4.5)[2].

4.5.1.2 Erosional features and turbidites in the lower Nazaré Canyon

Nazaré Canyon widens out abruptly ~130 km from its head, leading into its lower section with a 4-5 km-wide flat floor and narrow thalweg running along the deeper

---

[2] The method for calculating the sediment accumulation rates was revised following publication of this paper in Marine Geology, and the correct values are stated here.

southern margin (Fig. 4.6). In addition, a 2 km-long erosional scar is visible, with a thin channel-like feature extending downslope beyond it. Backscatter variations on the TOBI record indicate heterogeneous distribution of sediment across the canyon floor in this area.

Two cores, CD56420 and D15763, were recovered from the broad canyon floor at a height of ~40 m above the thalweg (Figs. 4.6-4.7), and show the same two types of turbidite that are observed on upper canyon terraces (described in the previous section). These are 1) stacked, thin-bedded, fine-grained turbidites rich in carbonaceous fragments and mica (photographed in Fig. 4.7), and 2) thicker, normally-graded, coarse- to medium-sand turbidites that are rich in quartz and mica but lack carbonaceous fragments. This latter clean siliciclastic sand makes up almost the entire 4 m of core CD56419, which was recovered in this area but closer to the thalweg than the previous cores, just 10-20 m above it (Figs. 4.6-4.7).

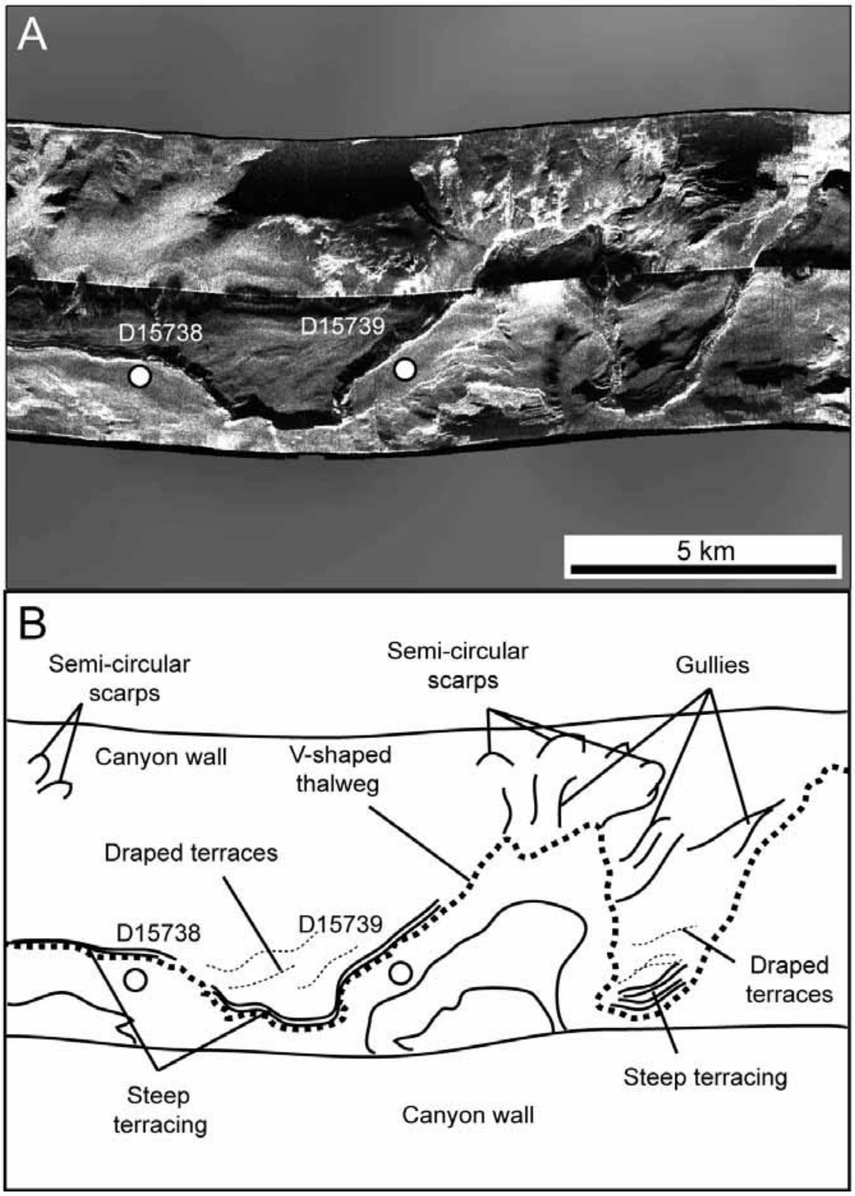

Fig. 4.4. Representative sidescan sonar image (**A**) and interpretation (**B**) showing upper Nazaré Canyon features (~2500-3500 m WD). They clearly show the narrow and highly sinuous V-shaped thalweg (black dotted line) bound by steep canyon walls. Abundant erosive features are also present, such as gullying, landslide scarps and terracing. Cores D15738 and D15739 are described in Fig. 4.5.

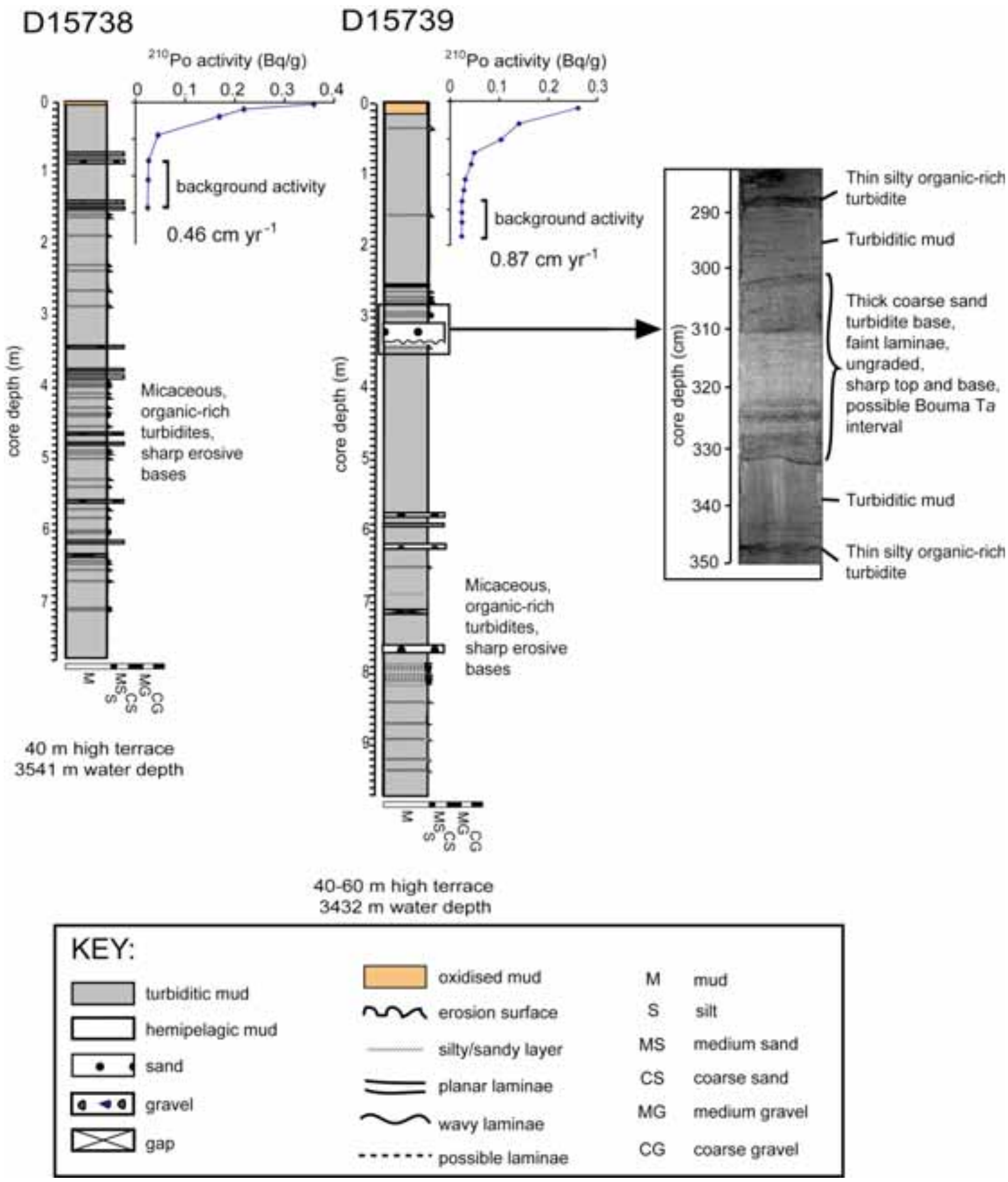

Fig. 4.5. Sedimentary logs of two cores recovered from the upper Nazaré Canyon terraces shown in Fig. 4.4. ^{210}Pb analysis has revealed unusually high Holocene sedimentation rates of 0.46 and 0.87 cm yr^{-1} (see footnote 2). The photograph shows an example of a clean, siliciclastic turbidite sand, with an irregular erosional base.

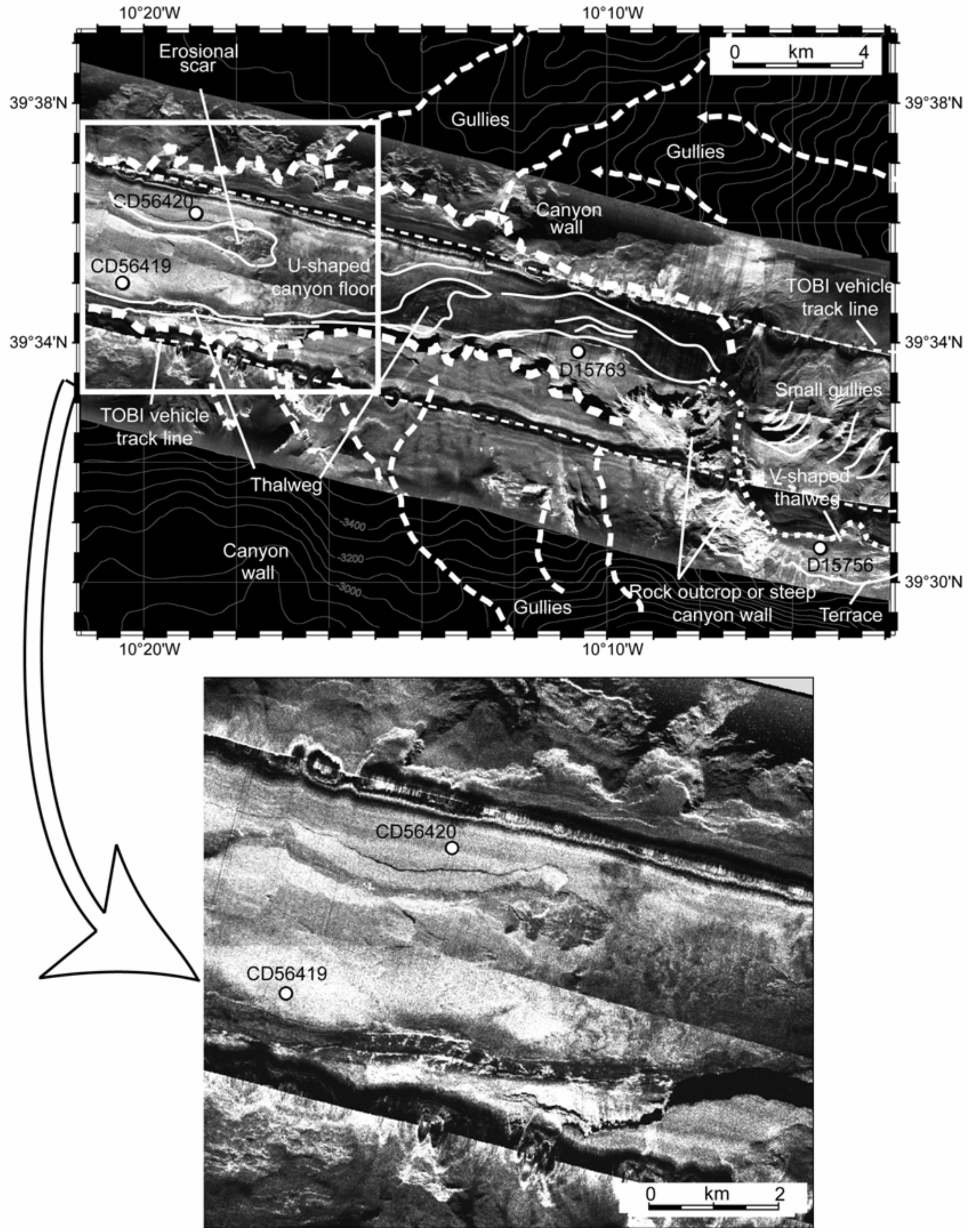

Fig. 4.6. The transition from upper to lower Nazaré Canyon coincides with the abrupt widening of the canyon at the base of the continental slope (~4000 m WD), which is shown by the transition from a narrow thalweg (white dotted line) to the wide lower canyon floor (margins shown by thick dashed white lines). Beyond this point, the canyon gradient and walls are flatter, although gullies are still present (dashed white lines with arrowheads). The lower canyon scours, thalweg and cores CD56419 and CD56420 are highlighted in the boxed area that is also shown in detail in the lower image. 100 m contours; cores CD56419, CD56420, D15756 and D15763 are described in Fig. 4.7.

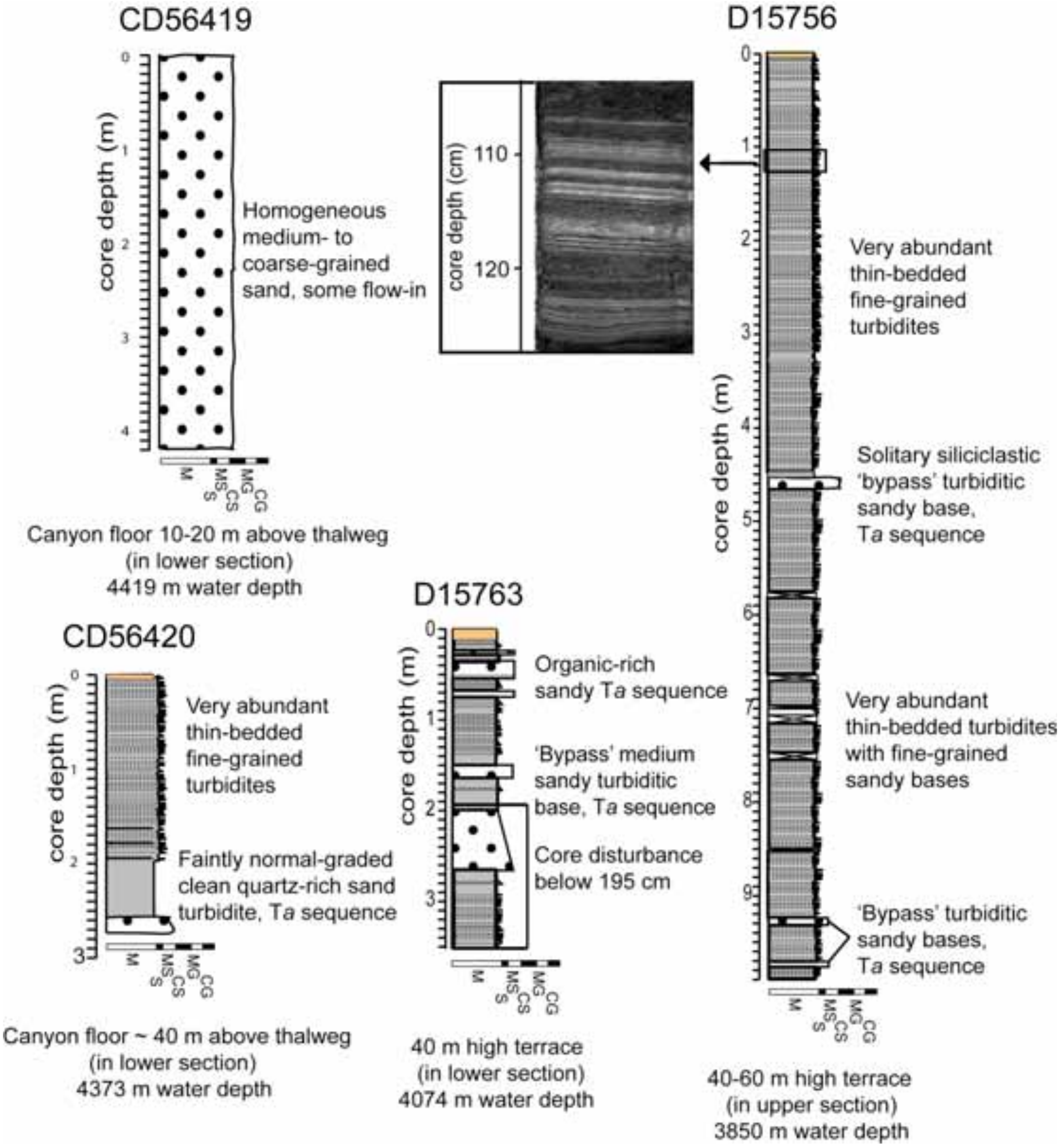

Fig. 4.7. Sedimentary logs of cores shown in Fig. 4.6, showing the occurrence of two types of turbidite: clean siliciclastic sand and thin-bedded, fine-grained organic- and mica-rich (photographed). Refer to Fig. 4.5 for a key of sedimentary structures and symbols.

4.5.1.3 Depositional bedforms in the lower Nazaré Canyon and mouth

TOBI sidescan sonar data reveal a distinctive ‘zebra-stripe’ backscatter pattern on the gently sloping southern margin of Nazaré Canyon mouth (Fig. 4.8A). The alternating dark-light (low-high) backscatter patches are oriented oblique to the canyon axis, but are sub-parallel to the local bathymetric contours. Some of these patches are overprinted by slope-perpendicular lineations. A 3.5 kHz profile running across these features reveals them to be depositional wave-like bedforms (Fig. 4.8C), with the high backscatter on TOBI corresponding to the near-horizontal upslope-facing flanks and the low backscatter to steeper downslope-facing flanks. Wavelengths are in the order of 5 km and amplitudes are up to 10 m.

Cores were recovered from both flanks of the bedforms in order to calibrate the geophysical data. Core CD56429, which penetrated a high backscatter (upslope-facing) flank, contains a 4.5 m-thick sequence of interbedded sand-silt turbidites and hemipelagites (Fig. 4.9). Turbidites are 1-40 cm thick and are mostly sand-dominated, structureless or faintly planar-laminated (Bouma sequences T*a* and T*b*) with sharp bases and tops, although some grade up into silt (T*d*). Turbidite sands are fine- to medium-grained and are rich in quartz and mica, with no concentrations of carbonaceous material.

In contrast, core CD56428, which penetrated a low backscatter (downslope-facing) flank, contains a 6.5 m-thick sequence of bioturbated and interbedded turbiditic and hemipelagic muds (Fig. 4.9). Some of the turbidites show thin (<1-2 cm) bioturbated silty bases, but they are mostly mud-dominated.

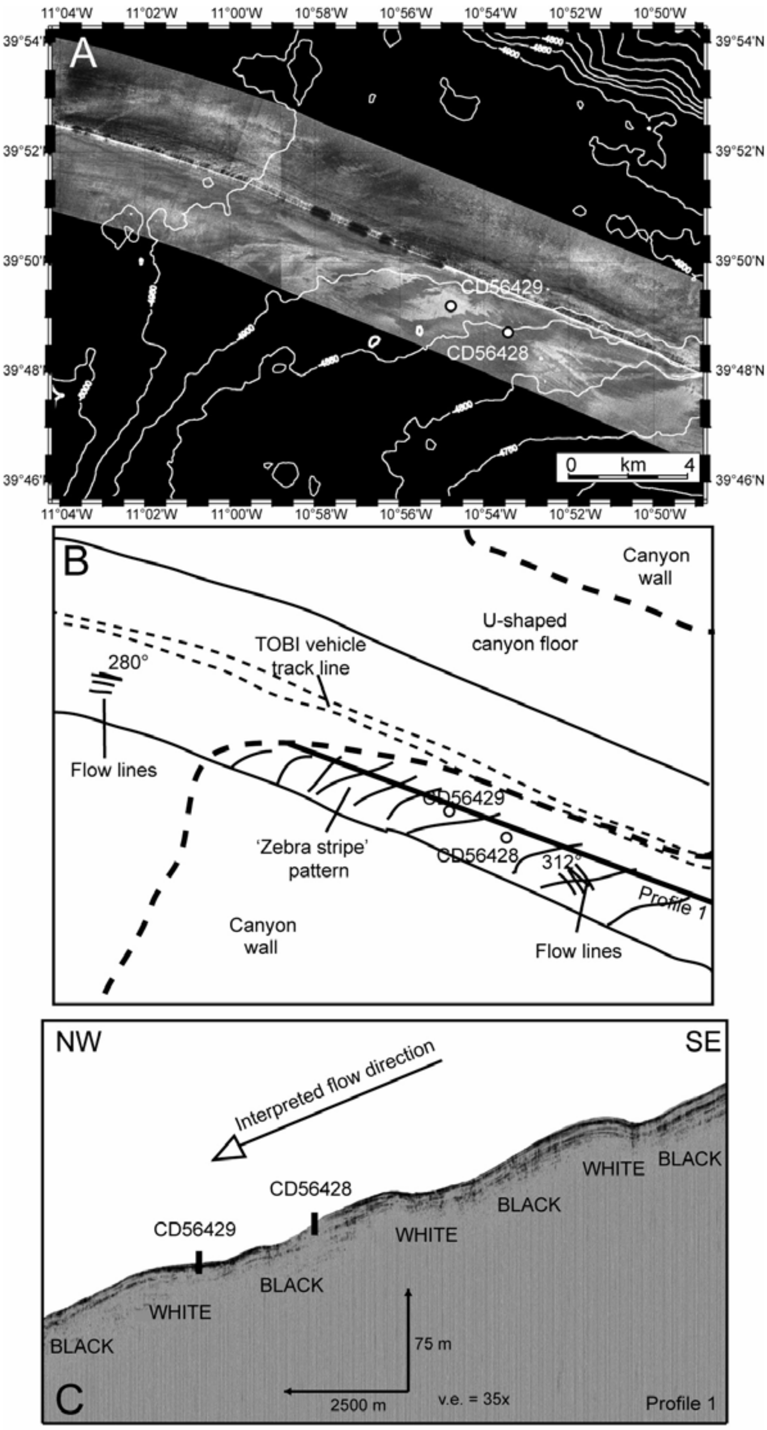

Fig. 4.8. TOBI sidescan sonar image (**A**) and interpretation (**B**) of Nazaré Canyon mouth, with 50 m contours. A dark/light 'zebra-stripe' backscatter pattern is observed on the southern canyon margin. Bold black line indicates the location of seismic profile 1, shown in **C**. Note the wavy topography and wave asymmetry (near-horizontal upslope-facing flanks compared to the steeper downslope-facing flanks). The locations of the black and white backscatter patches in the sidescan sonar image correlate with the upslope- and downslope-facing wave flanks respectively. Vertical exaggeration (v.e.) = 35x.

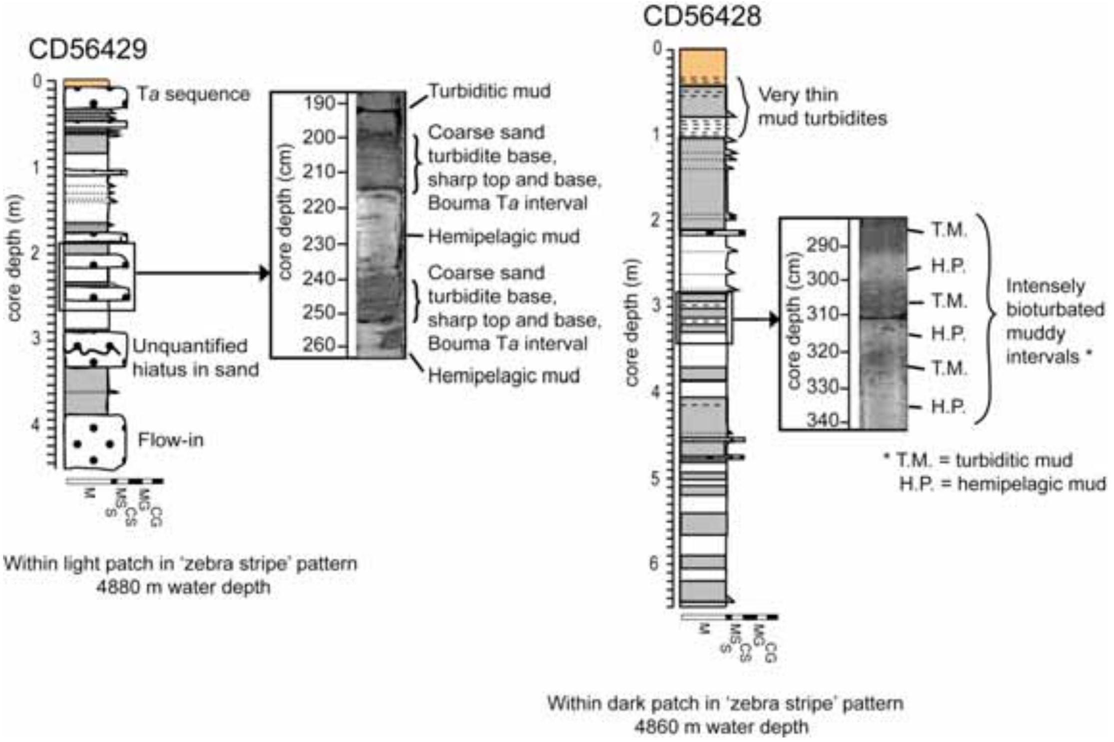

Fig. 4.9. Sedimentary logs and photographs of cores shown in Fig. 4.8A help to interpret the backscatter pattern in the mouth of Nazaré Canyon as fine-grained sediment waves. Dark = low backscatter (mud-dominated), found on the near-horizontal upslope-facing wave flanks; light = high backscatter (interbedded sands/muds), found on the steeper downslope-facing wave flanks. Refer to Fig. 4.5 for a key of sedimentary structures and symbols.

4.5.2 Setúbal Canyon

4.5.2.1 *Terraces and mass wasting in the upper Setúbal Canyon*

The upper Setúbal Canyon (<4000 m WD) is V-shaped with steep terraced walls and a narrow thalweg (Figs. 4.3, 4.10, 4.11 and 4.12). As with Nazaré Canyon, terraces, gullies and erosional scarps are all visible on TOBI data. Cores CD56825 and CD56417 were recovered from terraces at ~3800-3900 m WD (Fig. 4.11), and contain a sequence of interbedded fine-grained turbidites and hemipelagites (Fig. 4.13). These turbidites are comprised of greatly bioturbated, olive greenish-grey mud (Bouma sequence T*e*) with thin (<5 cm), structureless sand bases, although the thickest unit in CD56825 shows development of basal sandy laminae and cross-laminae (T*b* and T*c*). Similar turbidite structures are observed in the nearby core CD56416, which was recovered about 5 km down-canyon from CD56417, on the outside of a marked right-hand bend in the canyon (Fig. 4.12).

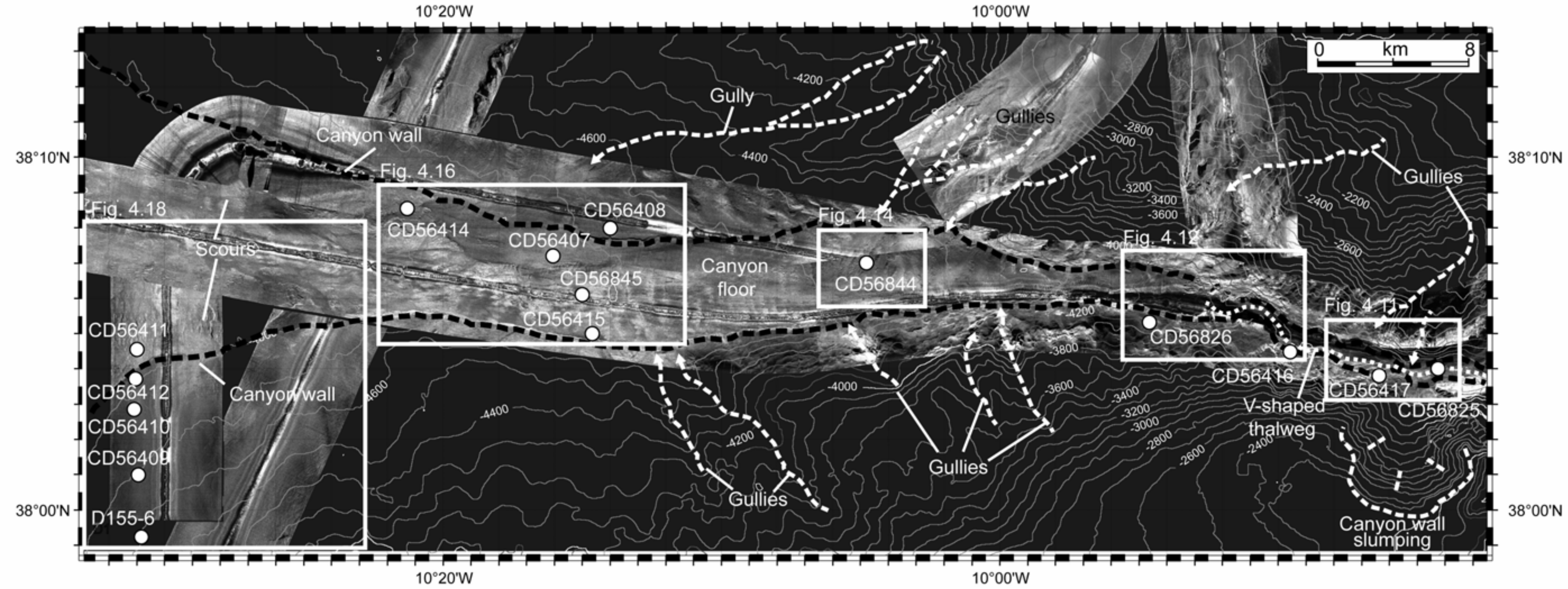

Fig. 4.10. Transition from upper to lower Setúbal Canyon. The narrow V-shaped thalweg of the upper canyon (white dotted line) is bound by steep walls that result in abundant mass wasting events such as landslides and rock avalanches, and associated slump scars (e.g. bottom right hand corner of image). In contrast, the lower section, with edges marked by the dashed black lines, has a much wider and flatter canyon floor with less steep walls, although slope failures also occur here (an example reflected by an area of uniform dark backscatter is shown in more detail in Fig. 4.16A). 100 m contours.

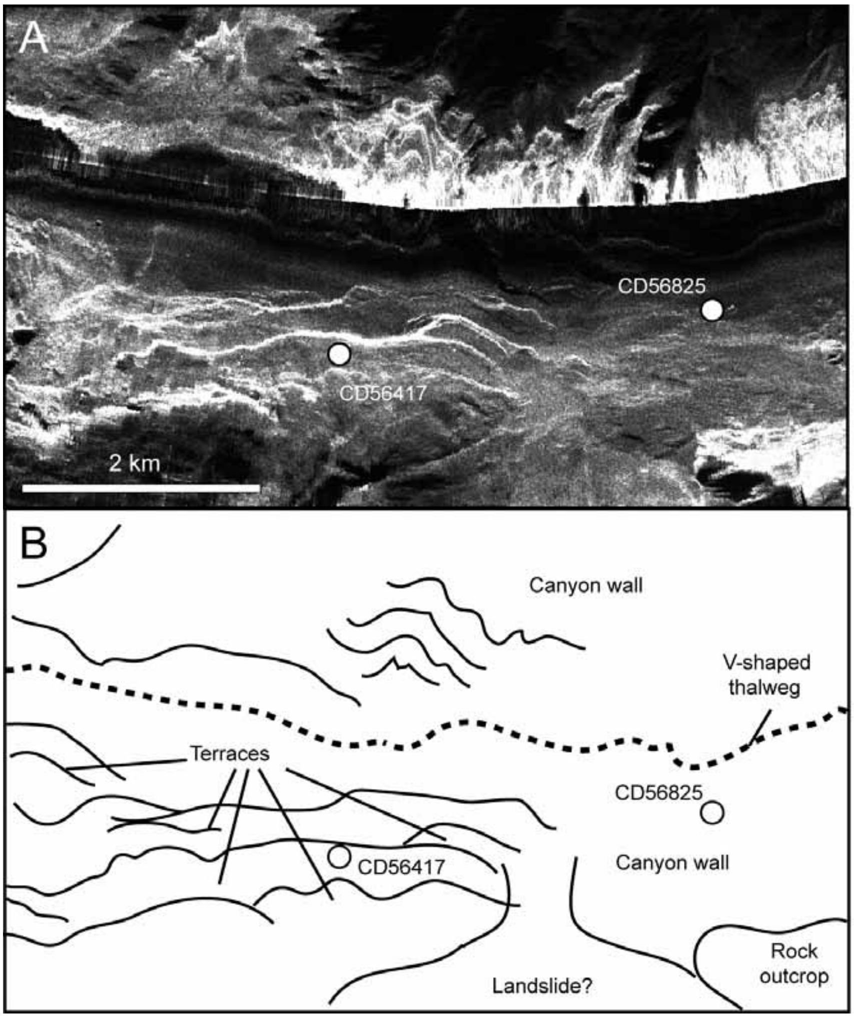

Fig. 4.11. Representative sidescan sonar image (**A**) and interpretation (**B**) of upper Setúbal Canyon (~3000-3600 m WD). Its relative location is shown in Fig. 4.10. The steep topography in the upper canyon causes sediment instability, which has resulted in a possible landslide. Terracing is caused by incision of the narrow thalweg into the steep canyon margin. Cores CD56417 and CD56825 are described in Fig. 4.13.

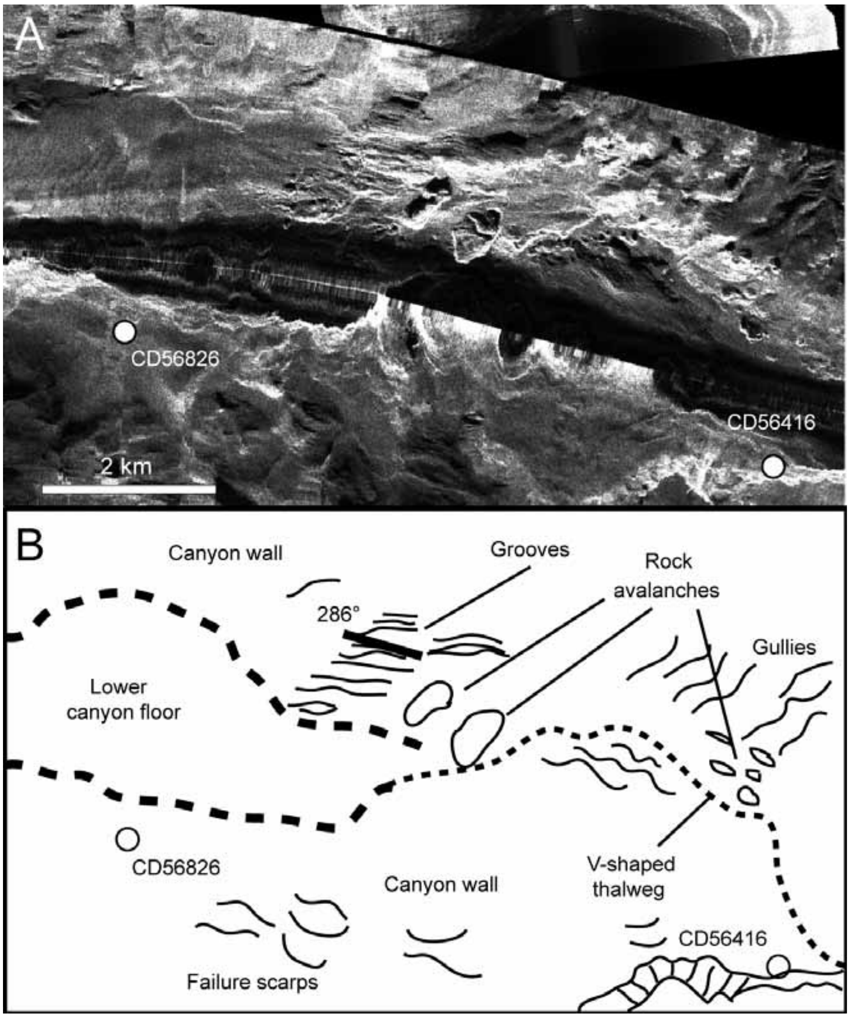

Fig. 4.12. Representative sidescan sonar image (**A**) and interpretation (**B**) of upper Setúbal Canyon (~3700-4200 m WD). Its relative location is shown in Fig. 4.10. A rock avalanche and grooves indicate that this part of the canyon is depositionally unstable and highly erosive. Cores CD56416 and CD56826 are described in Fig. 4.13.

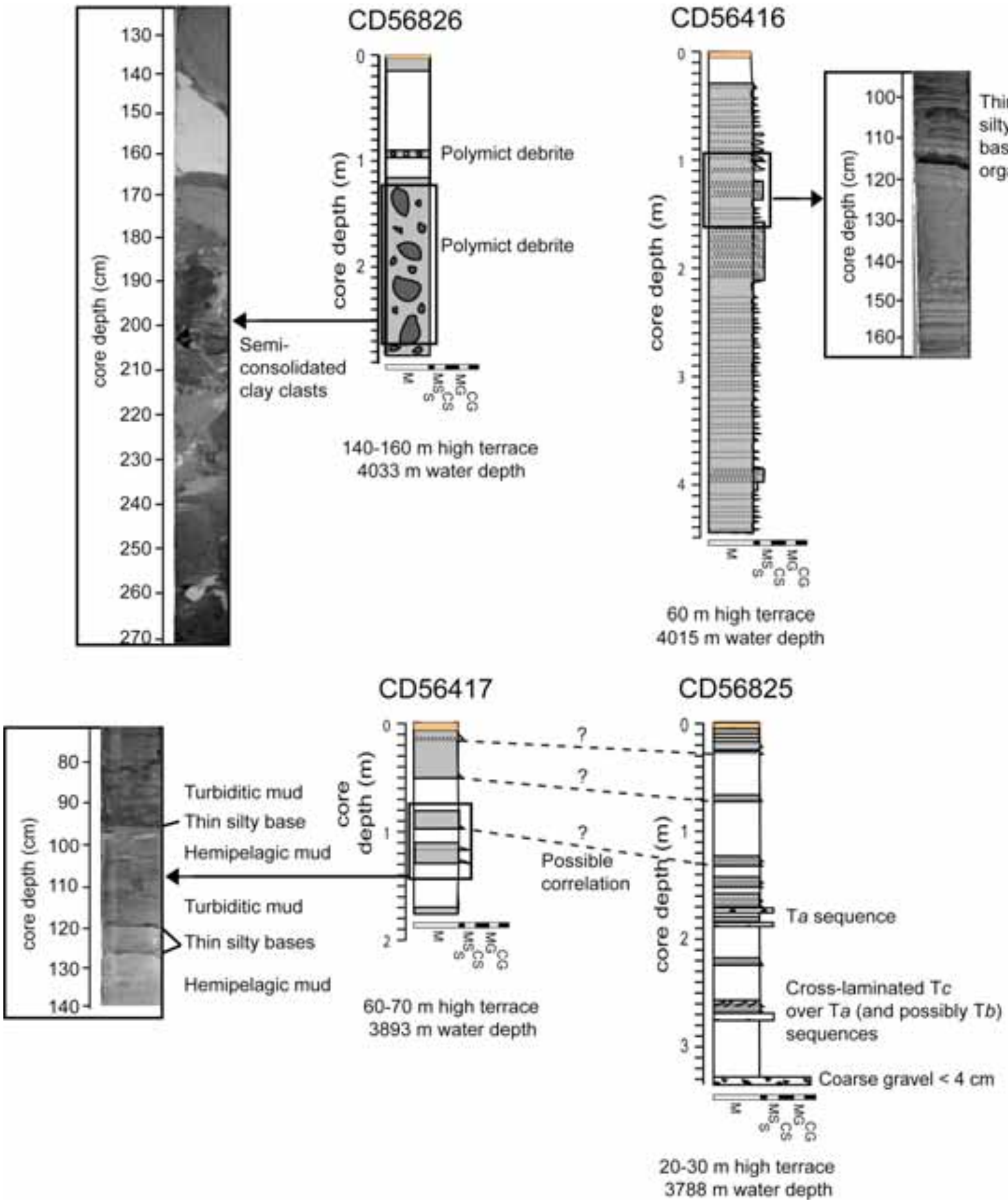

Fig. 4.13. Sedimentary logs and photographs of cores recovered from terraces of different heights (in Figs. 4.11 and 4.12) give examples of different types of mass wasting. These include debris flow deposits and thin-bedded, fine-grained turbidites similar to those in Nazaré Canyon (*c.f.* Fig. 4.7). Dashed lines between cores CD56417 and CD56825 show possible correlating sequences. Refer to Fig. 4.5 for a key of sedimentary structures and symbols.

At ~4000 m WD, a striking example of a canyon margin failure can be seen on TOBI data (Fig. 4.12), with blocks up to several hundred metres across scattered over the canyon floor adjacent to an area of 1 km-long erosional lineations oriented down-canyon. Core CD56826 was recovered from the opposite side of the canyon to this rock avalanche, and was located about 140-160 m above the canyon floor on an area of irregular canyon wall topography whose surface appears relatively smooth on TOBI records. This core contains a spectacular polymict debrite comprising a variety of sub-rounded, semi-lithified silt and mud clasts up to 25 cm in diameter (Fig. 4.13).

4.5.2.2 Canyon floor bedforms and slope failures in the lower Setúbal Canyon

The lower Setúbal Canyon rapidly widens below 4000 m WD, about 120 km from its head (Fig. 4.10). The relatively flat canyon floor initially opens out to a width of 2 km before gradually widening to 12 km near the canyon mouth. A series of transverse bedforms can be seen on TOBI records across the canyon floor at ~4550 m WD (Fig. 4.14). They have a wavelength of ~500 m and are oriented slightly oblique to the canyon axis. Core CD56844 was recovered from within this area and contains a 1.2 m-thick, very coarse-grained, normally-graded unit overlain by 44 cm of interbedded turbidite and hemipelagite muds (Fig. 4.15). The coarse unit is well-sorted, matrix-poor and polymict, with cobbles and pebbles (composed of various metamorphosed argillaceous rocks) up to 8 cm in diameter at the base, fining upwards to oxidized coarse sand.

Another series of poorly-defined transverse bedforms is visible at ~4700 m WD (Fig. 4.16A). Core CD56845 was recovered from within this area and contains a very similar sequence to core CD56844, including a 55 cm-thick, normally-graded, polymict gravel unit that is well-sorted at the base and increasingly poorly-sorted towards the top (Fig. 4.17). Pebbles at the base reach a maximum diameter of 4 cm and are composed of a variety of metamorphosed argillaceous rocks. The top 27 cm of the core consists of interbedded turbiditic and hemipelagic muds.

An area of uniform low backscatter with positive relief can be seen on sidescan sonar data extending from the northern canyon margin and across part of the canyon floor with transverse bedforms (Figs. 4.10 and 4.16A). Two cores from the low backscatter area on the northern canyon margin contain thick remobilised sequences composed of contorted fine-grained hemipelagic and turbiditic sediments (CD56407 and CD56408; Fig. 4.17). The turbidites are similar to those observcd on the upper Setúbal and Nazaré Canyon terraces (Figs. 4.7 and 4.13), and underlie remobilised coarse gravel deposits in CD56407. Two other cores from the southern and northwest margins of the canyon floor in this area (CD56414 and CD56415, respectively) also contain thick remobilised units of contorted fine-grained turbiditic and hemipelagic sediments, as well as remobilised layers of poorly sorted gravel, similar to that in CD56845 and CD56407. The disturbed sediments in cores CD56407, CD56408, CD56414 and CD56415 (Fig. 4.17) suggest that they have been remobilised by one or more slope failure events.

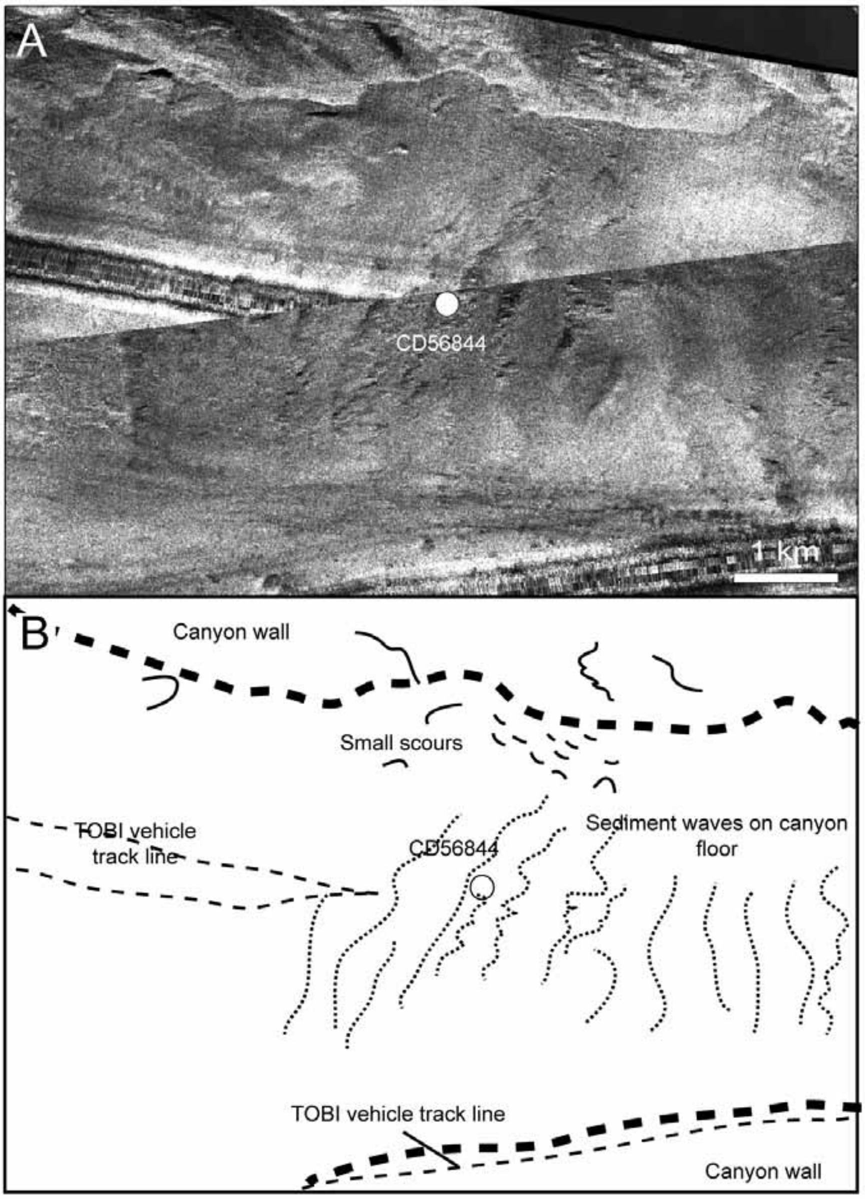

Fig. 4.14. Sidescan sonar image (**A**) and interpretation (**B**) showing detail of the canyon floor in lower Setúbal Canyon (see location in Fig. 4.10), with transverse linear bedforms and location of core CD56844.

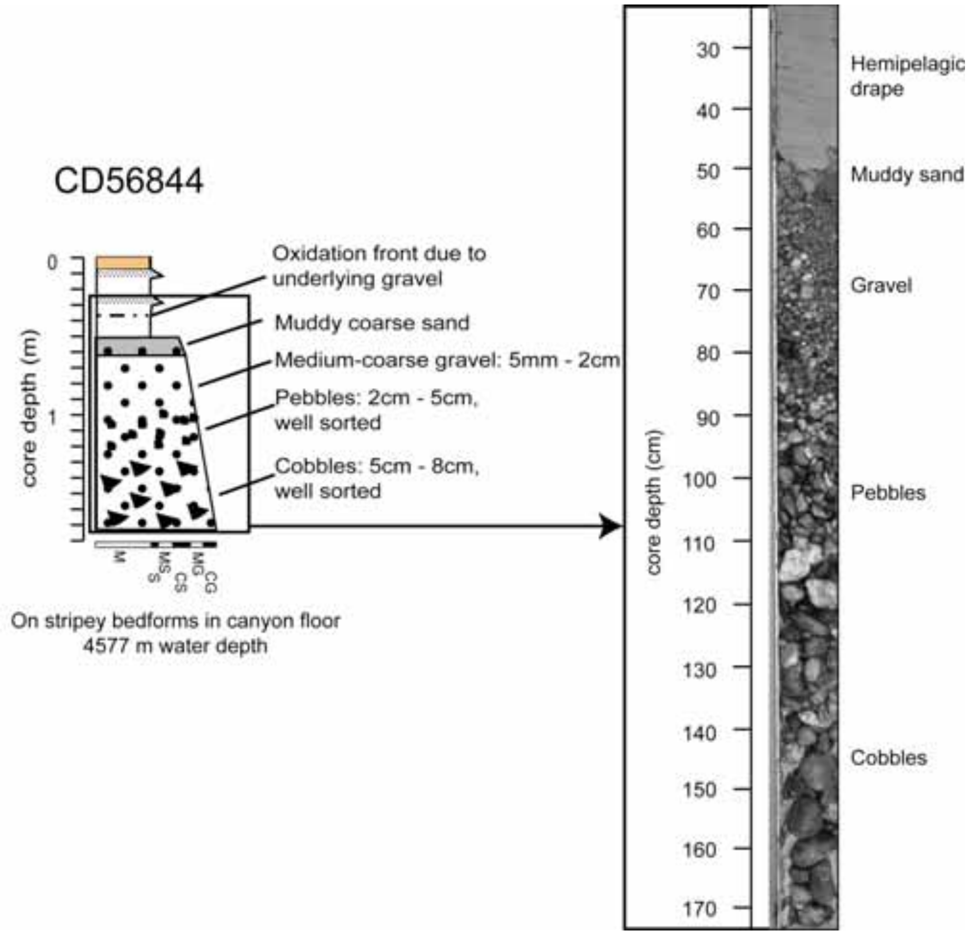

Fig. 4.15. Sedimentary log and photograph of core CD56844, interpreted to comprise of coarse-grained sediment wave deposits. Refer to Fig. 4.5 for a key of sedimentary structures and symbols.

4.5.2.3 Erosional scours and canyon margin deposits at the Setúbal Canyon mouth and fan

A series of irregularly-shaped, kilometre-scale, erosional scours are visible on TOBI data from the Setúbal Canyon mouth and eastern Tagus Abyssal Plain (Figs. 4.18A and 4.20A), interspersed with areas of patchy backscatter. The scours vary between being spoon-shaped (e.g. Fig. 4.6) and flute-shaped, with a pointed upslope end and flared downslope end (Fig. 4.18A). Like the smaller-scale groove fields in the upper canyon, the scours have their long axes oriented parallel to the inferred flow path of turbidity currents passing down through the canyon. They also tend to be asymmetrical, with a steeper, higher upslope edge and a shallower downslope edge. Some scours appear to have amalgamated in places to form chevron-like scour features (e.g. Fig. 4.20A).

Core CD65411 was recovered from the scoured canyon mouth floor at 4845 m WD (Fig. 4.18A) and contains at least 50 cm of hemipelagic mud (in the trigger core) overlying a 2.5 m-thick sequence of greatly disturbed turbidite sand that is medium- to coarse-grained, homogeneous and quartz-rich (Fig. 4.19). This core has clearly been severely affected by sand 'flow-in' during the coring process, but is still an indicator of the coarse-grained fill in the scours. The cores from the adjacent canyon margin were recovered at heights varying from ~10-20 m to 230-240 m above the canyon mouth floor (CD56412, CD56410, CD56409 and D155-6; Fig. 4.19), and contain a series of interbedded hemipelagic and turbiditic muds, with decreasing abundance of thin, bioturbated, fine-grained turbidite sand-silt bases (<3 cm thick) with increasing height up the canyon margin. A 3.5 kHz profile crossing this transect (profile 3, Fig. 4.18C) reflects the change from low acoustic penetration on the canyon floor (reflected in the sand-dominated deposits of core CD56411) to increased acoustic penetration and development of sub-bottom layering on the canyon margin (reflected in the mud-dominated sediments of the margin cores).

Scours on the 'proximal' abyssal plain are similar to those observed in the canyon mouth. Core CD56404, from the floor of one scour at 5020 m WD (Figs. 4.20 and 4.21), contains at least 50 cm of hemipelagic and turbiditic drape (in the trigger core) overlying ~1.5 m of massive, coarse-grained homogeneous sand with some evidence for flow-in. This in turn overlies distorted and, in some cases, overturned muddy and silty turbidites. Another core was attempted outside of and directly adjacent to this scour, but it failed, presumably due to the presence of thick homogeneous sand (Fig. 4.21).

4.6 Sedimentary processes of Nazaré and Setúbal canyons

4.6.1 Localised mass wasting in the upper canyons

Several examples of localised, small-scale (<10 km^2), intra-canyon mass wasting are observed in the upper Nazaré and Setúbal canyons, including landslides, debris flows and rock avalanches (Figs. 4.11 and 4.12). Such slope failures can be initiated by two types of factor (e.g. Canals et al., 2004; Masson et al., 2006): preconditioning factors include geological weakness such as low sediment strength, permeability and architecture, and underconsolidation (e.g. Pinheiro et al., 1996; Terrinha et al., 2003; Puig et al., 2004a), whilst triggering factors include dynamic loading by earthquakes (Jones and Omoto, 2000), sediment overpressure caused by rapid deposition, oversteepening, and longer-lasting effects of sea-level change induced by climatic oscillations (Weaver and Kuijpers, 1983).

There are two probable triggers of slope failure in the Portuguese canyons. The first is under-cutting and oversteepening of the upper canyon margins by erosive turbidity currents (evidenced by the large number of terraces and steep canyon walls). The second is ground shaking during regional earthquakes. The role of earthquakes in causing slope failure is believed to be particularly important here since the Iberian Peninsula is located just north of the present-day Africa/Eurasia plate boundary along the Azores-Gibraltar Fracture Zone. Tectonic activity along this plate boundary since the Variscan has resulted in the development of several faults in the region, some of which run directly through the canyons on the west Iberian margin (e.g. Nazaré Fault in upper Nazaré Canyon and Grándola Fault in upper Setúbal Canyon, Alves et al., 2006, Fig. 2.1). These faults may be associated with historical large earthquakes in the area (such as the 1755 Lisbon earthquake, e.g. Weaver et al., 2000). Although there are indications of at least some fault control on the evolution of these canyons (Vanney and Mougenot, 1990), the majority of slope failures likely relate to more than one factor (Masson et al., 2006), making it less straightforward to identify the causes of mass wasting events.

4.6.2 Anomalously high Holocene sedimentation rates in the upper Nazaré Canyon

The extremely high sediment accumulation rates observed in the upper Nazaré Canyon (0.46-0.87 cm yr^{-1} or 460-870 cm kyr^{-1}; Fig. 4.5) are about 2 orders of magnitude higher than the average rates along the west Iberian continental slope (approximately 0.003-0.01 cm yr^{-1} or 3-10 cm kyr^{-1}, van Weering et al., 2002). This can be expected for an incision in the slope, which acts to funnel sediment down it at a faster rate, but even so, the rates found at ~3500 m WD in Nazaré Canyon are far higher than the 0.4-0.9 cm yr^{-1} rates found between ~320 and 3200 m WD (van Weering et al., 2002; de Stigter et al., 2007). The high accumulation rates are closer to those found at the canyon head at 200-300 m WD (de Stigter et al., 2007). These rates suggest that this part of Nazaré Canyon has been a site of enhanced sediment accumulation for at least the past ~100 years (Appleby and Oldfield, 1978), and may imply that a mid-canyon depocentre has developed in this area. The presence of turbidites in the top 2 m of these cores might imply spurious sedimentation rate calculations since they represent rapidly deposited events. However, they make up less than 5 % of the total analysed core length in each core, and do not coincide with any abrupt changes in ^{210}Pb activity. Thus, their effect on the overall rates calculated can be assumed to be negligible.

The cause of this localised high sedimentation remains unknown; however, it is thought to be related to the interaction of a number of regional oceanographic processes. On the exposed northern part of the west Iberian shelf (including the shelf around Nazaré Canyon), water masses are affected by seasonal wind-driven surface changes (e.g. Drago et al., 1998). Northerly winds in the summer months drive south-flowing surface waters, while offshore-directed Ekman transport results in upwelling as deep water rises to replace the seaward-exported surface water (Fiúza, 1983; Vitorino et al., 2002a).

The opposite processes take place in the winter months, with southerly winds leading to downwelling and onshore transport of warm surface waters. This leads to an increase in the stratification of the bottom water on the shelf and to the development of internal waves (Vitorino et al., 2002a, b). Internal waves also develop preferentially near the head of Nazaré Canyon, where longshore sediment transport intersecting this shallow area leads to enhanced particle entrapment and thus a sharp density contrast (Schmidt et al., 2001). This results in these internal waves evolving into turbid nepheloid layers that transport enhanced suspended particle concentrations down through the canyon, similar to true gravity flows (Gardner, 1989; Schmidt et al., 2001; McCave and Hall, 2002; Oliveira et al., 2002b; van Weering et al., 2002). Resuspension of surface sediments on the continental slope is therefore enhanced by the combination of seasonal downwelling and internal wave-generated nepheloid layers. Other factors that may have an influence are floods (increased export of suspended sediment) and storms (increased wave velocity and turbulence), suggesting that resuspension would be most prominent during the winter months, although in situ recording of bottom water turbidity and sediment flux in Nazaré Canyon show no evidence of such seasonality (de Stigter et al., 2007).

Since the effects of turbulence are enhanced in steeper, narrower areas (Buscail et al., 1997; Puig et al., 2004b), enhanced resuspension and fallout of nepheloid sediments is expected to occur in the steep upper section (~3000-3500 m WD) of Nazaré Canyon, thus producing the high sedimentation rates in this area. This would also explain the appearance of the sediment in these cores, and why it is different to the turbiditic T*e* mud observed in the majority of cores throughout these canyons. The top 2 m or so of cores D15738 and D15739 are composed of mainly very soft, dark olive-brown mud with sparsely scattered silt throughout, which could be interpreted as being characteristic of nepheloid fallout.

4.6.3 Sedimentary bedforms

The sedimentary bedforms on the distal levee of Nazaré Canyon (Fig. 4.8A) and lower canyon floor of Setúbal Canyon (Figs. 4.14A and 4.16A) are interpreted to be fine- and coarse-grained sediment waves respectively (after Faugères et al., 2002; Wynn and Stow, 2002). They have also been documented in this area by other authors (e.g. Wynn et al., 2002b). There are two main types of sediment waves, those produced by turbidity current input and those by contour current input. Both instances where sediment waves have been identified in Nazaré and Setúbal canyons are believed to have been formed by turbidity currents because they are in a clearly defined turbidite system (i.e. the distal section of a canyon), and the fine-grained sediment waves in Nazaré Canyon are clearly composed of interbedded fine-grained turbidite and hemipelagic deposits, with no evidence for contourite deposits. The processes for producing fine- and coarse-grained sediment waves are believed to be different, and are discussed separately below.

4.6.3.1 Fine-grained sediment waves on the distal levee of Nazaré Canyon

Initiation of sediment wave topography is due to heterogeneous deposition from sediment gravity currents flowing over discrete obstacles on the seafloor, e.g. mounded debris flow deposits. The basal coarse-grained bedload layer ‘feels’ the topography; consequently this lower portion of the flow accelerates and bypasses sediment across the downslope-facing flanks, and decelerates and deposits sediment on the upslope-facing flanks of the waves. In contrast, the fine-grained suspended load is thicker and less affected by topography, so deposits a drape of roughly equal thickness over both flanks.

The end result is a sequence of interbedded sand-mud turbidites on the upslope-facing flanks, and mud-dominated turbidites on the downslope-facing flanks, shown clearly in the Nazaré Canyon mouth (Fig. 4.9). This explains the observed dark/light ‘zebra-stripe’ backscatter pattern on sidescan sonar records (Fig. 4.8A). Note the strong wave asymmetry between the near-horizontal upslope-facing flanks and the steeper downslope-facing flanks (Fig. 4.8C). This represents greater accumulation of sediment on the upslope-facing flank (due to the flow direction), which results in the inferred up-canyon migration of the waves (Wynn et al., 2002b; Wynn and Stow, 2002).

The crests of the sediment waves on the southern levee in the Nazaré Canyon mouth point are aligned northeast-southwest, being distinctly oblique to the east-west canyon axis and sub-parallel to the contours on the southern margin (Fig. 4.8A). This contrasts with their expected orientation roughly perpendicular to the canyon margin if they were overbank deposits of turbidity currents flowing out of the canyon and spilling over the levee, or if they were produced by bottom currents following the contours perpendicular to the canyon axis. This suggests that the sediment gravity flows that produced the sediment waves are compatible with turbidity currents, and that they did not flow down through the lower canyon floor axis to reach the canyon mouth, but that they probably entered the canyon mouth from the direction of the southern canyon wall. A likely scenario is that higher sinuosity further up Nazaré Canyon led to super-elevation of the denser part of turbidity currents at the outside of a large bend, which then spilled up and over the bend margin and flowed outside of the main canyon trajectory before re-entering further downslope (Keevil et al., 2006). The sharp change in direction of the lower canyon floor from west to northwest (Fig. 4.2A) could be a suitable location for this to happen. This would imply that very large and high-energy turbidity currents would be required to flow up the ~700 m-high canyon margin and re-enter the canyon at the mouth over a distance of ~40 km (similar to the flows interpreted to spill over the Zaire Canyon levees; Khripounoff et al., 2003). The fact that turbidites are observed depositing throughout the lower canyons and in the adjacent abyssal plain shows that turbidity currents flowing down Nazaré Canyon are of large volume and therefore capable of attaining substantial flow thicknesses and super-elevation. Similar scenarios where changes in path direction have led to flow overspill and development of sediment wave fields on levees have been observed in Monterey Fan, California (Normark et al., 2002) and Hikurangi Canyon, east of New Zealand (Lewis, 1994).

4.6.3.2 Coarse-grained sediment (gravel) waves in the lower Setúbal Canyon

Coarse-grained sediment waves in the lower Setúbal Canyon (Figs. 4.14-4.16) are composed of mature, argillaceous, meta-sedimentary pebbles and cobbles whose high degree of rounding and smooth surfaces imply frequent grain-to-grain collisions within a turbulent body. Whether the grain-to-grain collisions took place on the shelf beneath along-shelf currents or within turbidity currents as they transported the clasts down the canyon is not known, however, the clasts are inferred to have originally come from a shelf or fluvial (Tagus or Sado River?) source. The observation that the majority of the clasts have partial manganese oxidation on their surface indicates that they may have been in contact with seawater prior to their deposition as sediment waves. This would imply that the coarse-grained sediment waves formed through secondary remobilisation of pre-existing canyon floor deposits, unlike the fine-grained waves in Nazaré Canyon that formed through primary deposition beneath flow originating from the canyon head. The fact that the coarse-grained sediment waves are entirely normally-graded indicates that they represent a single flow deposit, rather than the accumulation of several flow deposits over time, such as in the fine-grained sediment waves of Nazaré Canyon. Calculating a flow velocity for the formation of these gravel waves is difficult from the available data; however, since wavelength is directly proportional to flow velocity (Wynn et al., 2002b) and gravel waves with 50-100 m wavelengths on the Laurentian Fan and Var Canyon are related to flow velocities greater than 20 m/s (Hughes Clarke, 1988; Mulder et al., 1997), then it can be assumed that the observed ≤ 600 m wavelengths in Setúbal Canyon will have been produced by even faster flowing currents.

Fig. 4.16 (*following page*) (**A**) Sidescan sonar image from the lower Setúbal Canyon, showing an area of low backscatter covering the northern margin and part of the canyon floor, which is interpreted to be a debris or slide deposit. 20 m contours show that the debrite has positive relief, while the area directly above it on the northern margin has negative relief. Black line is 3.5 kHz profile 2, shown in C. (**B**) Interpretative sketch shows the interpreted pathway of the mass wasting event (grey shading and arrows), and the edges of the canyon floor (thick dashed black lines). A suite of cores was recovered across this area and described in Fig. 4.17. (**C**) Seismic profile 2 shows the contrast between the steep canyon walls and edge of the northern margin terrace, and the wide, relatively flat but slightly domed canyon floor.

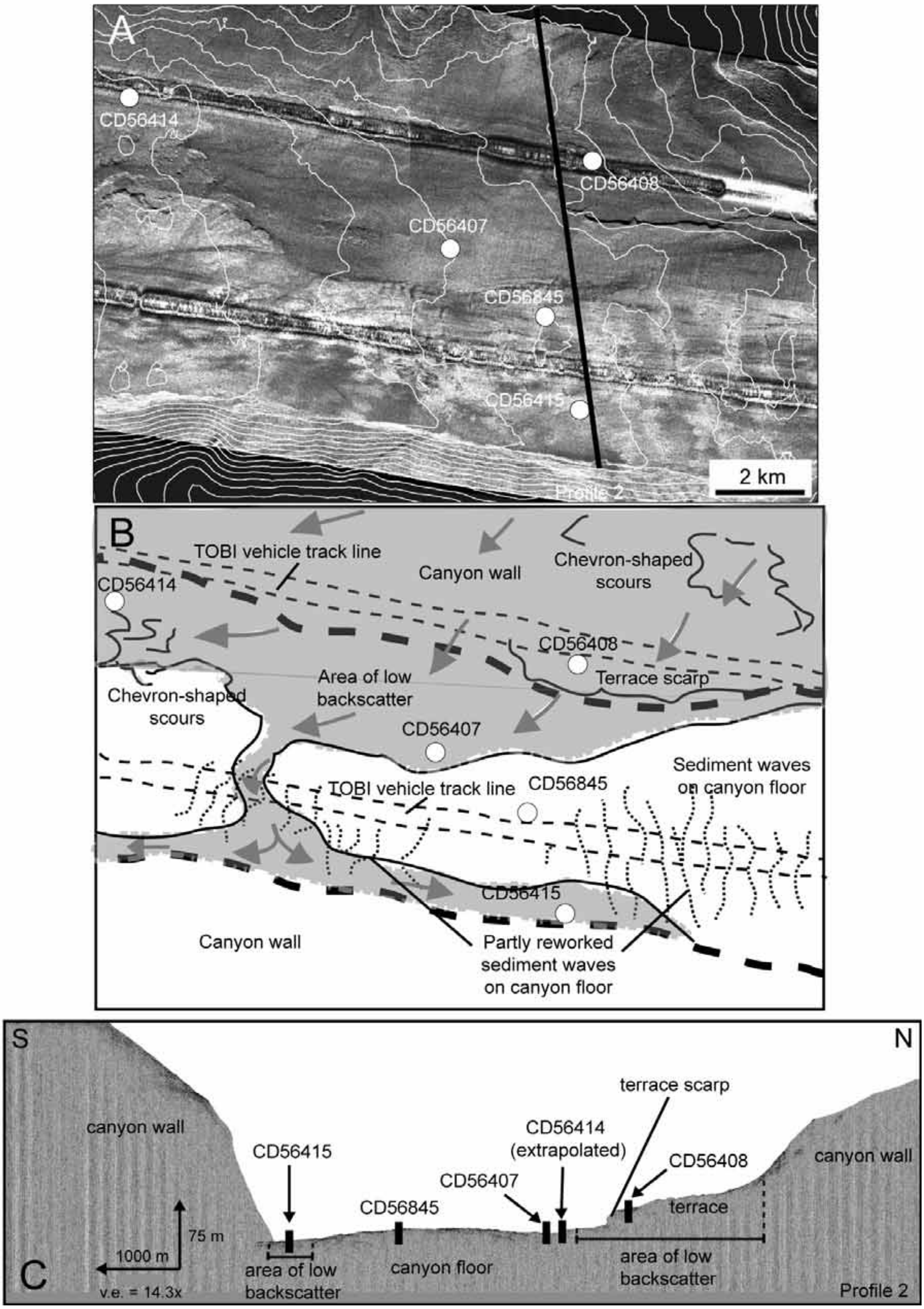
A
CD56414
CD56408
CD56407
CD56845
CD56415
2 km
Profile 2
B
TOBI vehicle track line
Canyon wall
Chevron-shaped scours
CD56414
CD56408
Terrace scarp
Area of low backscatter
Chevron-shaped scours
CD56407
TOBI vehicle track line
CD56845
Sediment waves on canyon floor
CD56415
Canyon wall
Partly reworked sediment waves on canyon floor
S
N
canyon wall
terrace scarp
CD56414 (extrapolated)
CD56415
CD56408
canyon wall
CD56407
CD56845
terrace
75 m
1000 m
area of low backscatter
canyon floor
area of low backscatter
C
v.e. = 14.3x
Profile 2

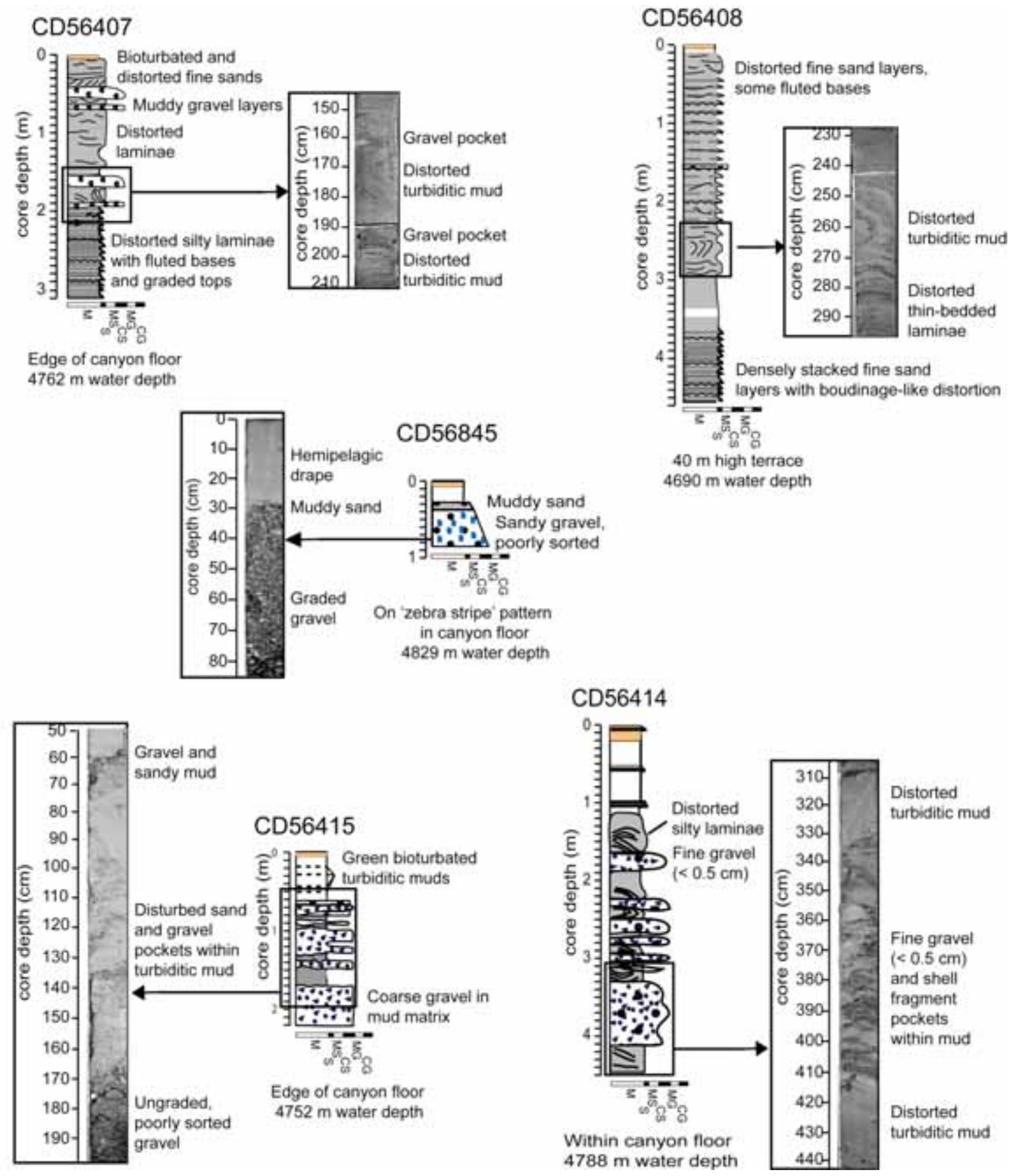

Fig. 4.17. Sedimentary logs and photographs of the cores shown in Fig. 4.16A. They imply that the low backscatter area is the deposit of a debris flow or slide that remobilised both terrace turbidites and canyon floor coarse-grained sediment waves, but that its trajectory did not affect core CD56845 (c.f. Fig. 4.16). Refer to Fig. 4.5 for a key of sedimentary structures and symbols.

4.6.4 Erosional features on the lower canyon and mouth floor

Considerable erosion has been identified on the floor of the lower canyon and canyon mouth of both Nazaré and Setúbal canyons, in the form of large-scale scours and grooves that incise the uppermost sediment deposits (Figs. 4.6, 4.8A and 4.18A). Evidence that they have been caused by erosive turbidity currents is in their shape and orientation (e.g. Wynn et al., 2002b). Their location in the lower canyon floor and mouth, directly beyond the base of the continental slope (Figs. 4.6, 4.10, 4.18A and, to some extent, 4.20A), suggests that the erosive features may have been produced by turbidity currents undergoing a hydraulic jump as a result of the sharp decrease in gradient (Normark and Piper, 1991; Mulder and Alexander, 2001; Wynn et al., 2002a). A hydraulic jump will cause a flow to rapidly become more turbulent (e.g. Komar, 1971), and could result in locally enhanced erosion. The relatively distal location of the scours implies that they were produced by low frequency, large-volume flows. This is supported by the large size of scours in and beyond the Setúbal Canyon mouth (Figs. 4.18 and 4.20 respectively), which are at least 3 km wide and 4-5 km long. Cores recovered from scour floors reveal that they are filled with a mix of turbidite sands and muds (Fig. 4.19), although it is impossible to know what proportion of the scour fill has been sampled. Overall, scour fill sediments do appear to be markedly sandier than adjacent canyon margin sediments.

The above observations provide an important insight into the nature of turbidity currents in the lower Setúbal Canyon. The medium- to coarse-grained sandy basal layer of turbidity currents is relatively thin (i.e. confined to within ~10-20 m of the canyon floor with no sand deposition above this height). This implies that the turbidity currents responsible for generating the scours were relatively thin but high-energy and erosive, which has also been interpreted for equally large scours in other channel-lobe transition zones (Piper and Savoye, 1993; Fildani et al., 2006). This interpretation contrasts with the greater thickness that is commonly attributed to high-energy and erosive turbidity currents (e.g. Mulder and Alexander, 2001).

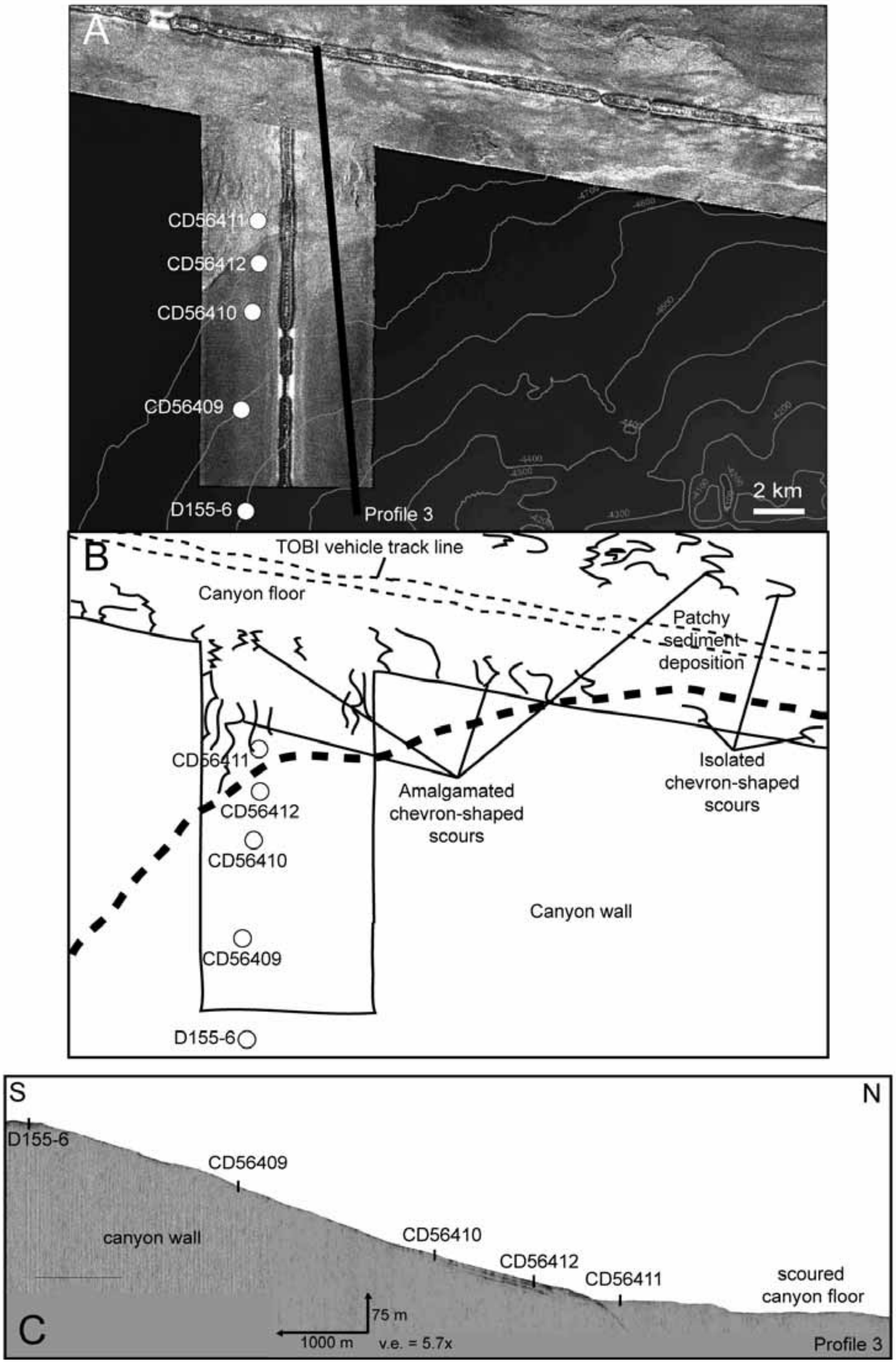

Fig. 4.18. Sidescan sonar image (**A**) and interpretation (**B**) of Setúbal Canyon mouth (100 m contours), showing a suite of cores collected from the scoured canyon floor and from successive heights along the southern margin (CD56409, CD56410, CD56411, CD56412 and D155-6, described in Fig. 4.19). (**C**) 3.5 kHz seismic profile 3. Although this profile is of poor quality, it shows the difference in gradient between the flat canyon floor and the gently sloping southern margin. Vertical exaggeration (v.e.) = 5.7x.

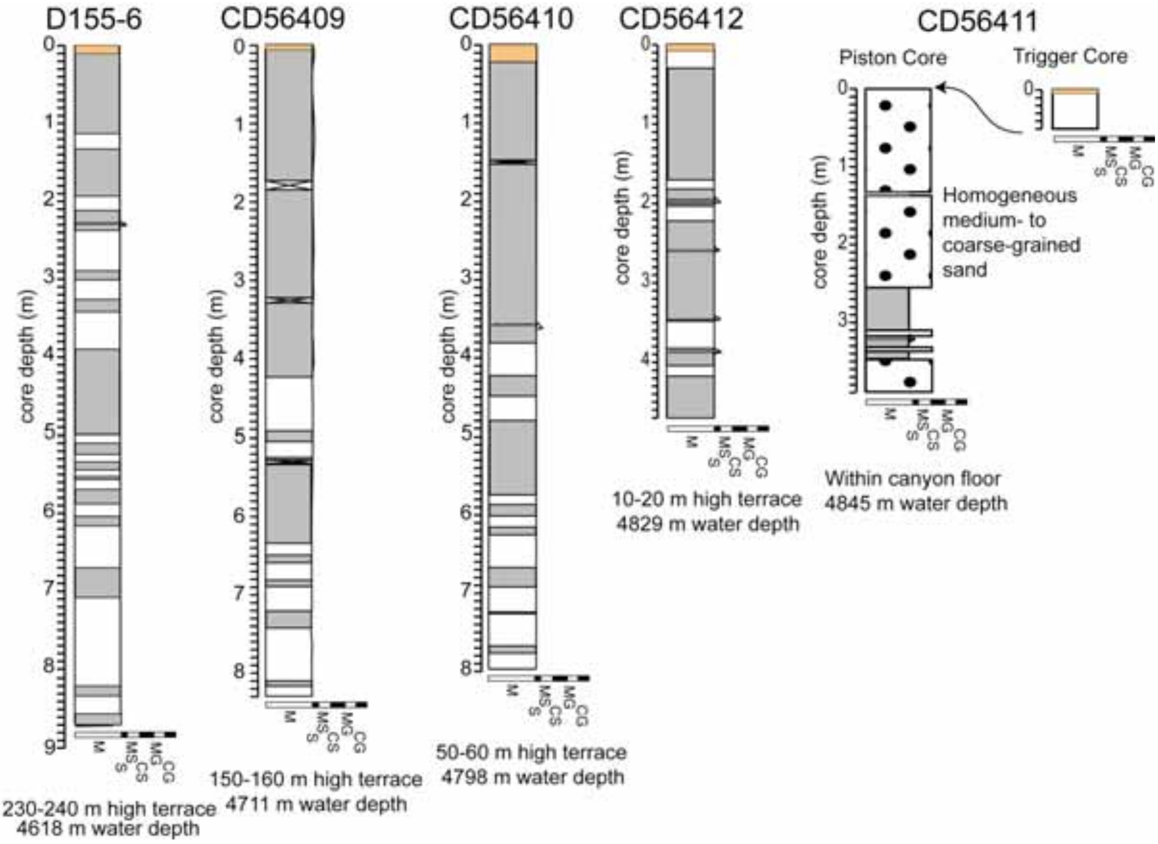

Fig. 4.19. The cores recovered from the area shown in Fig. 4.18A show an abrupt transition from dominantly thick sand in the canyon floor (white backscatter), to increasing mud content and no sand up the canyon wall (dark backscatter), over a relatively small vertical distance of only 10-20 m. Refer to Fig. 4.5 for a key of sedimentary structures and symbols.

4.6.5 Canyon margin failure in the lower Setúbal Canyon

The area of uniform low backscatter observed over the northern margin and partly across the canyon floor in the lower Setúbal Canyon (Fig. 4.16A) is believed to be a slide or debrite that has remobilised pre-existing deposits. This is evidenced by its positive relief and the area of negative relief directly above it on the northern margin, indicating the area of depletion associated with a mass wasting event. Cores CD56414 and CD56415, from the northern and southern edges of the canyon floor respectively, are comprised of gravely debrite that is inferred to have originally been deposited as graded coarse-grained sediment waves, and to have subsequently been greatly remobilised by a debris flow into their present unsorted state, as is observed in core CD56845 (Fig. 4.17). Core CD56408, located on a terrace on the northern canyon margin, is made up of slightly distorted terrace deposits (stacked thin-bedded, fine-grained sand turbidites), which are also observed in core CD56407, on the canyon floor, along with greatly remobilised gravel deposits. The turbidites in the latter core are inferred to have originally been located on a terrace or levee, and to have been moved south towards the canyon floor by the debris flow. However, the terrace facies turbidites lie below the canyon floor facies gravel, implying that a significant amount of shearing must have taken place within the debris flow.

A possible mechanism that explains the occurrence of gravel over thin-bedded turbidites within the dark backscatter area is a two-phase flow (Gee et al., 1999), whereby a cohesive flow (the muddy debris flow containing whole sequences of thin-bedded turbidites) overrides a non-cohesive layer (the gravel). The resulting overpressure of the gravel leads to mixing of the gravel upwards into the cohesive muddy sediments. This would explain why the gravel is greatly remobilised with no remnants of its original well-sorted, upward-grading state, whilst the turbidite sequences have only undergone slight distortion and remain as discrete layers. Although the turbidites have potentially been transported a greater distance within the debris flow than the gravel has, they have done so preserved as a single block due to their cohesive nature.

The only core that has not been affected by the debris flow/slide in this area is core CD56845, which still shows vertically continuous, upward-graded gravel (Fig. 4.17) located in a sediment wave field in the centre of the canyon floor. Thus, core CD56845 is inferred to have been missed by the debris flow. The reason for this is that it is located slightly higher than the other two canyon floor cores (Fig. 4.16C), and debris flows will tend to flow along the deepest parts of a canyon because of their high density. The debris flow would therefore have flowed down the northern margin, transporting whole sequences of terrace turbidites as it did so (in cores CD56407 and CD56408), then spread out laterally along the deep northern edge of the canyon floor, remobilising the gravel waves (in core CD56414). The flow must have then moved up and across a small area of the canyon floor to the even deeper southern edge where again it spread out and remobilised the gravel waves there (in core CD56415). However, it must have moved across locally rather than throughout the canyon floor axis in order to miss the site of core CD56845.

A likely cause of such a localised slope failure event on the northern levee is seismic shaking, to which the rapidly deposited fine-grained levee sequences may be vulnerable, such as is seen in the Amazon Fan (Piper and Normark, 2001). Other triggers such as overloading of sediment accumulations by storms or floods are more influential in the shallower reaches of the canyons, so these can be discounted at these depths. It should also be noted that this is the largest failure deposit that can be observed in the entire Setúbal Canyon, which concurs with the observations of Hühnerbach et al. (2004), that the largest landslides along the Atlantic passive margin tend to occur on the lowest slopes, even though they are more numerous and frequent in the upper steeper slopes.

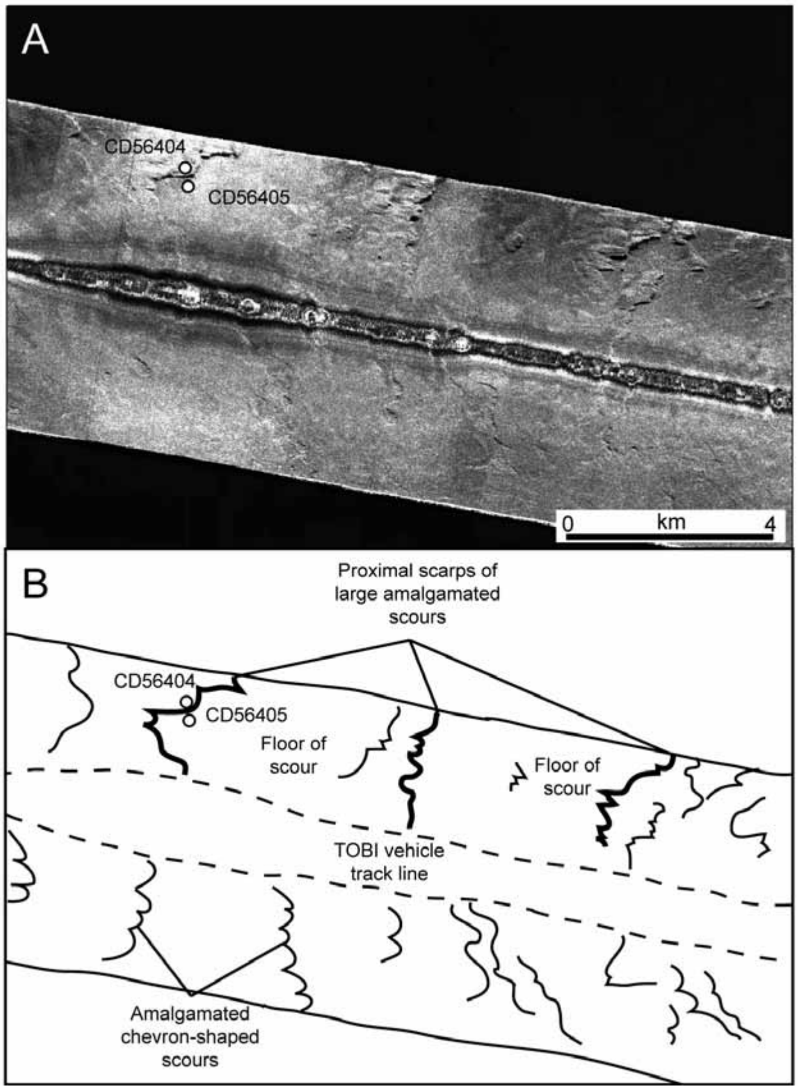

Fig. 4.20. Sidescan sonar image (**A**) and interpretation (**B**) of the Setúbal Canyon fan, showing a number of large-scale scours. Note the sharp upslope edges compared to the more gradual downslope edges of all three scours, the differences in backscatter and their apparent equidistance. Water depth is ~5000 m in the whole area.

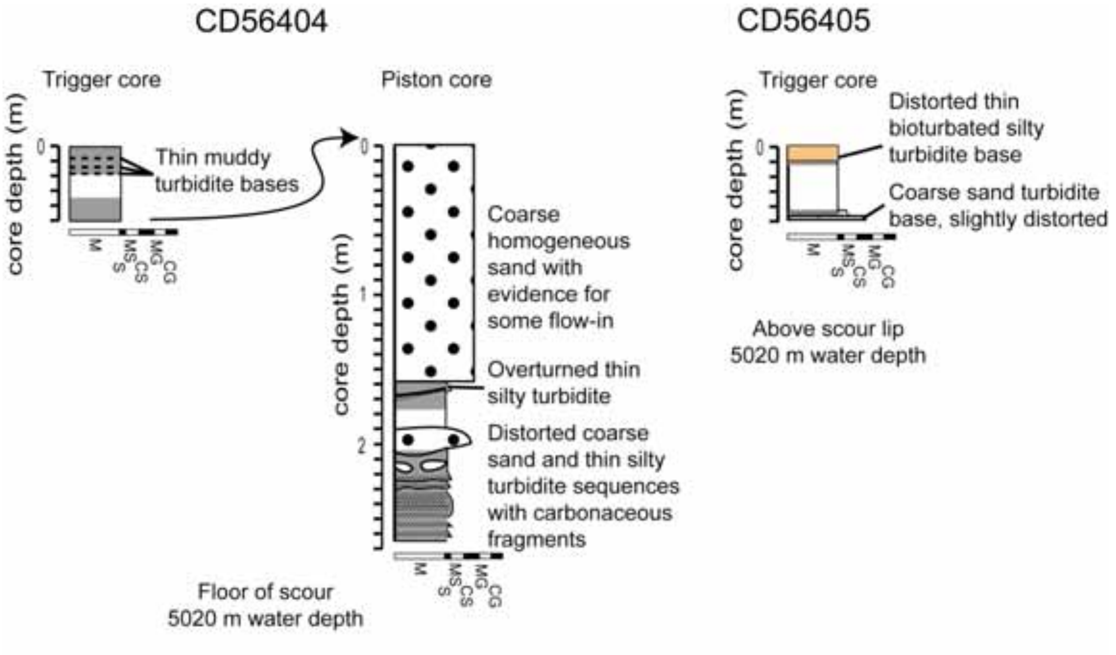

Fig. 4.21. Core CD56404 was recovered from the floor of one of the scours in Fig. 4.20A, and shows that the scour infill is composed mainly of thick homogeneous coarse sand with a turbidite/hemipelagic drape (in the trigger core) over distorted muddy and silty turbidites that possibly reflect a debris flow/slump deposit. Core CD56405 shows similar distorted thin sandy turbidite bases, possibly reflecting a failure deposit.

4.6.6 Turbidity current processes and sources

There appear to be two main types of turbidity current in Nazaré and Setúbal canyons: those that form stacked, thin-bedded, fine-grained turbidites that are rich in mica and carbonaceous fragments, and those that produce thicker, siliciclastic, medium- to coarse-grained turbidites. They are hereby described as turbidite types 1 and 2 respectively.

4.6.6.1 Turbidite type 1: thin-bedded, fine-grained, organic-rich turbidites

Type 1 deposits have been successfully cored both on upper and lower canyon terraces ~40-60 m above the floor in both canyons (Figs. 4.5, 4.7, 4.13 and 4.17). The small thickness, high mud content and regular spacing of these deposits, as well as their location on intra-canyon terraces above the thalweg, suggest that these deposits originate from the upper suspended load of super-critical turbidity currents flowing through the highly sinuous upper canyon sections.

Type 1 deposits are predominantly muddy, and their close and regular spacing (one every 1-2 cm in the cores) indicates that they resulted from regular flows that probably entered the canyon semi-continuously in the form of small pulses of sediment. Based on the uniform small size of the deposits throughout the canyons (1-2 cm-thick sand-silt bases and <5 cm-thick mud caps; Figs. 4.5, 4.7, 4.13 and 4.17), it seems unlikely that type 1 turbidity currents transported much sediment beyond the canyon mouths. These turbidity currents are thus inferred to be small-scale, relatively regular events; possibly on an annual scale, as proposed by de Stigter et al. (2007). They are probably the result of failures generated by overloading and over-steepening of sediment during floods and/or storms (similar to processes that occur in the Var Canyon system, Mulder et al., 1998).

Although the regularity and high organic matter of these deposits may suggest a fluvial or hyperpycnal origin, this cannot be the case for both canyons. Hyperpycnal turbidity currents are the result of high-density plumes of sediment from ‘dirty’ rivers (Mulder et al., 2001). Setúbal Canyon is fed by the high discharge Tagus and Sado Rivers, so these deposits could superficially be interpreted as hyperpycnites; however, the same deposits are also found in Nazaré Canyon, which lacks direct access to a river mouth. Additionally, hyperpycnites have a characteristic coarsening-upward basal unit (Mulder et al., 2001) that is not observed in these deposits. Therefore a hyperpycnal origin cannot be compatible for the same deposits in both canyons.

Additionally, the organic material found in Type 1 turbidites displays large differences in composition, state and abundance between the two canyons, implying different sources. In Setúbal Canyon they are brownish plant fragments including pollen spores and wood fragments, which suggest that they were fresh when they entered the basin and that they have had a low residence time in the system. This seems plausible because the mouths of the Tagus and Sado Rivers lead almost directly into the head of Setúbal Canyon. The carbonaceous material in Nazaré Canyon, however, is entirely black and coalified in comparison, suggesting a forest fire debris origin (e.g. Oliveira et al., 2007). The more forested north of Iberia is prone to annual forest fires, which may explain the regional occurrence of burnt wood fragments in Nazaré Canyon if they are exported to the sea along with fluvial sediment via the northern Mondego or Douro Rivers (e.g. Vitorino et al., 2002b; Oliveira et al., 2007).

4.6.6.2 Turbidite type 2: thick-bedded, coarse-grained, siliciclastic turbidites

The second type of turbidite that is observed in the Nazaré and Setúbal canyons is generally found on the terraces and floor of the lower section, beyond ~4000 m WD (Figs. 4.7, 4.9 and 4.19). These deposits represent the coarse bedload fraction of flows, which generally bypass the steep upper section and deposit in the deeper parts of the canyon, with any finer-grained suspended fraction bypassing the canyon completely (a common occurrence in most canyon systems, e.g. Var Canyon off southeast France, (Klaucke et al., 2000). The occasional occurrence of siliciclastic sandy bases on upper canyon terraces (Figs. 4.5 and 4.13), is probably due to centrifugal forces causing basal parts of flows to be deflected towards the outside of large bends, where they undergo super-elevation (Keevil et al., 2006).

Turbidity currents that produce type 2 deposits are inferred to flush through the entire canyons, as their deposits are found in the lower canyon floor and the abyssal plains (Thomson and Weaver, 1994). Evidence for considerable erosion by these flows in the lower canyon and mouth floor of both canyons includes large-scale scours and grooves that incise recent sediment deposits (Figs. 4.6 and 4.20).

Type 2 turbidites are comparable in both Nazaré and Setúbal canyons, implying that their source in both canyons is the same. The quartz- and feldspar-rich beaches and cliffs towards the north of Nazaré Canyon (the Espinho-Mondego Cap sector) are possible candidates, with erosion by winds and waves resulting in southward transport of coarse-grained siliciclastic sand along the west Iberia shelf. Further evidence for these northern sources is in the north-south decrease in quartz concentration along the shelf (Oliveira et al., 2007), indicating increasing distance from source. Wind-driven flow on the shelf is estimated to be sufficient to transport sediment locally, and tidal flow efficiently winnows the sediment, allowing the sand (high settling velocities) to remain on the shelf whilst the fine mud fraction (low settling velocities) is exported (Huthnance et al., 2002). Thus, accumulation of quartz-rich, clean sand across the shelf over time could be prone to episodes of failure and lead to the initiation of episodic turbidity currents that flush through the entire canyons.

Possible triggers of shelf failures are regional earthquakes (through ground shaking and instability, (e.g. Jones and Omoto, 2000) or overloading of sediment during storms

(Pinheiro et al., 1996; Terrinha et al., 2003; Puig et al., 2004a). Similar deposits are observed in the Var Canyon system and are also interpreted as being the result of large, earthquake-induced ignitive turbidity currents that are highly erosive and deposit extensive thick sandy turbidites throughout the canyon (Mulder et al., 1998). A likely centennial or longer timescale is implied for this type of turbidity current in the Portuguese canyons (de Stigter et al., 2007).

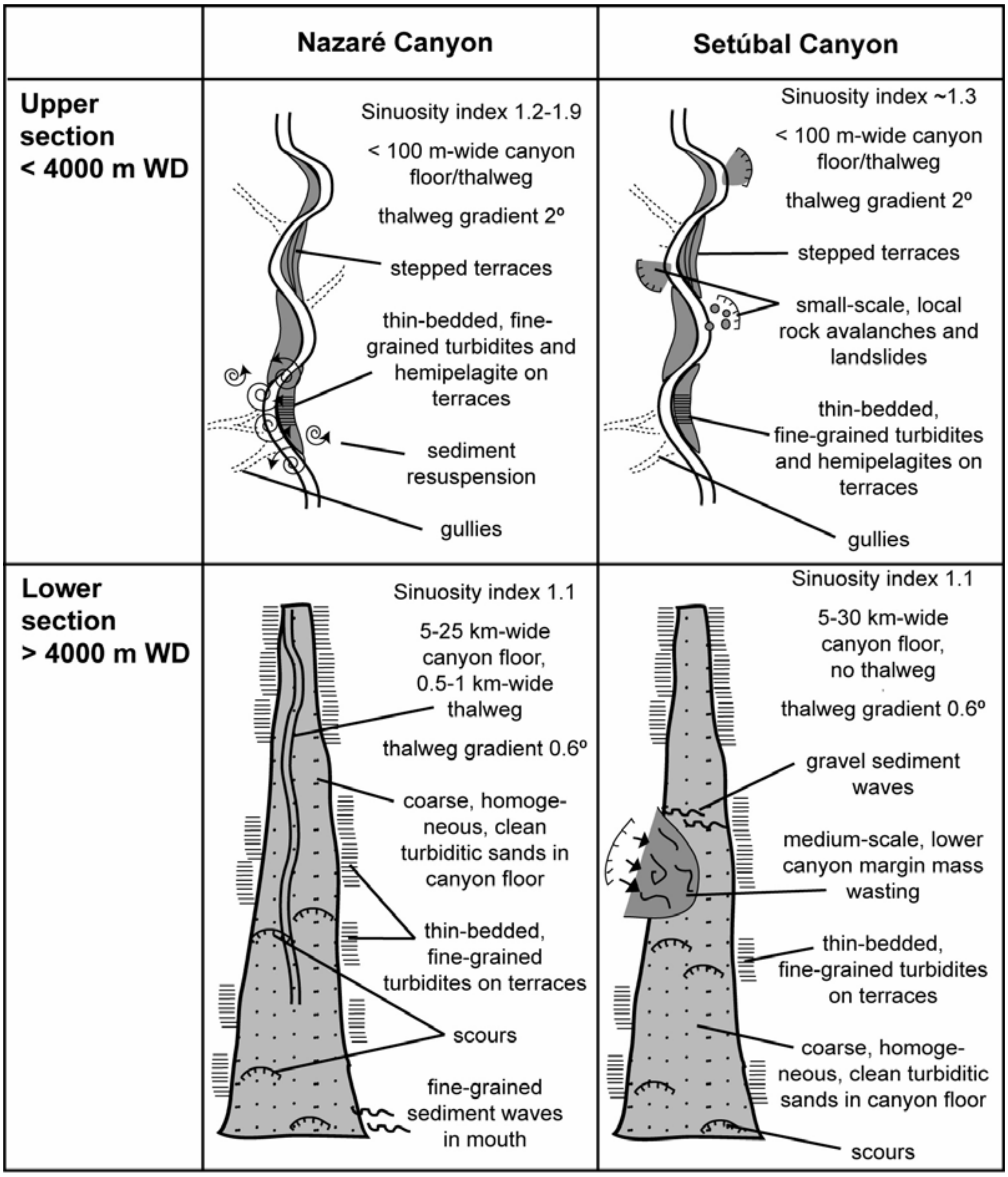

Fig. 4.22. Cartoon summarising the main sedimentary features and processes that are observed in the upper and lower sections of Nazaré and Setúbal canyons.

4.7 Conclusions

This new dataset comprises data at a range of scales, from multibeam bathymetry (hundreds of km) to piston cores (millimetres to centimetres). The integration of all these data highlights the high level of complexity that exists throughout all scales in Nazaré and Setúbal canyons. The key findings can be summarised as follows (and in Fig. 4.22):

1. Turbidity currents are the dominant process of sediment transport, erosion and deposition in Nazaré and Setúbal canyons, evidenced by the dominance of gravity flow deposits and erosive scours throughout both canyons, which have led to their deep incision into the continental shelf and slope.
2. There are two main types of turbidity current that occur in the canyons: type 1 are small-volume, high-frequency, carbonaceous- and mica-rich turbidity currents that deposit mainly on the shallower intra-canyon terraces from suspended load fall-out, and type 2 are large-volume, low-frequency, canyon-flushing turbidity currents that bypass the upper section and deposit mainly in the deeper parts of the canyon and the abyssal plains.
3. The source of terrigenous sediment in both types of turbidity current is thought to be the shelf. However, the source for the abundant carbonaceous material in type 1 deposits in Nazaré Canyon is unknown, but a possibility may be forest fire debris brought to the shelf via fluvial transport. Probable triggers for the first type of turbidity current are thought to be small-scale shelf break failures due to frequent overloading and over-steepening by storms and/or floods, and larger-scale (possibly earthquake-generated) shelf break failures for the second type.
4. The turbidity currents that transport coarse sand to the lower reaches of the canyons are very erosional and produce large-scale scours (megaflutes) and grooves in the canyon floor; There is some evidence that flows responsible for forming these scours had a relatively thin, erosional lower section, <10-20 m thick.
5. Anomalously high sedimentation rates are evident in upper Nazaré Canyon, compared with upper Setúbal Canyon, probably as a result of enhanced upwelling and internal wave/nepheloid layer generation in this region. This possible nepheloid layer-derived sediment could therefore represent a third type of

sedimentary flow process separate from type 1 and 2 turbidites.

6. Both fine- and coarse-grained (gravel) sediment waves are present in the canyons, with the former on the canyon margin and the latter on the lower canyon floor of Nazaré and Setúbal canyons, respectively.
7. Mass wasting events tend to be small-scale (<10 km^2) and localised in the steep and erosional upper canyon sections, especially in Setúbal Canyon, and take the form of rock avalanches and landslides. Slope failures in the lower sections are rare, as these areas are dominantly depositional and have more gentle gradients; however, a large debris flow/slide has been identified in the lower Setúbal Canyon, and comprises remobilised canyon margin and canyon floor sediments.

CHAPTER 5

A forest fire record from the last 1000 years preserved in a deep-sea setting: Nazaré Canyon, west Iberian margin[3]

---

[3] Arzola, R.G., Masson, D.G., Roberts, A.P., Weaver, P.P.E. (submitted). A forest fire record from the last 1000 years preserved in a deep-sea setting: Nazaré Canyon, west Iberian margin. *Quaternary Science Reviews*.

5.1 Abstract

A sediment depocentre with extremely high sediment accumulation rates has been found in the middle section of the Nazaré Canyon, west Iberian margin. Five piston cores from terraces within a 6 km radius contain thick muddy accumulations with a distinct magnetic susceptibility signal that spans the time interval from 700 to 100 years before present. Magnetic, chemical and mineralogical analyses indicate that the high magnetic susceptibility values are due to relatively high concentrations of terrigenous ferrimagnetic minerals that are associated with high abundances of charcoal. We conclude that the high magnetic susceptibility values result from increased terrigenous sediment supply of magnetically enhanced soil material that resulted from increased erosion after intense forest fire activity. These fires were probably triggered by favourable Little Ice Age conditions and possibly also by anthropogenic activity over the last 700 years. Geochemical and lithological evidence point to the Tagus Estuary as the source of the sediment. The data presented here therefore provide a high-resolution record of the effects of short-lived climate change and/or anthropogenic activity on the landscape, preserved in a unique deep-sea setting.

5.2 Introduction

The west Iberian margin is incised with numerous canyons (Fig. 5.1). The two largest, Nazaré and Setúbal, have been intensively studied for several decades and are complex in terms of geomorphology, oceanography and sedimentary processes (e.g. Vanney and Mougenot, 1981, 1990; Pinheiro et al., 1996; Drago et al., 1998; Schmidt et al., 2001; Epping et al., 2002; van Weering et al., 2002; Alt-Epping et al., 2007; de Stigter et al., 2007; Oliveira et al., 2007; Arzola et al., 2008; Lastras et al., 2009). These canyons also provide good examples of the different ways in which terrigenous material is distributed beyond the continental shelf. The two upper canyon tributaries of Setúbal Canyon, one of which is Lisbon Canyon, lead out from the Sado and Tagus Estuaries (Fig. 5.1) and funnel fluvial terrigenous material directly into the canyon. Nazaré Canyon, however, is not directly fed by a river and is believed to receive terrigenous material via lateral advection on the shelf from beaches and small rivers (e.g. Oliveira et al., 2002a, b, 2007; van Weering et al., 2002; Alt-Epping et al., 2007).

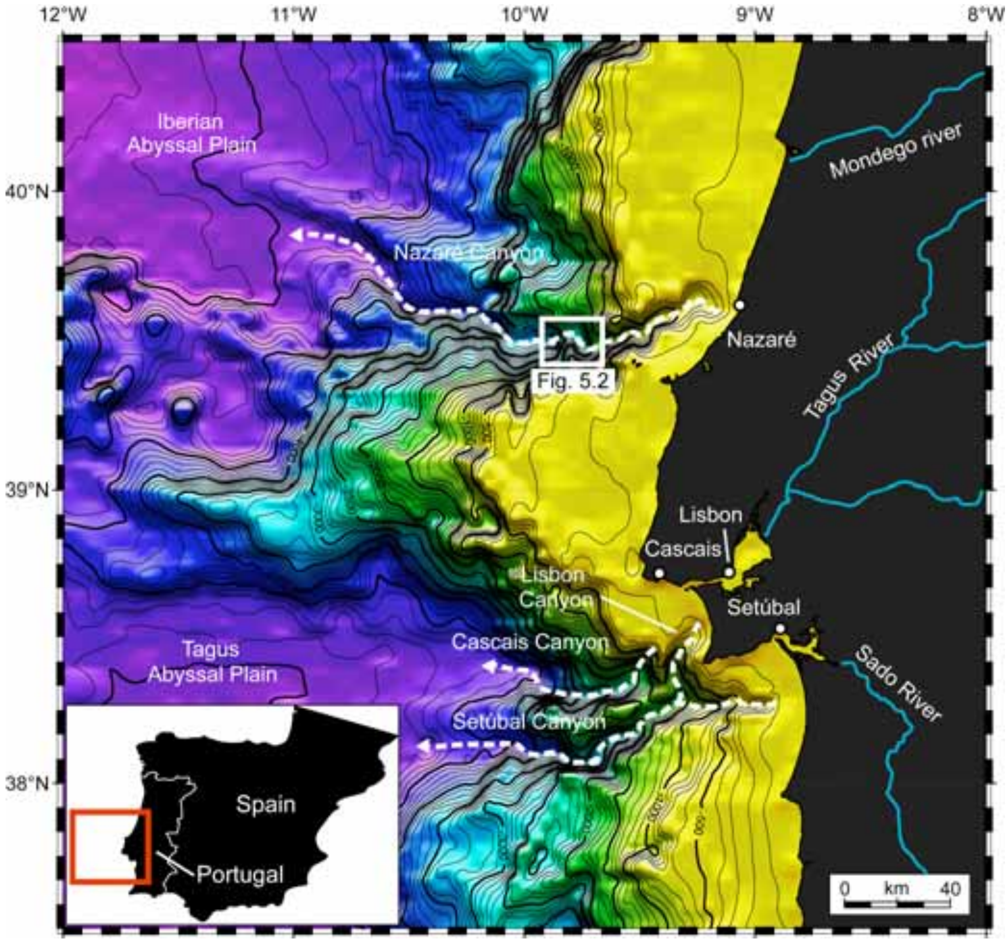

Fig. 5.1. Bathymetric map of the west Iberian margin, with locations of the Nazaré, Setúbal-Lisbon and Cascais Canyons (with 100 m contours). The location of Fig. 5.2 is indicated by the white box.

The upper and middle sections of both Nazaré and Setúbal canyons (shallower than ~4000 m water depth (WD), after de Stigter et al., 2007) are mainly erosional with numerous gullies, grooves and landslide scars, while depositional features such as levees and sediment waves are more prevalent in the lower section (Arzola et al., 2008; Lastras et al., 2009). However, deposition also occurs in the middle section of Nazaré Canyon at about 3500 m WD (Schmidt et al., 2001; van Weering et al., 2002; de Stigter et al., 2007; Arzola et al., 2008). This is thought to be a direct result of the hydrographic and sedimentary conditions in the northern part of the margin where Nazaré Canyon is located (de Stigter et al., 2007).

The supply of fine sediment into Nazaré Canyon is much higher than in the other canyons on the west Iberian margin (van Weering et al., 2002; de Stigter et al., 2007). The reasons for this are still being investigated, but the position of the canyon head near the coast and the resulting exposure to incoming ocean waves may be contributing factors. Diurnal tides interacting with the topography of the canyon head rim lead to the development of internal waves (McCave and Hall, 2002; Vitorino et al., 2002a, b; Quaresma et al., 2007), and the action of these waves on the seabed causes high amounts of suspended sediment at the canyon head. As a result, there is a permanent bottom nepheloid layer on the adjacent shelf, which becomes detached at the shelf edge. Where it crosses the canyon rim, this bottom nepheloid layer forms shallow intermediate nepheloid layers within the canyon (Schmidt et al., 2001; van Weering et al., 2002; de Stigter et al., 2007; Oliveira et al., 2007). The nepheloid layers are carried down the canyon by internal tides, and are deposited as the tidal currents weaken with depth. The result is an area with high rates of deposition in the canyon at about 3500 – 3900 m WD, particularly on terraces adjacent to the incised canyon axis (Fig. 5.2; Schmidt et al., 2001; van Weering et al., 2002; de Stigter et al., 2007; Arzola et al., 2008). This terraced area in the middle part of Nazaré Canyon preserves a unique high-resolution late Holocene deep-sea record that is the focus of this study.

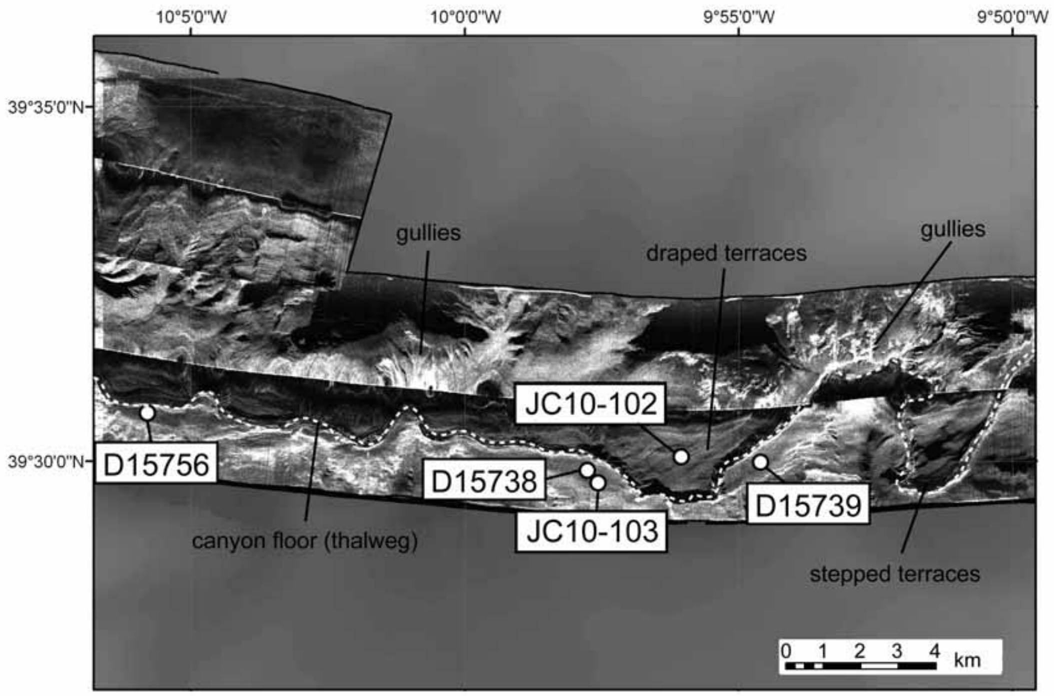

Fig. 5.2. Sidescan sonar image of the middle section of Nazaré Canyon (~3400-3900 m water depth) with piston core locations. Backscatter is an indicator of surface reflectivity due to sediment type and surface, i.e. dark greys and black represent sediments with low reflectivity and smooth surfaces such as muddy terraces, while light greys and white represent highly reflective sediments and rough surfaces such as steep rocky slopes and sandy patches. The white dashed line indicates the incised canyon floor or thalweg.

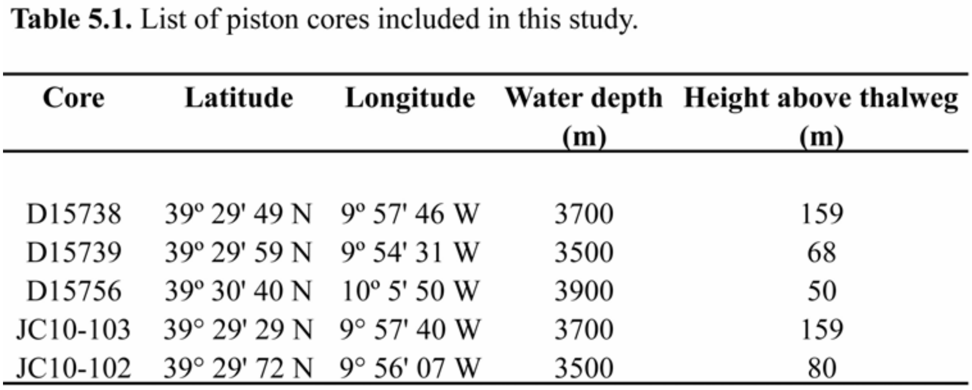
Table 5.1. List of piston cores included in this study.

Core	Latitude	Longitude	Water depth (m)	Height above thalweg (m)
D15738	39º 29' 49 N	9º 57' 46 W	3700	159
D15739	39º 29' 59 N	9º 54' 31 W	3500	68
D15756	39º 30' 40 N	10º 5' 50 W	3900	50
JC10-103	39° 29' 29 N	9° 57' 40 W	3700	159
JC10-102	39° 29' 72 N	9° 56' 07 W	3500	80

5.3 Methods

5.3.1 Core collection

Five piston cores and two trigger cores were collected from the terraced area between ~3500 and 3900 m WD in Nazaré Canyon during HERMES cruises D297 (2005) and JC10 (2007; Table 5.1).

5.3.2 Magnetic susceptibility measurements

Split core sections were measured using a Bartington Instruments MS2E point sensor to obtain non-destructive, low-field magnetic susceptibility measurements at 1 cm intervals (e.g. Gunn and Best, 1998). U-channel samples (4 cm^2 cross-section, Weeks et al., 1993) of the upper 6.2 m of core JC10-103 were also measured using a Bartington Instruments MS2C loop sensor at 0.5 cm intervals. A volume correction factor of 2.02 (Sagnotti et al., 2003) was applied to the U-channel data. The same correction was applied to data from the other cores.

5.3.3 Environmental magnetic analyses

Magnetic minerals are sensitive to a wide range of environmental processes. Environmental magnetic analyses can therefore be useful for investigating present and past environmental and climatic conditions in sediments (e.g. Verosub and Roberts, 1995). Remanent magnetisation measurements were made on U-channel samples from core JC10-103 using a 2-G Enterprises cryogenic magnetometer to measure the natural (NRM), anhysteretic (ARM) and isothermal (IRM) remanent magnetisation at 1 cm intervals (Weeks et al., 1993; Roberts, 2006). The measurement sequence was as follows.

- The NRM was measured and progressively stepwise alternating field (AF) demagnetised at 5, 10, 15, 20, 25, 30, 40, 50, 60 and 80 mT. The NRM was measured after each demagnetisation treatment.
- An ARM was imparted using a 90 mT AF and an axial 0.05 mT DC bias field. The ARM was then measured and progressively AF demagnetised at 10, 20, 30, 40, 50, 60, 80 and 90 mT.

- An $IRM_{900\ mT}$ (or SIRM) was imparted to the U-channel samples by applying a 900 mT DC field using a 2-G Enterprises pulse magnetiser, and was then measured and progressively demagnetised at 10, 20, 30, 40, 50, 60, 80, 90 and 100 mT. An $IRM_{-300\ mT}$ was then imparted by applying a 300 mT DC field to the sample in the opposite direction to the SIRM. This allows calculation of the S-ratio ($-IRM_{-300\ mT}/SIRM$) and of the HIRM or 'hard IRM' ($(SIRM - IRM_{-300\ mT}) / 2$, e.g. King and Channell, 1991).

Magnetic hysteresis properties were measured along with first-order reversal curves (FORCs; Roberts et al., 2000) on 0.5 g samples using a Princeton Measurements Corporation vibrating sample magnetometer. In each case, 100 FORCs were measured with an averaging time of 200 ms. The FORC data were processed using the FORCinel software package (Harrison and Feinberg, 2008) and a smoothing factor of 5 (c.f. Roberts et al., 2000).

5.3.4 Age model

An age model for the last ~100 years was obtained for cores D15738, D15739, JC10-102 and JC10-103 using the ^{210}Pb decay method (after Appleby and Oldfield, 1978; Table 5.2). Core D15756 was not analysed because ^{210}Pb is associated with the fine-grained fraction and the sediment in this core is too coarse-grained to give meaningful ^{210}Pb data. Accelerator mass spectrometry (AMS) radiocarbon dating of planktonic foraminifera was carried out on cores D15738 and D15739 and was used to extend the ^{210}Pb age model beyond 100 years before present (yr BP). The age model was then extrapolated across the remaining three cores using magnetic susceptibility profiles as the basis for correlation. Conventional radiocarbon ages were converted to calibrated ages using the Marine04 calibration curve (after Stuiver et al., 1998; Hughen et al., 2004; Reimer et al., 2004), using a 400 yr reservoir age for the deep sea (Table 5.3). An overall average sedimentation rate was calculated for each of the two cores.

Table 5.2. Measured ^{210}Po activity, calculated excess ^{210}Pb and sediment accumulation rates (after Appleby and Oldfield, 1978).

Core[a]		**Sample depth**[b] **(cm)**	**^{210}Po activity (Bq g^{-1})**	**Value of constant ^{210}Pb at depth**	**Excess ^{210}Pb**	**ln(excess ^{210}Pb)**	**Sediment accumulation rate (cm yr^{-1})**
D15738	TC	1 (11)	0.199	0.026	0.173	-1.756	
		10 (20)	0.181	0.026	0.155	-1.861	
		20 (30)	0.133	0.026	0.107	-2.231	
		35 (45)	0.041	0.026	0.015	-4.195	**0.43**
	PC	3	0.360	0.026	0.334	-1.097	
		10	0.219	0.026	0.193	-1.645	
		20	0.170	0.026	0.144	-1.939	
		45	0.046	0.026	0.020	-3.896	**0.47**
	TC and PC						**0.46**
D15739	TC	3	0.316	0.026	0.290	-1.238	
		20	0.258	0.026	0.188	-1.672	
		38	0.214	0.026	0.104	-2.262	**1.06**
	PC	10	0.140	0.026	0.232	-1.462	
		32	0.130	0.026	0.114	-2.175	
		55	0.104	0.026	0.078	-2.556	
		74	0.050	0.026	0.024	-3.736	
		90	0.044	0.026	0.018	-3.998	
		112	0.032	0.026	0.006	-5.056	
		127	0.030	0.026	0.004	-5.637	**0.86**
	TC and PC						**0.87**
JC10-102	PC	1.5	0.251	0.032	0.219	-1.519	
		5.5	0.220	0.032	0.188	-1.672	
		10.5	0.195	0.032	0.163	-1.814	
		15.5	0.187	0.032	0.155	-1.865	
		20.5	0.198	0.032	0.166	-1.797	
		25.5	0.083	0.032	0.051	-2.968	
		29.5	0.145	0.032	0.113	-2.182	
		35.5	0.138	0.032	0.106	-2.245	
		40.5	0.160	0.032	0.128	-2.053	
		45.5	0.119	0.032	0.087	-2.442	
		50.5	0.128	0.032	0.096	-2.344	
		55.5	0.134	0.032	0.102	-2.283	
		65.5	0.103	0.032	0.071	-2.649	
		75.5	0.080	0.032	0.048	-3.029	
		85.5	0.064	0.032	0.032	-3.439	
		95.5	0.062	0.032	0.030	-3.506	
		105.5	0.053	0.032	0.021	-3.885	
		125.5	0.044	0.032	0.012	-4.442	
		135.5	0.040	0.032	0.008	-4.863	**1.37**
JC10-103	PC	4.5	0.360	0.026	0.334	-1.097	
		10.5	0.272	0.026	0.246	-1.403	
		15.5	0.308	0.026	0.282	-1.265	
		20.5	0.207	0.026	0.181	-1.712	
		25.5	0.218	0.026	0.192	-1.650	
		32.5	0.179	0.026	0.153	-1.878	
		38.5	0.152	0.026	0.126	-2.069	
		44.5	0.128	0.026	0.102	-2.284	
		50.5	0.117	0.026	0.091	-2.393	
		58.5	0.099	0.026	0.073	-2.615	
		69.5	0.057	0.026	0.031	-3.466	
		79.5	0.051	0.026	0.025	-3.699	
		89.5	0.041	0.026	0.015	-4.225	
		100.5	0.032	0.026	0.006	-5.091	
		111.5	0.029	0.026	0.003	-5.741	**0.75**

[a] TC = trigger core, PC = piston core.

[b] Brackets indicate the extrapolated total core depth of a TC or PC sample when both lengths are combined.

Table 5.3. AMS radiocarbon data with conversion from conventional to calibrated ages, and average sedimentation rates (Fig. 5.4B).

Core	Sample depth (cm)	NERC sample ID	Conventional radiocarbon age (yr BP)	Error range ± (1 sigma yr)	Calibration curve	Reservoir age (yr)	Calibrated radiocarbon age range (2 sigma Cal yr BP)	Average radiocarbon age (Cal yr BP)	Average sedimentation rate (cm Cal yr^{-1})
D15738	178.5	SUERC-18143	573	37	Marine04	400	90-290	190	
	250.5	SUERC-18146	738	37	Marine04	400	290-460	375	
	335	SUERC-18147	934	37	Marine04	400	480-620	550	
	405	SUERC-18148	1204	37	Marine04	400	660-850	755	
	509.5	SUERC-18149	1482	35	Marine04	400	940-1130	1035	**0.39**
D15739	334.5	SUERC-18150	703	37	Marine04	400	270-435	352.5	
	489.5	SUERC-18151	821	37	Marine04	400	370-520	445	
	628	SUERC-18152	816	37	Marine04	400	360-520	440	
	829.5	SUERC-18153	1245	37	Marine04	400	700-890	795	
	959.5	SUERC-18156	1411	37	Marine04	400	890-1050	970	**1.01**

5.3.5 X-ray diffraction (XRD) and scanning electron microscope (SEM) analyses

Mineralogical identifications of the combined clay (15 μm) and coarse silt (63 μm) fractions of core JC10-103 (accurate to ± 1 %) were carried out using XRD results obtained at the University of Aveiro. Carbonate was removed from the sediment samples by dissolution with acetic acid (10%). XRD analysis was complemented by SEM identification of mineral grains. Sediment samples from six core depths were impregnated with resin and polished, and were visually analysed using a Zeiss Leo 1450VP SEM. Chemical and reflective backscatter analysis of the sediment grains was carried out using a Princeton Gamma Tech (IMIX-PTS) X-ray energy dispersive spectrometer (EDS). Real time data were processed using the SmartSEM software.

5.3.6 Grain size measurements

Bulk grain size measurements were carried out at 50 cm stratigraphic intervals on core JC10-103 using a Malvern Laser Mastersizer 2000 particle sizer. The laser diffraction method operates using the Mie theory of particle diffraction, whereby particles of a given size diffract light through a given angle, which increases with decreasing particle size, assuming that particles are spherical and in a dilute suspension (McCave and Syvitski, 2007).

5.3.7 X-ray fluorescence (XRF) analysis

Surface elemental concentration profiles and microradiographs were obtained for core D15738 using a Cox ITRAX analyser, and processed using the Q-Spec software (after Croudace et al., 2006).

5.3.8 Total and inorganic carbon measurements

The total carbon content of samples from core D15738 was analysed by measuring the amount of carbon dioxide liberated by heat-decomposition. To determine the inorganic carbon content, each sample was treated with a phosphoric acid solution to acid-decompose the inorganic carbon content only (because the acid does not affect the organic carbon content). The organic carbon was then inferred as the difference between the two determinands. The instruments used in both analyses were manufactured by UIC Inc.

5.3.9 Vitrinite reflectance measurement

Charcoal is composed of organic components or macerals, the most significant being vitrinite, which is derived from the cell-wall material or woody tissue of plants (Stach et al., 1975). Vitrinite (and therefore charcoal) has a much higher reflectance than non-burnt wood and other organic matter (Hoffmann and Jenkner, 1932), and is used to confirm and quantify the amount of charcoal present in sediments and rocks. The carbonate and silicate content of the sediment samples was removed by digestion in hydrochloric and hydrofluoric acids, which leaves only the organic matter. The organic matter was mounted on slides, polished (after Hillier and Marshall, 1988), analysed (using a Zeiss UMSP 50 reflectance microscope calibrated with a diamond standard reflectivity of 5.227) and measured (using a x 40 antiflex objective under cedar oil at a refractive index of 1.515). In order to make the reflectance analysis as unbiased as possible, the grain closest to the centre of the field of view was measured each time, regardless of what the grain was, and only one measurement was made per field of view. Approximately 300 random measurements were made for each homogenised slide.

5.4 Results

5.4.1 Lithology

Cores D15738, D15739, D15756, JC10-102 and JC10-103 are all composed of the same homogeneous olive green-brown silty mud, with foraminifera and black specks scattered throughout the sediment (Fig. 5.3). The cores were taken at different heights above the canyon floor/thalweg, which is reflected in the sequence of silty-sandy turbidite bases. The most distal studied core (D15756), which was also from the deepest water, is composed of numerous 1-2-cm-thick silty-sandy turbidite bases with no intervening hemipelagic layers and no bioturbation, which suggests that deposition occurred through frequent small events. The number of clearly identifiable turbidite bases decreases and the degree of bioturbation increases in cores D15738 and JC10-103, which are from shallower terraces, up to the two highest cores (JC10-102 and D15739), which are dominated by turbiditic mud with sparse and strongly bioturbated turbidite bases. All five cores have orange-pink mud at the top, which represents the oxidised surface layer. The presence of this layer indicates that little sediment is missing from the tops of the cores.

5.4.2 Magnetic susceptibility

Magnetic susceptibility (MS) profiles are similar for all five cores (Fig. 5.3) and can be divided into five zones. Using the longest core (JC10-103) as an example, zone 1 has initially consistent MS values (~350 S.I. units) in the uppermost 1 m that increase rapidly to ~500 S.I. units between sub-seabed depths of 1 and 1.5 m. These values remain relatively constant through zone 2 (1.5-2.5 m) before decreasing rapidly to 200 S.I. units over ~40 cm in zone 3. There is a small peak in zone 4 (3.3-3.6 m) that reaches a maximum value of ~250 S.I. units, followed by low values in zone 5 that decrease gradually from ~100 to ~25 S.I. units over ~10 m of core. This overall pattern of MS variation can be visually correlated across the other cores (Fig. 5.3), with some variations in the thickness of each zone (due to variable sedimentation rates) and with MS reaching a maximum value of 700 S.I. units in zone 2 of core D15739.

None of the cores have any obvious visual relationship between MS and lithology. However, detailed analysis of turbidites in core D15756 (Fig. 5.3) indicates that the total thickness of the silt and sand fraction (analysed visually) per 10 cm interval of core increases with depth from an average of 0.6 cm above depths of 4.5 m (coinciding with the high MS zones), to an average of 3.8 cm below this depth.

Fig. 5.3. (*following page*) Lithological logs and MS profiles for the five studied piston cores and associated trigger cores. Five MS zones (labelled 1-5 in red) can be identified in all cores except for core JC10-102, which only penetrates as far as zone 3. AMS radiocarbon age ranges (in black, Cal yr BP) for cores D15738 and D15739 confirm that the MS variations correlate across all cores. MS profiles in green correspond to the trigger cores, and ‘ca 100’ refers to sediments with an age of 100 yr BP based on ^{210}Pb sediment accumulation rates (Table 5.2 and Fig. 5.4A). A detailed turbidite thickness analysis is shown for core D15756. The dashed line at a depth of 4.5 m reflects a sharp boundary in both turbidite thickness and MS (see text).

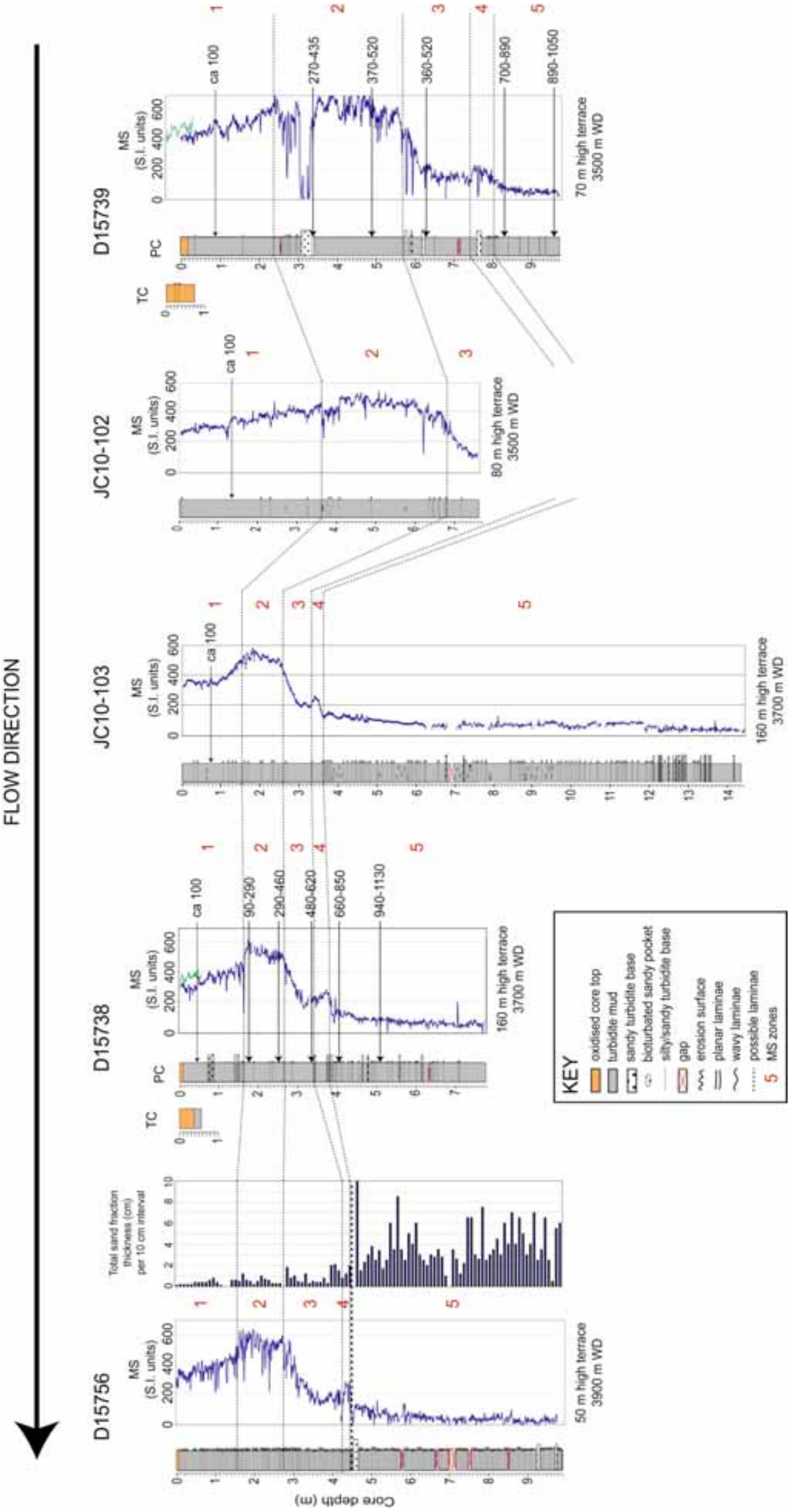
FLOW DIRECTION
D15739
TC
PC
MS (S.I. units)
0 200 400 600
ca 100
270-435
370-520
360-520
700-890
890-1050
1 2 3 4 5
70 m high terrace 3500 m WD
JC10-102
80 m high terrace 3500 m WD
JC10-103
160 m high terrace 3700 m WD
D15738
90-290
290-460
480-620
660-850
940-1130
160 m high terrace 3700 m WD
D15756
Total sand fraction thickness (cm) per 10 cm interval
0 2 4 6 8 10
50 m high terrace 3900 m WD
Core depth (m)
KEY
oxidised core top
turbidite mud
sandy turbidite base
bioturbated sandy pocket
silty/sandy turbidite base
gap
erosion surface
planar laminae
wavy laminae
possible laminae
5 MS zones

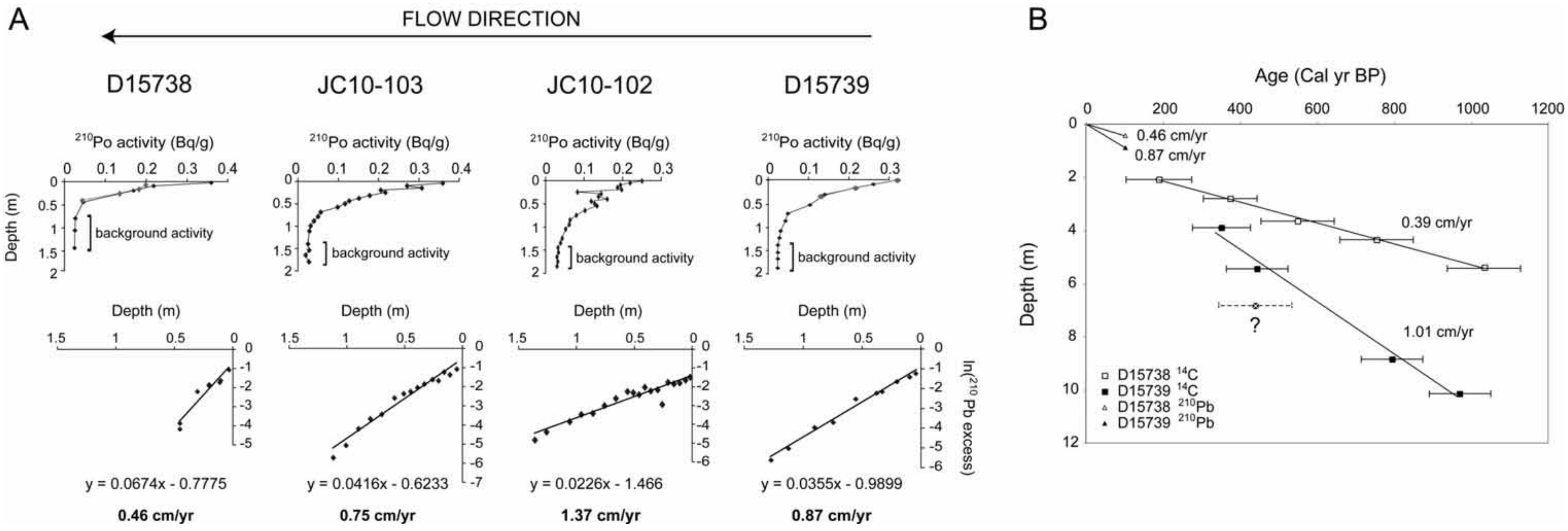

Fig. 5.4. (**A**) Top row: ^{210}Po decay profiles for the uppermost 2 m of cores D15738, JC10-103, JC10-102 and D15739. The background ^{210}Po activity (labelled on the figure) was subtracted from the measured activity when calculating the sediment accumulation rates (Table 5.2). Where trigger cores are available (cores D15738 and D15739), relevant data points are plotted in green. Bottom row: natural logarithm of excess ^{210}Pb plotted against depth for each core, with log-linear best-fit lines and their equations. The gradient of the line is proportional to the sediment accumulation rate, as indicated in bold text. (**B**) Sedimentation rates calculated from AMS radiocarbon data for cores D15738 and D15739. Apart from one spurious date in core D15739, the remaining dates indicate constant sedimentation rates. Error bars refer to minimum and maximum ages (see Table 5.3). ^{210}Pb sediment accumulation rates for these cores are also shown for comparison.

5.4.3 Age model

^{210}Pb data for the upper part of cores D15738, D15739, JC10-102 and JC10-103 give sediment accumulation rates of 0.46, 0.87, 1.37 and 0.75 cm yr^{-1}, respectively (Table 5.2, Fig. 5.4A). These rates are valid for the last ~100 years. Cores D15739 and JC10-103, both of which are on the outside terraces of a large bend in the canyon floor (Fig. 5.2), have the most similar rates. The much higher rate for core JC10-102 may be explained by its location on the inside terrace of the bend, where flow deceleration and centrifugal forces combine to cause superelevation of the upper part of the flow that leads to enhanced deposition on the terrace (Piper and Normark, 1983; Keevil et al., 2006). This higher sediment accumulation rate in core JC10-102 is also indicated by its expanded MS profile (Fig. 5.3). Calibrated (Cal) AMS radiocarbon (^{14}C) ages extend the sedimentation rates beyond ~100 years, giving constant down-core sediment accumulation rates of 0.39 and 1.01 cm yr^{-1} respectively for cores D15738 and D15739 (Table 5.3, Fig. 5.4B). These rates correlate well with those determined using ^{210}Pb dating for these cores. The MS zones have the same ages in both of these cores, therefore the MS variations can be used to correlate the entire suite of cores. These ages indicate that the top and base of zone 2, which has the highest MS values, have ages of ca 200 and 400 yr BP, respectively. The top and base of zone 4, which has the small peak in MS values, have ages of ca 600 and 700 yr BP, respectively (Fig. 5.3).

5.4.4 Mineralogy and chemical composition

XRF data show no systematic changes in elemental concentrations throughout the high-MS section of core D15738 (0.35-4.79 m; Fig. 5.5), and there is no correlation between the XRF data and any part of the MS signal. A slight increase in calcium content down-core between depths of ~2.7 and 4.8 m is the only significant change observed, and this correlates well with the inorganic carbon (IC) profile. Deposition of inorganic calcium carbonate in hemipelagic sediments generally opposes that of iron- and silica-rich detrital sediment due to competition between marine and terrigenous sources. This suggests that the relatively lower concentration of calcium and inorganic carbon in zones 1 and 2 compared to zones 3 and 4 may indicate a more dominant terrigenous sediment source down to ~2.7 m than below this depth. The total carbon (TC) and organic carbon (OC) contents do not clearly correlate with MS.

Mineralogical profiles were obtained by XRD analysis for the uppermost 6.2 m of core JC10-103. The non-carbonate sediment fraction is composed mainly of 49-82 % quartz, 1-39 % phyllosilicate, 1-24 % plagioclase and 1-34 % K-feldspar (Fig. 5.6). There are small down-core changes in these abundances, with quartz decreasing by 5-10 % between zones 1 and 2, being replaced by the combined increase in feldspars and mica over this zone. Pyrite, a common indicator of reducing diagenetic processes, is present mainly in abundances below 1 % and therefore no variations can be accurately identified using XRD analysis, apart from a sharp peak to 1.2-1.6 % at a depth of 4 m in the upper part of zone 5.

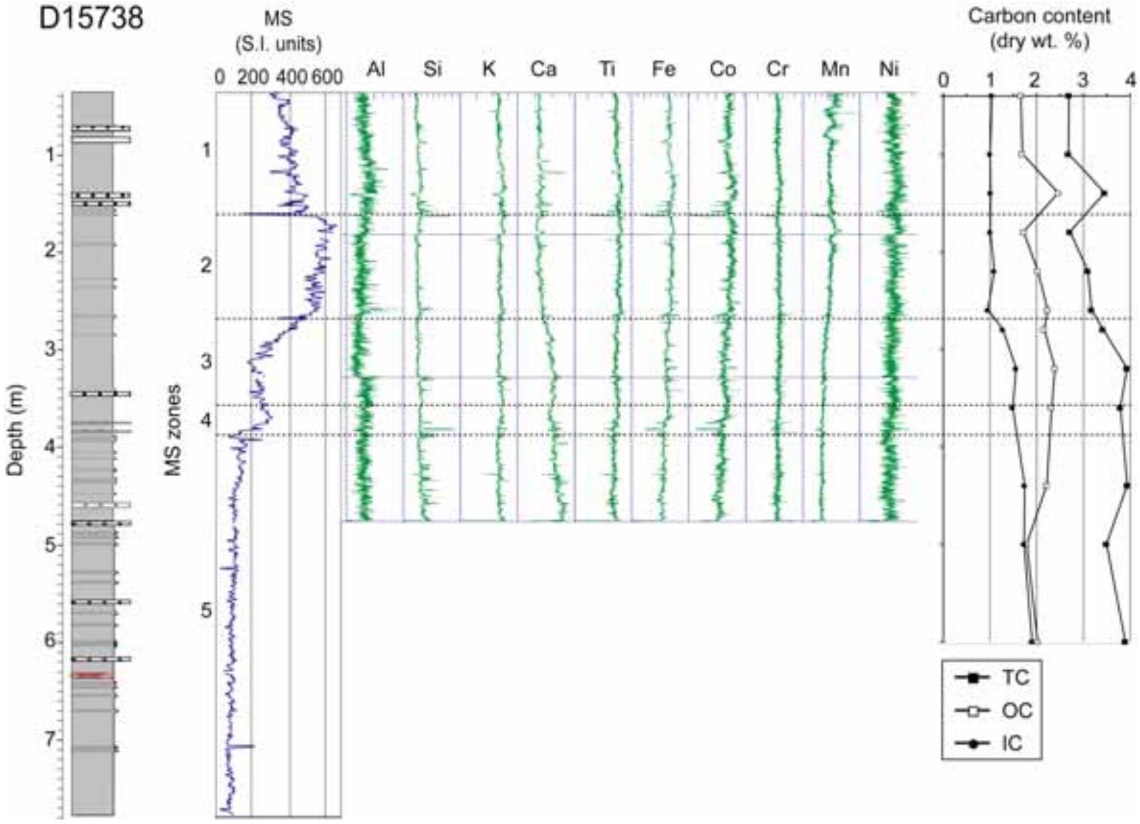

Fig. 5.5. X-ray fluorescence (XRF) elemental concentration profiles (measured using an ITRAX system) and total carbon (TC), inorganic carbon (IC) and organic carbon (OC) profiles for the high-MS section of core D15738.

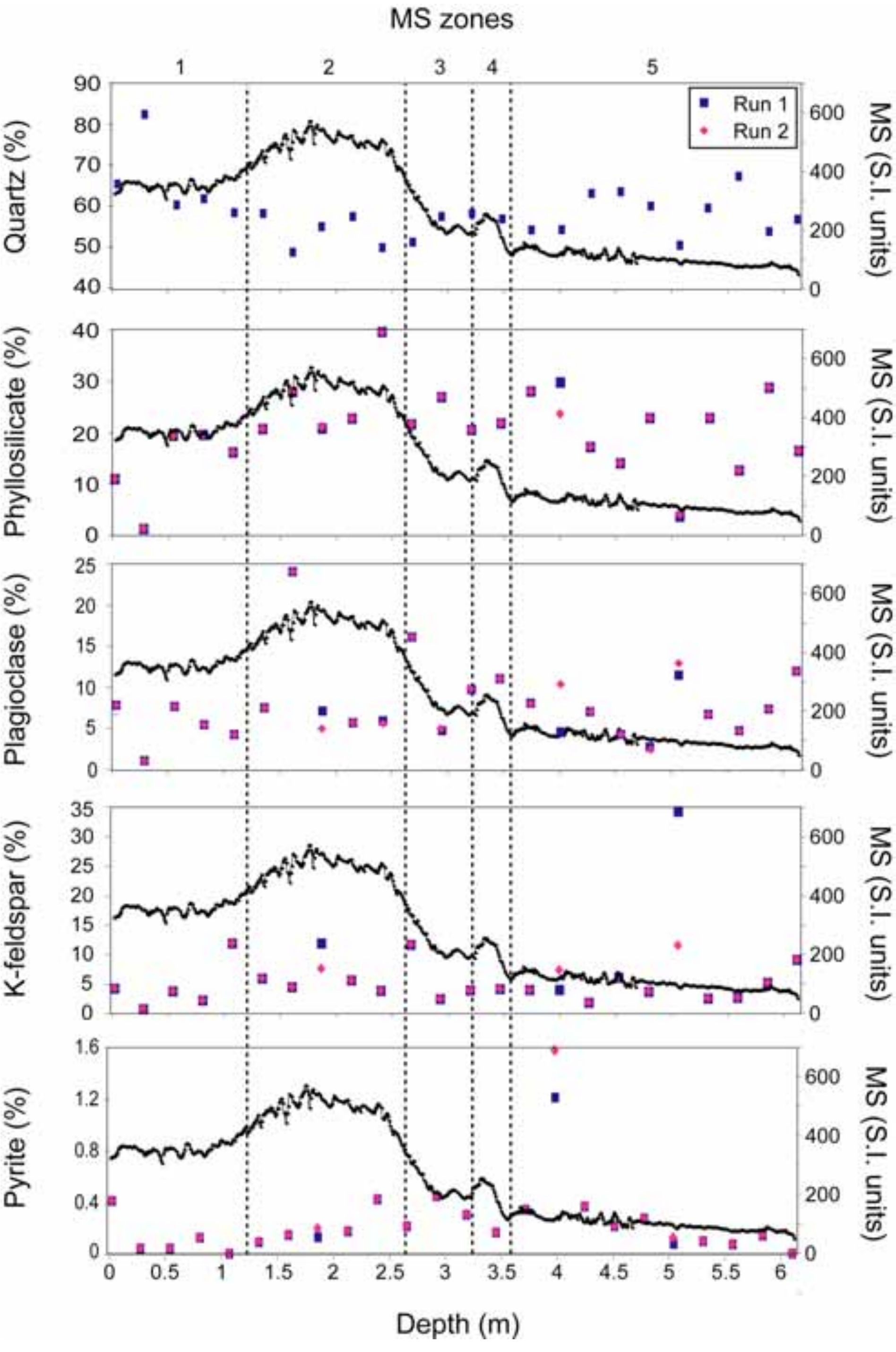

Fig. 5.6. Mineralogy profiles obtained by X-ray diffraction (XRD) plotted onto the MS profile for the uppermost 6.2 m of core JC10-103. Two XRD runs were carried out to obtain an accurate spread of data (represented with blue and pink symbols, respectively).

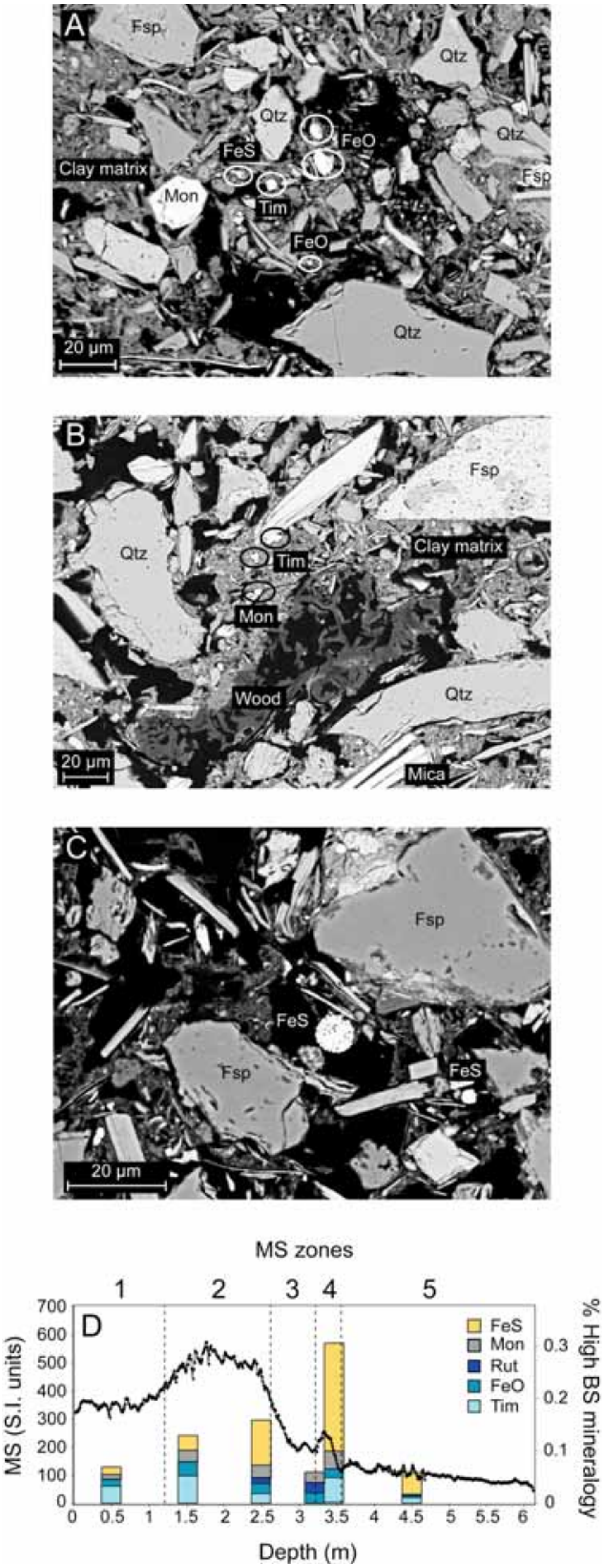
A
Fsp
Qtz
Qtz
FeO
Qtz
FeS
Clay matrix
Fsp
Mon
Tim
FeO
Qtz
20 µm
B
Fsp
Qtz
Tim
Clay matrix
Mon
Wood
Qtz
20 µm
Mica
C
Fsp
FeS
Fsp
FeS
20 µm
MS zones
1
2
3
4
5
D
MS (S.I. units)
700
600
500
400
300
200
100
0
FeS
Mon
Rut
FeO
Tim
% High BS mineralogy
0.3
0.2
0.1
0
0
0.5
1
1.5
2
2.5
3
3.5
4
4.5
5
5.5
6
Depth (m)

Fig. 5.7. (*previous page*) Scanning electron microscope (SEM) backscatter (BS) images at depths of (**A**) 1.5 m and (**B, C**) 2.5 m in core JC10-103. The estimated percentage of high-BS grains at six depths in core JC10-103, and their chemical composition, is indicated in bar charts (**D**). FeS = iron sulphides (framboidal pyrite and greigite), Mon = monazite (an alluvial phosphate mineral), Rut = rutile (titanium oxide), FeO = iron oxides (possibly magnetite, haematite or maghemite), Tim = titanomagnetite (titanium-iron oxide).

SEM analysis was carried out on samples from six depths in core JC10-103 in order to identify specific mineral grains within their microtextural context (Fig. 5.7A-C). There is a greater abundance of high-backscatter minerals (iron oxides and sulphides) coinciding with the higher MS values in zones 1-4 (Fig. 5.7D), especially in zones 2 (~1.25-2.6 m) and 4 (~3.3-3.6 m). EDS analysis indicates that between a third and half of high-backscatter grains (and thus 0.05-0.1 % of the total sediment content) in the upper 3.25 m of the core are composed of iron oxide, titanium oxide and titanium-iron oxide. The iron oxides have Fe concentrations between 70 and 72 %, which indicate that they could either be magnetite (~72 % Fe), haematite (~70 % Fe) or maghemite (~70 % Fe). The titanium oxide grains are likely to be rutile, while the titanium-iron oxides have approximate proportions of 50 % Ti, 40 % Fe and 5 % Mn, which suggest that these grains are either ilmenite or titanomagnetite grains. Examples of iron oxides and titanium-iron oxides (labelled FeO and Tim, respectively) are indicated in Fig. 5.7A-B. The rest of the high-backscatter grains in the upper 3.25 m of the core consist of framboidal iron sulphide (indicated as FeS in Fig. 5.7C) and a rare earth metal phosphate that is identified as monazite (labelled Mon). Pyrite abundances increase down-core between zones 1 and 3, but decrease again from zone 4 to zone 5 (Fig. 5.7D).

Vitrinite reflectance analysis of core JC10-103 indicates that vitrinite (which typically has reflectance values of 2-4 %, Stach et al., 1975) is most abundant at depths of 1.8 and 2.6 m (high-MS zone 2) and at 3.6 m (the MS peak in zone 4, Fig. 5.8). This indicates that vitrinite (and therefore charcoal) is present, as was previously observed by Arzola et al. (2008), and that its abundance correlates positively with the MS signal. Grains with reflectance values below 2 % correspond to other type of organic matter, such as non-burnt wood, humic soils such as peat, foraminifera, plant spores and seeds.

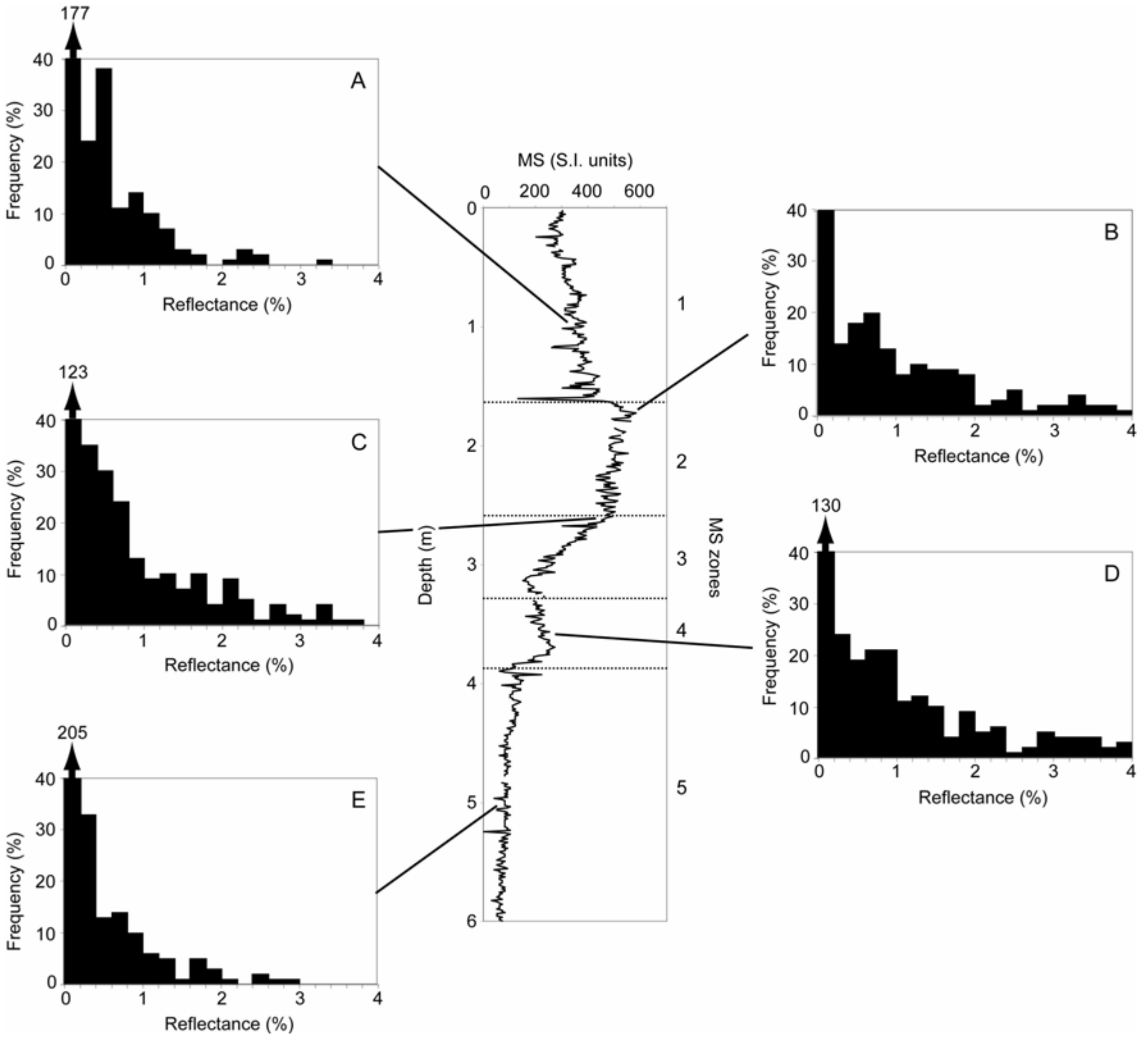

Fig. 5.8. Histograms of the frequency of organic matter reflectance values measured in core D15738 at depths of (**A**) 1 m, (**B**) 1.8 m, (**C**) 2.6 m, (**D**) 3.6 m and (**E**) 5 m. Vitrinite (a component of charcoal) gives reflectance values of 2-4 % (Stach et al., 1975), which are most frequent at depths of 1.8, 2.6 and 3.6 m, corresponding to MS zones 2 and 4.

Fig. 5.9. (*following page*) Magnetic parameter profiles for the uppermost 6.2 m of core JC10-103. SIRM = saturation isothermal remanent magnetisation; HIRM = ‘hard’ isothermal remanent magnetisation; S-ratio = $-\mathrm{IRM}_{-300\mathrm{mT}}$/SIRM; ARM = anhysteretic remanent magnetisation. These parameters are indicators of the concentration, coercivity and relative grain size of the magnetic fraction (e.g. King and Channell, 1991). The down-core trend in bulk sediment grain size for the uppermost 5.5 m of core JC10-103 shows a broadly inverse correlation with MS.

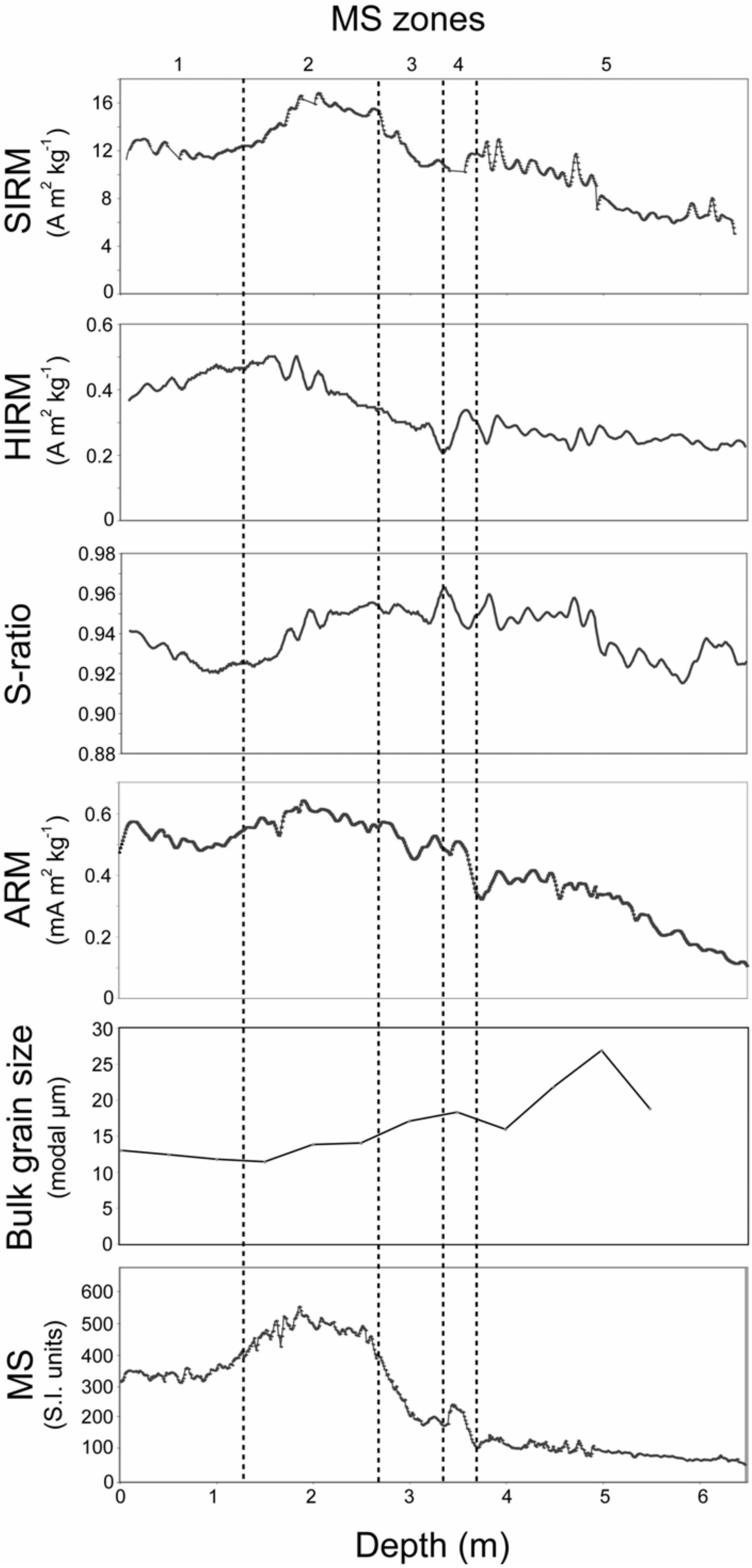
MS zones
1
2
3
4
5
SIRM (A m^2 kg^{-1})
0
4
8
12
16
HIRM (A m^2 kg^{-1})
0
0.2
0.4
0.6
S-ratio
0.88
0.90
0.92
0.94
0.96
0.98
ARM (mA m^2 kg^{-1})
0
0.2
0.4
0.6
Bulk grain size (modal µm)
0
5
10
15
20
25
30
MS (S.I. units)
0
100
200
300
400
500
600
0
1
2
3
4
5
6
Depth (m)

5.4.5 Environmental magnetism and grain size data

The SIRM profile for the uppermost 6.2 m of core JC10-103 correlates well with MS variations (Fig. 5.9). This indicates that the high-MS zones 1-4, and especially zone 2, have a higher total concentration of magnetic minerals than the low-MS zone 5. Additionally, zones 1 and 2 have higher HIRM values, which suggest the presence of higher concentrations of high-coercivity magnetic minerals such as haematite (e.g. King and Channell, 1991). The S-ratio profile is variable and does not correlate well with MS (Fig. 5.9). The variable S-ratios indicate that zones 1 and 2 contain variable concentrations of both high- and low-coercivity minerals. As indicated by SEM observations, detrital ferrimagnetic minerals that can retain a remanent magnetisation, such as titanomagnetite, are present along with haematite.

The ARM profile also broadly correlates well with MS (Fig. 5.9). A change in gradient of ARM/MS (Fig. 5.10A) between high and low MS values occurs at MS values of 75-85 S.I. units, which implies that sediment with MS values above ~80 in core JC10-103, i.e. in MS zones 1-4, have a much coarser magnetic grain size (see King et al., 1982; Sagnotti et al., 2003) than sediment with lower MS values in zone 5 (Fig. 5.10B). This positive correlation between MS and magnetic grain size is the opposite, however, to that of the bulk grain size data (Fig. 5.9). The modal grain size decreases down-core from 13 to 11 μm between depths of 0 and 1.5 m, before increasing gradually at first and then more abruptly until reaching a maximum of 27 μm at a depth of 5 m. Thus, the smallest bulk grain size occurs in zone 2 and the highest occurs in zone 5. This inverse relationship between MS and bulk sediment grain size is also indicated by the detailed turbidite thickness analysis in core D15756 (Fig. 5.3).

The coercivity (relative to field strength) of the magnetic fraction in core JC10-103 is indicated in FORC diagrams (Fig. 5.11). These diagrams, in turn, indicate the type and activity of magnetic grains present. The FORC diagrams for samples from depths of 1 cm to 2.5 m are almost identical, with low coercivity (B_c) peaks at ~10 mT that diverge along the vertical field strength (B_b) axis, and maximum coercivity values of ~80 mT. This pattern is typical of multi-domain magnetic grains (Roberts et al., 2000), which appear to dominate zones 1 and 2. Below depths of 3 m in zone 3, this pattern changes gradually as the peak of the FORC distributions become even more divergent along the

B_b axis, and a secondary peak starts to develop with a higher average coercivity (~30-50 mT). This composite pattern is typical of mixed multi-domain and single domain magnetic mineral assemblages (Roberts et al., 2000). Therefore, as indicated by the ARM/MS data (Fig. 5.10), the down-core trend for the magnetic fraction is from coarse grains at depths of 1 cm to 2.5 m depth (zones 1 to 2), to a combination of coarse and fine grains below depths of 3 m (zones 3 to 5). Regardless, the coarse-grained magnetic fraction that dominates in zones 1 and 2 is still present in zones 3 to 5. The development of a higher coercivity FORC distribution in zones 3 to 5 probably reflects authigenic growth of greigite (Fe_3S_4) grains, as is suggested by the peak in concentration of pyrite (Fig. 5.6) and iron sulphides (Fig. 5.7D), and by relatively high SIRM values (Fig. 5.9) at depths of 3.7 - 5 m, as a result of diagenetic processes at depth (Rowan et al., in press).

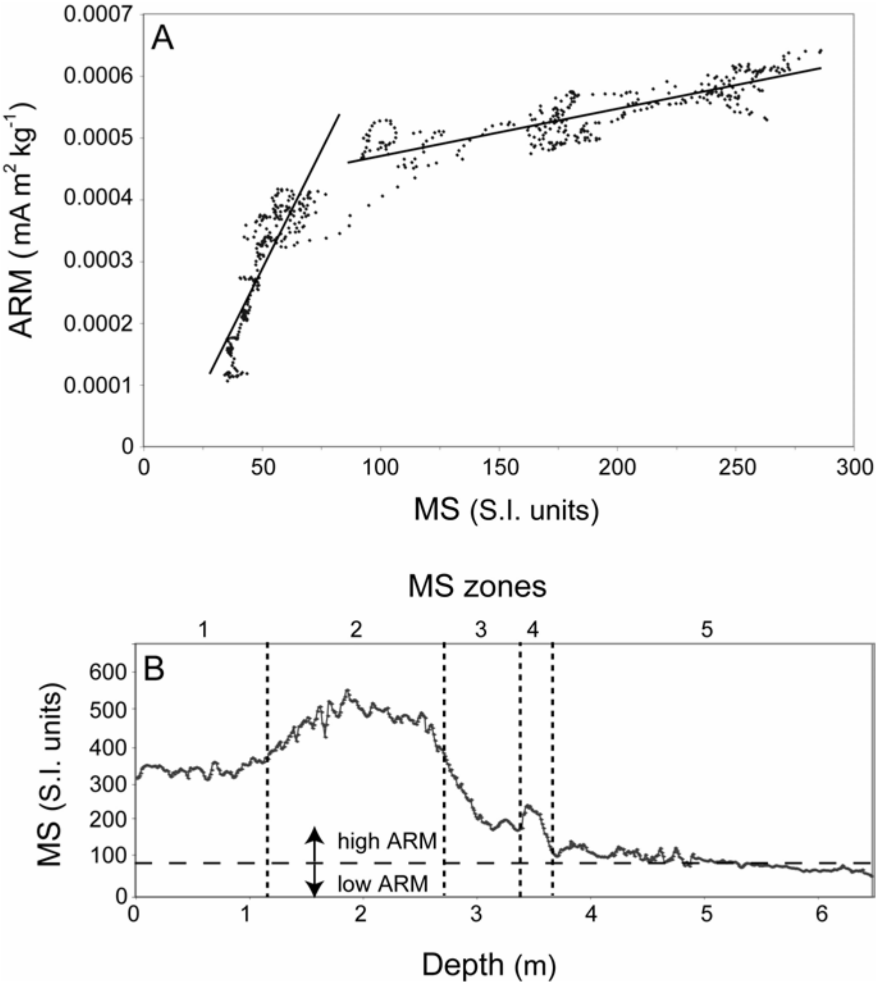

Fig. 5.10. (**A**) Anhysteretic remanent magnetisation (ARM) plotted against MS for core JC10-103. The change in gradient indicates an abrupt decrease in the grain size of the magnetic fraction (corresponding to MS values above ~80 S.I. units) below a depth of ~3 m in core JC10-103 (**B**).

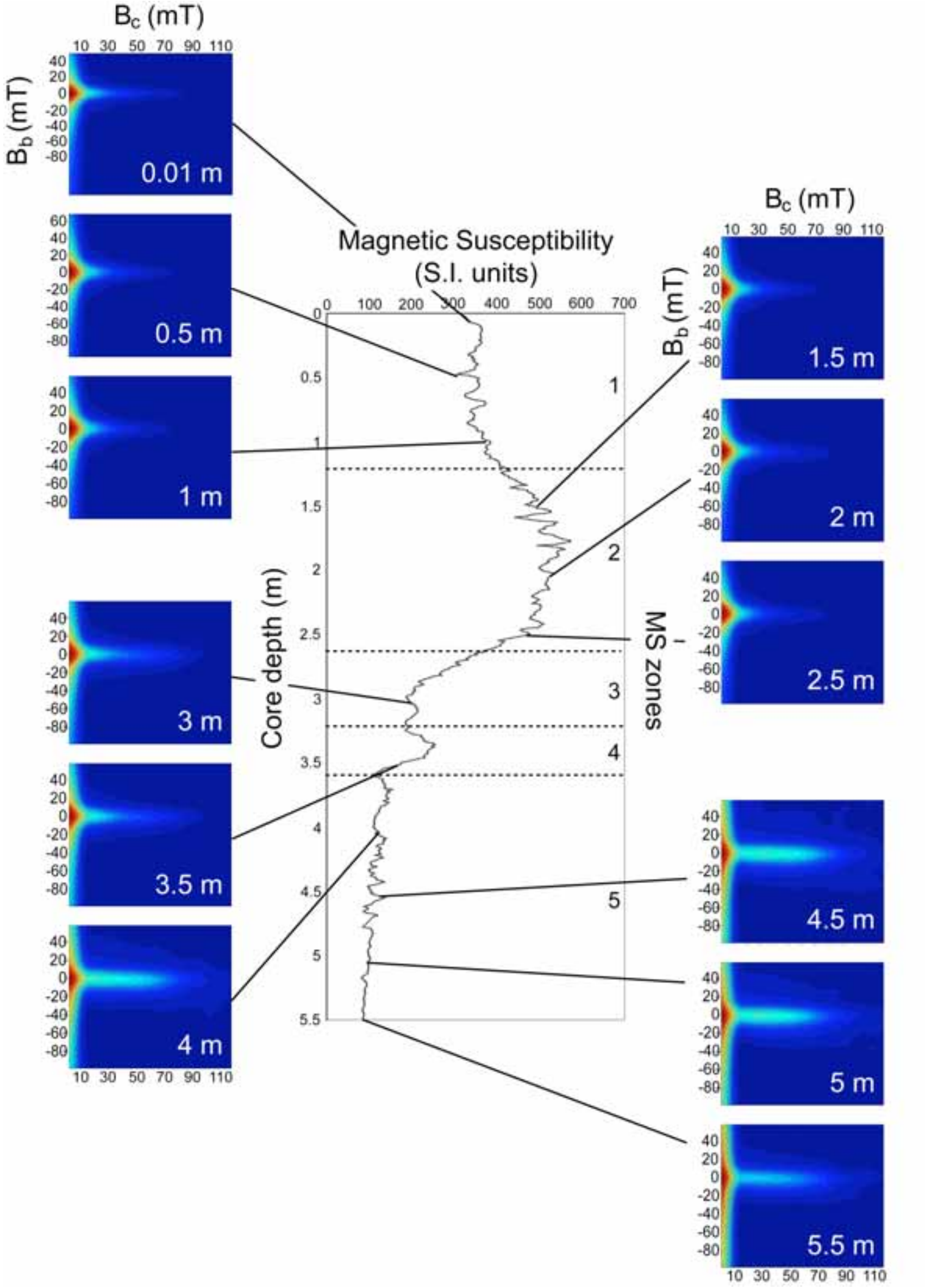

Fig. 5.11. FORC diagrams (plots of coercivity (B_c) against interaction field strength (B_b); Roberts et al., 2000) indicate a transition in the dominant grain size from detrital multi-domain grains down to depths of 2.5 m, followed by a mixed multi-domain and single domain magnetic mineral assemblage below 4 m in core JC10-103.

5.4.6 Summary of results

Despite relatively constant sedimentological and geochemical properties throughout zones 1-5, there are significant variations in MS, which are evidently due to variations in the concentrations and grain size of the magnetic mineral assemblages within the sediment. The greater abundance and grain size of ferrimagnetic minerals, mainly magnetite, haematite, maghemite and titanomagnetite in zones 1 and 2 (Figs. 5.7, 5.9, 5.10, 5.11), coincides with a greater abundance of charcoal fragments in this part of the record (Fig. 5.8).

5.5 Discussion

5.5.1 Detrital vs. diagenetic source of high-MS sediment

The presence of primary ferrimagnetic minerals (i.e. titanomagnetite and magnetite), terrestrial plant material (i.e. charcoal fragments, spores and seeds) and sustained high sediment accumulation rates (0.4-1.4 cm yr^{-1}) all point to a significant terrigenous input in the sediments with high MS values.

Anaerobic decomposition of organic matter in organic-rich marginal environments commonly results in diagenetic dissolution of detrital iron-bearing minerals, such as titanomagnetite, and formation of pyrite (Karlin and Levi, 1983; Karlin, 1990a, b). It is therefore possible that the precipitous down-core decline in MS in zone 3 represents the onset of diagenetic sulphate reduction. This possibility is supported by the measured abundance of pyrite in zone 4 and the upper part of 5 (Fig. 5.7D). However, other characteristic diagenetic features such as pitted surfaces of detrital ferrimagnetic grains (Snowball and Thompson, 1990) are absent from the sediments in zone 5. Overall, however, the probable growth of greigite in zone 5 (Fig. 5.11; Rowan et al., in press) indicates that reductive diagenesis is a major contributor to the magnetic properties of this zone. Thus, the magnetic signature of the high-MS sediment is dominated by detrital particles, while a secondary post-depositional diagenetic imprint becomes increasingly important in and below zone 3.

5.5.2 Natural sources of detrital mineral influx

All sources of anthropogenic influence on the observed MS signal are precluded by the simple fact that the chronology of evolution of mining and polluting activities in the area is not easily reconciled with the observed MS signal (mining took place mainly between ca 900 BC and 400 AD and from 1836 until the present, and pollution has only been significant since the late 1800s, e.g. Mil-Homens et al., 2006). Thus, natural processes must be the primary cause of the MS signal in sediments of the Nazaré Canyon.

The Holocene has had a number of short-lived climatic events, the most recent being the Little Ice Age of ~1300-1850 AD (Jones et al., 2001). This event is believed to have occurred during a negative North Atlantic Oscillation (NAO) index (Hurrell, 1995; Grudd et al., 2002), which induced downwelling offshore of west Iberia (Fiúza, 1983) and increased precipitation and flooding frequency across Europe (Grove, 2001). The combination of these processes resulted in a marked increase in fluvial sedimentation onto the west Iberian continental margin (Dias et al., 2000; Trigo et al., 2002). This period of increased erosion and transport of sediment has been interpreted as the cause of a MS peak in shelf sediments near the Tagus Estuary (Abrantes et al., 2005; Bartels-Jónsdóttir et al., 2006), which is contemporaneous with the Little Ice Age. Negative NAO conditions during cold periods cause surface currents to flow north along the west Iberian shelf (e.g. Fiúza, 1983; Lebreiro et al., 2006). These currents may have transported sediment from the Tagus Estuary towards the head of the Nazaré Canyon during the Little Ice Age, thereby accounting for the observed high-MS values in the canyon sediments. Enhanced sediment transport rates onto the shelf would account for the greater abundance of charcoal fragments and immature (phyllosilicates and feldspar) relative to mature (quartz) detrital minerals in the sediment. This is due to their reduced residence time on the shelf. However, increased sediment transport would also result in increased sedimentation rates, which are neither observed here nor in Tagus estuary cores that go back 1500 years (Abrantes et al., 2005, 2008), although the lack of earlier sedimentation rate data in the studied cores makes it impossible to know whether these rates have changed over time.

Changes in soil mineralogy related to forest fires can also affect MS. Heating of soils to high temperatures transforms weakly magnetic forms of iron into strongly ferrimagnetic minerals with MS values that are 2-3 orders of magnitude higher (Le Borgne, 1955; Rummery et al., 1979). For example, heating goethite to >300º C produces maghemite, which is an iron oxide similar in structure and composition to magnetite, with much higher MS than goethite (Ketterings et al., 2000). Heating maghemite or magnetite to higher temperatures of >600-900º C reduces its grain size and produces haematite (Oldfield et al., 1981; Ketterings et al., 2000). Heating sediments that contain low coercivity iron oxides can thus result in a mixed high and low coercivity iron oxide content with overall higher MS values, as found in Nazaré Canyon. The optimum conditions for maghemite production are rapid heating to >400º C followed by cooling, a reducing soil atmosphere and the presence of organic matter (Rummery, 1983), all of which occur during a typical ground forest fire. Analysis of charcoal from lacustrine sediments indicates that the highest incidence of Holocene forest fires in Iberia occurred during the last 1000 Cal yr (Carrión García, 2002). Charcoal fragments dated <650 Cal yr BP have also been found in fluvial Tagus Valley sediments (Vis et al., 2008). These observations are consistent with the age of the MS peak in sediments from the Nazaré Canyon, which also correlates with higher charcoal concentrations (Fig. 5.8).

The most common natural causes of forest fires are lightning (Batchelder, 1967) and spontaneous combustion by the generation of heat in accumulated plant litter (Scott, 2000) aided by the emission of flammable ethylene from plants under stress, e.g. during a drought (Kurchii, 1992). These processes are most likely to operate when the climate is hot and dry. However, some authors infer a relationship between forest fires and biomass (Black et al., 2006; Daniau et al., 2007), which in turn is indirectly linked to climate (Verardo and Ruddiman, 1996). Thus, dry conditions during glacial stages lead to semi-desert vegetation in Iberia and low fire activity, while wet interglacial conditions allow growth of open Mediterranean forests and high fire activity (Daniau et al., 2007). This conclusion opposes that of Carcaillet et al. (2002), who concluded that forest fires in Europe were much more abundant during the drier Last Glacial than during the Holocene, and that a relative increase after 6000 yr BP was due to a regional aridification event across the Mediterranean region (Carcaillet et al., 2002). However, higher fire activity during wet conditions is consistent with the inferred climate of west Iberia during the Little Ice Age (~700-150 Cal yr BP; Hurrell, 1995; Grove, 2001; Trigo et al., 2002). Increased vegetation cover, production of charcoal and strongly magnetic minerals through heating of soils, and increased soil erosion and transport of terrigenous sediment to the shelf are all consistent with inferred forest fire activity during this period.

It is possible that anthropogenic activity, contemporaneous with a change in climate, could also be related to the inferred forest fire activity. Rapidly rising populations during the Roman Era in Iberia (ca 200 BC – 400 AD) have been linked to changes in land use and clearing of forests to make way for agriculture (e.g. Carrión García, 2002; Ruddiman, 2007). These activities may have continued as populations rose over the last 700 years, possibly augmented by the growth of open forests during wet Little Ice Age conditions.

We recommend that further work is carried out to determine the total spatial extent of the high concentration of charcoal along the west Iberian margin over the ~750-100 Cal yr BP time interval, including onshore.

5.6 Conclusions

Combined environmental magnetic, chemical and mineralogical analyses were used to determine the cause of a distinctive magnetic susceptibility signal in deep-sea cores from Nazaré Canyon, west Iberian margin. The high-MS signal, dated between ~700 and 100 years BP, is directly caused by an increased concentration of ferrimagnetic minerals, mainly titanomagnetite and magnetite/maghemite. The sediment also has a high abundance of immature detrital minerals and a low concentration of marine $CaCO_3$, thus suggesting a dominantly terrestrial origin. The high abundance of charcoal fragments associated with the high-MS signal suggests a relationship between it and forest fires, whereby heating of iron-bearing minerals within soils leads to production of maghemite, oxidation of magnetite to haematite and an enhanced MS signal. Below the MS peak in the studied cores, charcoal concentrations are diminished and the detrital magnetic concentration also decreases. An increasingly important diagenetic influence becomes apparent in the lower part of the sequence with replacement of detrital magnetic minerals by authigenic pyrite and greigite.

We conclude that the Little Ice Age in Iberia (~700-150 yr BP), and associated wet conditions, led to increased growth of open forests. This resulted in a greater availability of biomass for forest fire activity, the debris of which included magnetically enhanced ferrimagnetic minerals and charcoal fragments, which were exported to the continental shelf and slope. Existence of a sediment depocentre with high resuspension rates in the mid Nazaré Canyon has therefore resulted in a unique high-resolution record of Little Ice Age-controlled forest fire activity in a deep-sea setting. The results also prove that Nazaré Canyon currently receives sediment from the Tagus Estuary, which has implications for current models of sediment transport along the west Iberian margin.

CHAPTER 6

Regional and eustatic climate control on turbidite sedimentation on the west Iberian margin[4]

---

[4] Arzola, R.G., Weaver, P.P.E., Masson, D.G., Wynn, R.B. (submitted). Regional and eustatic climate control on turbidite sedimentation on the west Iberian margin. *Journal of Sedimentary Research*.

6.1 Abstract

This work is the first attempt at a detailed, large-scale correlation of sedimentary events throughout the Setúbal and Cascais submarine canyons and Tagus Abyssal Plain located west of Iberia. A combination of multi-sensor core logging, lithological and radiocarbon data has been used to identify the main controls on sedimentation across the margin. In addition to changes in global sea level and seismicity along the Azores-Gibraltar fracture zone, regional climatic events have also been identified as being a significant control on sedimentary activity in this area. These include the African Humid Period of 9-7 ka, which led to a short period of enhanced turbidite deposition, especially in the Tagus Abyssal Plain, and the 6.4 ka Mediterranean aridification event, which resulted in the complete cessation of turbidite deposition throughout the canyons and abyssal plain. This work has important implications for our understanding of the controls on sedimentation in continental margins, and of the sedimentary processes, including timing and frequency of turbidite emplacement, that link submarine canyons to abyssal plains.

6.2 Introduction

6.2.1 Submarine canyons as sediment pathways

Submarine canyons are incisions in the continental shelf and/or slope that act as fast-track pathways for the offshore transport of sediment, organic carbon and pollutants derived from land (e.g. Berner, 1982; van Weering et al., 2002; Alt-Epping et al., 2007). This funnelling of sediment can take various forms, from near-continuous deposition of hemipelagic material to episodic dense water cascading and turbidity current activity to catastrophic mass wasting events (e.g. Normark and Piper, 1991; Mullenbach et al., 2004; Puig et al., 2004a; Canals et al., 2006).

The factors that control turbidity current sedimentation in canyons are: 1) the sediment itself, including its composition, grain size, the rate at which it is supplied and whether it is transported through the canyon immediately or temporarily accumulates on the shelf/canyon head before being transported basinward (e.g. Mulder and Alexander, 2001; Mastbergen and van den Berg, 2003); 2) the oceanographic conditions of the area, e.g. canyons can funnel ocean currents, leading to enhanced stratification, upwelling/downwelling regimes and internal waves that transport suspended sediment down the canyon and resuspend pre-existing deposits (e.g. Vitorino et al., 2002a, b; Puig et al., 2004b; de Stigter et al., 2007); 3) earthquakes that cause cyclic loading and liquefaction of the ground, disturbing deposits on steep and unstable slopes and causing mass wasting (Normark and Piper, 1991; Jones and Omoto, 2000); and 4) large-scale external factors, such as eustatic sea level change or global climate variation, that are well known to exert a control on sedimentation in continental margin areas (Normark and Piper, 1991; Weltje and de Boer, 1993). What is less well understood is the relevant importance of global versus regional climatic events on the sedimentary activity (Weaver, 2003). Here, ‘regional changes’ refers to potentially oceanographic-induced climatic changes in Iberia that may lead to changes in surface runoff, as opposed to global eustatic changes.

6.2.2 Rationale and aims

The ability to characterise the timescales at which sediment is transported and deposited through submarine canyons has important implications for a number of applications. With a large part of today’s hydrocarbon reserves being found in deep water channel and fan depositional systems, understanding the processes of sediment deposition/erosion, including timing and frequency, will enable more accurate volume predictions of high net:gross deposits. It will also help to understand the risk of failure of marine infrastructures such as pipelines or telecommunication cables, which are routinely placed along continental slopes and shelves. Finally, submarine canyons are potentially a ‘hotspot’ of biodiversity since they contain numerous microenvironments each with its own unique ecosystem, but which at present remain poorly understood (Weaver et al., 2004). Establishing how sedimentary processes affect the biodiversity and recolonization of these ecosystems will help to better understand their functioning.

The study area is the central west Iberian margin, which provides two canyons of different sizes that feed into a large flat abyssal plain, thus potentially enabling correlation of events at different spatial scales spanning a very large area. Previous stratigraphic studies in this area focused only on the large flat abyssal plains (e.g.

Lebreiro, 1995; Lebreiro et al., 1997) and did not use absolute dating techniques. Recent improvements in our ability to map canyons in high resolution and accurately locate cores using GPS and/or ROVs means that we can now sample relatively small features within canyons such as terraces. The importance of correctly interpreting canyon geomorphology and ground-truthing sidescan data with accurately targeted piston cores has already been shown by two recent studies on the west Iberian margin (Arzola et al., 2008; Lastras et al., 2009). Here we present the first attempt at correlating events within a large-scale canyon and abyssal plain system using a combination of radiocarbon dating, multi-sensor core logging and lithological data.

The aims of this study are: 1) to document the sedimentary activity of the central west Iberian margin, from the canyons to the abyssal plain, and from the last glacial to the present day, and 2) to determine the factors that control sedimentary activity in this area, distinguishing between global and regional events, and between the major controlling factors, such as seismicity and climate change. These aims will be achieved by correlating sedimentary flow deposits and other events across cores from different settings. An ‘event’ is thus defined here as any sedimentary deposit (turbidite or debrite) or change in lithology, and is labelled ‘E’ in the correlation panels.

6.3 Study area

The study area comprises the central part of the west Iberian margin, also known as the Lisbon sub-margin, between 38 and 39º N (Fig. 6.1). It includes the Lisbon-Setúbal and Cascais canyons and extends from the inception of the canyons on the shelf to the Tagus Abyssal Plain. The shelf along this sub-margin is relatively narrow (30-50 km), composed of thick (>1000 m) Cenozoic sediments draping a Mesozoic substrate (Jouanneau et al., 1998; Alves et al., 2003), and leads to a steep (≤6º) continental slope (Weaver and Canals, 2003). The Tagus and Sado river estuaries lead almost directly into the heads of the Cascais and Lisbon-Setúbal canyons, although far higher annual discharge and turbidity rates in the Tagus estuary mean that this river is the more significant source of suspended particulate matter into the canyons (e.g. Jouanneau et al., 1998 and references therein). As no cores were collected from the Lisbon tributary of the Lisbon-Setúbal Canyon (see below), this canyon is hereafter referred to simply as Setúbal Canyon.

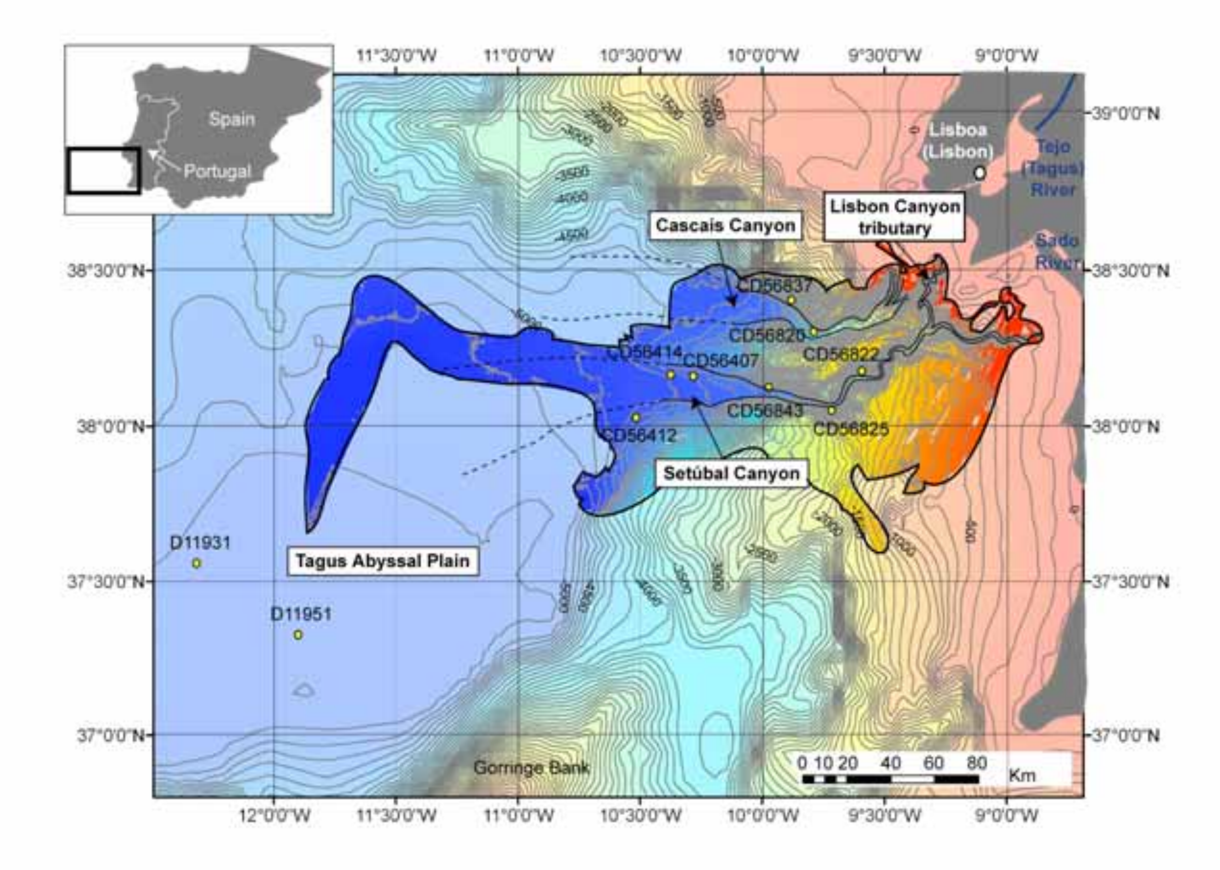

Fig. 6.1. Multibeam bathymetry map of the study area showing location of cores (labelled circles) in Cascais and Setúbal canyons and the Tagus Abyssal Plain. 100 m contours. More detailed GEBCO bathymetry data (courtesy of C. L. Jacobs) is outlined in black. Colours represent 0-500 m WD (red), 500-1000 m WD (orange), 1000-2500 m WD (yellow), 2500-4500 m WD (turquoise) and 4500-5000 m WD (blue).

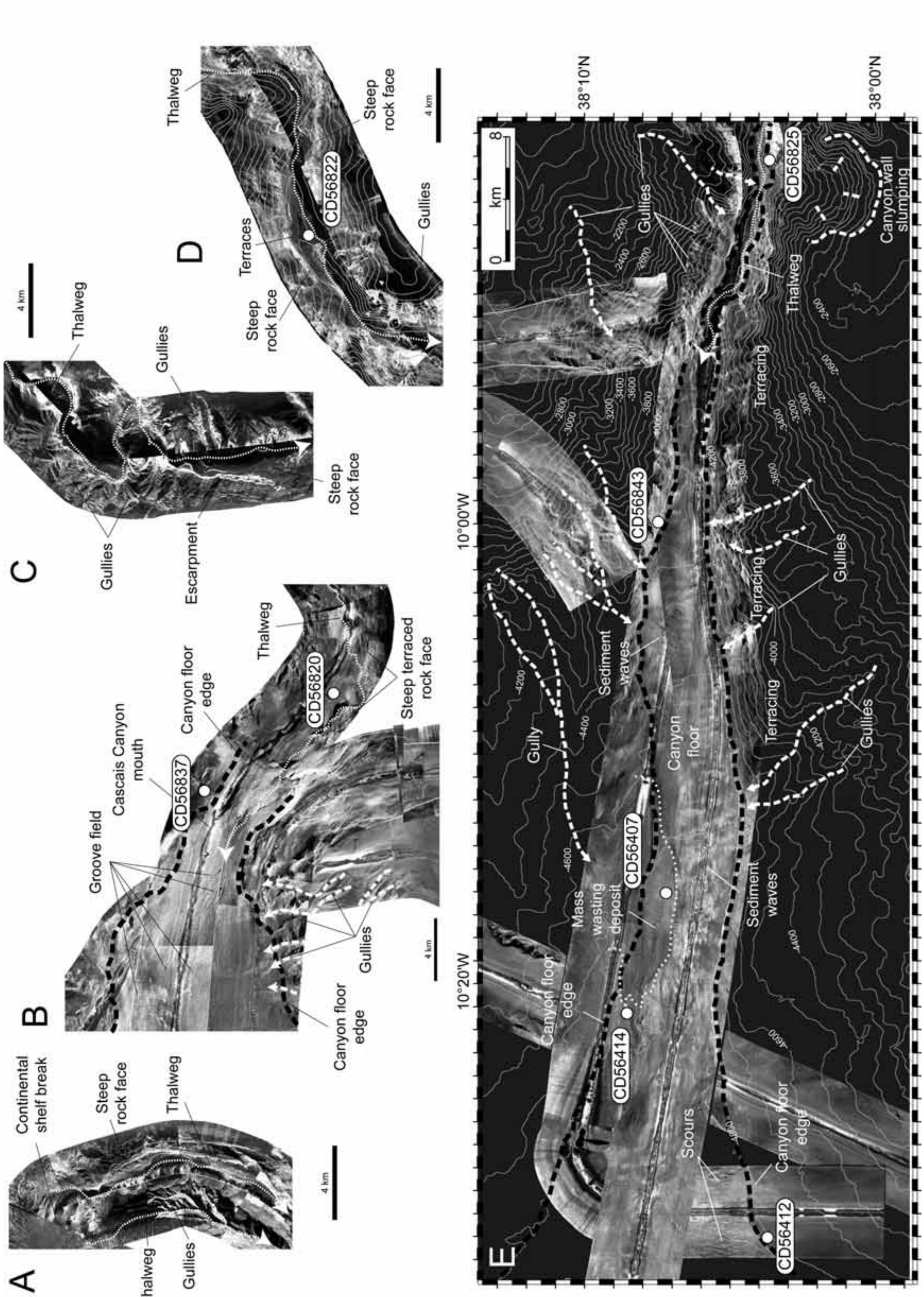

Fig. 6.2. Side-scan sonar images of the canyons. (**A**) Upper Cascais Canyon, (**B**) middle and lower Cascais Canyon, (**C**) Lisbon tributary of upper Setúbal Canyon, (**D**) Setúbal tributary of upper Setúbal Canyon, (**E**) middle and lower Setúbal Canyon. Thin dotted white lines are the thalweg (deepest incised part of the canyon floor), thick dashed black lines are the edges of the canyon floor, thick dashed white arrows are gullies pointing in the downslope direction, white circles show piston core locations, contours are 100 m (shown in D and E only).

6.3.1 Cascais Canyon

Cascais Canyon extends over 62 km from the shelf edge to the Tagus Abyssal Plain (Fig. 6.1). The canyon head is made up of three separate tributaries that begin at ~175 m water depth (WD). After the tributaries are combined, the canyon extends westward before taking a sharp turn to the northwest on the mid slope, giving the entire canyon a large average sinuosity index of 1.44 (Lastras et al., 2009). The sinuosity index is the sinuous distance divided by the straight distance. The upper and middle sections (above the break in slope at ~4000-4500 m WD, after de Stigter et al., 2007 and Lastras et al., 2009) are V-shaped with near-vertical rock walls up to 1800 m high and a narrow <100 m-wide thalweg (i.e the deepest part of the canyon floor; Fig. 6.2A). These sections have a high but widely ranging axial slope of 8-30º.

The lower section of Cascais Canyon starts at about 4500 m WD where the slope of the margin decreases abruptly. Here, the canyon widens considerably into a U-shaped, flat-bottomed and less incised canyon as it opens onto the Tagus Abyssal Plain (Fig. 6.2B). The canyon mouth is dominated by pervasive grooving and comet marks on the flat floor (Lastras et al., 2009), which are oriented parallel to the lower canyon axis and are thought to be caused by erosional flows exiting the canyon.

6.3.2 Setúbal Canyon

At 175 km long, Setúbal Canyon is much larger than Cascais Canyon (Fig. 6.1). Its upper section is composed of two tributaries that join at ~2000 m WD. The head of the Setúbal tributary is located at ~90 m WD after cutting 40 km into the shelf, and lies close to the Sado River mouth. The head of the Lisbon tributary extends northward toward the head of Cascais Canyon and the mouth of the Tagus River. This tributary cuts ~30 km into the shelf. The two tributaries give the upper section of Setúbal Canyon an average axial slope of 2º and a sinuosity index of 1.2-1.4 (Lastras et al., 2009), lower than that of Cascais Canyon. Both tributaries have a steep V-shaped profile with a maximum incision depth of 1.5-2 km and a <100 m-wide thalweg (Fig. 6.2C, D).

The middle section of the Setúbal Canyon extends from 2700 to 4000 m WD, in which the thalweg remains ~100 m wide and very sinuous (sinuosity index of 1.36). This middle canyon is also very strongly incised into the slope, and the steep walls are characterised by gullying and numerous small-scale failures (Arzola et al., 2008; Lastras et al., 2009; Fig. 6.2E). At approximately 4000 m WD, the V-shaped thalweg widens abruptly to >5 km as it enters the lower section of the canyon and approaches the Tagus Abyssal Plain. This lower section has a reduced axial slope of 0.6º and a smaller sinuosity index of ≤1.1 (Lastras et al., 2009). Its profile is U-shaped with a flat floor marked by scouring, sediment bedforms and large mass-wasting events, flanked by stepped terraces of over 200 m in width (Arzola et al., 2008; Fig. 6.2E). It shows no evidence for an incised thalweg.

6.3.3 Tagus Abyssal Plain

The Tagus Abyssal Plain is pentagonal in shape and covers 18,200 km^2 at the 5100 m isobath (Fig. 6.1). To the NE is a very gently sloping continental rise connecting it with the Cascais and Setúbal canyons. Lebreiro (1995) correlated turbidites throughout the Tagus Abyssal Plain based on carbonate content, foraminiferal species, sediment physical properties and grain size. She found that its sediment infill is composed of layered turbidites that reach a maximum combined thickness of 1.8 km, and that large flows arrive from the continental margin via the canyons, while small flows originate on the surrounding elevated areas. However, this correlation was based solely on cores from this and an adjacent abyssal plain and not from any of the canyons leading into them. Additionally, although some age control was provided by the identification of Heinrich layers in the cores, no radiocarbon dates were used and therefore no absolute dates were assigned to the interpreted sea level changes and seismic events.

6.4 Methods

6.4.1 Piston core collection

Piston cores were used for this stratigraphic study because they allow a good quality and long sedimentary record to be retrieved from a relatively precise location (Table 6.1). They have an estimated accuracy on the sea floor of between 50 and 200 m, based on the amount of drift experienced by the corer and vessel, and on the position of the side-scan sonar data relative to the bathymetry. Coring was guided by the deep-towed side-scan sonar records produced by TOBI (Towed Ocean Bottom Instrument), and the main coring targets were terraces adjacent to but elevated above the thalweg. Terraces in the canyons are relatively wide and flat, making it possible to target them with the corer. They occur at heights between ~10 and >200 m above the canyon floor, where they receive a sediment supply from all but the smallest turbidity currents that flow down the canyon. They should therefore preserve relatively complete depositional records, especially where they are composed of mud rather than sand, which indicates depositional rather than erosional events. Terraces with dark backscatter in the side-scan sonar images were targeted because this indicates low reflective sediments such as mud, and offer a higher coring success rate than the steep and narrow terraces of the upper section or the erosional sandy canyon floor.

No cores were recovered from the Lisbon tributary of Setúbal Canyon or the upper part of Setúbal Canyon itself because these areas are too steep and narrow, and no suitable coring sites were found. Only two cores were successfully recovered from a canyon floor setting (CD56407 and CD56414), due to the presence of a muddy debris flow deposit. Cores from the Tagus Abyssal Plain were recovered during cruise D187 in 1989.

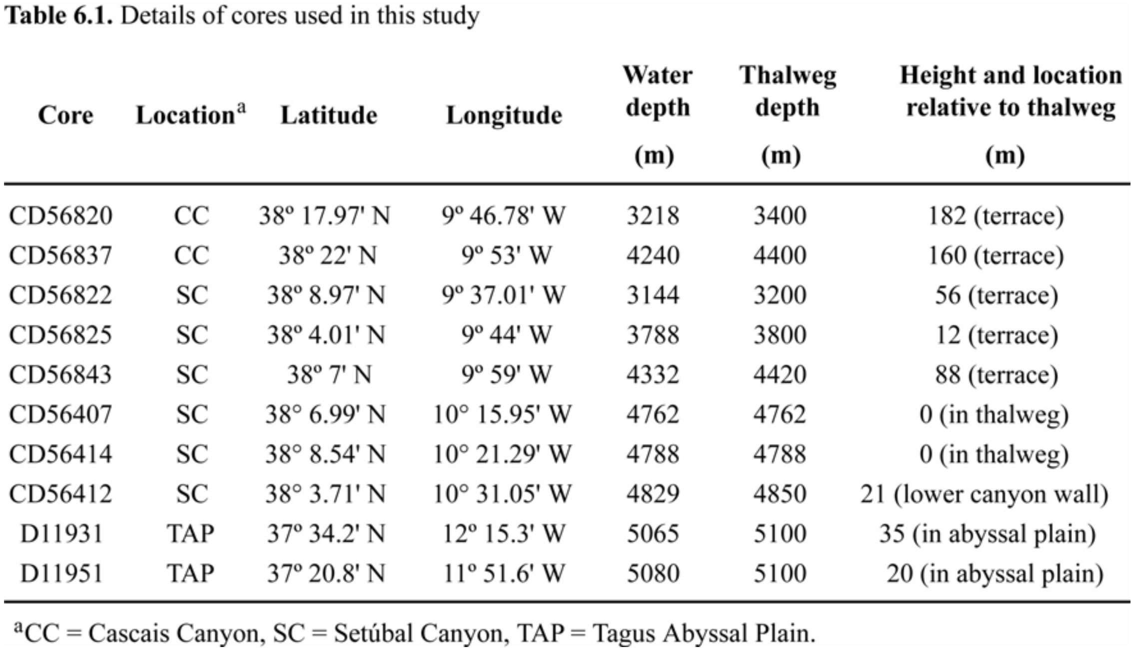

Table 6.1. Details of cores used in this study

Core	Location[a]	Latitude	Longitude	Water depth (m)	Thalweg depth (m)	Height and location relative to thalweg (m)
CD56820	CC	38º 17.97' N	9º 46.78' W	3218	3400	182 (terrace)
CD56837	CC	38º 22' N	9º 53' W	4240	4400	160 (terrace)
CD56822	SC	38º 8.97' N	9º 37.01' W	3144	3200	56 (terrace)
CD56825	SC	38º 4.01' N	9º 44' W	3788	3800	12 (terrace)
CD56843	SC	38º 7' N	9º 59' W	4332	4420	88 (terrace)
CD56407	SC	38° 6.99' N	10° 15.95' W	4762	4762	0 (in thalweg)
CD56414	SC	38° 8.54' N	10° 21.29' W	4788	4788	0 (in thalweg)
CD56412	SC	38° 3.71' N	10° 31.05' W	4829	4850	21 (lower canyon wall)
D11931	TAP	37º 34.2' N	12º 15.3' W	5065	5100	35 (in abyssal plain)
D11951	TAP	37º 20.8' N	11º 51.6' W	5080	5100	20 (in abyssal plain)

[a] CC = Cascais Canyon, SC = Setúbal Canyon, TAP = Tagus Abyssal Plain.

6.4.2 Multi-sensor core logging

Aside from visual identification of turbidites and hemipelagic intervals based on colour, sedimentary structures and grain size, the canyon cores were logged with the Geotek^{TM} Multi-sensor core logger (MSCL). This is an automated, non-destructive and high-resolution system that was used to measure bulk density (gamma ray attenuation) and magnetic susceptibility (using a MS2E point source sensor) at 1 cm intervals down split cores (after Gunn and Best, 1998). Changes in downcore lithology can thus be interpreted from changes in these profiles (e.g. Robinson, 1993). In broad terms, silt and mud turbidite units correspond with positive peaks in density and magnetic susceptibility because they contain clay minerals. Turbiditic sand units are typically composed of clean quartz and feldspar grains, which result in peaks in density but not in magnetic susceptibility. These properties therefore allow a rough estimation of sediment grain size in the cores. Hemipelagite does not produce any significant variation in the physical property profiles because it is mainly composed of foraminifera and other carbonate material.

P-wave velocity data have not been included because problems with calibrating the sensor gave inaccurate absolute values, although the profiles broadly mirror those of the bulk density data. Therefore, the P-wave velocity profiles for the Tagus Abyssal Plain cores (obtained from Lebreiro, 1995) can be confidently correlated with the density profiles of the canyon cores.

6.4.3 Radiocarbon dating

The strategy for radiocarbon dating was to target sedimentary deposits and sequences that could potentially be correlated across more than one core. Only hemipelagite with sufficient foraminifera was sampled, avoiding debrites and turbidite mud units, and collected, where possible, directly below any redeposited unit of interest, as this minimises the risk of sampling reworked sediment (Thomson and Weaver, 1994).

Approximately 1-4 cm^3 of sediment was sampled per horizon, washed through a 63 μm sieve and dried under a hot lamp. 10-20 mg of planktonic foraminifera (approx. 1000 individuals) were picked under a binocular microscope in order to yield the minimum

1-2 mg of carbon required. Main planktonic species found were *Globigerina bulloides, Globorotalia scitula, Neo-globoquadrina pachyderma, Globorotalia truncatulinoides, Globigerinoides ruber, Globorotalia inflata, Globoritalia hirsute* and *Orbulina universa*.

The picked samples were dated by the AMS (Accelerator Mass Spectrometry) method at the NERC Radiocarbon Laboratory in Scotland and at Beta Analytic in Florida. The results were returned as conventional radiocarbon ages and converted to calibrated (Cal) radiocarbon ages (Table 6.2) that are used hereafter. This conversion was done using the latest MARINE04 database and IntCal04 calibration curve (after Stuiver and Reimer, 1993; Stuiver et al., 1998; Hughen et al., 2004; Reimer et al., 2004). This calibration uses a 400-year reservoir age for a deep-sea setting, which is valid up to 21,786 Cal a BP. For older ages, the Fairbanks0107 calibration curve of Fairbanks et al. (2005) was used instead with a 255-year reservoir age. Age ranges are reported as 2 sigma (i.e. 95 % confidence limit), and a non-modal range is used because it is based on the intercept of an erratic database curve.

Sedimentation rates were calculated for the combined hemipelagic and turbiditic sequence, as well as for the hemipelagic-only sequence (Table 6.2). To extrapolate ages, it was assumed that an oxidised core top, indicated by pale orange-pink coloured sediment (see Fig. 6.3), shows that the sediment sequence is complete, and that calculated sedimentation rates remain constant between any two measured dates. For example, the age of the base of core CD56412 has been estimated by assuming that the sedimentation rate at the base of the core will be close to the average sedimentation rate calculated from the available radiocarbon dates farther up the core. Therefore, 258 cm of hemipelagite from the last measured sample to the base of the core, divided by the average measured hemipelagic sedimentation rate (7.4 cm/Cal ka), gives an estimated age of 73 ka for the base of the core. The ages of the bases of cores D11951 and D11931 have been calculated in the same way (Table 6.2).

Table 6.2. Conversion from conventional to calibrated radiocarbon ages, and sedimentation rates.

								Sedimentation rate[b]	
Core	Sample depth (cm)	Sample ID	Conventional radiocarbon age (a BP)	Error range (1 sigma)	Calibration curve	Reservoir age (a)	Calibrated radiocarbon age range (2 sigma Cal a BP)	Hemipelagite only (cm/Cal ka)	Hemipelagite and turbidites (cm/Cal ka)
CD56820	27-28 (TC)[a]	Beta - 241118	1030	40	Marine04	400	**530-660**	34.9	46.8
	3-4	SUERC - 14436	1232	35	Marine04	400	**690-880**	n/a[c]	n/a[c]
	104-105	SUERC - 14437	7534	38	Marine04	400	**7920-8110**	19.3	19.6
CD56837	8-10	Beta - 241116	1570	40	Marine04	400	**1040-1230**	3.5	8.0
	74-76	Beta - 241117	6040	50	Marine04	400	**6350-6590**	12.4	12.4
CD56822	1-5 (TC)[a]	SUERC - 14438	26	35	Marine04	400	**0-60**	50.0[d]	50.0[d]
	16-18	Beta - 241124	650	40	Marine04	400	**250-390**	66.5	82.2
	41-42 (TC)[a]	Beta - 241123	1420	40	Marine04	400	**900-1050**	20.1	28.1
	104-105	SUERC - 14439	2634	35	Marine04	400	**2200-2430**	52.5	53.3
	204-205	SUERC - 14440	4328	35	Marine04	400	**4360-4570**	44.7	47.0
	265-266	SUERC - 14443	5900	37	Marine04	400	**6240-6410**	20.1	33.1
CD56825	36-37 (TC)[a]	Beta - 241119	1500	40	Marine04	400	**950-1150**	16.7	35.1
	25-27	Beta - 241120	1570	40	Marine04	400	**1040-1230**	12.7	44.3
	155-157	Beta - 241121	4330	50	Marine04	400	**4350-4580**	24.3	33.9
	278-280	Beta - 241122	6790	50	Marine04	400	**7230-7410**	25.3	43.3
	296-298	Beta - 246923	7400	40	Marine04	400	**7780-7940**	51.4	51.4
CD56843	96-98	Beta - 241125	6040	50	Marine04	400	**6350-6590**	14.1	15.0
CD56407	39-44 (TC)[a]	SUERC - 7431	3855	25	Marine04	400	**3700-3900**	9.1	10.9
CD56414	6-9	SUERC - 7428	937	21	Marine04	400	**500-600**	26.7	32.1
	66-69	SUERC - 7429	5155	22	Marine04	400	**5460-5580**	8.9	12.1

Table 6.2. Conversion from conventional to calibrated radiocarbon ages, and sedimentation rates. *(Continued).*

Core	Sample depth (cm)	Sample ID	Conventional radiocarbon age (a BP)	Error range (1 sigma)	Calibration curve	Reservoir age (a)	Calibrated radiocarbon age range (2 sigma Cal a BP)	Sedimentation rate[b] Hemipelagite only (cm/Cal ka)	Sedimentation rate[b] Hemipelagite and turbidites (cm/Cal ka)
CD56412	10-14 (TC)[a]	SUERC - 7421	1932	21	Marine04	400	**1400-1550**	8.2	8.2
	58-62	SUERC - 7423	16,984	70	Marine04	400	**19,530-19,880**	4.0	5.0
	123-127	SUERC - 7424	26,149	210	Fairbanks0107	255	**31,130-31,660**	5.3	5.6
	202-206	SUERC - 7425	32,398	462	Fairbanks0107	255	**37,300-38,280**	12.1	12.5
								7.4[f]	**7.8**[f]
D11931	15-18	SUERC - 14444	4637	36	Marine04	400	**4800-4960**	5.9	6.8
	38-41	SUERC - 14445	6364	36	Marine04	400	**6730-6940**	1.8	11.1
	81-84	SUERC - 14446	8104	37	Marine04	400	**8450-8690**	8.8	25.2
	151-154	SUERC - 14447	11,888	41	Marine04	400	**13,250-13,420**	7.4	14.7
	225-227	SUERC - 14449	15,314	51	Marine04	400	**17,990-18,530**	10.9	15.0
	250-252	SUERC - 14450	16,227	53	Marine04	400	**18,900-19,180**	33.7	44.3
	308-310	SUERC - 14453	17,214	57	Marine04	400	**19,840-20,140**	23.2	67.3
	353-356	SUERC - 14454	18,992	67	Marine04	400	**22,040-22,340**	7.2	21.1
								12.4[f]	**25.7**[f]
D11951	10-12	SUERC - 14455	6565	37	Marine04	400	**6970-7190**	n/a[e]	n/a[e]
	76-78	SUERC - 14456	8018	37	Marine04	400	**8390-8560**	5.8	48.3
	130-132	SUERC - 14457	9700	39	Marine04	400	**10,490-10,650**	2.9	25.9
	168-170	SUERC - 14458	15,884	52	Marine04	400	**18,690-18,900**	4.5	4.6
	229-231	SUERC - 14459	17,171	56	Marine04	400	**19,810-20,120**	12.6	54.8
								6.5[f]	**33.4**[f]

[a] TC = trigger core samples.

[b] Sedimentation rates were calculated for intervals between dated horizons, and each one applies to the interval immediately above the dated sample.

[c] Sample CD56820 3-4 cm was omitted from calculation of sedimentation rates because of likely core disturbance (see text).

[d] The rate for the top 1-5 cm of core CD56822 is a minimum value only because the maximum rate would be based on 3 cm per 0 years, which would give a spuriously high value.

[e] A rate for the top of core D11951 was not calculated due to absent core top.

[f] Average sedimentation rates for each basin core are shown in bold. These values were used in calculating the extrapolated age of the base of these cores (see text).

Fig. 6.3. The pink-orange mud of the oxidised layer that indicates the core top (above black arrow). Taken from trigger core CD56825 from Setúbal Canyon. Scale is in cm on the left and in inches on the right.

Fig. 6.4. *(following page)* Multi-sensor core logging (MSCL) profiles for core CD56412 from the mouth of Setúbal Canyon: gamma density (g cc^{-1}) and magnetic susceptibility (S.I. units). Top axis in black corresponds to the trigger core, bottom axis in blue to the piston core. Profiles for cores D11951 and D11931 from the Tagus Abyssal Plain show p-wave velocity (m s^{-1}) and magnetic susceptibility (c.g.s. units), from Lebreiro (1995). Horizontal lines show tentative correlation of events across cores based on lithology and MSCL profiles, and correspond to the base of the coloured bands in Fig. 6.6

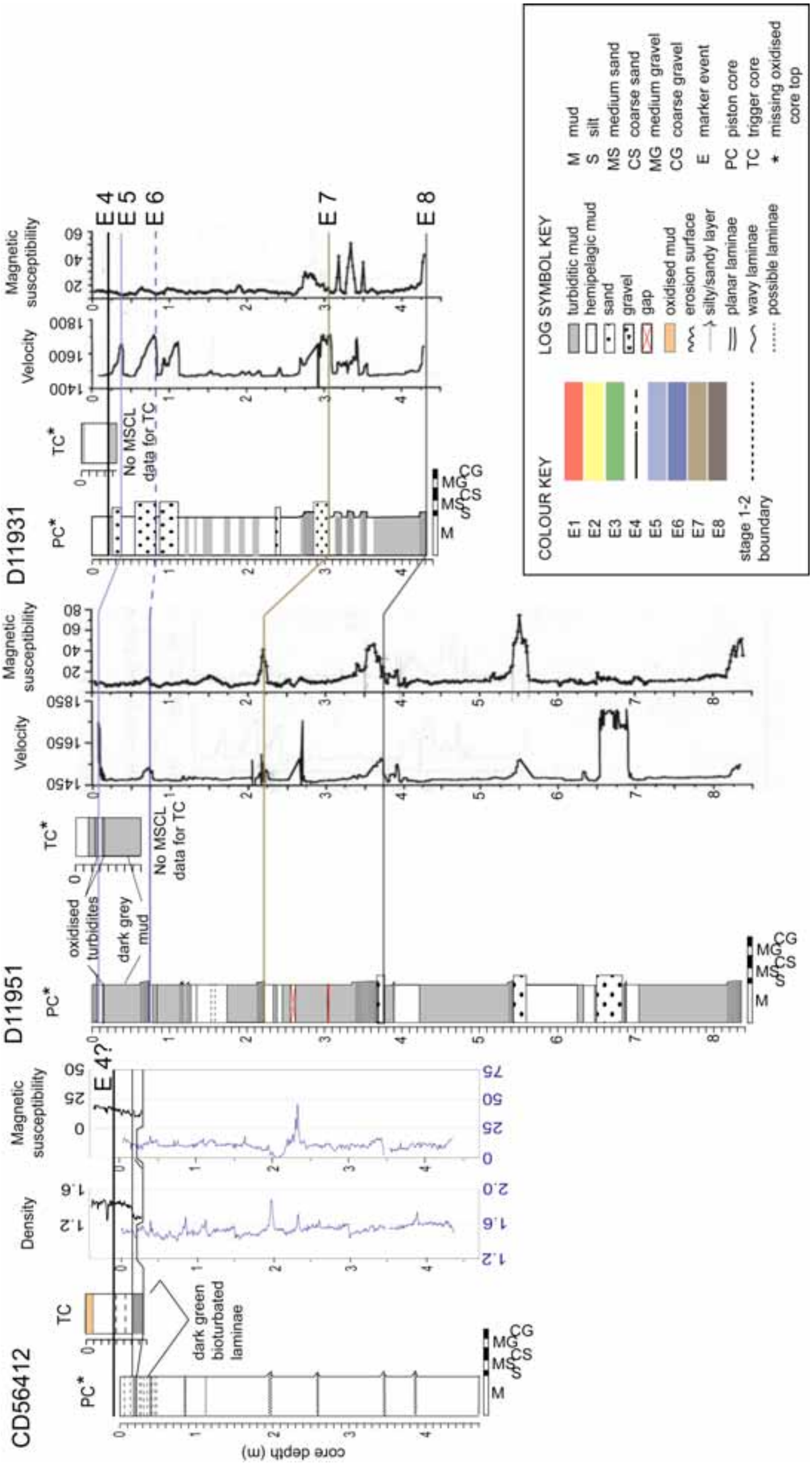
CD56412
PC*
TC
dark green bioturbated laminae
Density
Magnetic susceptibility
E 4?
core depth (m)
M MS S CS MG CG
D11951
PC*
TC*
oxidised turbidites
dark grey mud
No MSCL data for TC
Velocity
Magnetic susceptibility
D11931
PC*
TC*
No MSCL data for TC
Velocity
Magnetic susceptibility
E 4
E 5
E 6
E 7
E 8
COLOUR KEY
E1
E2
E3
E4
E5
E6
E7
E8
stage 1-2 boundary
LOG SYMBOL KEY
turbiditic mud
hemipelagic mud
sand
gravel
gap
oxidised mud
erosion surface
silty/sandy layer
planar laminae
wavy laminae
possible laminae
M mud
S silt
MS medium sand
CS coarse sand
MG medium gravel
CG coarse gravel
E marker event
PC piston core
TC trigger core
* missing oxidised core top

6.5 Results and interpretation

The sediment cores can be divided into two geographic groups: those from the basin (Tagus Abyssal Plain including the distal mouth of Setúbal Canyon) and those from the Setúbal and Cascais canyons.

6.5.1 Basin cores

The three basin cores show sediment sequences dominated by turbidite deposits (Fig. 6.4). Core D11951 from the distal part of the Tagus Abyssal Plain consists mainly of thick muddy turbidites, some of which have silty bases and three that grade from sand to mud. Core D11931 from a more proximal location shows thinner but coarser units with less turbiditic mud. Where a turbidite is lacking its mud top, this implies that the suspended mud cloud of the turbidity current bypassed this part of the basin and continued further basinward to deposit in a more distal and/or deeper location. Absence of the coarser units, however, implies that the coarse traction layer of the flow deposited further upslope, i.e. most likely in the canyon, and did not make it as far as the abyssal plain.

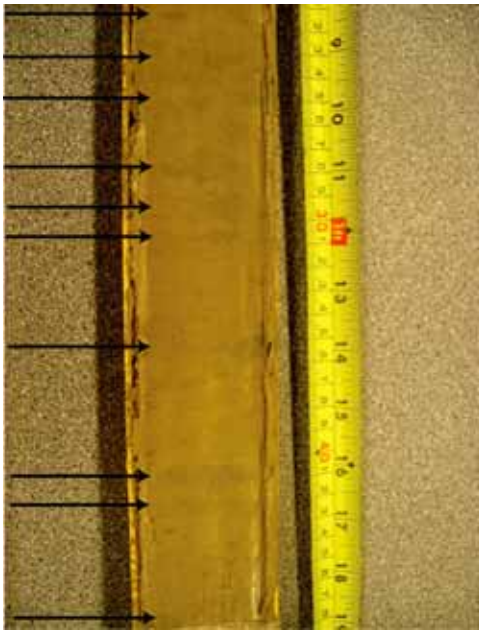

Fig. 6.5. Thin bioturbated laminae of turbiditic mud within hemipelagite, as indicated by black arrows. Taken from trigger core CD56412 in the mouth of Setúbal Canyon. Scale is in cm on the left and in inches on the right.

Hemipelagic mud can be distinguished from turbiditic mud because it contains abundant white foraminifera tests, the latter completely absent from turbidite mud because of size sorting in the parent turbidity current. Typically a bioturbated boundary is seen between turbiditic mud units and the overlying hemipelagic mud. The Setúbal Canyon mouth core, CD56412, is composed almost entirely of hemipelagite mixed with thin turbiditic mud laminae and only four thin silty turbidite bases are recognised. This muddy hemipelagite (see Fig. 6.5) is thought to be the result of muddy suspension clouds from turbidity current tails being incorporated into the slowly settling hemipelagic material, and these being subsequently bioturbated.

Radiocarbon data provide a time framework for the cores and can thus confirm correlations made using lithological and multi-sensor core logging data. Combining these three data sets enables the correlation of at least four single turbidite events (E5-E8) across cores D11951 and D11931 (Fig. 6.6). E8 is the oldest turbidite in core D11931 and has an extrapolated age of ca 23,000 Cal a BP (Table 6.3). E7 is the next thick turbidite in the sediment record, and has measured ages in both cores that date it at approximately 20,000 Cal a BP. Both E8 and E7 are composed of thick mud and silt/sand sequences that correspond to large positive peaks in p-wave velocity and magnetic susceptibility, the latter especially within the silt fraction (the sand fraction is composed of clean terrigenous quartz and therefore does not produce a magnetic susceptibility excursion).

Turbidites E6 and E5 are composed of thick sand units with very thin or no mud tops in core D11931 (Fig. 6.6). In core D11951, E6 is a thick mud turbidite with a silt base and E5 is a thin mud turbidite, implying that the coarse traction layer of the turbidity currents preferentially deposited in the more proximal area of the Tagus Abyssal Plain (core D11931), while the muddy suspension clouds preferentially deposited in the more distal area (core D11951). Both events E6 and E5 have similar positive p-wave velocity peaks across both cores, and the silt base of E6 in D11951 has a slight positive magnetic susceptibility peak. E6 is dated at ~8400-8700 Cal a BP and E5 at ~6700-7200 Cal a BP (Table 6.3).

None of the abyssal plain turbidites can be correlated with core CD56412 in the distal mouth of Setúbal Canyon. This is because the sedimentation rate in this core is far lower, so that the ~20,000 year sedimentation interval that makes up all of core D11931 and most of D11951 only corresponds to the record in the top ~50 cm of core CD56412 plus its trigger core (Fig. 6.6). This condensed record is therefore unsuitable for correlation of individual events.

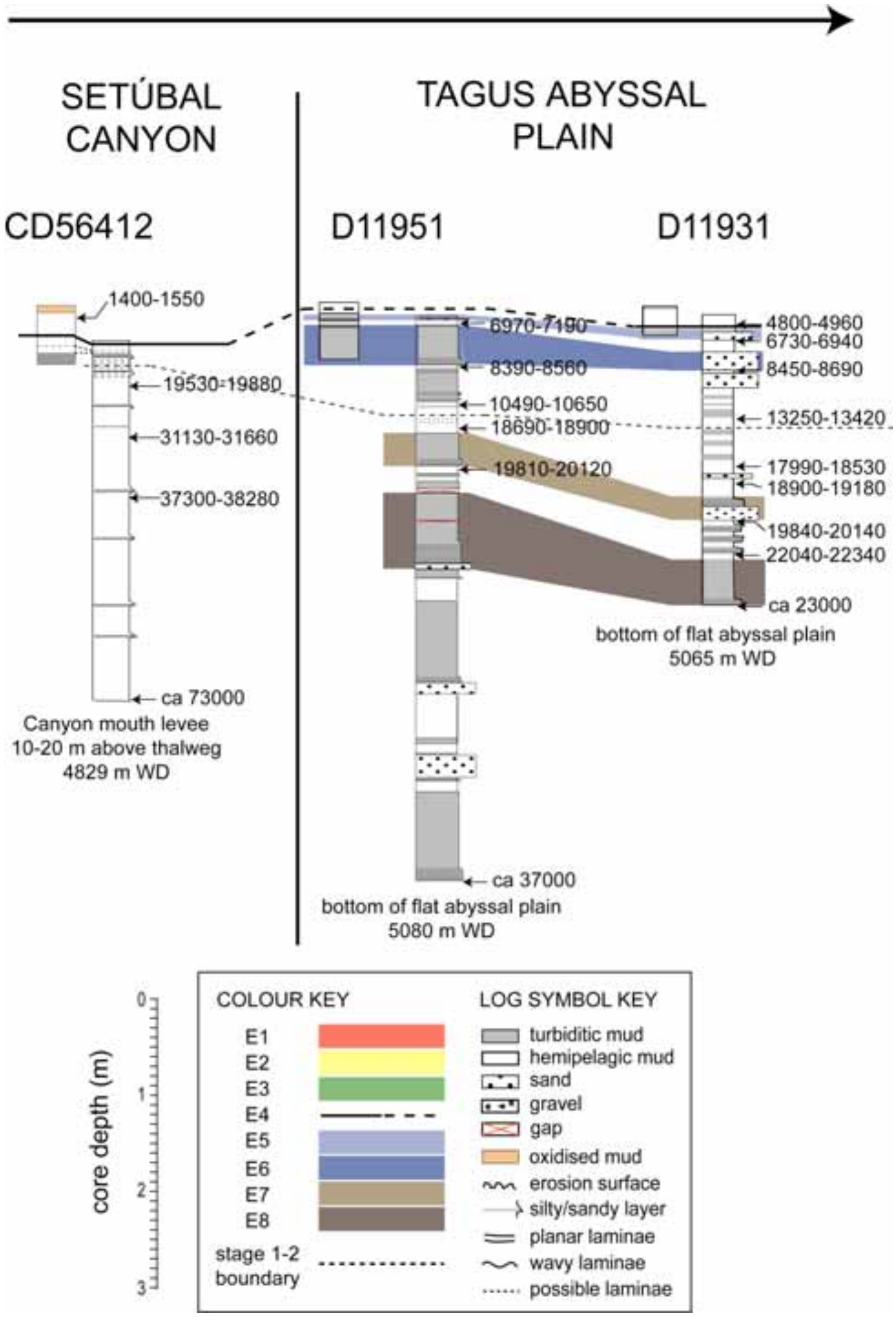

Fig. 6.6. Panel correlation between cores from the mouth of Setúbal Canyon and the Tagus Abyssal Plain. Arrow indicates flow direction, dashed line is the approximate depth of the stage 1-2 boundary based on radiocarbon dates. Ages are measured radiocarbon dates except for the ages at the base of the cores, which are estimated from the sedimentation rates (see Table 6.2).

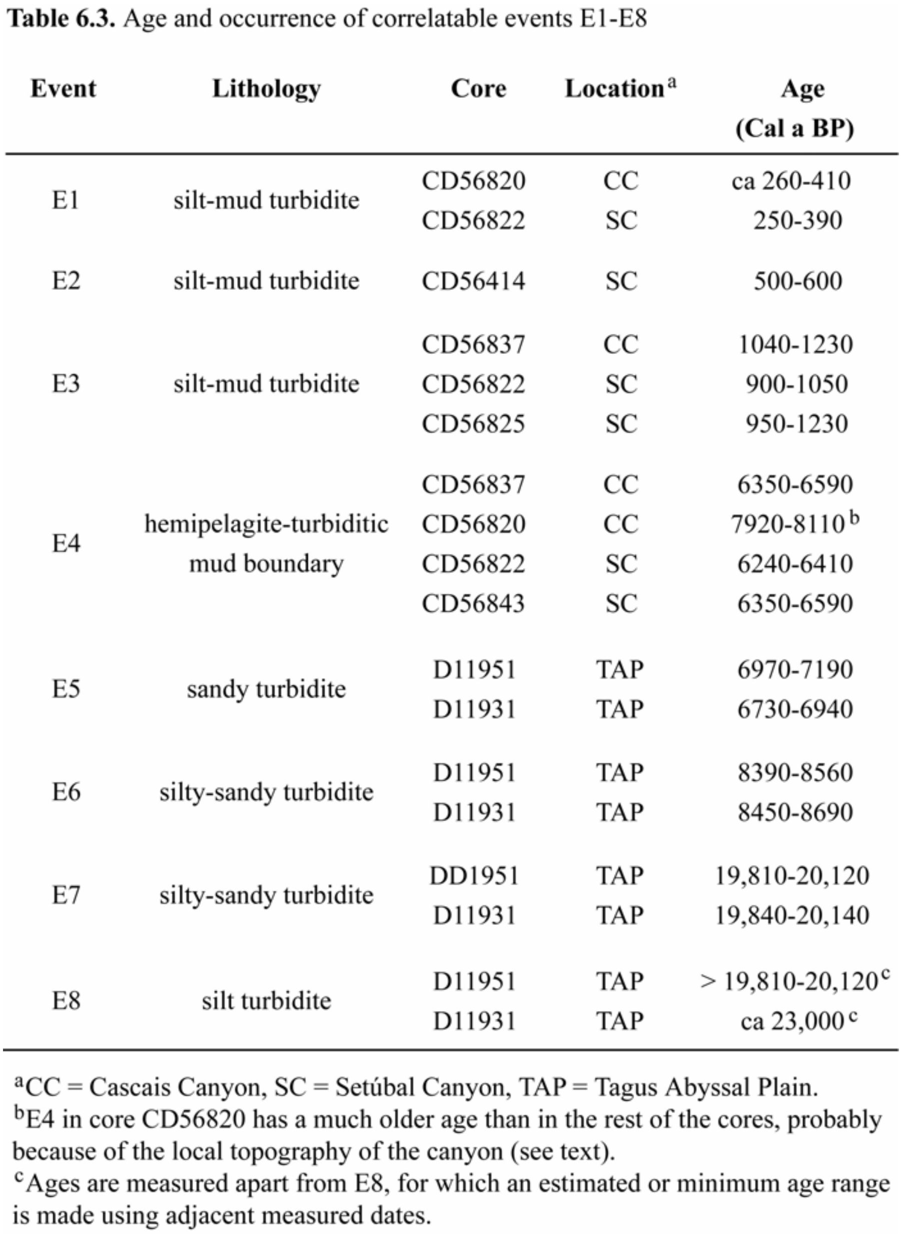

Table 6.3. Age and occurrence of correlatable events E1-E8

Event	Lithology	Core	Location[a]	Age (Cal a BP)
E1	silt-mud turbidite	CD56820	CC	ca 260-410
		CD56822	SC	250-390
E2	silt-mud turbidite	CD56414	SC	500-600
E3	silt-mud turbidite	CD56837	CC	1040-1230
		CD56822	SC	900-1050
		CD56825	SC	950-1230
E4	hemipelagite-turbiditic mud boundary	CD56837	CC	6350-6590
		CD56820	CC	7920-8110[b]
		CD56822	SC	6240-6410
		CD56843	SC	6350-6590
E5	sandy turbidite	D11951	TAP	6970-7190
		D11931	TAP	6730-6940
E6	silty-sandy turbidite	D11951	TAP	8390-8560
		D11931	TAP	8450-8690
E7	silty-sandy turbidite	DD1951	TAP	19,810-20,120
		D11931	TAP	19,840-20,140
E8	silt turbidite	D11951	TAP	> 19,810-20,120[c]
		D11931	TAP	ca 23,000[c]

[a] CC = Cascais Canyon, SC = Setúbal Canyon, TAP = Tagus Abyssal Plain.

[b] E4 in core CD56820 has a much older age than in the rest of the cores, probably because of the local topography of the canyon (see text).

[c] Ages are measured apart from E8, for which an estimated or minimum age range is made using adjacent measured dates.

The sedimentation rates for the basin cores are shown in Fig. 6.7 and Table 6.2. Core CD56412 has very similar sedimentation rates and smooth profiles for both the combined hemipelagic-turbiditic and hemipelagic-only sequences. This indicates that this core either does not contain a significant proportion of turbidite units or that any turbidite material has been thoroughly mixed with the hemipelagic layers by biotubation so that it is not now distinguishable. The average rate of accumulation for this core of over 5 cm/Cal ka suggests that some additional sediment has been added to the pelagic supply (probably less than 2 cm/Cal ka at this deep location) and the most likely source is from turbidity currents. In the abyssal plain cores D11951 and D11931, the combined turbiditic and hemipelagic rates are considerably higher than the hemipelagic-only rates.

Cores D11951 and D11931 show two periods of increased turbiditic sedimentation, the first at ~23-18 ka and the second at ~9-7 ka (Fig. 6.7). This is also reflected in the frequencies of turbidite emplacement during these intervals (Table 6.4), especially that of core D11931. Core CD56412 does not show any periods of enhanced turbidite deposition.

The oxidised mud layer that typically indicates the core top is missing in cores D11951 and D11931 (Fig. 6.6). However, the radiocarbon age data suggest that only a minimal amount of sediment could be missing at the top of core D11931 (Fig. 6.7). The thickest hemipelagite, and assumed quiescent, interval in this core lies between E5 and the core top, i.e. between ca 6-5 ka and the present day. This time period is absent in core D11951, but occupies approximately the top 35 cm depth in trigger core CD56412 (using its sedimentation rate profiles in Fig. 6.7). This interval is represented by hemipelagite deposits in core CD56412 with an interval of muddy laminae deposition beneath (Fig. 6.6). Thus, the last period of turbidity current activity appears to have ended between 6 and 5 ka.

Lebreiro (1995) identified ice-rafted deposits from two Heinrich Events in core D11931, based on magnetic susceptibility, mineralogical and foraminiferal species data. She identified magnetic susceptibility peaks at 191 cm and 350 cm depth and assigned these to Heinrich Events 1 and 2 respectively, dated at 13.95 and 20.23 Cal ka (after the isotope boundaries presented in Martinson et al., 1987). More recently, the ages of these events offshore western Portugal have been modified to 14.9-17.6 and 23.1-24.3 Cal ka using radiocarbon dating (Abreu et al., 2003; Hemming, 2004). The position of the first event (H1) correlates well with the radiocarbon data presented here. Heinrich Layer 2, however, was assigned by Lebreiro (1995) to the deepest of three thin silty turbidites with extremely high magnetic susceptibility values, which we date here at 22,040-22,340 Cal a BP (Fig. 6.6). This suggests that Heinrich Layer 2 may have been reworked by a turbidity current.

Neither Heinrich Events 1 nor 2 were identified in core D11951 by Lebreiro (1995), possibly because the core is dominated by turbiditic mud. However, the slight magnetic susceptibility peak in the hemipelagic unit at 150 cm depth may correlate with Heinrich Event 1 in core D11931. Additionally, the large magnetic susceptibility peak at 235 cm depth in core CD56412 suggests it could be Heinrich Event 4 (38-40 Cal ka, Abreu et al., 2003; Hemming, 2004).

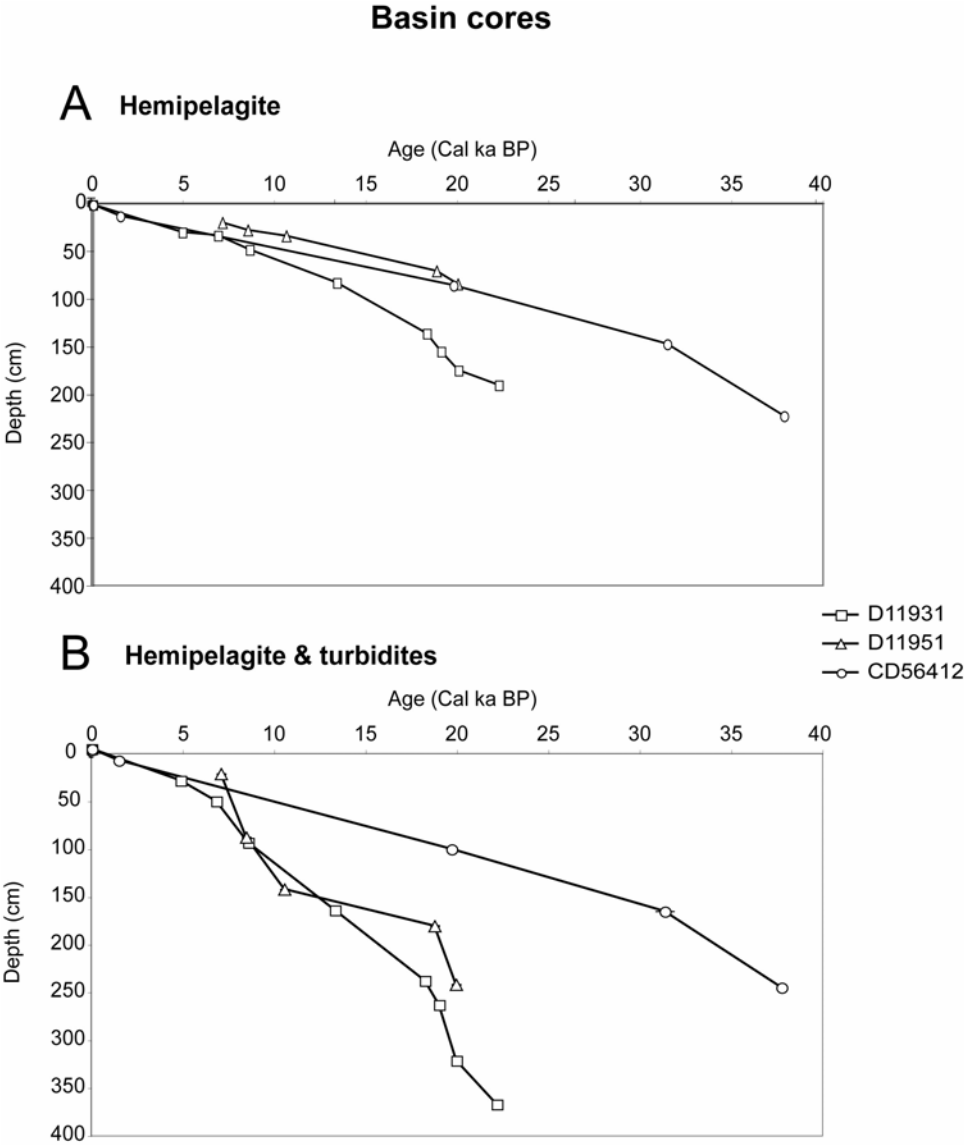

Fig. 6.7. Sediment depth-age plots showing sedimentation rates for the Tagus Abyssal Plain and Setúbal Canyon mouth cores. (**A**) Hemipelagic-only sequence, (**B**) combined hemipelagic and turbiditic sequence.

6.5.2 Canyon cores

The cores from Cascais and Setúbal canyons were mostly collected on terraces adjacent to the canyon floor and ranging from 12 to 182 m above the canyon floor (Table 6.1). Only two cores were successfully collected from the canyon floor (CD56407 and

CD56414). As with the basin cores, the canyon cores are also dominated by turbidites. However, in the canyon cores, turbidites occur either in a thick sequence of stacked, thin-bedded, fine-grained, silt-mud deposits (see an example in Fig. 6.8), or as individual thin silt-mud or mud deposits within thick hemipelagite. The visual logs of the canyon cores are shown in Figs. 6.9 and 6.10. These contrast sharply with the much thicker muddy turbidites with sandy bases in the Tagus Abyssal Plain cores, and with the thin silty turbidite bases in core CD56412 (Fig. 6.4). The hemipelagic unit at the top of cores CD56837, CD56820, CD56822 and CD56414 has several thin, olive green-brown and bioturbated muddy laminae. These are interpreted as being the bioturbated remnants of muddy turbidites (similar to those in Fig. 6.5), as they occur with dense *chondrites*-type burrows. These organisms burrow through and feed on the clayey organic-rich layers, and their burrows are visible only because of the layers of differently coloured sediment, i.e. the pale beige hemipelagite and the green-grey turbiditic mud.

Fig. 6.8. A stacked sequence of thin silty turbidites, typical of the pre-6.4 ka interval in the canyon cores. Taken from core CD56837 in Cascais Canyon. Scale is in cm on the left and in inches on the right.

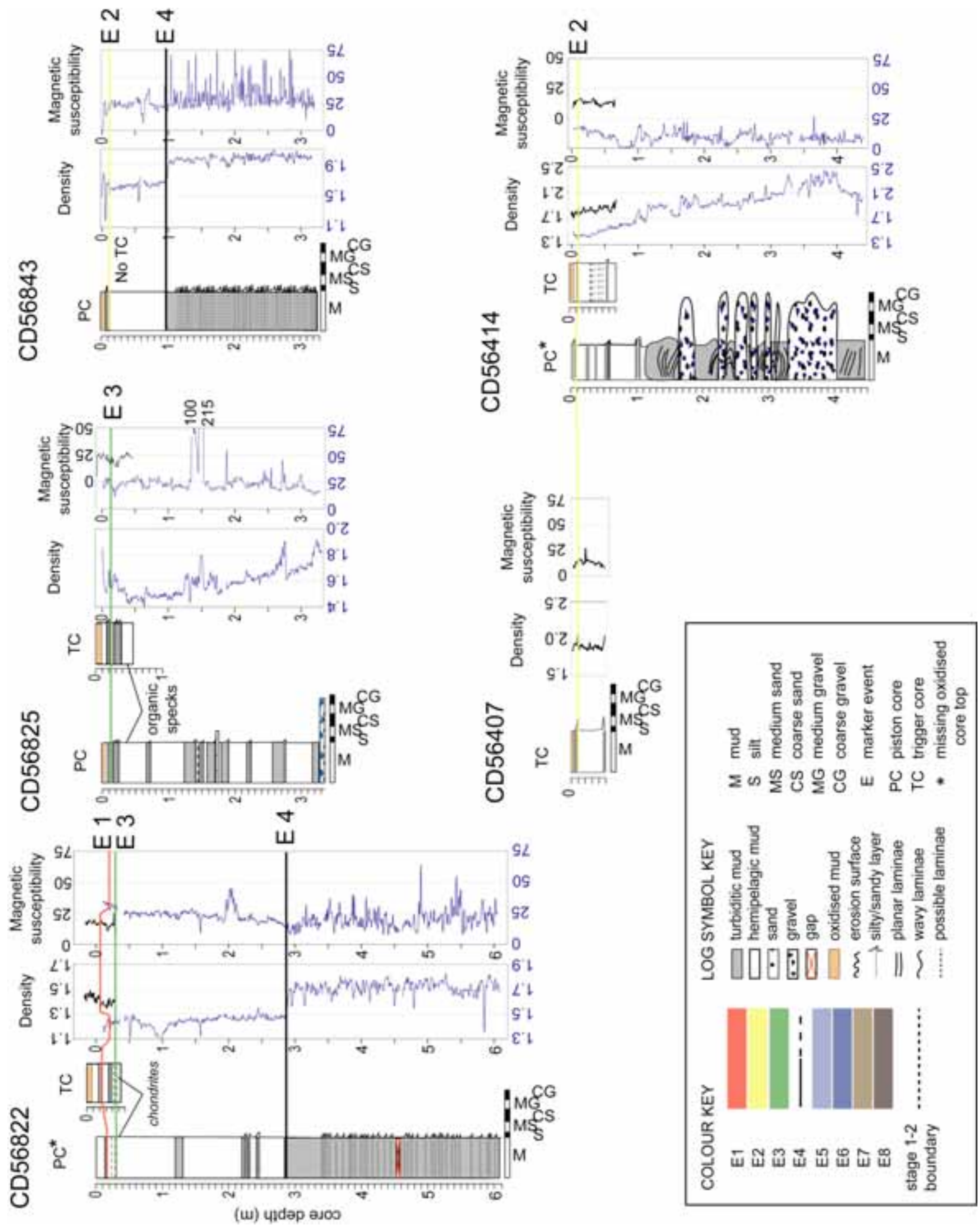

Fig. 6.9. MSCL profiles for the Setúbal Canyon cores: gamma density (g cc^{-1}) and magnetic susceptibility (S.I. units). Top axis in black corresponds to the trigger cores, bottom axis in blue to the piston cores. For key of symbols, see Fig. 6.4. Horizontal lines show tentative correlation of events across cores based on lithology and MSCL profiles, and correspond to the base of the coloured bands in Fig. 6.11.

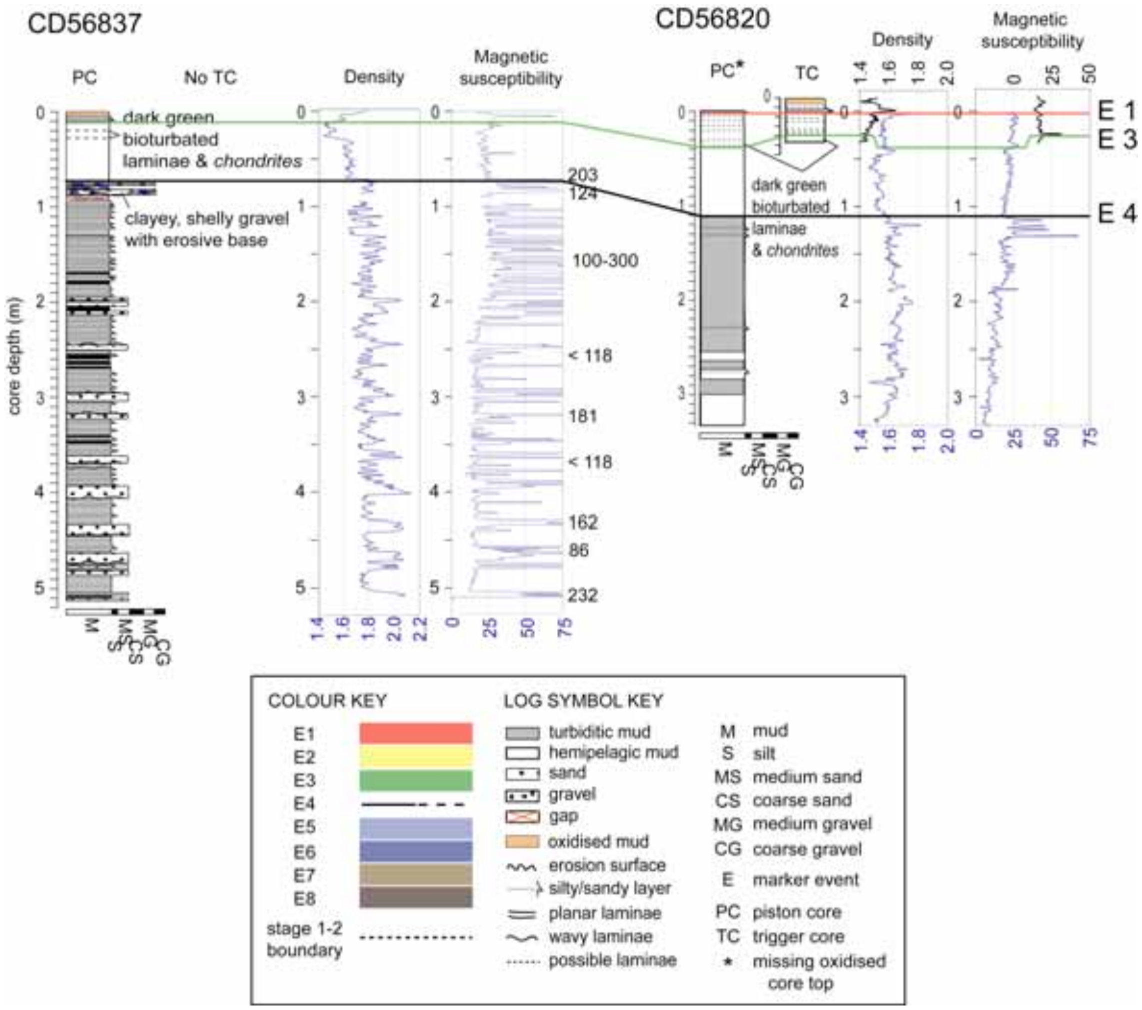

Fig. 6.10. MSCL profiles for the Cascais Canyon cores: gamma density (g cc^{-1}) and magnetic susceptibility (S.I. units). Top axis in black corresponds to the trigger cores, bottom axis in blue to the piston cores. For key of symbols, see Fig. 6.4. Horizontal lines show tentative correlation of events across cores based on lithology and MSCL profiles, and correspond to the base of the coloured bands in Fig. 6.12.

There are also a number of debris flow deposits in the canyon cores. These are found in cores CD56837 (75-87 cm), CD56825 (320-330 cm) and CD56414 (115-145 cm; Figs. 6.9, 6.10). Debris flows are the result of mass wasting of pre-existing sediment in the canyons and from the canyon walls and levees. These deposits are thus composed of reworked turbiditic mud, silt, sand and gravel units, the latter being sub-rounded pebbles up to 4 cm in diameter and composed of a variety of metamorphosed argillaceous rocks. The deposit in core CD56414 and the piston core part of CD56407 (not shown) has been interpreted in a previous study as reworked gravel wave deposits

(Arzola et al., 2008), and its cohesive mud content enabled the successful recovery of these cores from a canyon floor setting.

The sequence of stacked thin-bedded turbidites, whose top boundary is labelled E4, is found in cores CD56822 and CD56843 from Setúbal Canyon (Fig. 6.11) and in both Cascais Canyon cores (CD56837 and CD56820; Fig. 6.12). Cores CD56407 and CD56414 were recovered from the site of a mass wasting event (Arzola et al., 2008) that occurred after E4, and as a result this event cannot be recognised in these cores. The abrupt change in sediment style at E4, between the stacked turbidites below and the thick hemipelagite above, is clearly shown in Fig. 6.13 and also reflected in the sharp down-core jump in the density and magnetic susceptibility profiles (Figs. 6.9, 6.10). This boundary is dated at ca 6.4 ka in cores CD56837, CD56822 and CD56843 (Table 6.2).

Event E4 has an older age of ca 8 ka in core CD56820, but this may be attributed to the local topography in the canyon, where the height of the core above the thalweg (~180 m) places it toward the upper boundary of the turbidity currents. The presence of very few silty bases and mainly turbiditic mud agrees with this. Core CD56837 is located at about 160 m above the canyon floor and has a thick sequence of stacked turbidites, suggesting that many turbidity currents exceeded 160 m in height with fewer exceeding 180 m. E4 is not recognizable in core CD56825, which may suggest that the thin-bedded turbidites only deposit on terraces that are a few tens to over 100 m above the thalweg. Core CD56825 is only 20-30 m above the thalweg, and the flows may be bypassing these lower terraces. Therefore, 6.4 ka is taken as the average real age of E4. The lack of datable hemipelagic material within the pre-6.4 ka sequence precludes the estimation of a sedimentation rate and turbidite frequency for this interval.

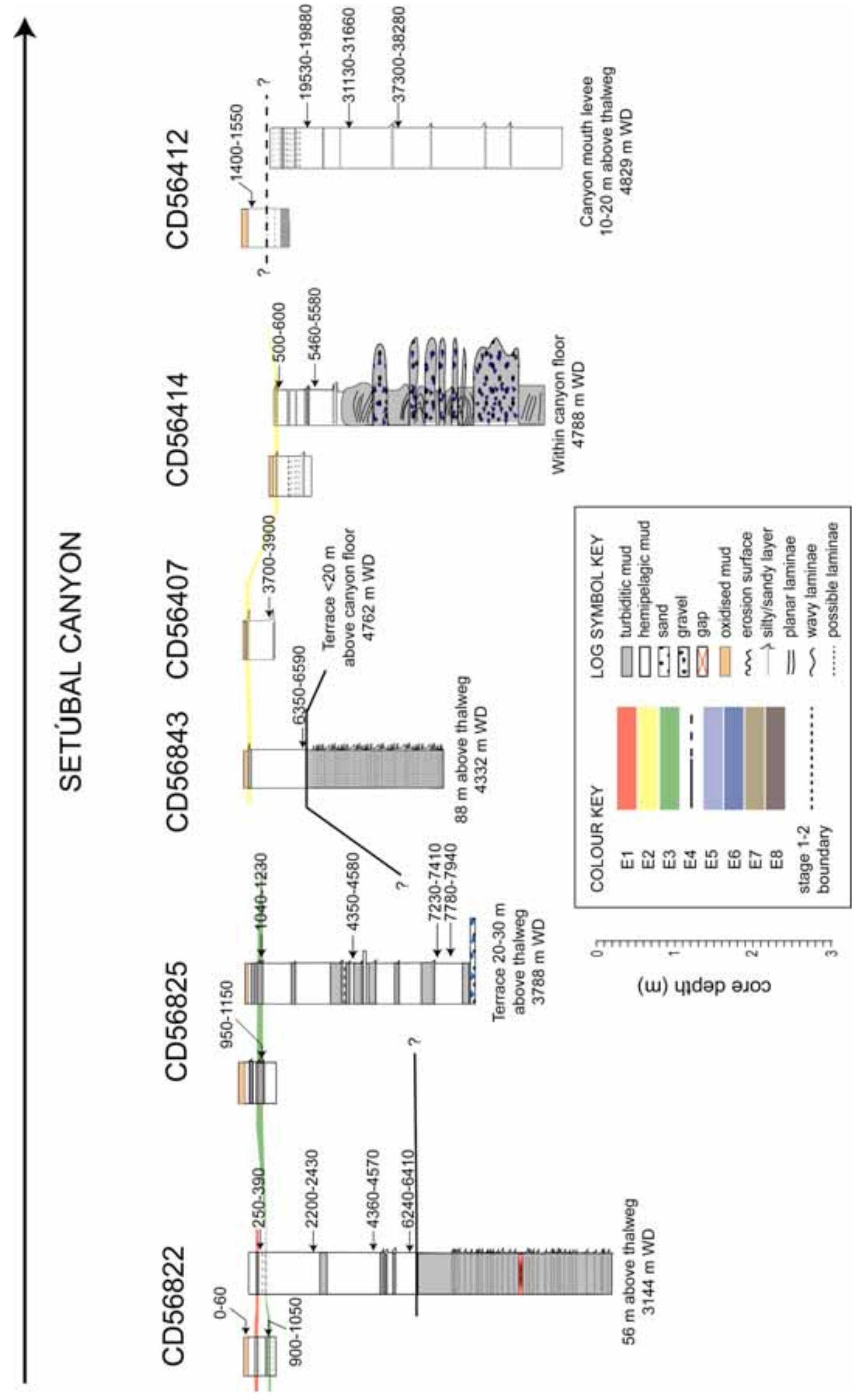

Fig. 6.11. Panel correlation between cores from Setúbal Canyon, including core CD56412 from the distal canyon mouth. Arrow indicates flow direction. For key of symbols, see Fig. 6.6.

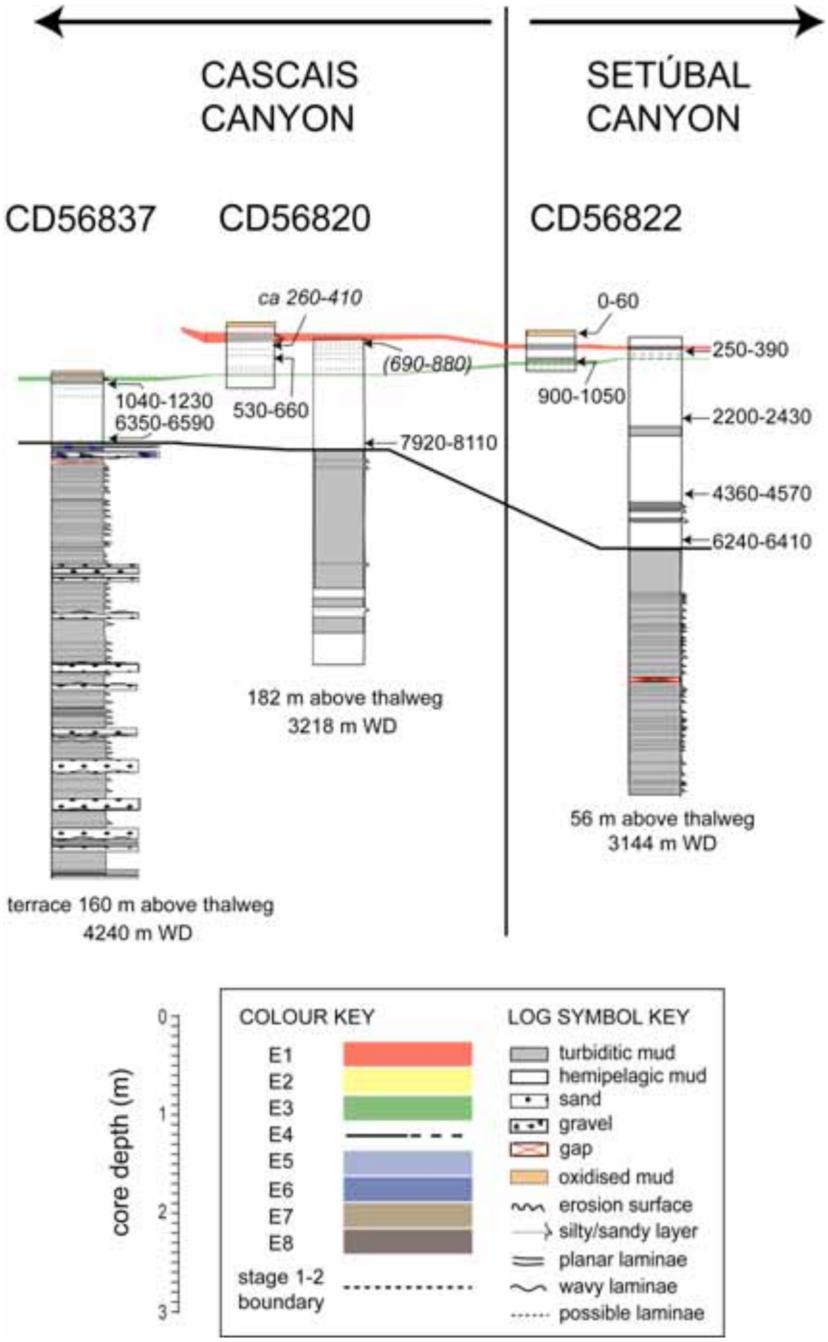

Fig. 6.12. Panel correlation between cores from Cascais Canyon and the uppermost core from Setúbal Canyon. Arrows indicate flow direction. The age range in brackets is believed to be anomalous (see text). For key of symbols, see Fig. 6.6.

The entire post-6.4 ka interval varies greatly across different locations. Cores CD56822 and CD56825 have between two and six thin silty-muddy turbidites separated by hemipelagite, while cores CD56837, CD56820 and CD56843 have none, or only thin bioturbated muddy laminae (Figs. 6.11, 6.12). The individual turbidites in this section above event E4 allow only tentative correlations between cores, as they are all composed of similar lithology, grain size and physical properties. Also, core compaction and compression are more likely closer to the core top, making radiocarbon ages less precise. Only three distinct and correlatable events are suggested (E1-E3).

The three uppermost turbidites are similar in thickness and composed of the same lithology. Apart from E3, which has a small peak in magnetic susceptibility and a high organic content indicated by an abundance of *chondrites*-type burrows (cores CD56822 in Fig. 6.9, CD56820 and CD56837 in Fig. 6.10), E1 and E2 do not show any significant peaks in their MSCL profiles. They can be differentiated most accurately based on their age ranges, which are 250-410 (E1), 500-600 (E2) and 900-1230 Cal a BP (E3; Table 6.3).

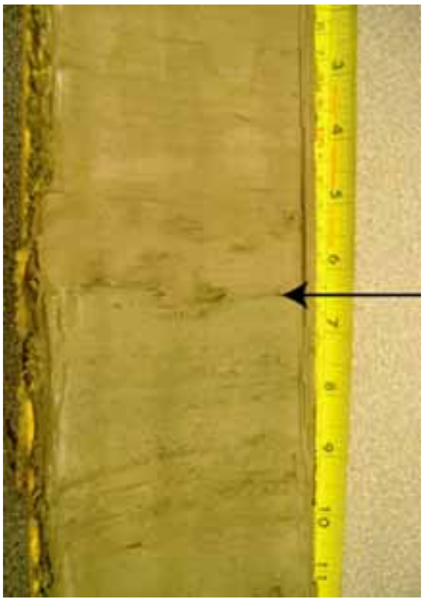

Fig. 6.13. Black arrow indicates the sharp transition from pale beige hemipelagite (above) to olive green-brown turbiditic mud (below) at the E4 boundary. Taken from core CD56822 in Setúbal Canyon. Scale is in cm on the left and in inches on the right.

There is a discrepancy between the date obtained below E1 in the trigger core for CD56820 and the uppermost date obtained from the main piston core, the latter being considerably older (Fig. 6.12 and Table 6.2). The piston core date is also older than dates obtained below E1 in several other cores (Figs. 6.11, 6.12). The lithological correlation between piston and trigger core in CD56820 is supported by multi-sensor core logging data. The reason for the anomalously old date (690-880 Cal a BP) is unclear, but could be related to core disturbance in the uppermost part of the core or, less likely, to an error in correlation between piston and trigger core. Therefore, the piston core date (690-880 Cal a BP) has been omitted in calculating the sedimentation rate of this interval (Table 6.2).

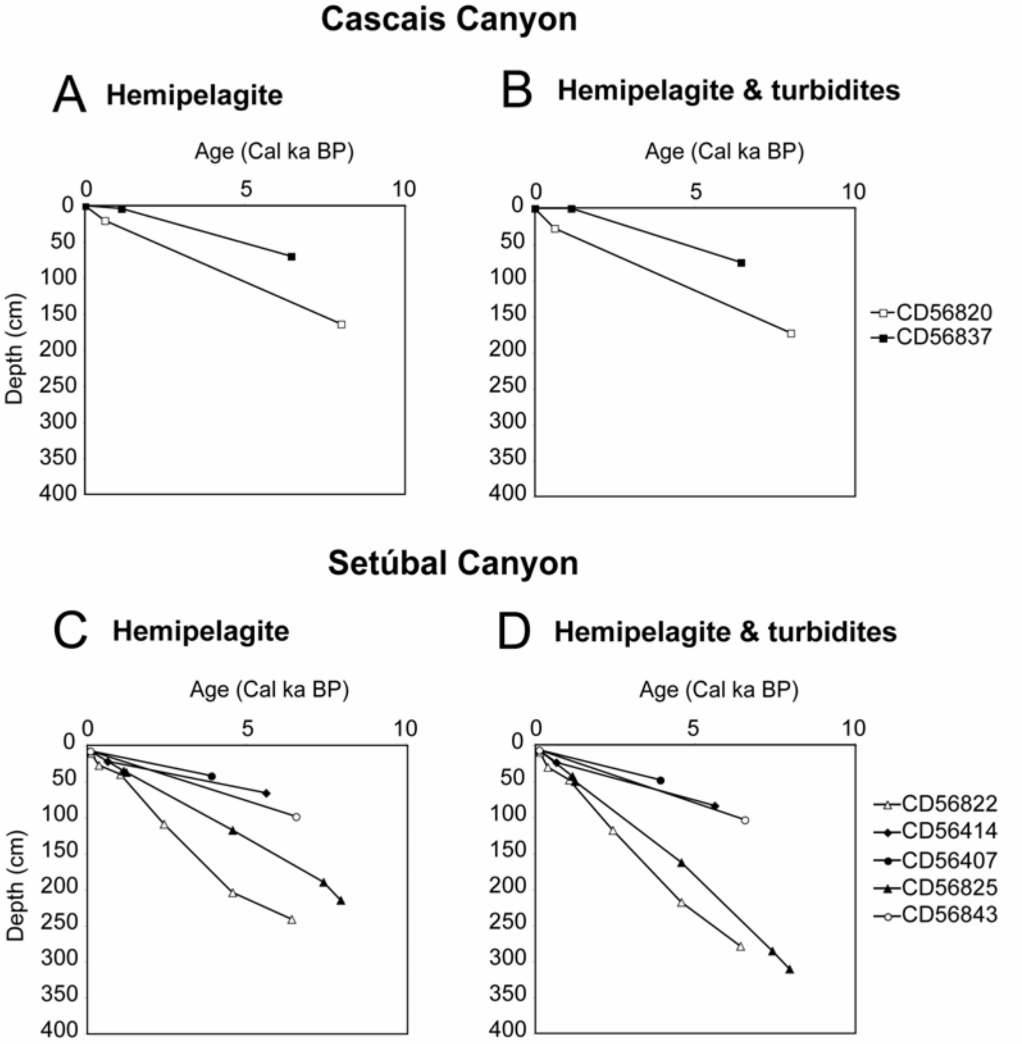

Fig. 6.14. Sediment depth-age plots showing hemipelagic-only and combined hemipelagic-turbiditic sedimentation rates respectively for the post-6.4 ka interval in (**A, B**) Cascais Canyon and (**C, D**) Setúbal Canyon.

Hemipelagic sedimentation rate profiles for the post-6.4 ka interval in Cascais and Setúbal canyons are relatively smooth (Fig. 6.14), although values vary from 3.5 to 66.5 cm/Cal ka between different cores (Table 6.2). These rates increase to between 8.0 and 82.2 cm/Cal ka for the combined hemipelagic-turbiditic sequence, especially for cores CD56822 and CD56825 as they have the highest number of turbidites in this interval. This is also reflected in the turbidite frequencies (Table 6.4), which vary from 1 event per 6.4 ka in core CD56843 to at least 1 event per 0.8 ka in cores CD56822 and CD56825.

Table 6.4. Frequency of turbidite emplacement over different time intervals in the basin and canyon areas

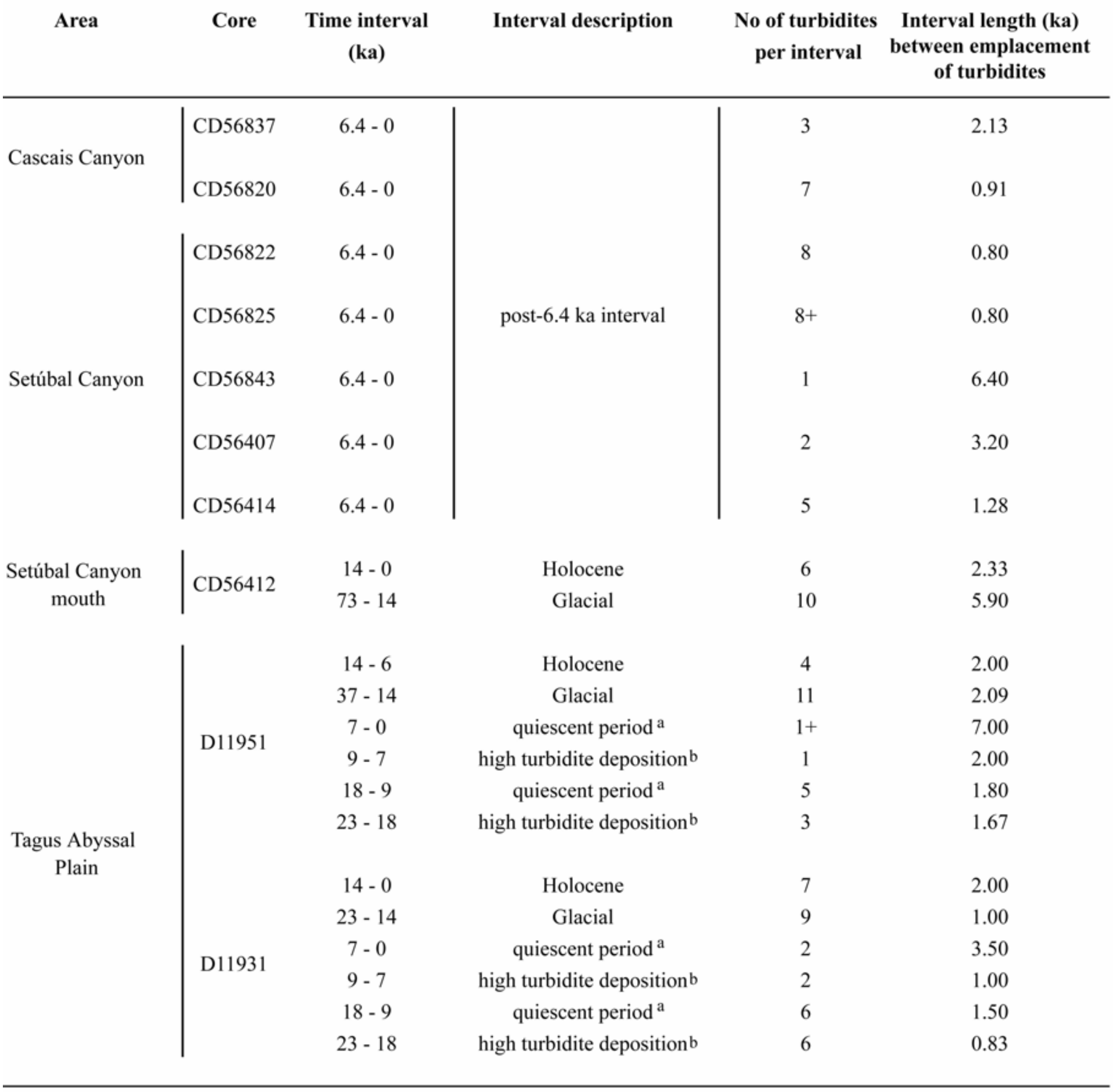

Area	Core	Time interval (ka)	Interval description	No of turbidites per interval	Interval length (ka) between emplacement of turbidites
Cascais Canyon	CD56837	6.4 - 0	post-6.4 ka interval	3	2.13
	CD56820	6.4 - 0		7	0.91
Setúbal Canyon	CD56822	6.4 - 0		8	0.80
	CD56825	6.4 - 0		8+	0.80
	CD56843	6.4 - 0		1	6.40
	CD56407	6.4 - 0		2	3.20
	CD56414	6.4 - 0		5	1.28
Setúbal Canyon mouth	CD56412	14 - 0	Holocene	6	2.33
		73 - 14	Glacial	10	5.90
Tagus Abyssal Plain	D11951	14 - 6	Holocene	4	2.00
		37 - 14	Glacial	11	2.09
		7 - 0	quiescent period [a]	1+	7.00
		9 - 7	high turbidite deposition [b]	1	2.00
		18 - 9	quiescent period [a]	5	1.80
		23 - 18	high turbidite deposition [b]	3	1.67
	D11931	14 - 0	Holocene	7	2.00
		23 - 14	Glacial	9	1.00
		7 - 0	quiescent period [a]	2	3.50
		9 - 7	high turbidite deposition [b]	2	1.00
		18 - 9	quiescent period [a]	6	1.50
		23 - 18	high turbidite deposition [b]	6	0.83

[a, b] Intervals refer to the changes in sedimentation rate shown by Fig. 6.7 (see text).

6.6 Discussion

A major change in sedimentation occurs in both the Tagus Abyssal Plain and the Cascais and Setúbal canyons at ca 6.4 ka.

6.6.1 Pre-6.4 ka interval

In the Tagus Abyssal Plain, this interval is dominated by large gravity flows that are fairly frequent and energetic, producing thick coarse-grained deposits in a distal location. Within this sequence, which goes back to at least ~37 ka (base of core D11951, Fig. 6.7), there are two short-lived periods of increased turbidite deposition, one at ~20-18 ka and another at ~10-7 ka (Fig. 6.6). The first coincides with the 19 ka Deglaciation (Yokoyama et al., 2000; Lambeck et al., 2002) and implies that enhanced turbidity current activity is triggered by changes in sea level and increased fluvial runoff, as is also observed in the Madeira Abyssal Plain (Weaver and Kuijpers, 1983; Weaver et al., 1992). The second period, which occurs during the Holocene highstand (dated after Johnsen et al., 1992), coincides with the African Humid Period that took place ca 9-7 ka in the Mediterranean region (Ritchie et al., 1985; Arz et al., 2003). This event was also characterised by increased fluvial runoff. The Younger Dryas deglaciation of ca 11 ka (Lambeck et al., 2002), although slightly earlier, may also have had a triggering effect. Therefore, either the African Humid Period or a combination of this and the Younger Dryas, is the likely cause of the observed high turbidity current activity between ca 10 and 7 ka.

Despite not being able to correlate unit-by-unit into the canyons, the pre-6.4 ka sediments in the canyons consist of thick sequences of stacked thin turbidites that were clearly emplaced at very frequent intervals. Even without any quantitative age data available for this sequence, the turbidite frequency can be inferred to be much more frequent than in the post-6.4 ka interval, and may even be annual (e.g. Zaragosi et al., 2006; Arzola et al., 2008). Unfortunately, the lack of dating at the base of this sequence in the canyons means that it cannot be easily compared to the abyssal plain sequence.

The mouth of Setúbal Canyon (core CD56412) shows a very different depositional record to the canyons and abyssal plain, probably because of its distal setting that is also out of the direct path of turbidity currents flushing out of the canyon. It therefore only receives the muddy tails of distal turbidity currents that are incorporated into settling hemipelagic material, and very few turbidity current bases. Even so, core CD56412 may also show a change in activity at ca 6.4 ka, shown by a change from closely deposited thin muddy laminae to thick hemipelagite that closely resembles the top of core D11931 in the Tagus Abyssal Plain (Fig. 6.6). This potential E4 boundary is shown with a dashed black line in Figs. 6.6 and 6.11.

6.6.2 Post-6.4 ka interval

The sharp and widespread change in activity (labelled E4) that takes place ca 6.4 ka in both the abyssal plain and the canyons reflects the transition from very frequent turbidity currents to relatively inactive hemipelagic sedimentation. This abrupt drop in activity during a sea level highstand can be explained by a change in the regional climate.

Following the post-glacial transgressive phase that began with the Deglaciation ca 19 ka (Lambeck et al., 2002), an abrupt deceleration in rising sea level began at 7-6.5 ka and continued until ca 5 ka (Vis et al., 2008; Zazo et al., 2008). In west Iberia, the Tagus Valley was progressively filled by fluvial sediments, which were transferred to the shelf and accumulated in a marine prodelta (Vanney and Mougenot, 1981), preventing their export to the canyons and the Tagus Abyssal Plain (Vis et al., 2008). This slow transgressive period from 7-6.5 ka is also associated with a change from relatively wet to more arid conditions in the NW African and Mediterranean regions, including southern Portugal (Kuhlmann et al., 2004; Zühlsdorff et al., 2007; Zazo et al., 2008). It is difficult to separate the effects of the regional aridification event from the impact of sea level rise decline in the sedimentary record; however, either scenario would have resulted in reduced fluvial sediment supply to the canyons and can account for the cessation in gravity flow activity in the canyons and abyssal plain after ca 6.4 ka.

6.6.3 Seismicity

While a climatic control can explain the broad patterns of turbiditic input to the Tagus Abyssal Plain, it does not explain the occurrence of every individual turbidite. Although the western Iberian margin is a passive margin, it is adjacent to the active Azores-Gibraltar fracture zone and frequent large earthquakes (Mw ≥6) take place with a return period of 475 years (Peláez and López Casado, 2002). Lebreiro (1995) thus inferred a seismic control for some turbidites that appear to be randomly superimposed on the broader climatic pattern in the Tagus Abyssal Plain. However, given that 1) it is currently not possible to determine the trigger of a turbidity current from the sediment record, 2) not every earthquake will generate a turbidity current, e.g. if there is insufficient sediment available, and 3) turbidity currents can be generated by other means such as surface runoff or low sea level, it is therefore only possible at this stage to observe that the earthquake and turbidity current frequencies presented here are broadly compatible. It is not, however, possible to determine whether any of the turbidites are seismic in origin.

A ‘worst case scenario’, assuming that every turbidite in the Tagus Abyssal Plain was generated by an earthquake, would give a maximum earthquake return period of 2 ka during the Holocene (Table 6.4). This estimation agrees with other studies in the region (Gràcia et al., 2003; Vizcaino et al., 2006) based on extrapolated sediment and historical records of palaeoearthquakes. Additionally, the most recent turbidite to be emplaced on the Tagus Abyssal Plain has been dated as the deposit from the 1755 AD Lisbon earthquake (Thomson and Weaver, 1994) of magnitude 8.8-9.0 (e.g. Mader, 2001). This may correspond to the uppermost turbidite in the D11931 trigger core, although no definite correlation can be made using the available data.

The few small turbidites that were emplaced during the last 6.4 ka in the canyons may also reflect a seismic trigger on the west Iberian margin. This inference can be made because the turbidites occur during a sea level highstand and appear to be relatively random in timing and spacing (Table 6.4).

The youngest turbidite in the post-6.4 ka interval (E1) is dated at 250-410 Cal a BP (Table 6.3), and could be the deposit from the 1755 AD earthquake (Thomson and Weaver, 1994; Garcia-Orellana et al., 2006). However, there are many large earthquakes (magnitude ≥6) recorded on the west Iberian margin over the last ~100 years (e.g. 1971, 1969, 1964, 1960 and 1909) that have been correlated to turbidites on the shelf (Garcia-Orellana et al., 2006) but that are not recorded in the canyons. Possible explanations for this are that the turbidity currents bypassed the terraces where these cores have been recovered, or they were initiated on the shelf and were too small to enter the canyons, or perhaps they produced deposits in the upper canyon sections (<2700 m WD) that are too steep and narrow for successful piston coring. Alternatively, these earthquakes may not have generated turbidity currents at all. Abrantes et al. (2008) interpret thin layers of ‘anomalous sediment’ on the shelf offshore Lisbon as being the remnant of these recent earthquakes, and this may explain the presence of thin bioturbated muddy laminae towards the tops of most canyon cores and core CD56412 from the mouth of Setúbal Canyon.

6.6.4 Sedimentary processes and sources

A thinning and coarsening trend is observed in turbidites from cores D11951 to D11931 (Fig. 6.6). Lebreiro (1995) interprets this to be due to a change in mineralogy that results in a lateral discontinuity of deposits between both cores. She thus assigns two different sediment sources for the cores: a Tagus River and Cascais Canyon source for core D11931 and a Sado River and Setúbal Canyon source for D11951 (Lebreiro, 1995, p. 87). However, this interpretation lacks absolute age control, which in this study has confirmed correlation of these turbidites between cores, and there is no evidence for significant mineralogical compartmentalization along the Lisbon margin (Dias and Nittrouer, 1984; Lebreiro et al., 1997). Hence the sediment from both rivers entering the two canyons is the same.

The data presented here thus infer this thinning and coarsening trend to be a result of core D11931 being 15 m shallower than D11951 (Table 6.1). Since turbidity currents are primarily influenced by momentum, slight changes in gradient will affect their flow and even a small difference in height has been shown to be significant (e.g. in the Madeira Abyssal Plain, Weaver, 2003). Therefore the mud fraction must be ponding in the lower ground, i.e. where core D11951 is located.

In terms of the provenance of turbidites in the abyssal plain, a good level of lateral correlatability between cores D11951 and D11931, which are ~60 km apart, implies that the turbidity currents must have been relatively large and travelled a long distance to be deposited in both cores. Thus, they are more likely to have been large turbidity currents that were initiated in a canyon or on the slope, rather than small failures from the adjacent abyssal plain margins or seamounts (such as Tore Seamount, 39º 02’ N, 12º 35’ W, or the Gorringe Bank, 36º 15’ N, 11º 10’ W).

In the canyons, sedimentary processes are a direct reflection of the geomorphology and also of the turbidity currents’ properties. For instance, the canyon cores have varying numbers of small turbidites in the post-6.4 ka sequence, most of which are only composed of the muddy fraction of turbidity currents (Figs. 6.9, 6.10). This suggests that the steepness of these areas prevents the deposition of the coarse fraction on the terraces as turbidity currents flow down the canyon, and that only the muddy suspension cloud is large or thick enough to deposit on the terraces where these cores were collected. Alternatively, the coarse fraction may be deposited further upslope nearer to the canyon head and only the muddy fraction is transported down through the upper and middle canyon sections. The spatial distribution of the turbidites also correlates directly with their magnitude, e.g. turbidites E1-E3 are not present in the abyssal plain cores because these flows were probably too small to reach this distal setting.

The origin of the turbidity currents in the canyons must be the shelf or the canyon margins. The available data, however, cannot separate those flows that travelled through the canyons from those that might have resulted from small and localised margin failures, as is suggested by the side-scan sonar evidence in the upper canyon sections (Fig. 6.2) and by other studies (Arzola et al., 2008; Lastras et al., 2009).

6.7 Conclusions

Radiocarbon dating of planktonic foraminifera has enabled a correlation between the sedimentary activity of the Cascais and Setúbal canyons and the Tagus Abyssal Plain on the west Iberian margin. Dating and correlation of individual beds and sequences of deposits has led to the conclusion that eustatic sea-level change is the dominant control on turbidite sedimentation in the basin while smaller-scale regional climatic events control sedimentation in the canyons, with seismicity leaving a secondary imprint throughout. The main findings are:

- Sedimentary activity in the canyons and the abyssal plain is dominated by turbidity current and hemipelagic sedimentation.
- Pre-6.4 ka, sedimentation in the Tagus Abyssal Plain is controlled primarily by climate. Higher turbidite deposition is recorded during the last glacial, especially during the 19 ka Deglaciation, than in the Holocene. Apart from these global changes in sea level, a short period of enhanced turbidite deposition at ca 10-7 ka is interpreted to be due to the African Humid Period, a regional climate event. A secondary underlying control on abyssal plain sedimentation is inferred to be the regional seismicity.
- In the Cascais and Setúbal canyons, the pre-6.4 ka sedimentation is inferred to be a result of fluvial runoff controlled by changes in climate and sea level that may be global and/or regional.
- An abrupt and widespread cessation in turbidity current activity took place at ca 6.4 ka throughout the canyons and abyssal plain. This is attributed to the possibly combined effects of a regional aridification event ca 7-5 ka throughout NW Africa and SW Europe, and of a rapid decline in sea level rise ca 7 ka.
- The post-6.4 ka sedimentation in both the abyssal plain and canyons is dominated by hemipelagite with some small turbidity currents. These are inferred to be the products of earthquakes generated along the margin, potentially including the 1755 AD Lisbon earthquake.
- The detrital sediment in the canyons is likely to be sourced at the shelf or shallower than 3000 m on the canyon walls, either from fluvial/longshore processes or from seismic-induced failure. Larger flows reach the Tagus Abyssal Plain and deposit there, with subtle basin topography controlling the areal distribution of sediment.

This work has implications for our understanding of the processes of turbidity current transport and deposition between continental slope canyons and the abyssal plain, especially with regards to the frequency and timing of turbidite emplacement since the last glacial. The finding that regional climatic events on the west Iberian margin may have a more important control on sedimentation than perhaps previously thought, can be applied globally to other canyon and abyssal plain systems.

CHAPTER 7

Discussion and conclusions

7.1 The submarine canyons of the west Iberian margin

This thesis has shown that the three main canyon systems of the central west Iberian margin – Nazaré, Cascais and Setúbal-Lisbon – share many similarities. They are comparable in size, geomorphology and age, and are all located on a 140 km-long stretch of the same continental margin where they share the same climatic and oceanographic regime. The only physical difference of any significance between these canyons is the fluvial supply that is adjacent to the heads of Setúbal-Lisbon and Cascais canyons but not to Nazaré Canyon. This single factor, however, appears to have important implications for the formation of these canyons and the sedimentary processes taking place in them, both over space and time.

7.1.1 Canyon formation

The proximity of the Tagus and Sado River mouths to the heads of Setúbal-Lisbon and Cascais canyons suggests that formation of these canyons was initiated through erosion of the continental slope by fluvial-sourced sediment flows. Pre-existing faults along the present canyon axes (Pinheiro et al., 1996; Alves et al., 2003, 2006) provide tectonic weaknesses on the slope into which gravity flows could erode and widen, leading to retrogressive failure and both headward erosion across the shelf and downslope erosion of the slope (Pratson and Coakley, 1996). Although these canyon heads are at present near the shelf break and several tens of km away from the river mouths, coastline reconstructions (e.g. Dias et al., 2000) suggest that these rivers led either directly into, or were within a few km of, the canyon heads during the last glacial.

Like Setúbal-Lisbon and Cascais canyons, Nazaré Canyon also has a fault running down its axis (Nazaré Fault, Alves et al., 2006, Fig. 2.1) and its head cuts across almost the entire width of the continental shelf. Tectonic activity during the late Oligocene-early Miocene could have led to slope failure along the fault, down-cutting of the continental slope and initial incision of a ‘proto-canyon’ (e.g. Alves et al., 2003). However, the absence of a significant river debouching anywhere near the canyon head, only a small river (the Lis) whose annual discharge is about 25 times lower than that of the Tagus River (Fiúza, 1984), suggests that an alternative supply of sediment was responsible, if not for forming the canyon initially, then for enlargening it into its present size. At present, transport of sediment on the west Iberian margin is dominantly by northward longshore drift from the Tagus Estuary (Vitorino et al., 2002a; Drago et al., 1998), although sources from northern rivers and the adjacent cliffs and beaches have also been suggested (e.g. Oliveira et al., 2007). A Tagus Estuary source of sediment into Nazaré Canyon is indicated by geochemical and lithological evidence presented in this thesis (Chapter 5). This longshore-transported sediment must have been focused down the fault weakness on the continental slope by a force that predates the canyon. The topography of the fault itself on the shelf may have been sufficiently pronounced to be able to trap suspended sediment on the shelf and funnel it down the slope. Alternatively, hydrodynamic processes may have led to funnelling of sediment along the fault. Significant hydrodynamic processes, such as seasonal downwelling, occur along the west Iberian margin, both near Nazaré Canyon (e.g. Oliveira et al., 2007) and on the open slope away from canyon influences (e.g. on the Galician margin, Diz et al., 2006). If pre-canyon hydrodynamic processes were indeed responsible for funnelling suspended sediment from the shelf down the fault weakness, then this would imply that the formation of Nazaré Canyon took place during a sea level highstand when the shelf was flooded. Nazaré Canyon therefore suggests that a river is not always a necessary prerequisite for canyon formation on continental slopes, and therefore that perhaps neither is a sea level lowstand.

7.1.2 Sedimentary activity

The distribution of sediment is consistent across the Portuguese canyons. The thalweg is dominantly coarse-grained with a thin or absent hemipelagic veneer, while the terraces are draped with fine-grained sediments (Chapters 4 and 6). This depositional heterogeneity is due to the flow processes of vertically thick turbidity currents flowing down a channelised environment, with the coarse-grained traction layer being confined within the thalweg and the fine-grained, muddy suspension cloud reaching the high terraces above the thalweg. This pattern of gravity flow deposition is controlled by canyon morphology and sediment character (composition and grain size), both of which are largely the same in the canyons of the west Iberian margin.

The down-slope and temporal sedimentary activity in the Portuguese canyons, however, is very different. During the last sea level lowstand, small turbidity currents deposited in the middle-lower sections of Setúbal Canyon while larger flows flushed through the entire canyon and deposited mainly in the Tagus Abyssal Plain (Chapters 4 and 6). Evidence of erosion by gravity flows at the mouth of Cascais Canyon (see Fig. 7D in Lastras et al., 2009, Appendix A3) also implies canyon-flushing events during the last glacial in this canyon. This implies that the canyon heads were connected to the mouths of the Tagus and Sado Rivers during the last sea level lowstand, and received high volumes of fluvial sediment that generated many small and proximal turbidity canyons as well as some large canyon-flushing turbidity currents. However, contrary to what classic models of continental slope activity suggest (e.g. Weaver and Kuijpers, 1983), turbidite sedimentation in Setúbal and Cascais canyons remained active during the early Holocene transgression, ceasing only ca 6.4 ka due to a regional aridification event (e.g. Kuhlmann et al., 2004; Zühlsdorff et al., 2007; Zazo et al., 2008; Chapter 6). This suggests that sedimentation in these river-fed canyons is controlled more by regional climate controls than by global eustatic climate controls. The Setúbal and Cascais canyons have remained largely abandoned and have accumulated only hemipelagite since 6.4 ka, experiencing only some small-scale sediment flows that were possibly driven by fluvial or tidal activity, or related to mass wasting by earthquakes such as the 1755 AD Lisbon earthquake.

Nazaré Canyon has a sediment depocentre in its middle section that has been active for the last 1000 years at least and has very high sediment accumulation rates (Chapter 5, Fig. 7.1), indicating that the middle section (and perhaps also the upper section) is an intermediate reservoir between source and deep-sea sink. This depocentre is controlled by the hydrodynamic processes that take place around the canyon head (Chapter 5), which is why it is still actively accumulating and resuspending sediment during the present sea level highstand. The turbidity currents are generated by hydrodynamic processes focusing longshore-transported suspended sediment into the canyon head, and are thus low density and low energy sediment flows that deposit in the mid-canyon. Unfortunately, the lack of dated cores throughout the lower canyon prevents any further comparisons beyond 1000 years BP to be made between this canyon and the Setúbal-Lisbon and Cascais canyons.

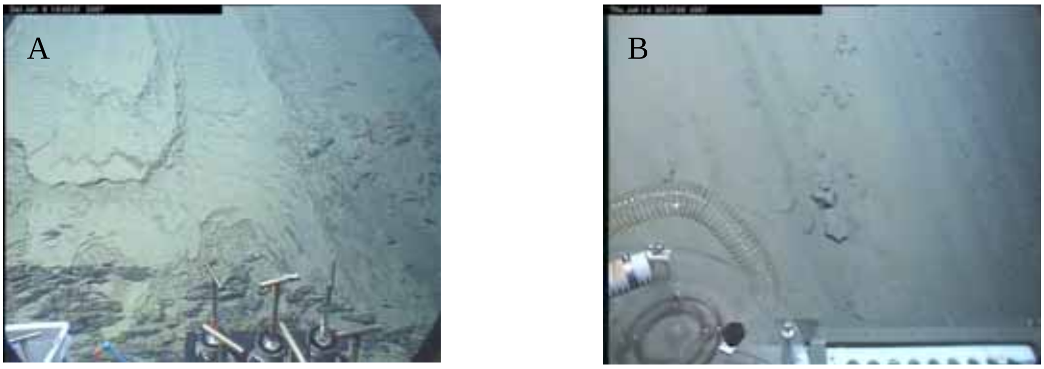

Fig. 7.1. (**A, B**) Bottom photographs of thick muddy deposits on thalweg walls of Nazaré Canyon (3400 m WD), taken with the ROV *Isis*. Note the absence of benthic fauna. This area is also characterised by particulate transport through the water, known as marine 'snow'.

The uppermost one and two turbidites in the Tagus (TAP) and Horseshoe abyssal plains (HAP), respectively, have been dated as corresponding to the 1755 AD Great Lisbon earthquake (Thomson and Weaver, 1994). Chapter 6 presents radiocarbon evidence for two turbidites in cores from the middle and lower sections of Setúbal and Cascais canyons, either of which may be the deposit from the event, but no trace of this deposit is observed elsewhere in the canyons. Additionally, the two TAP cores presented in Chapter 6 do not show any evidence for this turbidite, despite having complete core tops. This raises questions about the character and path of this turbidity current down the continental margin. The dated turbidites both in the canyons (Chapter 6) and in the TAP and HAP (Thomson and Weaver, 1994) indicate that at least one large turbidity current was generated by the earthquake and that it was large and powerful enough to reach the abyssal plains. A plausible scenario is that the flow was very large and subsequently bypassed the Setúbal and Cascais canyons almost entirely, depositing only some fine-grained sediment on high terraces of the mid-lower canyon. The large erosive grooves and boulders at the Cascais Canyon mouth (Lastras et al., 2009) may well be related to this event, but further work dating these features is required before a conclusion can be made. An alternative scenario is that the earthquake did not cause any significant turbidity current in the canyons at all, and that the deposits in the TAP and HAP may be the products of distal failures from abyssal topographic features, e.g. the Gorringe Bank.

7.2 Comparisons with other canyon systems worldwide

The canyons of the west Iberian margin have shown that the differences in their sedimentary activity are ultimately controlled by the source and supply of sediment. These factors are now assessed in relation to canyon systems worldwide to determine whether they also control sedimentation in different environments and conditions.

7.2.1 Canyon formation

The generally accepted model of canyon formation is that during a sea level regression, when the continental shelf is exposed, rivers flow all the way to the shelf edge, eroding it and discharging large amounts of sediment in the form of gravity flows down the continental slope (Weaver and Kuijpers, 1983). Gullies form and undergo headward erosion and retrogressive failure (Pratson and Coakley, 1996) until developing into a canyon whose head cuts across the width of the shelf and connects to the river supply. There are many examples of canyons that were connected to a river during the last sea level lowstand, including Zaire Canyon (Heezen et al., 1964), Sepik Canyon in Papua New Guinea (Kineke et al., 2000; Walsh and Nittrouer, 2003), Monterey Canyon (Greene, 1990), Var Canyon (Pautot, 1981), Hueneme Canyon (Piper et al., 1999b; Normark et al., 2006), and Setúbal-Lisbon and Cascais canyons (Dias et al., 2000). Most canyons will no longer be connected to the river during a sea level highstand when the shelf is flooded, in which case they may become abandoned with only episodic sedimentary flow activity.

There are not many studied examples, besides Nazaré Canyon, of canyons that show no evidence of a river ever having led into their head, not even during sea level lowstands. Dume Canyon, offshore California, is one. It receives sediment from longshore drift (Piper et al., 1999b) and has active hydrodynamic processes that may be inferred to be responsible for its formation (as is suggested for Nazaré Canyon).

7.2.2 Sedimentary activity

During the sea level lowstand of the last glacial, all river-fed canyons were likely to have canyon-flushing turbidity currents like the Setúbal and Cascais canyons, e.g.

Monterey Canyon (Greene, 1990) and Hueneme Canyon (Piper et al., 1999b). Canyons with a very narrow or absent shelf may still be connected to a river source at present and may therefore also experience large canyon-flushing events. Examples that are used as analogues for canyon activity during sea level lowstands are Zaire/Congo Canyon (Heezen et al., 1964; Babonneau et al., 2002; Khripounoff et al., 2003), Var Canyon (Klaucke et al., 2000) and Eel Canyon (Mullenbach et al., 2004). These examples show that canyon activity is not always restricted to sea level lowstands or regressions, and that sediment transport through canyons during the Holocene is relatively widespread.

Resuspended sediment depocentres such as the one in Nazaré Canyon are another form of sedimentary process in canyons. They only develop in canyons that have a sufficient supply of sediment (fluvial or from longshore drift), steep slopes, a V-shaped head and hydrodynamic processes (e.g. internal tides or downwelling) that focus the sediment into the canyon head (e.g. Cacchione and Southard, 1974; Cacchione et al., 2002). Thus, Guadiaro Canyon off the south coast of Spain (Puig et al., 2004b), Baltimore Canyon off the east coast of the USA (Gardner, 1989), Capbreton Canyon in the Bay of Biscay (Cremer et al., 1999; Gaudin et al., 2006) and the canyons off the wide shelf of the Celtic margin (Reynaud et al., 1999; Huthnance et al., 2001; Wollast and Chou, 2001) all satisfy the necessary conditions for resuspension in their upper section and head. Canyons with high sediment accumulation rates but which have wide and gently sloping U-shaped heads do not develop resuspension depocentres because the sediment cannot be focused down into the canyon at a sufficient rate (e.g. Gardner, 1989; Cacchione et al., 2002). Evidence for sediment resuspension being active at present in the above canyons indicates that hydrodynamic-generated sedimentation can occur during sea level highstands and not only during lowstands. The main control is the topography and morphology of the canyon head, and the hydrodynamic regime.

Hydrodynamic processes are also an important control of sedimentary activity in canyons that are currently cut off from a river due to a flooded shelf, and can generate canyon-flushing sedimentary events without a direct fluvial supply. Monterey Canyon currently receives very high volumes of suspended sediment through a longshore transport cell at its head (Best and Griggs, 1991), and experiences very active flushing events that prevent infilling of the canyon head (Paull et al., 2003, 2005). Eel Canyon experiences high internal wave activity during storms that liquefy accumulated sediment at the head and periodically lead to transport of large and erosive gravity flows down the canyon (Puig et al., 2003, 2004a). Dense shelf water cascading processes, produced by the combination of a thermohaline along-slope current, wind-driven coastal circulation and seasonal cooling winds from land, generate powerful canyon-flushing flows in Cap Creus Canyon, Gulf of Lions (Canals et al., 2006; Palanques et al., 2008).

To summarise, this work is one of the most comprehensive studies on canyons yet, combining data on the geology, sedimentology, geochemistry and oceanography of the central Portuguese canyons in order to characterise the sedimentary processes taking place in them. The central Portuguese canyons were chosen to represent a typical river-fed canyon (Setúbal) and a typical longshore drift-fed canyon (Nazaré) that could be compared with each other. However, this study highlights the complexity in canyon systems and the difficulty in categorising 'typical' canyon types due to the large number of variables and the complex interplay of different controls, from canyon morphology to shelf width to hydrodynamic processes on the shelf and slope.

The results suggest that the classic view that sedimentation on continental slopes is only active during sea level regressions (Weaver and Kuijpers, 1983) may be outdated, as there is widespread evidence for gravity flow and other forms of sedimentary activity in canyons during the present sea level highstand that are controlled by the regional climate, sediment supply and hydrodynamic processes. Another classic view that large canyons are formed from large rivers is also shown to not necessarily be the case, as hydrodynamic processes and the presence of fault weaknesses may be suitable candidates for canyon formation without the presence of a river at its head. The results suggest that some proposed models for river-fed canyon formation during sea level lowstands may need to be readdressed.

7.3 Implications for studies on benthic ecosystems in canyons

This work forms part of the EU-funded integrated research project HERMES (Hotspot Ecosystem Research on the Margins of European Seas; Weaver et al., 2004). This project aims to gain new insights into the biodiversity, structure, function and dynamics of ecosystems in ‘hotspot’ areas along Europe’s oceanic margins, including submarine canyons. The above findings have contributed to furthering our understanding of the sedimentary processes and activity in the central Portuguese submarine canyons, which in turn has helped to explain the abundance, biodiversity and distribution of the biological communities within them.

Biological studies have shown that benthic megafauna have the highest abundance but lowest biodiversity in Nazaré Canyon, and the lowest abundance but highest biodiversity in Setúbal-Lisbon Canyon (Pattenden, submitted). A higher abundance of benthic foraminifera is also documented in the upper Nazaré Canyon (Koho et al., 2007). These observations are due to canyon activity. Enhanced current velocities and suspended sediment concentrations in the upper Nazaré Canyon also carry a higher concentration of organic particulates down the canyon, resulting in a higher abundance of organisms. However, the enhanced turbidity will overwhelm the enhanced organic matter, meaning that most species will be choked by the sediment particles and only a small number of species (i.e. suspension feeders and opportunistic species) will be able to harness the organic particles and thrive. A lower biodiversity is thus documented in the more turbid Nazaré Canyon (Pattenden, submitted).

The distribution of benthic faunal communities within canyons has been linked to gravity flow activity, topography and stratum type (Koho et al., 2007; Pattenden, submitted). Sessile suspension feeders are found attached to the bare and rocky thalweg walls where they can feed on organic particulates that are transported down the canyon, although these organisms are most abundant in the upper parts of the walls that are relatively undisturbed compared to the parts closest to the thalweg. Muddy terraces are relatively quiescent and host a large number of infaunal megafauna and microfauna, while the sandy thalweg itself is too disturbed and the substrate too unstable to host any organisms. The quiescent and rocky canyon flanks away from the thalweg have only non-suspension feeders.

The observations made using the piston cores, sidescan sonar data and ROV photographs in this thesis show that canyon morphology and sedimentary processes are two of the main controlling factors of benthic faunal abundance, biodiversity and distribution in canyons. The implications of these findings are a better understanding of ecosystem functioning and structure in submarine canyons in relation to sedimentary processes.

7.4 Further work

This thesis has attempted to fulfil the objectives stated in the introduction and, in so doing, contribute to the wider knowledge and understanding of submarine canyon systems. It recommends that the following areas be the subjects of further research:

1. Constraining the supply of sediment into the central Portuguese canyons and the residence time of longshore-transported sediment on the shelf and at the head of Nazaré Canyon.

2. A detailed canyon-to-abyssal plain event correlation needs to be carried out for Nazaré Canyon and the Iberian Abyssal Plain, from which no cores were available for this study. However, a number of cores have since been collected during cruise JC27 (August 2008). Such an event correlation can be compared with the one through Setúbal and Cascais canyons and the Tagus Abyssal Plain (Chapter 6) to characterise down-canyon sedimentary activity over time in both canyon systems.

3. No cores were collected from Lisbon Canyon because of its steep gradient and narrow morphology, but with rapidly improving ship positioning technology and core collection techniques, this should be possible in the near future. Cores from Lisbon Canyon will help to understand how sediment is supplied into Setúbal Canyon from the Tagus Estuary.

REFERENCES CITED

Abrantes, F., Alt-Epping, U., Lebreiro, S., Voelker, A., Schneider, R.R. (2008). Sedimentological record of tsunamis on shallow-shelf areas: The case of the 1969 AD and 1755 AD tsunamis on the Portuguese Shelf off Lisbon. *Marine Geology* **249**, 283-293.

Abrantes, F., Lebreiro, S., Rodrigues, T., Gil, I., Bartels-Jónsdóttir, H.B., Oliveira, P., Kissel, C., Grimalt, J.O. (2005). Shallow-marine sediment cores record climate variability and earthquake activity off Lisbon (Portugal) for the last 2000 years. *Quaternary Science Reviews* **24**, 2477-2494.

Abreu, L., Shackleton, N.J., Schönfeld, J., Hall, M., Chapman, M. (2003). Millennial-scale oceanic climate variability off the Western Iberian margin during the last two glacial periods. *Marine Geology* **196**, 1-20.

Abreu, V., Sullivan, M., Pirmez, C., Mohrig, D. (2003). Lateral accretion packages (LAPs): an important reservoir element in deep water sinuous channels. *Marine and Petroleum Geology* **20**, 631-648.

Alonso, J., García, M.J., Díaz del Río, G. (1993). Medidas de corrientes en un punto de la plataforma gallega. Efecto de la marea y el viento a distintas profundidades. *Boletín del Instituto Español de Oceanografía* **9**, 323-342.

Alt-Epping, U., Mil-Homens, M., Hebbeln, D., Abrantes, F., Schneider, R.R. (2007). Provenance of organic matter and nutrient conditions on a river- and upwelling-influenced shelf: a case study from the Portuguese Margin. *Marine Geology* **243**, 169-179.

Alves, T.M., Gawthorpe, R.L., Hunt, D.W., Monteiro, J.H. (2003). Cenozoic tectono-sedimentary evolution of the western Iberian margin. *Marine Geology* **195**, 75-108.

Alves, T.M., Moita, C., Sandnes, F., Cunha, T., Monteiro, J.H., Pinheiro, L.M. (2006). Mesozoic-Cenozoic evolution of North Atlantic continental-slope basins: the Peniche basin, western Iberian margin. *American Association of Petroleum Geologists Bulletin* **90**, 31-60.

Amy, L.A., Talling, P.J., Peakall, J., Wynn, R.B., Arzola Thynne, R.G. (2005). Bed geometry used to test recognition criteria of turbidites and (sandy) debrites. *Sedimentary Geology* **179**, 163-174.

Andeweg, B. (2002). Cenozoic tectonic evolution of the Iberian Peninsula: causes and effects of changing stress fields. Ph.D. Thesis, Netherlands Research School of Sedimentary Geology, Vrije Universiteit Amsterdam, Amsterdam, 178 pp.

Appleby, P.G., Oldfield, F. (1978). The calculation of lead-210 dates assuming a constant rate of supply of unsupported ^{210}Pb to the sediment. *Catena* **5**, 1-8.

Arz, H., Lamy, F., Pätzold, J., Müller, P.J., Prins, M.A. (2003). Mediterranean moisture source for an early-Holocene humid period in the northern Red Sea. *Science* **300**, 118-122.

Arzola, R.G., Wynn, R.B., Lastras, G., Masson, D.G., Weaver, P.P.E. (2008). Sedimentary features and processes in the Nazaré and Setúbal submarine canyons, west Iberian margin. *Marine Geology* **250**, 64-88.

Babonneau, N., Savoye, B., Cremer, M., Klein, B. (2002). Morphology and architecture of the present canyon and channel system of the Zaire deep-sea fan. *Marine and Petroleum Geology* **19**, 445-467.

Bagnold, R.A. (1962). Autosuspension of suspended sediment. *Proceedings of the Royal Society of London* **265**, 315-319.

Bartels-Jónsdóttir, H.B., Knudsen, K.L., Abrantes, F., Lebreiro, S., Eiríksson, J. (2006). Climate variability during the last 2000 years in the Tagus Prodelta, western Iberian Margin: Benthic foraminifera and stable isotopes. *Marine Micropaleontology* **56**, 83-103.

Batchelder, R.B. (1967). Spatial and temporal patterns of fire in the tropical world. *Proceedings of the Tall Timbers Fire Ecology Conference*. Tallahassee, Florida, USA, 171-208.

Baztan, J., Berné, S., Olivet, J.L., Rabineau, M., Aslanian, D., Gaudin, M., Réhault, J.P., Canals, M. (2005). Axial incision: the key to understand submarine canyon evolution (in the western Gulf of Lion). *Marine and Petroleum Geology* **22**, 805-826.

Berner, R.A. (1982). Burial of organic carbon and pyrite sulphur in the modern ocean: its geological and environmental significance. *American Journal of Science* **282**, 451-473.

Best, T.C., Griggs, G.B. (1991). A sediment budget for the Santa Cruz littoral cell, California. In: Osbourne, R.H. (Ed.). From shoreline to abyss: contributions in marine geology in honor of Francis Parker Shepard. *SEPM Special Publication* **46**, 35-50.

Black, M.P., Mooney, S.D., Martin, H.A. (2006). A >43,000-year vegetation and fire history from Lake Baraba, New South Wales, Australia. *Quaternary Science Reviews* **25**, 3003-3016.

Bouma, A.H. (1962). Sedimentology of some flysch deposits: a graphic approach to facies interpretation. Ph.D. Thesis, Netherlands Research School of Sedimentary Geology, Vrije Universiteit Amsterdam, 168 pp.

Bouma, A.H., Normark, W.R., Barnes, N.E. (1985). Submarine fans and related turbidite systems. Springer-Verlag, New York, 351 pp.

Buscail, R., Ambatsian, P., Monaco, A., Bernat, M. (1997). ^{210}Pb, manganese and carbon: indicators of focusing processes on the northwestern Mediterranean continental margin. *Marine Geology* **137**, 271-286.

Cacchione, D.A., Drake, D.E. (1986). Nepheloid layers and internal waves over continental shelves and slopes. *Geo-Marine Letters* **6**, 147-152.

Cacchione, D.A., Pratson, L.F., Ogston, A.S. (2002). The shaping of continental slopes by internal tides. *Science* **269**, 724-727.

Cacchione, D.A., Southard, J.B. (1974). Incipient sediment movement by shoaling internal gravity waves. *Journal of Geophysical Research* **79**, 2237-2242.

Canals, M., Lastras, G., Urgeles, R., Casamor, J.L., Mienert, J., Cattaneo, A., De Batist, M., Haflidason, H., Imbo, Y., Laberg, J.S., Locat, J., Long, D., Longva, O., Masson, D.G., Sultan, N., Trincardi, F., Bryn, P. (2004). Slope failure dynamics and impacts from seafloor and shallow sub-seafloor geophysical data: case studies from the COSTA project. *Marine Geology* **213**, 9-72.

Canals, M., Puig, P., de Madron, X.D., Heussner, S., Palanques, A., Fabres, J. (2006). Flushing submarine canyons. *Nature* **444**, 354-357.

Carcaillet, C., Almquist, H., Asnong, H., Bradshaw, R.H.W., Carrión, J.S., Gaillard, M.-J., Gajewski, K., Haas, J.N., Haberle, S.G., Hadorn, P., Müller, S.D., Richard, P.J.H., Richoz, I., Rösch, M., Sánchez-Goñi, M.F., von Stedingk, H., Stevenson, A.C., Talon, B., Tardy, C., Tinner, W., Tryterud, E., Wick, L., Willis, K.J. (2002). Holocene biomass burning and global dynamics of the carbon cycle. *Chemosphere* **49**, 845-863.

Carrión-García, J.S. (2002). Patterns and processes of Late Quaternary environmental change in a montane region of southwestern Europe. *Quaternary Science Reviews* **21**, 2047-2066.

Clark, J.D., Gardiner, A.R. (2000). Outcrop analogues for deep-water channel and levee genetic units from the Grés d'Annot turbidite systems, SE France. Global deep-water reservoirs: Gulf Coast Section. *SEPM Foundation 20th Annual Bob F Perkins Research Conference*, 175-190.

Clark, J.D., Pickering, K.T. (1996). Architectural elements and growth patterns of submarine channels: applications to hydrocarbon exploration. *American Association of Petroleum Geologists Bulletin* **80**, 194-221.

Cochonat, P., Dodd, L., Bourillet, J.-F., Savoye, B. (1993). Geotechnical characteristics and instability of submarine slope sediments, the Nice slope (NW Mediterranean Sea). *Marine Georesources and Geotechnology* **11**, 131-151.

Coppier, G., Mougenot, D. (1982). Seismic stratigraphy and geological evolution of the Neogene and Quaternary from the Portuguese continental shelf south of Lisbon. *Bulletin de la Societé Géologique de France* **24**, 421-431.

Cremer, M., Weber, O., Jouanneau, J.-M. (1999). Sedimentology of box cores from the Cap-Ferret Canyon area (Bay of Biscay). *Deep-Sea Research* **46**, 2221-2247.

Cronin, B.T. (1995). Structurally-controlled deep sea channel courses: example from the Miocene of southeast Spain and the Alboran sea, southwest Mediterranean. In: Hartley, A.J., Prosser, D.J. (Eds.). Characterisation of deep marine clastic systems. *Special Publication of the Geological Society, London* **94**, 115-135.

Cronin, B.T., Hurst, A., Celik, H., Turkman, I. (2000). Superb exposures of a channel levee and overbank complex in an ancient deep-water slope environment. *Sedimentary Geology* **132**, 205-216.

Cronin, B.T., Kidd, R.B. (1998). Heterogeneity and lithotype distribution in ancient deep-sea canyons: Point Lobos deep-sea canyon as a reservoir analogue. *Sedimentary Geology* **115**, 315-349.

Croudace, I.W., Rindby, A., Rothwell, R.G. (2006). ITRAX: description and evaluation of a new multi-function X-ray core scanner. In: Rothwell, R.G. (Ed.). New techniques in sediment core analysis. *Special Publication of the Geological Society London* **267**, 51-63.

Daly, R.A. (1936). Origin of submarine 'canyons'. *American Journal of Science* **5**, 401-420.

Daniau, A.-L., Sánchez-Goñi, M.F., Beaufort, L., Laggoun-Défarge, F., Loutre, M.-F., Duprat, J. (2007). Dansgaard-Oeschger climatic variability revealed by fire emissions in southwestern Iberia. *Quaternary Science Reviews* **26**, 1369-1383.

de Madron, X.D., Zervakis, V., Theocharis, A., Georgopoulos, D. (2005). Comments to ‘Cascades of dense water around the world ocean’. *Progress in Oceanography* **64**, 83-90.

de Stigter, H., Boer, W., de Jesús Mendes, P.A., Jesús, C.C., Thomsen, L., van den Berg, G.D., van Weering, T.C.E. (2007). Recent sediment transport and deposition in Nazaré Canyon, Portuguese continental margin. *Marine Geology* **246**, 144-164.

Dias, J.M.A., Boski, T., Rodrigues, A., Magalhaães, F. (2000). Coast line evolution in Portugal since the Last Glacial Maximum until present - a synthesis. *Marine Geology* **170**, 177-186.

Dias, J.M.A., Jouanneau, J.M., Gonzalez, R., Araújo, M.F., Drago, T., García, C., Oliveira, A., Rodrigues, A., Vitorino, J., Weber, O. (2002). Present day sedimentary processes on the northern Iberian shelf. *Progress in Oceanography* **52**, 249-259.

Dias, J.M.A., Nittrouer, C.A. (1984). Continental-shelf sediments of northern Portugal. *Continental Shelf Research* **3**, 147-165.

Diz, P., Frances, G., Roson, G. (2006). Effects of contrasting upwelling-downwelling on benthic foraminiferal distribution in the Ria de Vigo (NW Spain). *Journal of Marine Systems* **60**, 1-18.

Dott Jr., R.H. (1963). Dynamics of subaqueous gravity depositional processes. *American Association of Petroleum Geologists Bulletin* **47**, 104-128.

Drago, T., Oliveira, A., Magelhaes, F., Cascalho, J., Jouanneau, J.-M., Vitorino, J. (1998). Some evidences of northward fine sediment transport in the northern Portuguese continental shelf. *Oceanologica Acta* **21**, 223-231.

Drexler, T.M., Nittrouer, C.A., Mullenbach, B.L. (2006). Impact of local morphology on sedimentation in a submarine canyon, ROV studies in Eel Canyon, Northern California, U.S.A. *Journal of Sedimentary Research* **76**, 839-853.

Elliott, T. (2000). Megaflute erosion surfaces and the initiation of turbidite channels. *Geology* **28**, 119-122.

Epping, E., van der Zee, C., Soetaert, K., Helder, W. (2002). On the oxidation and burial of organic carbon in sediments of the Iberian margin and Nazaré Canyon (NE Atlantic). *Progress in Oceanography* **52**, 399-431.

Fairbanks, R.G., Mortlock, R.A., Chiu, T.C., Cao, L., Kaplan, A., Guilderson, T.P., Fairbanks, T.W., Bloom, A.L., Grootes, P.M., Nadeau, M.J. (2005).

Radiocarbon calibration curve spanning 0 to 50,000 years BP based on paired Th-230/U-234/U-238 and C-14 dates on pristine corals. *Quaternary Science Reviews* **24**, 1781-1796.

Farre, J.A., McGregor, B.A., Ryan, W.B.F., Robb, J.M. (1983). Breaching the shelfbreak: passage from youthful to mature phase in submarine canyon evolution. In: Stanley, D.J., Moore, G.T. (Eds.). The shelfbreak: critical interface on continental margins. *SEPM Special Publication* **33**, 25-39.

Faugères, J.-C., Gonthier, E., Mulder, T., Kenyon, N., Cirac, P., Griboulard, R., Berné, S., Lesuavé, R. (2002). Multi-process generated sediment waves on the Landes Plateau (Bay of Biscay, North Atlantic). *Marine Geology* **182**, 279-302.

Faugères, J.-C., Stow, D.A.V. (1993). Bottom-current-controlled sedimentation – a synthesis of the contourite problem. *Sedimentary Geology* **82**, 287-297.

Ferreira, D.B., 1984. *Le systéme climatique de l'upwelling ouest Ibérique*. Linha de Acção de Geografia Física. Rel. no. 19. Centro de Estudos Geográficos, INIC, Lisboa, 91 pp.

Fildani, A., Normark, W.R., Kostic, S., Parker, G. (2006). Channel formation by flow stripping: large-scale scour features along the Monterey East Channel and their relation to sediment waves. *Sedimentology* **53**, 1265-1287.

Fiúza, A. (1983). Upwelling patterns off Portugal. In: Suess, E., Thiede, J. (Eds.). *Coastal Upwelling: Its Sediment Record. Part A.* Plenum, New York, 85-97.

Fiúza, A.F.G., Macedo, M.E., Guerreiro, M.R. (1982). Climatological space and time variation of the Portuguese coastal upwelling. *Oceanologica Acta* **5**, 31–40.

Fiúza A. (1984). Hidrologia e dinâmica das águas costeiras de Portugal. Ph.D. Thesis, Universidade de Lisboa, 294 pp.

Fraga, F. (1981). Upwelling off the Galician coast, northwest Spain. In: Richards, F.A. (Ed.). *Coastal Upwelling.* American Geophysical Union, Washington D.C., 176–182.

García-Orellana, J., Gràcia, E., Vizcaino, A., Masqué, P., Olid, C., Martínez-Ruiz, F., Piñero, E., Sanchez-Cabeza, J.-A., Dañobeitia, J. (2006). Identifying instrumental and historical earthquake records in the SW Iberian margin using ^{210}Pb turbidite chronology. *Geophysical Research Letters* **33**, art. no. L24601, doi: 10.1029/2006GLO28417.

Gardner, W.D. (1989). Baltimore Canyon as a modern conduit of sediment to the deep sea. *Deep-Sea Research* **36**, 323-358.

Gardner, M.H., Borer, J.M., Melik, J.J., Mavilla, N., Dechesne, M., Wagerle, R.D. (2003). Stratigraphic process-response model for submarine channels and related features from studies of Permian Brushy Canyon outcrops, West Texas. *Marine and Petroleum Geology* **20**, 757-788.

Gaudin, M., Berné, S., Jouanneau, J.-M., Palanques, A., Puig, P., Mulder, T., Cirac, P., Rabineau, M., Imbert, P. (2006). Massive sand beds attributed to deposition by dense water cascades in the Bourcart canyon head, Gulf of Lions (northwestern Mediterranean Sea). *Marine Geology* **234**, 111-128.

Gee, M.J.R., Masson, D.G., Watts, A.B., Allen, P.A. (1999). The Saharan debris flow: an insight into the mechanics of long runout submarine debris flows. *Sedimentology* **46**, 317-335.

Gibbons, W., Moreno, M.T. (2002). *The Geology of Spain.* Geological Society of London, 649 pp.

Gràcia, E., Dañobeitia, J., Vergés, J., PARSIFAL team (2003). Mapping active faults offshore Portugal (36ºN-38ºN): implications for seismic hazard assessment along the southwest Iberian margin. *Geology* **31**, 83-86.

Greene, H.G. (1990). Regional tectonics and structural evolution of the Monterey Bay region, central California. In: Garrison, R.E., Greene, H.G., Hicks, K.R., Weber, G.E., Wright, T.L. (Eds.). Geology and tectonics of the Central California coastal region, San Francisco to Monterey. Pacific Section. *American Association of Petroleum Geologists Volume and Guidebook* GB **67**, 31-56.

Grove, A.T. (2001). The 'Little Ice Age' and its geomorphological consequences in Mediterranean Europe. In: Ogilvie, A.E.J., Jónsson, T. (Eds.). *The iceberg in the mist: northern research in pursuit of a 'Little Ice Age'.* Kluwer Academic Publishers, Dordrecht, 121-135.

Grudd, H., Briffa, K.R., Karlen, W., Bartholin, T., Jones, P.D., Kromer, B. (2002). A 7400-year tree-ring chronology in northern Swedish Lapland: natural climatic variability expressed on annual to millenial timescales. *The Holocene* **12**, 657-666.

Gunn, D.E., Best A.I. (1998). A new automated non-destructive system for high resolution multi-sensor core logging of open sediment cores. *Geo-Marine Letters* **18**, 70-77.

Gutiérrez-Elorza, M., García-Ruiz, J.M., Goy, J.L., Gracia, F.J., Gutiérrez-Santolalla, F., Martí, C., Martín-Serrano, A., Pérez-González, A., Zazo, C. (2002).

Quaternary. In: Gibbons, W., Moreno, M.T. (Eds.). *The Geology of Spain*. Geological Society of London, 335-366.

Hampton, M.A. (1975). Competence of fine-grained debris flows. *Journal of Sedimentary Petrology* **45**, 834-844.

Hampton, M.A., Lee, H.J., Locat, J. (1996). Submarine landslides. *Review of Geophysics* **34**, 33-59.

Harrison, R.J., Feinberg, J.M. (2008). FORCinel: An improved algorithm for calculating first-order reversal curve distributions using locally weighted regression smoothing. *Geochemistry, Geophysics, Geosystems* **9**, art. no. Q05016, doi: 10.1029/2008GC001987.

Hay, A.E. (1987a). Turbidity currents and submarine channel formation in Rupert Inlet, British Columbia I. Surge observations. *Journal of Geophysical Research* **92**, 2875-2882.

Hay, A.E. (1987b). Turbidity currents and submarine channel formation in Rupert Inlet, British Columbia II. The roles of continuous and surge type flow. *Journal of Geophysical Research* **92**, 2883-2900.

Hay, A.E., Burling, R.W., Murray, J.W. (1982). Remote acoustic detection of a turbidity current surge. *Science* **217**, 833-835.

Heezen, B.C., Ewing, M. (1952). Turbidity currents and submarine slumps and the 1929 Grand Banks earthquake. *American Journal of Science* **250**, 849-873.

Heezen, B.C., Ewing, M., Granelli, N.C.L., Menzies, R.J., Schneider, E.D. (1964). Congo submarine canyon. *American Association of Petroleum Geologists Bulletin* **48**, 1126-1149.

Heezen, B.C., Hollister, C.D. (1971). *The face of the deep.* Oxford University Press, New York, 659 pp.

Hemming, S.R. (2004). Heinrich events: massive late Pleistocene detritus layers of the North Atlantic and their global climate imprint. *Reviews of Geophysics* **42**, art. no. RG1005, doi: 8755-1209/04/2003RG000128.

Hill, A.E., Souza, A.J., Jones, K., Simpson, J.H., Shapiro, G.I., McCandliss, R., Wilson, H., Leftley, J. (1998). The Malin cascade in winter 1996. *Journal of Marine Research* **56**, 87-106.

Hillier, S., Marshall, J.E.A. (1988). A rapid technique to make polished thin-sections of sedimentary organic-matter concentrates. *Journal of Sedimentary Petrology* **58**, 754-755.

Hoffmann, E., Jenkner, A. (1932). Die inkohlung und ihre erkennung im mikrobild. *Glückauf* **68**, 81-88.

Holloway, P.E. (1996). A numerical model of internal tides with application to the Australian North West Shelf. *Journal of Physical Oceanography* **26**, 21-37.

Hughen, K.A., Baillie, M.G.L., Bard, E., Beck, J.W., Bertrand, C.J.H., Blackwell, P.G., Buck, C.E., Burr, G.S., Cutler, K.B., Damon, P.E., Edwards, R.L., Fairbanks, R.G., Friedrich, M., Guilderson, T.P., Kromer, B., McCormac, G., Manning, S., Ramsey, C.B., Reimer, P.J., Reimer, R.W., Remmele, S., Southon, J.R., Stuiver, M., Talamo, S., Taylor, F.W., van der Plicht, J., Weyhenmeyer, C.E. (2004). Marine04 marine radiocarbon age calibration, 0-26 cal kyr BP. *Radiocarbon* **46**, 1059-1086.

Hughes Clarke, J.E. (1988). The geological record of the 1929 ‘Grand Banks’ earthquake and its relevance to deep-sea clastic sedimentation. Ph.D. Thesis, Dalhousie University, Halifax, Nova Scotia, 171 pp.

Hughes Clarke, J.E., Shor, A.N., Piper, D.J.W., Mayer, L.A. (1990). Large-scale current-induced erosion and deposition in the path of the 1929 Grand Banks turbidity current. *Sedimentology* **37**, 613-629.

Hühnerbach, V., Masson, D.G. (2004). Landslides in the north Atlantic and its adjacent seas: an analysis of their morphology, setting and behaviour. *Marine Geology* **213**, 343-362.

Hurrell, J. (1995). Decadal trends in the North Atlantic oscillation - regional temperatures and precipitation. *Science* **269**, 679.

Huthnance, J.M., Coelho, H., Griffiths, C.R., Knight, P.J., Rees, A.P., Sinha, B., Vangriesheim, A., White, M., Chatwin, P.G. (2001). Physical structures, advection and mixing in the region of Goban Spur. *Deep-Sea Research II* **48**, 2979-3021.

Huthnance, J.M., Humphery, J.D., Knight, P.J., Chatwin, P.G., Thomsen, L., White, M. (2002). Near-bed turbulence measurements, stress estimates and sediment mobility at the continental shelf edge. *Progress in Oceanography* **52**, 171-194.

Inman, D.L., Nordstrom, C.E., Flick, R.E. (1976). Currents in submarine canyons: an air-sea interaction. *Annual Review of Fluid Mechanics* **8**, 275-310.

Ivanov, V.V., Shapiro, G.I., Huthnance, J.M., Aleynik, D.L., Golovin, P.N. (2004). Cascades of dense water around the world ocean. *Progress in Oceanography* **60**, 47-98.

Johnsen, S.J., Clausen, H.B., Dansgaard, W., Fuhrer, K., Gundestrup, N.S., Hammer, C. U., Iversen, P., Jouzel, J., Stauffer, B., Steffensen, J.P. (1992). Irregular glacial interstadials recorded in a new Greenland ice core. *Nature* **359**, 311-313.

Johnson, A.M. (1970). *Physical processes in geology*. Freeman Cooper, San Francisco, 577 pp.

Jones, A.P., Omoto, K. (2000). Towards establishing criteria for identifying trigger mechanisms for soft-sediment deformation: a case study of Late Pleistocene lacustrine sands and clays, Onikobe and Nakayamadaira Basins, northeastern Japan. *Sedimentology* **47**, 1211-1226.

Jones, P.D., Osborn, T.J., Briffa, K.R. (2001). The evolution of climate over the last millenium. *Science* **292**, 662-667.

Jouanneau, J.M., Garcia, C., Oliveira, A., Rodrigues, A., Dias, J.A., Weber, O. (1998). Dispersal and deposition of suspended sediment on the shelf off the Tagus and Sado estuaries, S.W. Portugal. *Progress in Oceanography* **42**, 233-257.

Jouanneau, J.M., Weber, O., Drago, T., Rodrigues, A., Oliveira, A., Dias, J.M.A., García, C., Schmidt, S., Reyss, J.-L. (2002). Recent sedimentation and sedimentary budgets on the western Iberian shelf. *Progress in Oceanography* **52**, 261-275.

Kampf, J. (2007). On the magnitude of upwelling fluxes in shelf-break canyons. *Continental Shelf Research* **27**, 2211-2223.

Karlin, R. (1990a). Magnetic mineral diagenesis in suboxic sediments at Bettis site W-N, NE Pacific-Ocean. *Journal of Geophysical Research* **95**, 4421-4436.

Karlin, R. (1990b). Magnetite diagenesis in marine-sediments from the Oregon continental-margin. *Journal of Geophysical Research* **95**, 4405-4419.

Karlin, R., Levi, S. (1983). Diagenesis of magnetic minerals in recent hemipelagic sediments. *Nature* **303**, 327-330.

Keevil, G.M., Peakall, J., Best, J.L., Amos, K.J. (2006). Flow structure in sinuous submarine channels: velocity and turbulence structure of an experimental submarine channel. *Marine Geology* **229**, 241-257.

Kenyon, N.H., Millington, J.M., Droz, L., Ivanov, M.K. (1995). Scour holes in a channel-lobe transition zone on the Rhone Cone. In: Pickering, K.T., Hiscott, R.N., Kenyon, N.H., Ricci Lucchi, F., Smith, R. (Eds.). *Atlas of deep water environments: architectural style in turbidite systems.* Chapman & Hall, London, 212-215.

Ketterings, Q.M., Bigham, J.M., Laperche, V. (2000). Changes in soil mineralogy and texture caused by slash-and-burn fires in Sumatra, Indonesia. *Soil Science Society of America Journal* **64**, 1108-1117.

Khripounoff, A., Vangriesheim, A., Babonneau, N., Crassous, P., Dennielou, B., Savoye, B. (2003). Direct observation of intense turbidity current activity in the Zaire submarine valley at 4000 m water depth. *Marine Geology* **194**, 151-158.

Kineke, G.C., Woolfe, K.J., Kuehl, S.A., Milliman, J.D., Dellapenna, T.M., Purdon, R.G. (2000). Sediment export from the Sepik River, Papua New Guinea: evidence for a divergent sediment plume. *Continental Shelf Research* **20**, 2239-2266.

King, J.W., Banerjee, S.K., Marvin, J.A., Özdemir, Ö. (1982). A comparison of different magnetic methods for determining the relative grain size of magnetite in natural materials: some results from lake sediments. *Earth and Planetary Science Letters* **59**, 404-419.

King, J.W., Channell, J.E.T. (1991). Sedimentary magnetism, environmental magnetism and magnetostratigraphy. *Reviews of Geophysics* **29**, 358-370.

Klaucke, I., Cochonat, P. (1999). Analysis of past seafloor failures on the continental slope off Nice, SE France. *Geo-Marine Letters* **19**, 245-253.

Klaucke, I., Savoye, B., Cochonat, P. (2000). Patterns and processes of sediment dispersal on the continental slope off Nice, SE France. *Marine Geology* **162**, 405-422.

Kneller, B. (2003). The influence of flow parameters on turbidite slope and channel architecture. *Marine and Petroleum Geology* **20**, 901-910.

Kneller, B.C., Branney, M.J. (1995). Sustained high-density turbidity currents and the deposition of thick massive beds. *Sedimentology* **42**, 607-616.

Kneller, B., Buckee, C. (2000). The structure and fluid mechanics of turbidity currents: a review of some recent studies and their geological implications. *Sedimentology* **47**, 62-94.

Kneller, B., McCaffrey, W.D. (2003). The interpretation of vertical sequences in turbidite beds: the influence of longitudinal flow structure. *Journal of Sedimentary Research* **73**, 706-713.

Koho, K.A., Kouwenhoven, T.J., de Stigter, H.C., van der Zwaan, G.J. (2007). Benthic foraminifera in the Nazaré Canyon, Portuguese continental margin: sedimentary environments and disturbance. *Marine Micropalaeontology* **66**, 27-51.

Komar, P.D. (1971). Hydraulic jumps in turbidity currents. *Geological Society of America Bulletin* **82**, 1477-1487.

Komar, P.D. (1975). Supercritical flow in turbidity currents: a discussion. *Journal of Sedimentary Petrology* **45**, 747-749.

Kuenen, P.H. (1950). Turbidity currents of high density. *18th International Geological Congress, London*, 1948, Part 8, 44-52.

Kuenen, P.H. (1955). Experiments in connection with turbidity currents and clay suspensions. In: Whittard, W.F., Bradshaw, R. (Eds.). *Submarine geology and geophysics.* Butterworths, London, 47-74.

Kuhlmann, H., Meggers, H., Freudenthal, T., Wefer, G. (2004). The transition of the monsoonal and the N Atlantic climate system off NW Africa during the Holocene. *Geophysical Research Letters* **31**, art. no. L22204, doi:10.1029/2004GL021267.

Kunze, E., Rosenfeld, L.K., Carter, G.S., Gregg, M.C. (2002). Internal waves in Monterey Submarine Canyon. *Journal of Physical Oceanography* **32**, 1890-1913.

Kurchii, B.A. (1992). Possible mechanism of ethylene action. *Ethylene: Physiology, Biochemistry and Practical Applications. An international conference to mark the 90th anniversary on the discovery of ethylene as plant growth regulator by D.N. Nelubov (1886-1926).* Moscow-Puschino-St. Petersburg, 33-34.

Lambeck, K., Yokoyama, Y., Purcell, T. (2002). Into and out of the Last Glacial Maximum: sea-level change during Oxygen Isotope Stages 3 and 2. *Quaternary Science Reviews* **21**, 343-360.

Lastras, G., Arzola, R.G., Masson, D.G., Wynn, R.B., Huvenne, V.A.I., Huhnerbach, V., Canals, M. (2009). Geomorphology and processes in the Central Portuguese Canyons, Western Iberian Margin. *Geomorphology* **103**, 310-329.

Le Borgne, E. (1955). Susceptibilité magnetique anormale du sol superficiel. *Annales de Geophysique* **11**, 399-419.

Lebreiro, S. M. (1995). Sedimentation history off Iberia: Tore Seamount, Tagus and Horseshoe Abyssal Plains. Ph.D. Thesis, Cambridge University Press, Cambridge, 192 pp.

Lebreiro, S.M., Frances, G., Abrantes, F.F.G., Diz, P., Bartels-Jónsdóttir, H.B., Stroynowski, Z.N., Gil, I.M., Pena, L.D., Rodrigues, T., Jones, P.D., Nombela, M.A., Alejo, I., Briffa, K.R., Harris, I., Grimalt, J.O. (2006). Climate change and coastal hydrographic response along the Atlantic Iberian margin (Tagus Prodelta and Muros Ria) during the last two millennia. *The Holocene* **16**, 1003-1015.

Lebreiro, S.M., McCave, I.N., Weaver P.P.E. (1997). Late Quaternary turbidite emplacement on the Horseshoe Abyssal Plain (Iberian Margin). *Journal of Sedimentary Research* **67**, 856-870.

Lewis, K.B. (1994). The 1500-km-long Hikurangi Channel: trench-axis channel that escapes its trench, crosses a plateau, and feeds a fan drift. *Geo-Marine Letters* **14**, 19-28.

Liu, J.T., Liu, K., Huang, J.C. (2002). The effect of a submarine canyon on the river sediment dispersal and inner shelf sediment movements in southern Taiwan. *Marine Geology* **181**, 357-386.

Lowe, D.R. (1979). Sediment gravity flows: their classification and problems of application to natural flows and deposits. In: Doyle, L.J., Pilkey, O.H. (Eds.). Geology of continental slopes. *SEPM Special Publication* **27**, 75-82.

Lowe, D.R. (1982). Sediment gravity flows II: depositional models with special reference to the deposits of high-density turbidity currents. *Journal of Sedimentary Petrology* **52**, 279-297.

Lowe, D.R., Guy, M. (2000). Slurry-flow deposits in the Britannia Formation (Lower Cretaceous), North Sea: a new perspective on the turbidity current and debris flow problem. *Sedimentology* **47**, 31-70.

Mader, C.L. (2001). Modelling the 1755 Lisbon tsunami. *Science of Tsunami Hazards* **19**, 93-98.

Martinson, D.G., Pisias, N.G., Hayas, J.D., Imbrie, J., Moore, J.T.C., Shackleton N.J. (1987). Age dating and the orbital theory of the ice ages: development of a high-resolution 0 to 30,000 year chronostratigraphy. *Quaternary Research* **27**, 1-29.

Masson, D.G., Harbitz, C.B., Wynn, R.B., Pedersen, G., Lovholt, F. (2006). Submarine landslides: processes, triggers and hazard prediction. *Philosophical Transactions of the Royal Society of London A* **364**, 2009-2039.

Masson, D.G., Kenyon, N.H., Gardner, J.V., Field, M.E. (1995). Monterey Fan: channel and overbank morphology. In: Pickering, K.T., Hiscott, R.N., Kenyon, N.H., Ricci Lucchi, F., Smith, R. (Eds.). *Atlas of deep water environments: architectural style in turbidite systems.* Chapman & Hall, London, 74-79.

Mastbergen, D.R., van den Berg, J.H. (2003). Breaching in fine sands and the generation of sustained turbidity currents in submarine canyons. *Sedimentology* **50**, 625-637.

Mayall, M., Jones, E., Casey, M. (2006). Turbidite channel reservoirs – key elements in facies prediction and effective development. *Marine and Petroleum Geology* **23**, 821-841.

Mayall, M., Stewart, I. (2000). The architecture of turbidite slope channels. In: Weimer, P., Slatt, R.M., Coleman, J.L., Rosen, N., Nelson, C.H., Bouma, A.H., Styzen, M., Lawrence, D.T. (Eds.). Global deep-water reservoirs: Gulf Coast Section. *SEPM Foundation 20th Annual Bob F Perkins Research Conference*, 578-586.

McCave, I.N., Hall, I.R. (2002). Turbidity of waters over the Northwest Iberian continental margin. *Progress in Oceanography* **52**, 299-313.

McCave, I.N., Syvitski, J.P.M. (2007). Principles and methods of geological particle size analysis. In: Syvitski, J.P.M. (Ed.). *Principles, methods and application of particle size analysis.* Cambridge University Press, Cambridge, 3-21.

Menard, H.W. (1955). Deep-sea channels, topography and sedimentation. *American Association of Petroleum Geologists Bulletin* **39**, 236-255.

Menard, H.W. (1964). *Marine Geology of the Pacific*. McGraw-Hill, New York, 271 pp.

Middleton, G.V., Hampton, M.A. (1976). Subaqueous sediment transport and deposition by sediment gravity flows. In: Stanley, D.J., Swift, D.J.P. (Eds.). *Marine sediment transport and environmental management.* Wiley, New York, 197-218.

Mil-Homens, M., Stevens, R.L., Boer, W., Abrantes, F., Cato, I. (2006). Pollution history of heavy metals on the Portuguese shelf using ^{210}Pb-geochronology. *Science of the Total Environment* **367**, 466-480.

Morgenstern, N.R. (1967). Submarine slumping and the initiation of turbidity currents. In: Richards, A.F. (Ed.). *Marine Geotechnique*. University of Illinois Press, Urbana, 189-220.

Mulder, T. (1993). The velocity of the 1979 Nice turbidity-current – contribution of modelling. *Comptes Rendus de l’Academie des Sciences II* **317**, 1449-1455.

Mulder, T., Alexander, J. (2001). Abrupt change in slope causes variation in the deposit thickness of concentrated particle-driven density currents. *Marine Geology* **175**, 221-235.

Mulder, T., Cochonat, P. (1996). Classification of offshore mass movements. *Journal of Sedimentary Research* **66**, 43-57.

Mulder, T., Migeon, S., Savoye, B., Faugères, J.C. (2001). Inversely graded turbidite sequences in the deep Mediterranean: a record of deposits from flood-generated turbidity currents? *Geo-Marine Letters* **21**, 86-93.

Mulder, T., Savoye, B., Syvitski, J.P.M. (1997). Numerical modelling of a mid-sized gravity flow: the 1979 Nice turbidity current (dynamics, processes, sediment budget and sea-floor impact). *Sedimentology* **44**, 305-326.

Mulder, T., Savoye, B., Syvitski, J.P.M., Piper, D.J.W. (1998). The Var Submarine System: understanding Holocene sediment delivery processes and their importance to the geological record. In: Stoker, M.S., Evans D., Cramp A. (Eds.). Geological processes on continental margins: sedimentation, mass wasting and stability. *Geological Society of London Special Issue* **129,** 146-166.

Mulder, T., Syvitski, J.P.M. (1995). Turbidity currents generated at river mouths during exceptional discharges to the world oceans. *Journal of Geology* **103**, 285-299.

Mulder, T., Tisot, J.-P., Cochonat, P., Bourillet, J.-F. (1994). Regional assessment of mass failure events in the Baie des Anges, Mediterranean Sea. *Marine Geology* **122**, 29-45.

Mullenbach, B.L., Nittrouer, C.A., Puig, P., Orange, D.L. (2004). Sediment deposition in a modern submarine canyon: Eel Canyon, northern California. *Marine Geology* **211**, 101-119.

Mutti, E. (1979). Turbidites et cônes sous-marins profonds. In: Homewood, P. (Ed.). *Sédimentation détritique (fluviatile, littorale et marine).* Institut Géologique de l'Université de Fribourg, Switzerland, 353-419.

Mutti, E., Normark, W.R. (1987). Comparing examples of modern and ancient turbidite systems: problems and concepts. In: Leggett, J.K., Zuffa, G.G. (Eds.). *Marine clastic sedimentology*. Graham and Trotman, London, 1-38.

Normark, W.R. (1999). Late Pleistocene channel-levee development on Monterey submarine fan, central California. *Geo-Marine Letters* **18**, 179-188.

Normark, W.R., Piper, D.J.W. (1991). Initiation processes and flow evolution of turbidity currents: implications for the depositional record. *SEPM Special Publication* **46**, 207-230.

Normark, W.R., Piper, D.J.W., Posamentier, H., Pirmez, C., Migeon, S. (2002). Variability in form and growth of sediment waves on turbidite channel levees. *Marine Geology* **192**, 23-58.

Normark, W.R., Piper, D.J.W., Sliter, R. (2006). Sea-level and tectonic control of middle to late Pleistocene turbidite systems in Santa Monica Basin, offshore California. *Sedimentology* **53**, 867-897.

Oldfield, F., Thompson, R., Dickson, D.P.E. (1981). Artificial magnetic enhancement of stream bedload: a hydrological application of superparamagnetism. *Physics of the Earth and Planetary Interiors* **26**, 107-124.

Oliveira, A., Rocha, F., Rodrigues, A., Jouanneau, J.-M., Dias, A., Weber, O., Gomes, C. (2002a). Clay minerals from the sedimentary cover from the Northwest Iberian shelf. *Progress in Oceanography* **52**, 233-247.

Oliveira, A., Santos, A.I., Rodrigues, A., Vitorino, J. (2007). Sedimentary particle distribution and dynamics on the Nazaré canyon system and adjacent shelf (Portugal). *Marine Geology* **246**, 105-122.

Oliveira, A., Vitorino, J., Rodrigues, A., Jouanneau, J.M., Dias, J.A., Weber, O. (2002b). Nepheloid layer dynamics in the northern Portuguese shelf. *Progress in Oceanography* **52**, 195-213.

Palanques, A., Guillen, J., Puig, P., de Madron, X.D. (2008). Storm-driven shelf-to-canyon suspended sediment transport at the southwestern Gulf of Lions. *Continental Shelf Research* **28**, Special Issue 15, 1947-1956.

Parker, G., García, M., Fukushima, Y., Yu, W. (1987). Experiments on turbidity currents over an erodible bed. *Journal of Hydraulic Research* **25**, 123-147.

Pattenden, A.D.C. (submitted). The influence of submarine canyons on the structure and dynamics of megafaunal communities. Ph.D. Thesis, University of Southampton, Southampton, 183 pp.

Paull, C., Mitts, P., Ussler III, W., Keaten, R., Greene, H.G. (2005). Trail of sand in upper Monterey Canyon: offshore California. *Geological Society of America Bulletin* **117**, 1134-1145.

Paull, C.K., Ussler III, W., Greene, H.G., Keaten, R., Mitts, P., Barry, J. (2003). Caught in the act: the 20 December 2001 gravity flow event in Monterey Canyon. *Geo-Marine Letters* **22**, 227-232.

Pautot, G. (1981). Cadre morphologique de la Baie des Anges. Modèle d’instabilité de pente continentale. *Oceanologica Acta* **4**, 203-212.

Peakall, J., McCaffrey, B., Kneller, B. (2000). A process model for the evolution, morphology and architecture of sinuous submarine channels. *Journal of Sedimentary Research* **70**, 434-448.

Peláez, J.A., López Casado, C. (2002). Seismic hazard estimate at the Iberian Peninsula. *Pure Applied Geophysics* **159**, 2699-2713.

Petruncio, E.T., Rosenfeld, L.K., Paduan, J.D. (1998). Observations of the internal tide in Monterey Canyon. *Journal of Physical Oceanography* **28**, 1873-1903.

Pinheiro, L.M., Wilson, R.C.L., Pena dos Reis, R., Whitmarsh, R.B., Ribeiro, A. (1996). The Western Iberian Margin: a geophysical and geological overview. In: Whitmarsh, R.B., Sawyer, D.S., Klaus A., Masson D.G. (Eds.). *Proceedings of the Ocean Drilling Program*, Scientific Results **149**, 3-23.

Piper, D.J.W. (1970). Transport and deposition of Holocene sediment on La Jolla deep sea fan, California. *Marine Geology* **8**, 211-227.

Piper, D.J.W. (1978). Turbidite muds and silts on deepsea fans and abyssal plains. In: Stanley, D., Kelling, G. (Eds.). *Sedimentation in submarine fans and trenches*. Stroudsberg, Pennsylvania, Dowden, Hutchinson & Ross, 163-175.

Piper, D.J.W., Cochonat, P., Morrison, M.L. (1999a). The sequence of events around the epicentre of the 1929 Grand Banks earthquake: initiation of debris flows and turbidity current inferred from sidescan sonar. *Sedimentology* **46**, 79-97.

Piper, D.J.W., Hiscott, R.N., Normark, W.R. (1999b). Outcrop-scale acoustic facies analysis and latest Quaternary development of Hueneme and Dume submarine fans, offshore California. *Sedimentology* **46**, 47-78.

Piper, D.J.W., Normark, W.R. (1983). Turbidite depositional patterns and flow characteristics, Navy Submarine Fan, California Borderland. *Sedimentology* **30**, 681-694.

Piper, D.J.W., Normark, W.R. (2001). Sandy fans – from Amazon to Hueneme and beyond. *American Association of Petroleum Geologists Bulletin* **85**, 1407-1438.

Piper, D.J.W., Savoye, B. (1993). Processes of late Quaternary turbidity current flow and deposition on the Var deep-sea fan, north-west Mediterranean Sea. *Sedimentology* **40**, 557-582.

Pires, H.N.O. (1985). Alguns aspectos do clima de agitação marítima de interesse para a navegação na costa de Portugal. *O clima de Portugal* **37**, 34 pp.

Pratson, L.F., Coakley, B.J. (1996). A model for the headward erosion of submarine canyons induced by downslope-eroding sediment flows. *Geological Society of America Bulletin* **108**, 225-234.

Pratson, L.F., Ryan, W.B.F., Mountain, G.S., Twichell, D.C. (1994). Submarine canyon initiation by downslope-eroding sediment flows: evidence in late Cenozoic strata on the New Jersey continental slope. *Geological Society of America Bulletin* **106**, 395-412.

Prior, D.B., Doyle, E.H. (1985). Intra-slope canyon morphology and its modification by rockfall processes, U.S. Atlantic continental margin. *Marine Geology* **67**, 177-196.

Puig, P., Ogston, A.S., Mullenbach, B.L., Nittrouer, C.A., Parsons, J.D., Sternberg, R.W. (2004a). Storm-induced sediment gravity flows at the head of the Eel submarine canyon, northern California margin. *Journal of Geophysics Research C (Oceans)* **109**, art. no. C03019, doi: 10.1029/2003JC001918.

Puig, P., Ogston, A.S., Mullenbach, B.L., Nittrouer, C.A., Sternberg, R.W. (2003). Shelf-to-canyon sediment-transport processes on the Eel continental margin (northern California). *Marine Geology* **193**, 129-149.

Puig, P., Palanques, A., Guillen, J., El Khatab, M. (2004b). Role of internal waves in the generation of nepheloid layers on the northwestern Alboran slope: implications for continental margin shaping. *Journal of Geophysics Research C (Oceans)* **109**, art. no. C09011, doi: 10.1029/2004JC002394.

Quaresma, L., Vitorino, J., Oliveira, A. (2007). Evidences of sediment resuspension by nonlinear internal waves on the western Portuguese mid shelf. *Marine Geology* **246**, 123-143.

Reimer, P.J., Baillie, M.G.L., Bard, E., Bayliss, A., Beck, J.W., Bertrand, C.J.H., Blackwell, P.G., Buck, C.E., Burr, G.S., Cutler, K.B., Damon, P.E., Edwards, R.L., Fairbanks, R.G., Friedrich, M., Guilderson, T.P., Hogg, A.G., Hughen, K.A., Kromer, B., McCormac, G., Manning, S., Ramsey, C.B., Reimer, R.W., Remmele, S., Southon, J.R., Stuiver, M., Talamo, S., Taylor, F.W., van der Plicht, J., Weyhenmeyer, C.E. (2004). IntCal04 terrestrial radiocarbon age calibration, 0-26 cal kyr BP. *Radiocarbon* **46**, 1029-1058.

Reynaud, J.-Y., Tessier, B., Berné, S., Chamley, H., de Batist, M. (1999). Tide and wave dynamics on a sand bank from the deep shelf of the Western channel approaches. *Marine Geology* **161**, 339-359.

Richter, T.O., de Stigter, H.C., Boer, W., Jesus, C.C., van Weering, T.C.E. (in press). Dispersal of natural and anthropogenic lead through submarine canyons at the Portuguese margin. *Deep-Sea Research I*.

Ritchie, J.C., Eyles, C.H., Haynes, C.V. (1985). Sediment and pollen evidence for an early to mid-Holocene humid period in the eastern Sahara. *Nature* **330**, 645-647.

Roberts, A.P. (2006). High-resolution magnetic analysis of sediment cores: strengths, limitations and strategies for maximizing the value of long-core magnetic data. *Physics of the Earth and Planetary Interiors* **156**, 162-178.

Roberts, A.P., Pike, C.R., Verosub, K.L. (2000). First-order reversal curve diagrams: a new tool for characterizing the magnetic properties of natural samples. *Journal of Geophysical Research* **105**, 28461-28475.

Robinson, S.G. (1993). Lithostratigraphic applications for magnetic susceptibility logging of deep-sea sediment core: examples from ODP Leg 115. *High Resolution Stratigraphy Special Publication* **70**, 65-98.

Rowan, C.J., Roberts, A.P., Broadbent, T. (in press). Paleomagnetic smoothing and magnetic enhancement in marine sediments due to prolonged early diagenetic growth of greigite. *Earth and Planetary Science Letters,* doi:10.1016/j.epsl.2008.10.016.

Ruddiman, W.F. (2007). The early anthropogenic hypothesis: challenges and responses. *Reviews of Geophysics* **45**, art. no. RG4001, doi: 10.1029/2006RG000207.

Rummery, T.A. (1983). The use of magnetic measurements in interpreting the fire histories of lake drainage basins. *Hydrobiologia* **103**, 53-58.

Rummery, T.A., Bloemendal, J., Dearing, J., Oldfield, F., Thompson, R. (1979). The persistence of fire-induced magnetic oxides in soils and lake sediments. *Annals of Geophysics* **35**, 103-107.

Sagnotti, L., Rochette, P., Jackson, M., Vadeboin, F., Dinarès-Turell, J., Winkler, A., MAG-NET Science Team (2003). Inter-laboratory calibration of low-field magnetic and anhysteretic susceptibility measurements. *Physics of the Earth and Planetary Interiors* **138**, 25-38.

Salles, T., Mulder, T., Gaudin, M., Cacas, M.C., Lopez, S., Cirac, P. (2007). Simulating the 1999 Capbreton canyon turbidity current with a Cellular Automata model. *Geomorphology* **97**, 516-537.

Sanford, M.W., Kuehl, S.A., Nittrouer, C.A. (1990). Modern sedimentary processes in the Wilmington Canyon area, U.S. East Coast. *Marine Geology* **92**, 205-226.

Schmidt, S., de Stigter, H.C., van Weering, T.C.E. (2001). Enhanced short-term sediment deposition within the Nazaré Canyon, North-East Atlantic. *Marine Geology* **173**, 55-67.

Scott, A.C. (2000). The Pre-Quaternary history of fire. *Palaeogeography, Palaeoclimatology, Palaeoecology* **164**, 281-329.

Segall, M.P., Kuehl, S.A., Gipson Jr., M. (1989). Clay-size minerals as indicators of modern sedimentary processes in submarine canyons: application to the Wilmington Canyon system. *Marine Geology* **90**, 175-192.

Shanmugam, G., Moiola, R.J. (1982). Eustatic control of turbidites and winnowed turbidites. *Geology* **10**, 231-235.

Shapiro, G.I., Huthnance, J.M., Ivanov, V.V. (2003). Dense water cascading off the continental shelf. *Journal of Geophysical Research* **108**, art. no. 3390, doi:10.1029/2002JC001610.

Shepard, F.P., Buffington, E.C. (1968). La Jolla submarine fan-valley. *Marine Geology* **6**, 107-143.

Shepard, F.P., Dill, R.F., von Rad, U. (1969). Physiography and sedimentary processes of La Jolla Fan and Fan Valley. *American Association of Petroleum Geologists Bulletin* **53**, 390-420.

Shepard, F.P., McLoughlin, P.A., Marshall, N.F., Sullivan, G.G. (1977). Current-meter recordings of low-speed turbidity currents. *Geology* **5**, 297-301.

Snowball, I.F., Thompson, R. (1990). A mineral magnetic study of Holocene sedimentation in Lough Catherine, Northern Ireland. *Boreas* **19**, 127-146.

Stach, E., Mackowsky, M.-T., Teichmüller, M., Taylor, G.H., Chandra, D., Teichmüller, R. (1975). *Stach's textbook of coal petrology*. Gebrüder Borntraeger, Stuttgart, 428 pp.

Stanley, D.J., Cuver, S.J., Stubblefield, W.L. (1986). Petrologic and foraminiferal evidence for active downslope transport in Wilmington Canyon. *Marine Geology* **69**, 207-218.

Stuiver, M., Reimer, P.J. (1993). Extended C-14 data-base and revised CALIB 3.0 C-14 age calibration program. *Radiocarbon* **35**, 215-230.

Stuiver, M., Reimer, P.J., Bard, E., Beck, J.W., Burr, G.S., Hughen, K.A., Kromer, B., McCormac, G., van der Plicht, J., Spurk, M. (1998). INTCAL98 radiocarbon age calibration, 24,000-0 cal BP. *Radiocarbon* **40**, 1041-1083.

Talling, P.J., Amy, L.A., Wynn, R.B., Peakall, J., Robinson, M. (2004). Beds comprising debrite sandwiched within co-genetic turbidite: origin and widespread occurrence in distal depositional environments. *Sedimentology* **51**, 163-194.

Talling, P.J., Wynn, R.B., Masson, D.G., Frenz, M., Cronin, B.T., Schiebel, R., Akhmetzanov, A.M., Dallmeier-Tiessen, S., Benetti, S., Weaver, P.P.E., Georgiopoulou, A., Zühlsdorff, C., Amy, L.A. (2007). Onset of submarine debris flow deposition far from original giant landslide. *Nature* **450**, 541-544.

Terrinha, P., Pinheiro, L.M., Henriet, J.-P., Matias, L., Ivanov, M.K., Monteiro, J.H., Akhmetzhanov, A., Volkonskaya, A., Cunha, T., Shaskin, P., Rovere, M. (2003). Tsunamigenic-seismogenic structures, neotectonics, sedimentary processes and slope instability on the southwest Portuguese Margin. *Marine Geology* **195**, 55-73.

Thomson, J., Weaver, P.P.E. (1994). An AMS radiocarbon method to determine the emplacement time of recent deep-sea turbidites. *Sedimentary Geology* **89**, 1-7.

Traykovski, P., Geyer, W.R., Irish, J.D., Lynch, J.F. (2000). The role of wave-induced density-driven fluid mud flows for cross-shelf transport on the Eel River continental shelf. *Continental Shelf Research* **20**, 2113-2140.

Trigo, R.M., Osborn, T.J., Corte-Real, J. (2002). The North Atlantic oscillation influence on Europe: climate impacts and associated physical mechanisms. *Climate Research* **20**, 9-17.

Twichell, D.C., Roberts, D.G. (1982). Morphology, distribution and development of submarine canyons on the United States Atlantic continental slope between Hudson and Baltimore Canyons. *Geology* **10**, 408-412.

van Weering, T.C.E., de Stigter, H.C., Boer, W., de Haas, H. (2002). Recent sediment transport and accumulation on the NW Iberian margin. *Progress in Oceanography* **52**, 349-371.

Vanney, J.R., Mougenot, D. (1981). La plateforme continentale du Portugal et les provinces adjacentes: analyse géomorphologique. *Memorias dos Serviços Geológicos de Portugal* **28**, 1-156.

Vanney, J.R., Mougenot, D. (1990). A Gouf-type canyon, the Canhão-da-Nazaré (Portugal). *Oceanologica Acta* **13**, 1-14.

Verardo, D.J., Ruddiman, W.F. (1996). Late Pleistocene charcoal in tropical Atlantic deep-sea sediments: climatic and geochemical significance. *Geology* **24**, 855-857.

Verosub, K.L., Roberts, A.P. (1995). Environmental magnetism - past, present and future. *Journal of Geophysical Research* **100**, 2175-2192.

Vis, G.-J., Kasse, C., Vandenberghe, J. (2008). Late Pleistocene and Holocene palaeogeography of the Lower Tagus Valley (Portugal): effects of relative sea level, valley morphology and sediment supply. *Quaternary Science Reviews* **27**, 1682-1709.

Vitorino J., Coelho, E.F. (1998). Water mass dynamics at the northwest Iberian margin. *First scientific report of the project OMEX I-II*, 29 pp.

Vitorino, J., Oliveira, A., Jouanneau, J.M., Drago, T. (2002a). Winter dynamics on the northern Portuguese shelf. Part 1: physical processes. *Progress in Oceanography* **52**, 129-153.

Vitorino, J., Oliveira, A., Jouanneau, J.-M., Drago, T. (2002b). Winter dynamics on the northern Portuguese shelf. Part 2: bottom boundary layers and sediment dispersal. *Progress in Oceanography* **52**, 155-170.

Vizcaino, A., Gràcia, E., Pallàs, R., García-Orellana, J., Escutia, C., Casas, D., Willmott, V., Diez, S., Asioli, A., Dañobeitia, J. (2006). Sedimentology, physical properties and age of mass transport deposits associated with the Marques de Pombal Fault, Southwest Portuguese Margin. *Norwegian Journal of Geology* **86**, 177-186.

Walsh, J.P., Nittrouer, C.A. (2003). Contrasting styles of off-shelf sediment accumulation in New Guinea. *Marine Geology* **196**, 105-125.

Weaver, P.P.E. (2003). Northwest African Continental Margin: history of sediment accumulation, landslide deposits, and hiatuses as revealed by drilling the Madeira Abyssal Plain. *Paleoceanography* **18**, art. no. 1009, doi: 10.1029/2002PA000758.

Weaver, P.P.E., Billett, D., Boetius, A., Danovaro, R., Freiwald, A., Sibuet, M. (2004). Hotspot Ecosystem Research on Europe's Deep-Ocean Margin. *Oceanography* **17**, 132-143.

Weaver, P.P.E., Canals, M. (2003). The Iberian and Canaries Margin including NW Africa. In: Mienert J., Weaver, P.P.E. (Eds.). *European Margin Sediment Dynamics*, Springer-Verlag, Berlin, 251-260.

Weaver, P.P.E., Kuijpers, A. (1983). Climatic control of turbidite deposition on the Madeira Abyssal Plain. *Nature* **306**, 360-363.

Weaver, P.P.E., Rothwell, R.G., Ebbing, J., Gunn, D., Hunter, P.M. (1992). Correlation, frequency of emplacement and source directions of megaturbidites on the Madeira Abyssal-Plain. *Marine Geology* **109**, 1-20.

Weaver, P.P.E., Wynn, R.B., Kenyon, N.H., Evans, J. (2000). Continental margin sedimentation, with special reference to the north-east Atlantic margin. *Sedimentology* **47**, 239-256.

Weeks, R., Laj, C., Endignoux, L., Fuller, M., Roberts, A., Manganne, R., Blanchard, E., Goree, W. (1993). Improvements in long-core measurement techniques - applications in palaeomagnetism and palaeoceanography. *Geophysical Journal International* **114**, 651-662.

Weltje, G.J., de Boer, P.L. (1993). Astronomically induced palaeoclimatic oscillations reflected in Pliocene turbidite deposits of Corfu (Greece): implications for the interpretation of higher order cyclicity in fossil turbidite systems. *Geology* **21**, 307-310.

Wollast, R., Chou, L. (2001). Ocean Margin EXchange in the Northern Gulf of Biscay: OMEX I. An introduction. *Deep-Sea Research II* **48**, 2971-2978.

Wynn, R.B., Cronin, B.T., Peakall, J. (2007). Sinuous deep-water channels: genesis, geometry and architecture. *Marine and Petroleum Geology* **24**, 341-387.

Wynn, R.B., Kenyon, N.H., Masson, D.G., Stow, D.A.V., Weaver, P.P.E. (2002a). Characterization and recognition of deep-water channel-lobe transition zones. *American Association of Petroleum Geologists Bulletin* **86**, 1441-1462.

Wynn, R.B., Piper, D.J.W., Gee, M.J.R. (2002b). Generation and migration of coarse-grained sediment waves in turbidity current channels and channel-lobe transition zones. *Marine Geology* **192**, 59-78.

Wynn, R.B., Stow, D.A.V. (2002). Classification and characterisation of deep-water sediment waves. In: Wynn R.B., Stow, D.A.V. (Eds.). Recognition and interpretation of deep-water sediment waves: implications for palaeoceanography, hydrocarbon exploration and flow process interpretation. *Marine Geology Special Issue* **192**, 7-22.

Xu, J.P., Noble, M.A., Rosenfeld, L.K. (2004). In situ measurements of velocity structure within turbidity currents. *Geophysical Research Letters* **31**, art. no. L09311, doi: 10.1029/2004GL019718.

Yokoyama, Y., de Dekker, P., Lambeck, K., Jonhnston, P., Fifield, L.K. (2000). Timing of the Last Glacial Maximum from observed sea-level minima. *Nature* **406**, 713-716.

Zaragosi, S., Bourillet, J.F., Eynaud, F., Toucanne, S., Denhard, B., van Toer, A., Lanfumey, V. (2006). The impact of the last European deglaciation on the deep-sea turbidite systems of the Celtic-Armorican margin (Bay of Biscay). *Geo-Marine Letters* **26**, 317-329.

Zazo, C., Dabrio, C.J., Goy, J.L., Lario, J., Cabero, A., Silva, P.G., Bardají, T., Mercier, N., Borja, F., Roquero, E. (2008). The coastal archives of the last 15 ka in the Atlantic–Mediterranean Spanish linkage area: sea level and climate changes. *Quaternary International* **181**, 72-87.

Zhang, H., King, B., Swinney, H.L. (2008). Resonant generation of internal waves on a model continental slope. *Physical Review Letters* **100**, 244504.

Zühlsdorff, C., Wien, K., Stuut, J.-B.W., Henrich, R. (2007). Late Quaternary sedimentation within a submarine channel-levee system offshore Cap Timiris, Mauritania. *Marine Geology* **240**, 217-234.